Contributions on Sediment Transport

Kolumban Hutter

A Tutorial on Prograding and Retrograding Hypo- and Hyper-pycnal Deltaic Formations into Quiescent Ambients

Kolumban Hutter and Ioana Luca

A Global View of Sediment Transport in Alluvial Systems

David Vetsch

Force-coupled Lagrangian Approach for Numerical Modelling of Bed-load Transport

---

Berichte des Lehrstuhls und der Versuchsanstalt für
Wasserbau und Wasserwirtschaft

Herausgegeben von Prof. Peter Rutschmann

Technische Universität München

Lehrstuhl für Wasserbau und Wasserwirtschaft

80333 München, Arcisstraße 21
Germany

Tel.: 089 / 289 23161
Fax: 089 / 289 23172
E-Mail: wabau@bv.tum.de

Versuchsanstalt für Wasserbau und Wasserwirtschaft (Oskar von Miller - Institut)

82432 Obernach, Walchensee
Germany

Tel.: 08858 / 9203 0
Fax: 08858 / 9203 33
E-Mail: obernach@bv.tum.de

ISSN 1437-3513

ISBN 978-3-940476-25-8

Berichte des Lehrstuhls und der Versuchsanstalt für
Wasserbau und Wasserwirtschaft

Herausgegeben von Prof. Peter Rutschmann
Ordinarius für Wasserbau und Wasserwirtschaft, TU München

Druck und Einband: Meissner Druck GmbH, Oberaudorf

Vorwort des Herausgebers

Die Idee zur vorliegenden Mitteilung entstand vor gut einem Jahr, als Prof. Dr. Kolumban Hutter im Rahmen des Umweltingenieurstudiengangs an der TU München einen Blockkurs las. Er hatte zu dieser Zeit eine Arbeit zum Thema der Delta-Formation geschrieben, welche länger als ursprünglich angenommen ausfiel, die er aber nicht substantiell kürzen wollte. Im Gespräch entstand die Idee, den Beitrag zusammen mit anderen in einem Sammelband „Contributions on Sediment Transport“ zu publizieren.

Zur gleichen Zeit durfte ich die Promotion von Dr. David Vetsch an der Versuchsanstalt für Wasserbau, Hydrologie und Glaziologie der ETH Zürich (VAW) als zweiter Prüfer begleiten. Das Thema von Dr. Vetsch ging auf eine Idee zurück, für die ich vor meinem Weggang von der ETH noch ein Forschungsgesuch eingereicht hatte. Ich fand die Arbeit von David Vetsch so interessant, dass ich anfragte, eine Kurzfassung in unserem Sammelband veröffentlichen zu dürfen. Diese zwei Beiträge wollten wir mit einer eigenen Publikation über eine Auftragsarbeit des Lehrstuhls ergänzen. Leider wurden wir vom Auftraggeber gebeten, die Resultate nicht im jetzigen Zeitpunkt zu veröffentlichen, weswegen unser eigener Beitrag zu meinem großen Bedauern entfallen muss. Prof. Hutter sprang mit einem zweiten Beitrag zum Thema „Sediment Transport in Alluvialen Systemen“, den er zusammen mit Prof. Dr. Ioana Luca verfasste, in die Bresche.

Trotz der Enttäuschung über das Nichterscheinen des eigenen Beitrags, freut es mich außerordentlich, dass dieser Band zustande gekommen ist und in unserer Schriftenreihe publiziert werden kann. Zum einen, weil ich jahrelang mit Prof. Hutter und David Vetsch an der VAW - obschon in unterschiedlichen Abteilungen tätig - zusammen gearbeitet habe, zum anderen weil die Autoren für eine hohe Qualität der Beiträge garantieren.

Prof. Dr. Kolumban Hutter studierte Bauingenieurwesen an der ETH Zürich, wo er auch eine Stelle als wissenschaftlicher Mitarbeiter antrat. Es zog ihn allerdings nach Amerika, wo er in der angewandten Mechanik an der Cornell University, Ithaca, USA, promovierte, lehrte und forschte. Im Jahre 1972 kehrte er an die VAW zurück, wo er sich mit Arbeiten der Theoretischen Glaziologie, der Physikalischen Limnologie und der Lawinendynamik befasste.

Prof. Hutter wurde von zahlreichen Universitäten als Gastprofessor eingeladen, bevor er 1987 einem Ruf an die TU Darmstadt folgte und den Lehrstuhl für Mechanik übernahm. Er hat unzählige Publikationen in den renommiertesten Fachzeitschriften und mit einem außerordentlich breiten Fachspektrum veröffentlicht. Neben vielen Auszeichnungen seines wissenschaftlichen Wirkens ist insbesondere die Verleihung des Max-Plank Forschungspreises, 1994, des Alexander von Humboldt Forschungspreises in Polen, 1998, des Seligman-Cristal Awards der Glaziologischen Gesellschaft, 2003, und die Einladung zu einer Distinguished Russel Severance Springer Professur des Departements Maschineningenieurwesens der Universität von Kalifornien in Berkeley, 2004, zu erwähnen.

Prof. Dr. Ioana Luca hat in Bukarest Mathematik studiert und mit einem Thema der Kontinuums-thermodynamik, insbesondere hyperbolischer Wärmeleitungsgleichungen promoviert und arbeitet seither vorwiegend als Dozentin der Mathematik am Polytechnikum in Bukarest. In der Forschung hat sich Prof. Luca neben der Ausbreitung von Wellen mit Turbulenz granularer Medien, mit Gravitationsströmen, d. h, Lawinen, Murgängen von Fluid-Feststoff-Massen entlang allgemeiner Topografien und deren theoretisch-numerischer Vorhersage befasst. I. Luca hat Forschungsaufenthalte an der TU Berlin, TU Darmstadt und der Universität Bochum verbracht und war von 2007-2009 als Visiting Scientist an der Academia Sinica in Taiwan mit Gravitationsströmen befasst. Sie besitzt seit 2012 eine außerordentliche Professur.

Dr. David Vetsch studierte Bauingenieurwesen an der ETH Zürich. Nach seinem Studium trat er eine Stelle als wissenschaftlicher Mitarbeiter an der VAW an. Er beschäftigte sich seit Anbeginn seiner Tätigkeit sehr intensiv mit der numerischen Simulation und ist Geburtshelfer des mittlerweile weit verbreiteten Programms BASEMENT zur 1D und 2D Strömungsberechnung unter Berücksichtigung von Geschiebetransport. Für seine Diplomarbeit an der ETH Zürich erhielt er im Jahre 2000 den Culmann Preis.

München, den 22. Januar 2013
Prof. Dr. Peter Rutschmann

Contents

A Tutorial on Prograding and Retrograding Hypo- and Hyper-pycnal Deltaic Formations into Quiescent Ambients *

Kolumban Hutter†

†Bergstrasse 5, 8044 Zürich, Switzerland, hutter@vaw.baug.ethz.ch

Abstract

Sediment transport from mountainous rivers into a quiescent ambient with simultaneous formation of deltas is reviewed. To focus on the principal physical processes attention is restricted to flow in vertical cross-sections with no changes perpendicular to the plane of the flow. The bed load transport in the river is derived for quasi-steady situations using sediment mass balance and the MOHR-TERZAGHI shear stress-pressure relation with the angle of internal friction, ϕ as the essential frictional parameter. The emerging model is a diffusion equation for the upper surface of the moving sediment layer and corresponding boundary conditions. Its diffusivity is expressible in terms of the hydraulic discharge, the densities of the sediment and the turbid water, the angle of internal friction and a parameter characterizing the bed-parallel sediment velocity in terms of the average velocity in the turbid layer. When this river flow enters quiescent water, two different classes of deltas can be formed. When the entering water is either neutrally buoyant or lighter than the ambient water, the sudden reduction in tractive force along the bed generates a conspicuous avalanching flow to depth. This leads to steep-sloped foreset deposits with delta fronts inclined by the angle of internal friction. Such so-called GILBERT-type deltas are governed by a jump requirement of the sediment flux across the shore line and the geometry of the receiving basin. When the inflowing discharge is denser than the receiving ambient water, it will dive down as a turbulent under-current. The basal sediment transport in this subaqueous density current is analogous to the subaerial case and again described by a diffusion equation with similarly determined diffusivity. The combined dual subaerial-subaqueous sedimenting process is mathematically very similar to a (generalized) STEFAN problem, e.g. the freezing of an ice cover on a lake. We present (mostly analytical) solutions for (i) bedrock-alluvial transitions, (ii) overtopping failure of a dam, (iii) topset-foreset diffusion processes for hypo- and hyper-pycnal deltas. Laboratory experiments demonstrate the adequacy of the models.

*This manuscript intends to serve as a basis for the learning student or scientist. In all modesty, most work is by others and only a few small ideas seem to be my own. No claim of completeness is made, but I hope that a glimpse of elegance of this theory is recognizable. If it is so, it is the merit of the authors of the referenced papers.

Contents

1 Introduction. Estuarine development due to riverine sediment inflow

1.1 Fluvial-deltaic sedimentation in lakes from rivers

Sediment transport in alluvial rivers constitutes in mountainous lakes the dominant mode of sediment delivery. These modes arise generally in two different forms, as bedload transport of the coarse grains and as suspended matter of the clay and silt fractions. The amount of the dense, coarse movable sediment depends on the driving stress – in quasi-steady flows expressed by the MEYER-PETER [41] or similar formulae – the packing of the river bed and the size composition of the sand comprising the transported total sediment mass. Of the total sediment load a nominal threshold grain diameter $\phi_{bedload}^{thres}$ essentially separates the moving sediments into two classes, (i) the bedload, moving in the bottom saltation layer and (ii) the fine grains, which are suspended in the turbulent water above the saltation layer. The relative proportion of the dense bedload-mass flow and the suspended dilute sediment-mass diffusion depends in quasi-steady states on the local inclination of the river, provided this slope is smooth and suffers only small changes with position.

At the entrance of a river into relatively quiescent waters, an artificial reservoir, lake or the ocean, the entering bed and sediment loads will suddenly be subjected to an abrupt change of the hydrodynamic conditions, and depending on the relative hydro-physical changes, the subsequent process will differently evolve according to these conditions.

In what follows, we introduce a few terms from the geological nomenclature, which will facilitate later discussions, see SWENSON et al. (2000), [63], LAI & CAPART (2007), [33] and Fig. 1:

- Sediment laden river flow will be referred to as *subaerial* flow and the region of river flow is called *topset*.
- Correspondingly, the flow immediately beyond the shoreline is called the *subaqueous* flow, and the region of this flow is denoted as *foreset*. Beyond the delta region it is often called the *bottomset*.
- If the entering fluid flow as a mixture of water and sediment is lighter than, or equal to, the water density of the ambient, the flow characteristics will be called *hypopycnal* and *homopycnal*, respectively, if it is denser than the mixture density of the ambient, then it is called *hyperpycnal*.

Dismissing the complex transition conditions in the immediate vicinity of the advancing (or retreating) shoreline, the downstream subaqueous deposits differ for the three mentioned pycnal characterizations from one another. The sudden change in speed that occurs when the river water crosses the shoreline and enters the region of calm water generates 'for homopycnal and hypopycnal flows, in which the entering discharge is either neutrally buoyant or lighter than the ambient fluid, a sudden reduction in tractive force along the bed [. . .]. This leads to steep-sloped foreset deposits controlled by the angle of repose (approximately angle of internal friction)' (LAI & CAPART, 2007, [33]). The coarser grains will avalanche down the shore slope and the fines will stay afloat in a near surface jet-boundary layer and settle out further downstream as bottomset beds. 'Such deltas, and their topset-foreset-bottomset architecture were first described in a classical work by GILBERT (1890), [19] and are accordingly known as Gilbert-type deltas' (LAI & CAPART 2007, [33]).

Two quantities characterize GILBERT-type delta wedges, (i) the shoreline position $s(t)$, which is the horizontal distance of the shoreline (see Fig. 1a) from a Cartesian origin far upstream in the topset and

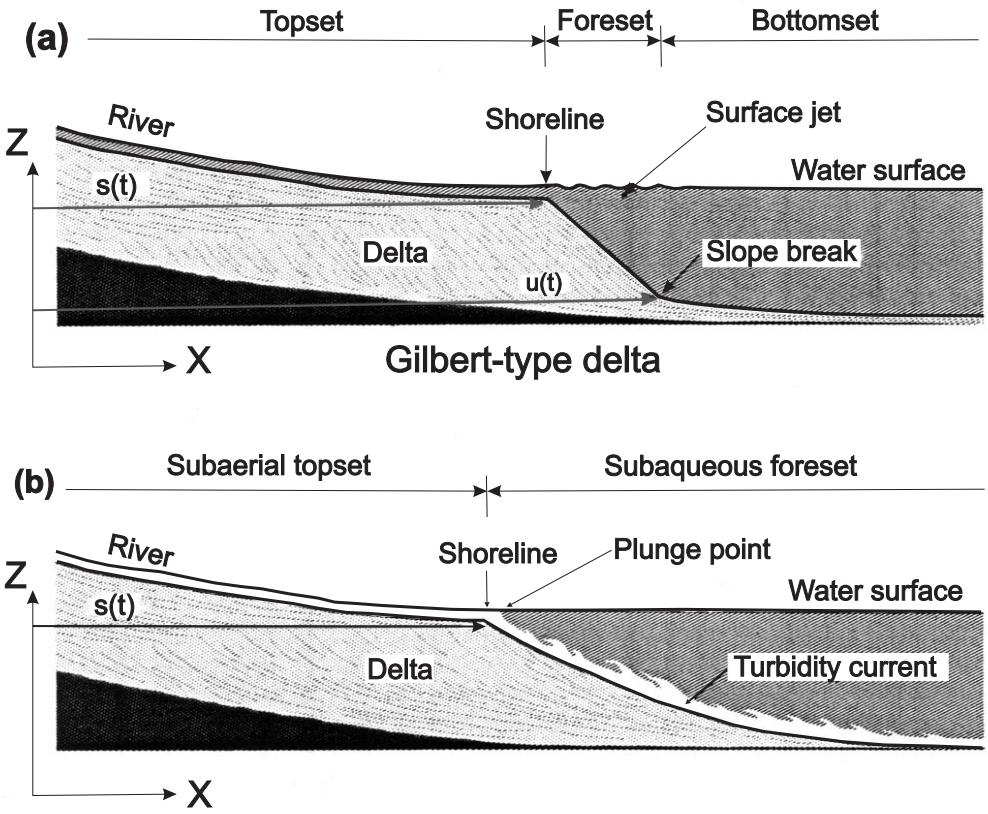

Figure 1: Alluvial river deltas under hypo- or homopycnal, GILBERT-type (a), and under hyperpycnal (b) conditions, illustrating the common nomenclature. GILBERT-type deltas have plane frontal slopes at the angle of repose of the coarse grained sediment, and delta growth is by granular avalanching. Hyperpycnal deltas evolve under the action of a turbidity current, and the basal sediment transport is analogous to sediment transport in alluvial rivers. The horizontal position of the shoreline is $x = s(t)$. Similarly, the toe of the slope break is given by $x = u(t)$. Figure after LAI & CAPART (2007), [33], with changes, © *J. Geophys. Res. Earth Surface*

(ii) the delta toe $u(t)$, which is the horizontal distance from the same Cartesian origin of the intersection point between the deposit-wedge front and the basement. The latter is in geological applications taken as a subsiding fault block or any well defined lower boundary of the Earth mantle, in engineering-type sedimentology of lake deposits a well defined lake bottom surface in the recent past or at present. Of interest are the time evolutions of $s(t)$ and $u(t)$. The following geological nomenclature is commonly used (see VOLLER et al., 2006, [66]).

- *Regression* and *transgression* refer, respectively, to the foreward $(\dot{s}(t) > 0)$ and landward $(\dot{s}(t) < 0)$ migration of the shoreline.
- *Progradation* and *retrogradation* refer, respectively, to the foreward growth $(\dot{u}(t) > 0)$ and landward retreat $(\dot{u}(t) < 0)$ of the entire fluvio-deltaic system.

1.2 Morpho-dynamics of hypo-, homo- and hyper-pycnal flows

According to LAI & CAPART (2007), [33] hyperpycnal flows occur when the inflowing discharge is denser than the receiving ambient water. This may occur e. g. when floodwater, laden with sediments, enters fresh water lakes, or when cold river water from snow melt enters a lake of warmer water. In these cases the denser river water will form a density current (Fig. 1b) moving down the littoral slope,

approximately in the direction of steepest descent of the lake bathymetry from the plunge point of the river. Entrainment of ambient water in such density currents is generally small (and in a first approximation negligible), because stable stratification inhibits turbulence at the upper boundary of the density current, (ELLISON & TURNER, 1959 [12], TURNER, 1973, [65]). Such flows maintain therefore, in general, their boundary-layer character as long as their density is larger than that of the ambient fluid. If this remains so through the entire depth such turbidity currents may travel over considerable distances, decaying primarily due to a continuous and size dependent settling-out of their suspended matter.

Whereas hypopycnal deltas have steep slopes of the size of the angle of internal friction, hyperpycnal deltas are much less steep, with generally convex shape (FLEMING and JORDAN 1989, [14], 1990 [26]; KOSTIC et al, 2002, [28]; KOSTIC and PARKER, 2003, [29], [30]). The steepest inclination occurs at the plunge point (Fig. 1b) and is commonly substantially smaller than the angle of repose of their Gilbert-type counter parts. As one moves farther away from the plunge point, their inclination tapers and smoothly approaches the far distant bathymetric profile. Moreover, the deltaic deposition rates in (mountainous) lakes are large as compared to the far distant sediment depositions due to the early fall-out of the coarse-grained suspended matter. It follows that in a first approximation for the estimation of the formation and erosion of deltas the far downstream lake bathymetry may be assumed to be steady. Contrary to processes on geological time scales, this assumption is appropriate for applications in water engineering.

Fluvio-deltaic sedimentation thus appears basically in two different forms, for homo- and hypopycnal flows as GILBERT-type deltas, and as hyperpycnal deltas. Both grow chiefly by dense granular transport at the bed, for GILBERT-type deltas as granular avalanches, which continuously adjust their slope to the angle of repose, for hyperpycnal deltas much like subaqueous streams of which the granular motion follows classical bedload transport rules.

In geological applications of Pleistocene or Holocene time scales transgressive and regressive ocean shore movement is linked to the sea level rise and fall and the corresponding topset and foreset estuarine developments (PITMAN, 1978, [56]). Furthermore, grain size variation in ocean or lake sediment cores is linked to the particle size segregation of delta deposits in alluvial basins (PAOLA et al. 1992, [52]). These models all operate with a subaerial bedload mode in the topset region and Gilbert-type deltas in the foreset. On the other hand, engineering applications may concern formation and decay of tributary dammed lakes (CAPART et al. 2010, [7]) or reservoir infill during and immediately after heavy rain fall (LAI & CAPART, 2009, [34]), or forced alteration of delta geometries with the intention to regulate the alluviation. These situations are characterized by hyperpycnal type foresets for which the Alpine Rhine River (Alpenrhein) at Lake Constance is a typical case. 'During flood conditions, the Rhine carries into the lake a large suspended load composed of 10% clay, 70% silt and 20% sand, at concentrations of up to 6000 mgl^{-1} (MÜLLER & FÖRSTNER, 1966, [44]; ROTH et al., 2001, [58]). This inflow generates turbidity currents along the bottom, with underflow velocities of more than 1 ms^{-1} (LAMBERT, 1982, [36]), carrying the clay and silt fractions to the deeper parts of the lake, [58]. The associated delta morphometry is illustrated in Fig. 2. Upstream of the shoreline the long profile of the Rhine River plain exhibits a mild inclination and a slightly concave curvature. At the shoreline a sharp break of slope is observed. Downstream the subaqueous foreset exhibits a steeper gradient and a concave profile of more marked curvature. Near the shoreline break, the maximum inclination of the foreset is of the order of 6° (ADAMS et al. 2001, [2]), much greater than the topset slope, but well below typical angles of repose.

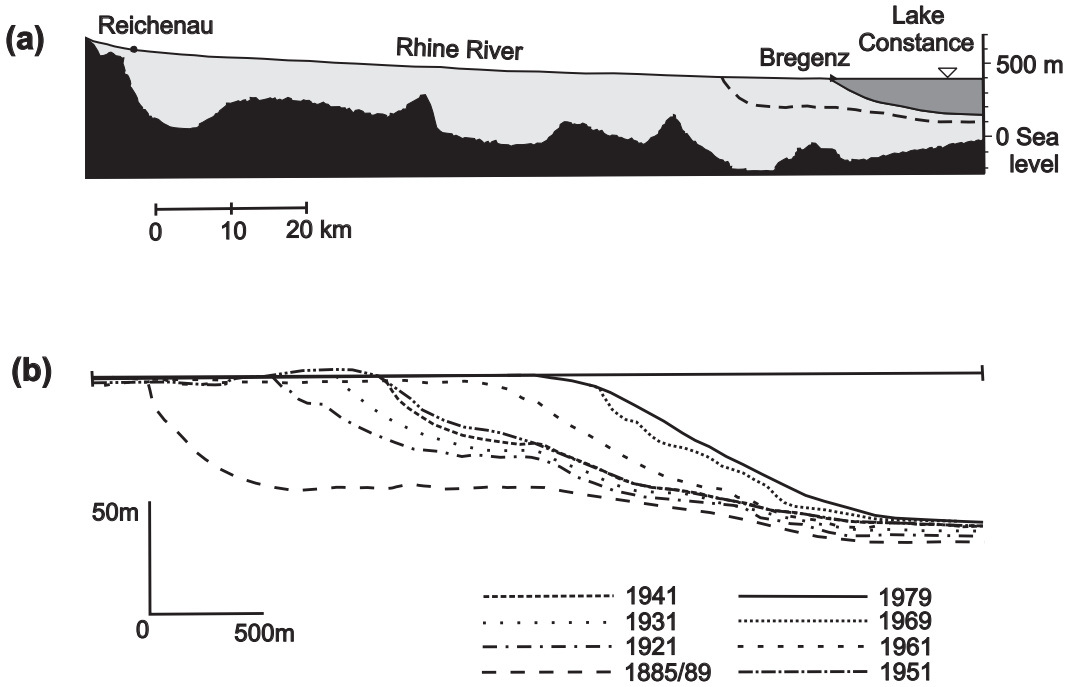

Figure 2: Rhine River delta (Alpenrhein) at Lake Constance, Switzerland. **(a)** Present subaerial and subaqueous long profile of the Rhine (after HINDERER, 2001, [23]). **(b)** Progradation of the subaqueous delta foreset from 1885/89 to 1979 (after KENYON & TURCOTTE, 1985, [27]; data from MÜLLER, 1966, [43], supplemented by more recent profiles from HINDERER, 2001, [23]), from LAI & CAPART (2007), [33], © *J. Geophys. Res. Earth Surface*

Towards the deep end of the lake, the leading edge of the foreset bed connects smoothly with the lake bathymetry. The shape of the delta front thus differs significantly from GILBERT's description. Plotted in Fig. 2b, the recorded evolution of the Rhine river delta front between 1885/89 and 1979 further shows that foresets have maintained a similar morphology over almost a century of progradation', after LAI & CAPART, 2007, [33]).

In the ensuing analysis we shall be involved with both GILBERT-type and hyperpycnal-type delta formations; however, our interest is less in the geological application on Pleistocene and Holocene time scales, but rather on decadal to century time scales, for which engineering-type regulations of foreset alluviations are of interest.

2 Sediment transport in the river

As Fig. 1 suggests, the topset is characterized by river dynamics and its fluvial transport. With the somewhat restricting simplifying assumptions stated below, the sediment transport process can be described by a diffusion equation for the interface position $Z = \hat{\zeta}(X,t)$ between the bedload layer and the suspension layer above it, see Fig. 3. 'The diffusion metaphor has long been used in modeling river systems [...][1] and has been applied to deltas (KENYON & TURCOTTE 1985 [27]) and foreland basins (FLEMING & JORDAN 1989 [14]; JORDAN & FLEMING 1990 [26])'. A detailed derivation is given by PAOLA et al. 1992 [52] using the MEYER-PETER MÜLLER formula [41] for sediment transport. Here, we follow LAI & CAPART 2007 [33], who base their derivation on the COULOMB-TERZAGHI yield criterion. These au-

[1] PAOLA et al. 1992 [52] cite a large number of references, of which we mention here SONI 1981 [62], GILL 1983 [20] and ZHANG & KAHAWITA 1987 [70] but CULLING 1960 [10] remains unmentioned as an early example of derivation of the diffusion equation for erosion problems.

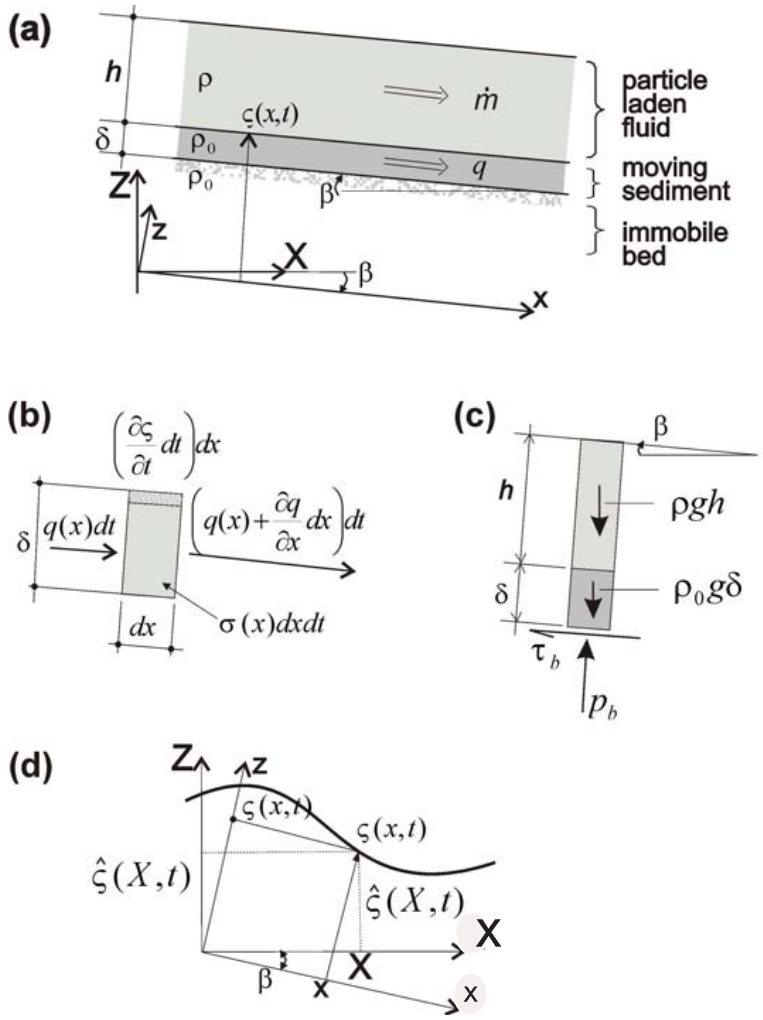

Figure 3: **(a)** Side view of a plane river section consisting of a turbid, particle laden fluid layer of homogeneous density ρ, mass flow $\dot{m}$ and thickness h, underlain by the moving sediment-water layer of constant density ρ_0, volume flux q parallel to the bed and thickness δ. Both are assumed to move immiscibly on an immobile bed, also assumed of density ρ_0 and inclined by the slope of angle β. The Cartesian coordinate system (x, t) is aligned with the bed. **(b)** Element of length dx of the moving sediment-water mixture with volume fluxes at the two side faces. Its growth in thickness is $[(\partial\,\varsigma/\partial\,t)\mathrm{d}t)]\mathrm{d}x$ and a possible external source is $[\sigma(x,t)\mathrm{d}t]\mathrm{d}x$. **(c)** Column of the particle laden and the sediment-water mixture with the corresponding gravity forces and basal shear traction τ_b and basal normal pressure p_b. **(d)** Horizontal-vertical coordinates (X, Z) and sediment-water interface $Z = \hat{\zeta}(X, t)$ and corresponding inclined (x, z) coordinates with $z = \zeta(x, z)$

thors present a clearly formulated list of assumptions on which their diffusion equation for $Z = \hat{\zeta}(X, t)$ is based. As with previous derivations the important information is a formula for the diffusivity in terms of parameters characterizing steady channel flows.

In what follows we list the salient assumptions which are imposed to derive the diffusion equation.

- The river flow in the valley stretch above the plunge point (the topset region) can be assumed to be one-dimensional. Sources in terms of precipitation or point sources from side tributaries are treated as continuous prescribed functions of space and time: $\sigma(x, t)$. This assumption is not very critical since the lowest stretch of a river before entering a basin is generally very flat, shallow and smooth. On century time scales meandering may occur (and has more frequently occurred in the past); in such a case the discharge is averaged and the average flow is assumed to be straight and unidirectional.

- The turbid water and the bedload sediment-water mixture are assumed homogeneous and taking

place in layers, see Fig. 3, for the suspended particle laden fluid as a slurry of thickness h and for the bedload as a dense granular water saturated fluid of thickness δ with particles moving under saltation.

- The motion of this two-layer system is assumed to take place sufficiently smoothly and slowly with no abrupt changes such that the currents in both layers adjust in a *quasi-steady* manner to the 'slowly varying conditions'. This implies in particular that deposition of fines from the particle laden layer into the moving bed is negligible. In other words, the interface between the moving sediment layer and the particle laden fluid layer is material.
  Analogously, it is also supposed that no particles of the moving sediment layer will settle, nor particles from the immobile bed will entrain into the moving sediment layer. Thus, also the bed surface is material.

- The inclination of the bed is small with negligible curvature; so, the river bed is locally straight and the local Cartesian coordinates (x, z) are, respectively, parallel and perpendicular to the bed.

- The flow depths of both layers and the river are small in comparison to significant longitudinal extents of typical variations of the river depth. This is the typical shallowness assumption.

- The bedload material consists of water with density ρ_w (w for 'water') and gravel with density ρ_s (s for 'soil' or 'sediment') and porosity n_0. Both densities are constant because of the incompressibility of water and gravel, but constant n_0 is a simplifying assumption. It is further also assumed that the soil of the immobile bed is the same as in the moving sediment bed, with the density given by
$$\rho_0 = n_0\rho_w + (1 - n_0)\rho_s. \tag{1}$$

In view of the constant density ρ_0 of the sediment layer, the mixture mass balance reduces to the mixture volume balance, which implies (see Fig. 3b)

$$\frac{\partial\,\zeta}{\partial\,t} + \frac{\partial\,q}{\partial\,x} = \sigma(x,t), \tag{2}$$

in which q is the variable volume flux and $\sigma(x,t)$ is a source term. In (2) x is measured tangential to the river bed and $\zeta(x,t)$ perpendicular to it. If $X, Z = \hat{\zeta}(X,t)$ are horizontal and vertical, respectively, it is easily seen that (see Fig. 1.3d)

$$\begin{pmatrix} X \\ \hat{\zeta} \end{pmatrix} = \begin{pmatrix} \cos\beta & \sin\beta \\ -\sin\beta & \cos\beta \end{pmatrix} \begin{pmatrix} x \\ \zeta \end{pmatrix}, \tag{3}$$

or, since $\mid \beta \mid \ll 1$,

$$\begin{pmatrix} X \\ \hat{\zeta} \end{pmatrix} \simeq \begin{pmatrix} 1 & \beta \\ -\beta & 1 \end{pmatrix} \begin{pmatrix} x \\ \zeta \end{pmatrix}. \tag{4}$$

Similarly, if $\hat{q} = q\,\cos\beta \simeq q$ is the horizontal volume flux, (2) may approximately be replaced by

$$\frac{\partial\,\hat{\zeta}}{\partial\,t} + \frac{\partial\,q}{\partial\,X} = \sigma + \mathcal{O}(\beta^2). \tag{5}$$

In steady state at constant velocity (no acceleration), the tangential normal force components of the

gravity force in the column of Fig. 3c balance with the shear traction at the base, τ_b and the normal basal pressure, p_b as follows, see Fig. 3c,

$$\tau_b = (\rho h + \rho_0 \delta)\, g \sin\beta, \tag{6}$$

$$p_b = (\rho h + \rho_0 \delta)\, g \cos\beta, \tag{7}$$

The normal-to-bed component of the submerged weight of the bedload, on the other hand, is given by

$$\sigma_b' = [(\rho\, h + \rho_0 \delta) - \rho(h + \delta)] g \cos\beta = (\rho_0 - \rho)\delta\, g \cos\beta, \tag{8}$$

and is known as 'effective stress'.

The lower interface separating the moving sediment bed and the immobile ground is a sliding surface at which the COULOMB yield criterion applies

$$\tau_b = \tan\phi\, \sigma_b', \tag{9}$$

in which τ_b and σ_b' are given as shown in (6) and (8) with ϕ as the angle of internal friction, in accordance with TERZAGHI's principle (FRACCAROLLO & CAPART 2002 [15]). If (6) and (8) are substituted into (9), and the resulting relation is somewhat manipulated, the equation

$$\frac{\delta}{h + \delta} = \frac{\rho \tan\beta}{(\rho_0 - \rho)(\tan\phi - \tan\beta)} \tag{10}$$

emerges, or since $\delta \ll h$ and $\mid \beta \mid \ll \phi$

$$\delta \simeq \frac{\rho\, h \tan\beta}{(\rho_0 - \rho)\tan\phi}. \tag{11}$$

It transpires that the thickness of the sediment layer is given, if the densities ρ and ρ_0 of the turbid layer and the sediment layer and the slope, β, and angle of internal friction, ϕ, are known.

The next step towards determination of the sediment mixture-volume flux is the determination of a velocity profile within the moving sediment layer. For this purpose application of the momentum principle is out of reach; instead we conjecture a linear relation between the mean velocities of the turbid, u, and the sediment, v, layers, viz.,

$$v = \alpha_1\, u, \tag{12}$$

where $\alpha_1 \leqslant 1$ is a dimensionless parameter, chosen to be constant. For plug flow over the entire depth $\alpha_1 = 1$ and for a linear profile in the sediment layer with value u at its upper boundary, $\alpha_1 = \frac{1}{2}$. With (11) and (12) one may easily deduce

$$\hat{q} \simeq q = \delta\, v = \frac{\alpha_1 \rho\, h u \tan\beta}{(1 - n_0)(\rho_s - \rho)\tan\phi} \tag{13}$$

for the derivation of which we have set $\rho = \rho_w$, i. e. the density ρ of the upper layer slurry is set equal to the water density. We emphasize, this formula has been derived under the assumption that the flow is quasi-steady, that particle sedimentation from the turbid layer and bed erosion into the moving sediment

layer are excluded (or negligible) and that the bed is flat. Under these conditions one also has

$$\frac{\mathrm{d}\rho}{\mathrm{d}x} = 0 \quad \text{and} \quad \frac{\mathrm{d}\dot{m}}{\mathrm{d}x} = 0. \tag{14}$$

These equations state that the density ρ and the turbid mass flow rate $\dot{m}$ do not change along their trajectories, which are here formally given by lines parallel to the x-coordinate. In the words of LAI & CAPART [33] 'the values of ρ and $\dot{m}$ along the topset are purely controlled by their upstream boundary values, i.e.,

$$\begin{aligned} &\rho(x,t) = \rho_{upstream} = \rho_1 = constant \quad \text{and} \\ &\dot{m}(x,t) = \dot{m}_{upstream} = \rho\, hu = \rho_1 Q = constant, \end{aligned} \tag{15}$$

where Q denotes the volumetric discharge of the turbid water supplied upstream of the delta'. Since

$$\tan\beta = -\frac{\partial\,\hat{\zeta}}{\partial\, X}, \tag{16}$$

equations (13) and (5) imply

$$q = -D_1 \frac{\partial\,\hat{\zeta}}{\partial\, x}, \qquad D_1 = \frac{\alpha_1 \rho_1 Q}{(1-n_0)(\rho_s - \rho_1)\tan\phi} \tag{17}$$

$$\frac{\partial\,\hat{\zeta}}{\partial\, t} - \frac{\partial}{\partial\, X}\left(D_1 \frac{\partial\,\hat{\zeta}}{\partial\, X} \right) = \sigma(X,t). \tag{18}$$

D_1 is a (constant) diffusivity, which is proportional to the discharge Q and inversely proportional to the tangent of the angle of internal friction, ϕ. Equation (18) is an inhomogeneous diffusion equation, written here for variable diffusivity, even though D_1 in (17) is constant. As already mentioned, there are alternative derivations, [10], [52] for geological applications, of which PAOLA et al. [52] use the MEYER-PETER MÜLLER [41] sediment transport formula instead of the COULOMB-TERZAGHI friction law (9).

Equation (18) is a linear parabolic partial differential equation. As it is second order in the spatial variable, two boundary conditions for its solution are required. In a so-called two-point boundary value problem such a condition is prescribed at each of the two end points of the interval (X_1, X_2), for which the solution is constructed. For the situation in question, an upstream flux will be prescribed as well as the vertical position of the sediment-turbid fluid interface,

$$\begin{aligned} &q = -D_1 \frac{\partial\,\hat{\zeta}}{\partial\, X}, \quad \text{at} \quad X = X_1 (= 0), \\ &\hat{\zeta} = \hat{\zeta}_0(t), \qquad\quad \text{at} \quad X = s(t), \end{aligned} \tag{19}$$

where $\hat{\zeta}_0(t)$ is a prescribed function monitoring the lake level fluctuation. These conditions do not suffice, however, as a further condition at the shore must connect the solution with the processes of the delta formation. The condition emerging from that analysis will determine the function $s(t)$. This additional condition depends on the type of delta that is formed.

3 Similarity solution for the homogeneous diffusion equation

It will now be assumed that $\sigma(X) \equiv 0$, i.e., we are looking for a solution of the homogeneous equation (18). It turns out that the one-dimensional diffusion equation with constant diffusivity allows construction of so-called similarity solutions, which are useful for the sediment transport problem at hand. Such solutions have self-similar structures; through adequate variable transformations the partial differential equation (PDE) transforms into an ordinary differential equation (ODE). For the diffusion equation the appropriate transformation is (see HYDON 2000, [25] or any other book on partial differential equations[2])

$$\hat{\zeta}(X,t) = f(\Xi)\xi(t), \quad \Xi = \frac{X}{\xi(t)}, \quad \xi(t) = 2\sqrt{D_1 t}, \tag{20}$$

with differentiable functions $f(\Xi)$ and $\xi(t)$. The function $f(\Xi)$ expresses the shape of the profile of the moving sediment layer as a function of the dimensionless argument Ξ. The factor '2' in the definition of $\xi(t)$ is introduced for convenience. $(20)_1$ is a product decomposition of $\hat{\zeta}$ into a function characterizing the time, but having the dimension of length, and a dimensionless function f of dimensionless variable Ξ.

It follows from (20) that

$$\frac{\mathrm{d}\,\xi}{\mathrm{d}\,t} = \frac{2D_1}{\xi}, \qquad \frac{\partial\,\hat{\zeta}}{\partial\,t} = \frac{2D_1}{\xi}\left(f(\Xi) - \frac{X}{\xi}\,f'(\Xi)\right),$$
$$\frac{\partial\,\hat{\zeta}}{\partial\,X} = f'(\Xi), \quad \frac{\partial^2\zeta}{\partial\,X^2} = \frac{1}{\xi}\,f''(\Xi),$$

in which primes on f denote differentiation, so that (18) takes the form

$$f''(\Xi) + 2\left\{\Xi\,f'(\Xi) - f(\Xi)\right\} = 0. \tag{21}$$

This is a linear, second order ODE for f as a function of Ξ. One solution is $f_1(\Xi) = -A\Xi$, where A is a constant. As known from elementary calculus, a second solution can then be constructed by the product decomposition

$$f_2(\Xi) := f_1(\Xi)\,g(\Xi) = -\Xi\,g(\Xi). \tag{22}$$

Indeed, with (22) and (18) and with

$$h(\Xi) := g'(\Xi) \tag{23}$$

[2]Other books are e.g. SOKOLNIKOFF-REDHEFFER 1966 [61], ABRAMOWITZ and STEGUN 1964 [1], KREYSZIG 2006 [31].

it is easy to show that $h(\xi)$ must satisfy the differential equation

$$\begin{aligned}
&\frac{h'(\Xi)}{h(\Xi)} = \frac{\mathrm{d}}{\mathrm{d}\Xi}\left(\ln(h(\Xi)\right) = -\frac{2(1+\Xi^2)}{\Xi} \\
\Longrightarrow\quad &\ln\left[h(\Xi)\right] = -\int_1^{\Xi}\frac{2(1+x^2)}{x}\mathrm{d}x - \ln\left(\frac{1}{B}\right) \\
&\qquad = -2\ln(\Xi) - \Xi^2 - \ln\left(\frac{1}{B}\right) \\
&\qquad = -\ln(\Xi^2) - \Xi^2 - \ln\left(\frac{1}{B}\right) \\
\Longrightarrow\quad &\ln\left(\frac{h(\Xi)\Xi^2}{B}\right) = -\Xi^2,
\end{aligned}$$

or

$$h(\Xi) := g'(\Xi) = B\frac{\exp(-\Xi^2)}{\Xi^2}. \tag{24}$$

B is a constant of integration. A further integration of (24) now yields[3]

$$\begin{aligned}
g(\Xi) &= B\int_{\Xi}^{A}\frac{\exp(-x^2)}{x^2}\mathrm{d}x \\
&= B\Big\{\frac{\exp(-\Xi^2)}{\Xi} + \underbrace{2\int_0^{\Xi}\exp(-x^2)\mathrm{d}x}_{\sqrt{\pi}\mathrm{erf}(\Xi)} + C\Big\}.
\end{aligned} \tag{25}$$

Here, erf is the error function,

$$\mathrm{erf}(x) = \frac{2}{\sqrt{\pi}}\int_0^x \exp(-y^2)\mathrm{d}y, \tag{26}$$

and C is again a constant of integration. Once a choice for C has been made, the most general solution of (18) is given by

$$f(\Xi) = -A\Xi + B\left\{\exp(-\Xi^2) + \sqrt{\pi}\Xi\left(\mathrm{erf}(\Xi) + C\right)\right\} \tag{27}$$

with derivative

$$f'(\Xi) = -A + B\sqrt{\pi}\{\mathrm{erf}(\Xi) + C\}. \tag{28}$$

[3]We compute this indefinite integral as follows:

$$\begin{aligned}
&\int_{\Xi}^{A}\frac{1}{x^2}\exp(-x^2)\mathrm{d}x = \int_{\Xi}^{A}\frac{\mathrm{d}}{\mathrm{d}x}\left(-\frac{1}{x}\right)\exp(-x^2)\mathrm{d}x \\
&= \int_{\Xi}^{A}\frac{\mathrm{d}}{\mathrm{d}x}\left[\left(-\frac{1}{x}\right)\exp(-x^2)\right]\mathrm{d}x - \int_{\Xi}^{A}\left(-\frac{1}{x}\right)(-2x)\exp(-x^2)\mathrm{d}x \\
&= -\frac{1}{x}\exp(-x^2)|_{\Xi}^{A} - 2\int_{\Xi}^{A}\exp(-x^2)\mathrm{d}x \\
&= -\frac{1}{A}\exp(-A^2) + \frac{1}{\Xi}\exp(-\Xi^2) + 2\underbrace{\int_A^{\Xi}\exp(-x^2)\mathrm{d}x}_{\int_A^0 + \int_0^{\Xi}} \\
&= \frac{\exp(-\Xi^2}{\Xi}) + \underbrace{2\int_0^{\Xi}\exp(-x^2)\mathrm{d}x}_{2\sqrt{\pi}\mathrm{erf}(\Xi)} - \underbrace{\frac{\exp(-A^2)}{A} - 2\int_0^{A}\exp(-x^2)\mathrm{d}x}_{C} \\
&= \frac{\exp(-\Xi^2)}{\Xi} + 2\sqrt{\pi}\mathrm{erf}(\Xi) + C,
\end{aligned}$$

which agrees with (25).

The construction of the solution (27) is standard. The above derivation, here given in details, follows essentially [6].

CAPART et al. [6] emphasize that 'the assumed similarity structure also imposes certain restrictions on the boundary conditions of ODE (21) to be specified at given values of the ratio $\Xi = X/\xi(t)$; the boundary positions X_1 and X_2 must be of the form

$$X_1 = \lambda_1 \xi(t), \qquad X_2 = \lambda_2 \xi(t), \tag{29}$$

where the scaling constants $\lambda_i, i = 1, 2$, can either be given or are unknown (and must then be subject to additional boundary conditions). Form (29) allows non-moving boundary conditions, but only at locations $X_i = 0$ and $X_i = \pm\infty$.

Conversely, any λ_i different from zero or infinity yields a moving boundary. Restrictions on boundary speeds then follow from

$$\frac{\mathrm{d}X_i}{\mathrm{d}\,t} = \lambda_i \frac{\mathrm{d}\,\xi}{\mathrm{d}\,t} = \frac{2D_1}{\xi}\lambda_i = \frac{2\,D_1}{X_i}\lambda_i^2, \tag{30}$$

which implies that products $X_i(\mathrm{d}X_i/\mathrm{d}\,t)$ must be invariants [constants]'. It is also easy to see that at boundary points the quantities

$$\frac{\hat{\zeta}_i}{\xi(t)}, \quad \frac{\hat{\zeta}_i}{X_i(t)}, \quad \left(\frac{\partial\,\hat{\xi}}{\partial\,X}\right)_i, \quad i = 1, 2$$

must equally be constant. Explicit examples of self-similar evolution for alluvial channels of semi-infinite length with moving boundaries are constructed by CAPART et al. 2007 [6]. Let us illustrate the application of the similarity solution to a number of lake-related hydraulic research problems.

3.1 Bedrock-alluvial transition

A somewhat academic example which demonstrates a hydraulic application, is given in [6], see Fig. 4; it is the sediment flow down a plane inclined bed, which suddenly changes its slope from $-S_1$ to $-S_2$. Far upstream and far downstream the steady bed has these slopes, but to adjust to these slopes, the bed will smoothly change from slope $-S_1$ to slope $-S_2$. We may interpret the far upstream bed as solid non-erodible rock and the downstream bed as the alluvial infill. The transition between the exposed upstream bedrock and the downstream alluvial channel is located at the evolving position $s(t)$. At time $t = 0$, it is assumed that $s = 0$ and that the alluvial cover has constant slope $S_2 < S_1$. (Note that this is the 'academic' and not realistic condition guaranteeing that the similarity solution is applicable.) A steady sediment flux Q is provided far upstream; for a flux $Q < D_1 S_1$ no deposition occurs in the upper stretch of the channel and the sediment simply is transported along the channel until it reaches the upstream edge of the alluvial channel. Clear water conditions can also be examined by setting $Q = 0$. (In this case it is assumed that the alluvial channel with slope $-S_1$ already exists at $Z = 0$.

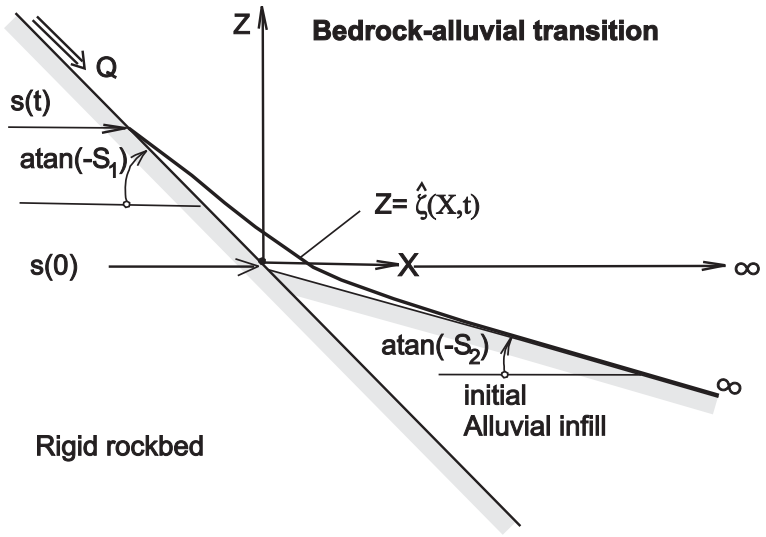

Figure 4: Definition sketch for a bedrock alluvial transition problem. The bedrock is a rigid non-erodible solid with bed-inclination angle $\arctan(-S_1)$ and an initial alluvial infill with slope angle $\arctan(-S_2)$. It is assumed that for an upstream sediment influx Q the sediment will either be deposited or eroded in the vicinity of the sudden change in slope at $X = 0$. It is assumed that as $X \to \infty$, the alluvial infill will approach the slope $-S_2$, from [6], © *J. Geophys. Res.*

The mathematical problem just outlined is given by the following initial boundary value problem:

$$\begin{aligned}
&\frac{\partial \hat{\zeta}}{\partial t} - D_1 \frac{\partial^2 \hat{\zeta}}{\partial X^2} = 0, && s(t) < X < \infty, \\
&\hat{\zeta} = -S_1 X, \qquad \frac{\partial \hat{\zeta}}{\partial X} = -\frac{Q}{D_1}, && X = s(t), \\
&\frac{\partial \hat{\zeta}}{\partial X} = -S_2, && X \to \infty, \\
&\hat{\zeta} = -S_2 X, \qquad X > 0, && t = 0.
\end{aligned} \tag{31}$$

Here, $(31)_1$ governs the evolution of the alluvial channel profile and is complemented by two upstream boundary conditions $(31)_{2,3}$, one downstream asymptote $(31)_4$ and an initial profile $(31)_5$. (Note, we have formulated three boundary conditions!) This initial boundary value problem is susceptible to a similarity solution, if the transformations (20) are applied and

$$s(t) = \lambda\, \xi(t) = 2\lambda \sqrt{D_1 t} \tag{32}$$

is used with the yet undetermined constant λ. In the dimensionless variables, (31) takes the form

$$\begin{aligned}
&f''(\Xi) + 2\{\Xi\, f'(\Xi) - f(\Xi)\} = 0, \quad \lambda < \Xi < \infty, \\
&f(\lambda) = -S_1 \lambda, \quad f'(\lambda) = -\frac{Q}{D_1}, \\
&f'(\infty) = -S_2.
\end{aligned} \tag{33}$$

The general solution of the first of (33) for f is given by (27), in which the constants A, B, C, and λ must be determined from $(33)_{2,4}$; however, these are not uniquely determined, unless a fourth condition is provided. This condition is actually implicitly contained in $(33)_4$ as it requires a constant slope of f as

$\Xi \to \infty$. Now, since

$$\lim_{\Xi\to\infty} f(\Xi) \sim \{-A + B\sqrt{\pi}(1+C)\}\Xi, \tag{34}$$

we may choose the level of the alluvial deposit for $\Xi \to \infty$ by correspondingly selecting the value for C. For the choice $C = -1$

$$\lim_{\Xi\to\infty} f(\Xi) = -A\,\Xi, \tag{35}$$

agreeing with the far-downstream profile at $t = 0$. In other words, there is no deposition far downstream in the bottomset. Now, it follows from $(33)_{3,4}$ that

$$A = S_2 \qquad B = \frac{S_2 - Q/D_1}{\sqrt{\pi}(\mathrm{erf}(\lambda) - 1)} \tag{36}$$

and from $(33)_2$

$$\lambda - \omega\,\frac{\exp(-\lambda^2) + \sqrt{\pi}\lambda(\mathrm{erf}(\lambda) - 1)}{\sqrt{\pi}(\mathrm{erf}(\lambda) - 1)} = 0, \quad \omega := \frac{Q/D_1 - S_2}{S_1 - S_2}. \tag{37}$$

This is a transcendental equation for λ when Q is prescribed.[4]

CAPART et al. [6] performed some computations. For $Q = 0$ 'the resulting sediment profiles are illustrated in Fig. 5a [...]. The results shown are obtained for an alluvial slope set to half the bedrock inclination, i.e. $S_2/S_1 = 0.5$, leading to a parameter value $\omega = -1$. The corresponding value for the root λ is $\lambda = 0.4328$. Profiles are given for equally spaced values of the similarity variable $\xi = 2\sqrt{D_1 t} = 0, 1, \ldots, 5$, rather than for equally spaced times t, and are plotted in dimensionless form using an arbitrary length scale L. Under zero upstream sediment supply, the clear water flow is erosive as it reaches the alluvial cover. Consequently, the transition gradually moves downstream, exposing new bedrock as time advances. The corresponding sediment elevation profiles are concave degrading an ever greater extent of the downstream alluvial channel. Contrasting with this behavior, convex profiles associated with overloading are illustrated in Fig. 5b. The parameters for this example are $S_2/S_1 = 0.2,\ \omega = 0.5, (Q = 0.6 D_1 S_1)$, and $\lambda = -0.3578$, [6].

Equation (37) can also be interpreted as an equation of λ for ω,

$$\omega = \Lambda(\lambda) = \frac{\sqrt{\pi}\lambda(\mathrm{erf}(\lambda) - 1)}{\exp(-\lambda^2) + \sqrt{\pi}\lambda(\mathrm{erf}(\lambda) - 1)}. \tag{38}$$

The inverse function $\lambda = \Lambda^{-1}(\omega)$ is plotted in Fig. 6a in the interval $-1 \leqslant \omega < 1$. 'For selected values of ω, marked as hollow symbols on the curve in panel (a) the alluvial channel responses are further documented in panel (b). Similarity profiles are shown, normalized with respect to the evolving scaling variable $\xi(t)$ [...]. Values $\omega < 0$ correspond to underloading. In this case the sediment supply Q is below the equilibrium transport capacity $D_1 S_2$ of the downstream alluvial channel and degradation results. The alluvial edge is gradually washed downstream. At value $\omega = 0$, the upstream supply is precisely equal to the equilibrium capacity of the alluvial channel, and there is no geomorphic change; this scenario corresponds to the classical 'graded river' of MACKIN 1948 [40], see later. Values $\omega > 0$ then correspond to overloading. The sediment supply is above the equilibrium transport capacity of the

[4] Had we chosen C differently from -1, then $(36)_1$ would read $A = S_2 + \sqrt{\pi}(1 + C)$ and the initial value for s at $t = 0$ would no longer be zero. Requesting that $s(0) = 0$ would in this case fix C to be again -1.

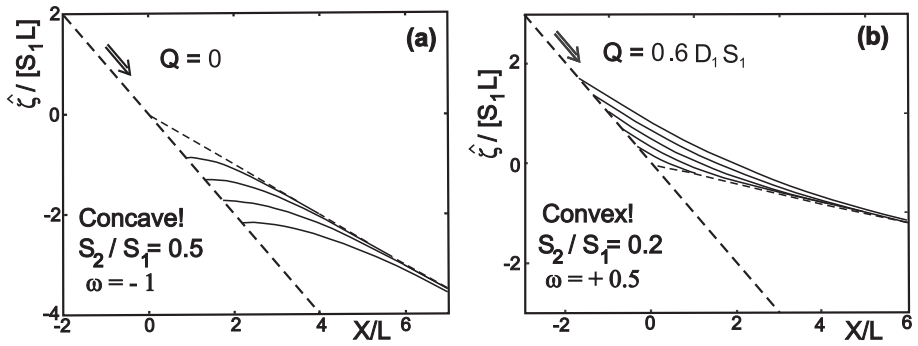

Figure 5: Profile evolution for bedrock-alluvial transition. **(a)** under loading with zero upstream sediment flux ($S_2/S_1 = 0.5, \omega = -1$); **(b)** overloading case ($S_2/S_1 = 0.2, \omega = 0.5$). Dashed lines show the initial profile of the downstream alluvial channel; continuous lines show successive snapshots of the alluvial channel profile for $\xi(t)/L = 1, 2, \ldots, 5$ where $\xi(t) = 2\sqrt{D_1 t}$, from CAPART et al. [6], © *J. Sedimentary Res.*

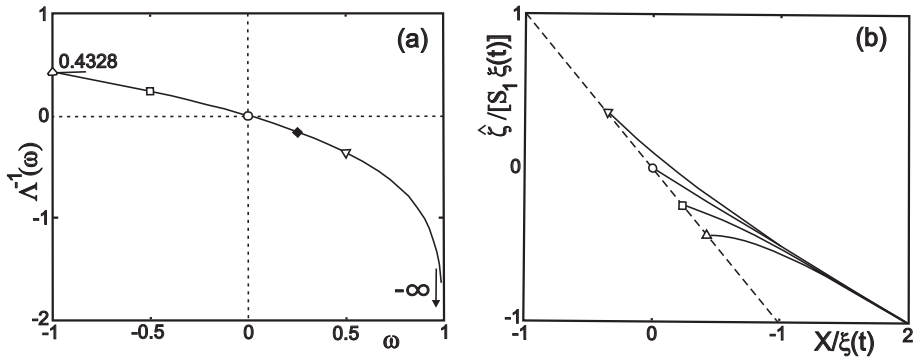

Figure 6: **(a)** Bedrock-alluvial transition, plotting $\lambda = \Lambda^{-1}(\omega)$, defined in (38), where $\omega = (Q/D_1 - S_2)(S_1 - S_2)$. Graphs for profiles are shown in panel (b) for the conditions $\triangle, \square, \bigcirc, \nabla$. **(b)** Positions of the moving boundary for various values of the supply parameter where the various symbols belong to: $(\triangle)\omega = -1$; $(\square)\omega = -\frac{1}{2}$; $(\bigcirc)\omega = 0$; $(\nabla)\omega = \frac{1}{2}$. Continuous lines are the corresponding alluvial channel profiles, and the dashed line is the underlying bedrock. Values $\omega < 0$ imply depletion and values $\omega > 0$ imply accretion upstream of the alluvial channel, from CAPART et al. [6], © *J. Sedimentary Res.*

downstream alluvial channel and deposition results at the transition. The alluvial edge moves upstream gradually draping sediment over the bedrock flow when $\omega > 1$, the sediment supply starts to exceed the equilibrium transport capacity $D_1 S_1$ of the bedrock channel itself. Sediment is deposited before reaching the transition covering the bedrock from upstream to downstream. Foreshadowing this complete change of behavior, the speed, at which the bedrock-alluvial transition moves upstream, becomes infinite as the value $\omega = -1$ is approached from below', [6].

3.2 Overtopping failure of a dam

A similar academic problem with a realistic touch is the overtopping failure of a sand dam. It turns out to be mathematically identical to the bedrock-alluvial transition problem. Figure 7a illustrates the situation. It is assumed that the dam consists of homogeneously packed sand. Given the experience with the alluvial sediment transport problem, the sediment flow of Fig. 7a at time t for $X > s(t)$ is given by

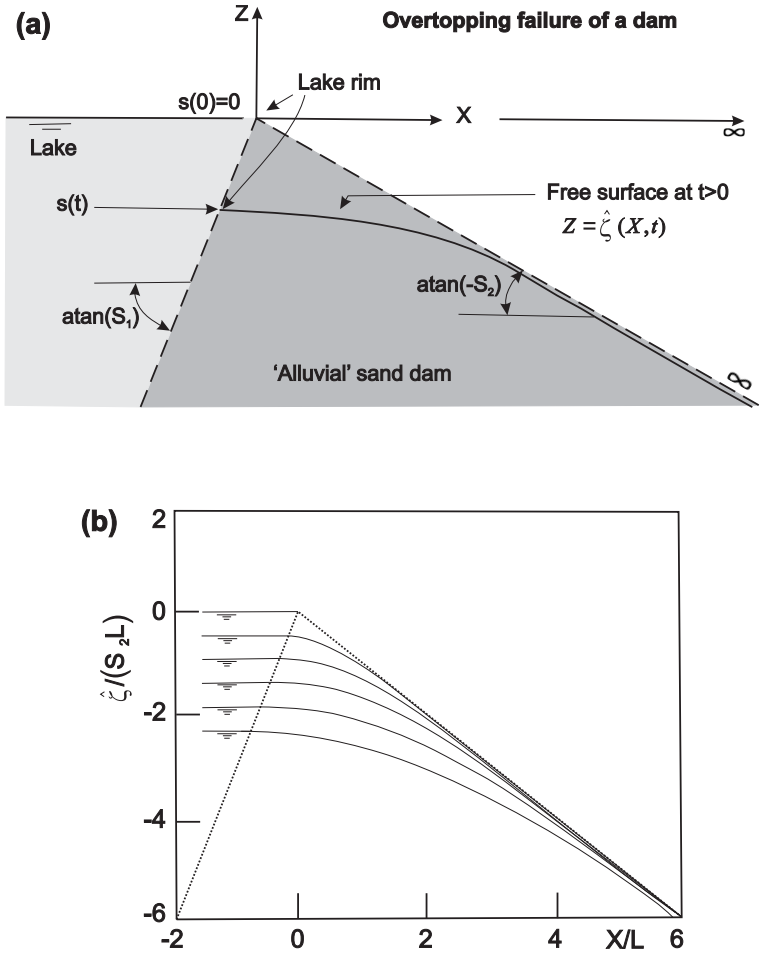

Figure 7: (a) Definition sketch for the overtopping failure problem of a dam. The upstream face of the dam has 'adverse' slope ($S_1 > 0$, for the chosen coordinate system). The sand dam is assumed to be homogeneously packed and to extend to $X \to \pm\infty$ with slopes $-S_2$ and S_1, respectively **(b)** Profile evolution for the overtopping dam failure problem. The dashed lines show the erodible dam for $t = 0$. The solid lines show snapshots for the alluvial channel profile for $\xi(t)/L = 1, 2, \ldots, 5$, where $\xi(t) = 2\sqrt{D_1 t}$ and $\omega = \frac{1}{4}$, $\lambda = -0.1562$. The value of $\lambda(\omega)$ is shown as black diamond in Fig. 6b; panel **(b)** from [6], © *J. Sedimentary Res.*

the following initial value problem.

$$\begin{aligned}
&\frac{\partial \hat{\zeta}}{\partial t} - D_1 \frac{\partial^2 \hat{\zeta}}{\partial X^2} = 0, && s(t) < X < \infty, \\
&\hat{\zeta} = +S_1 X, \quad \frac{\partial \hat{\zeta}}{\partial X} = 0, && X = s(t), \\
&\frac{\partial \hat{\zeta}}{\partial X} = -S_2, && X \to \infty, \\
&\hat{\zeta} = -S_2 X, \quad X > 0, && t = 0.
\end{aligned} \tag{39}$$

This is the same initial boundary value problem as (31). The only difference is that here $Q = 0$ and the slope S_1 has a different sign (see $(39)_2$). It follows that $s(t)$ is also given by (32) and λ is related to ω by equation (37) with ω now given by $\omega = S_2/(S_2 - S_1)$ and restricted to the range $0 \leqslant \omega < 1$. CAPART et al. [6] performed calculations for $S_2/S_1 = -\frac{1}{3}$, corresponding to $\omega = \frac{1}{4}$ and $\lambda = -0.1562$. Figure 7b displays the dam erosion $\hat{\zeta}/(S_2 L)$ plotted against X/L for $\xi(t)/L = 1, 2, \ldots, 5$, where $\xi(t) = 2\sqrt{D_1 t}$. Obviously, erosion of the dam crest leads to lake drainage.

4 Hypopycnal (Gilbert-type) deltas

As explained earlier in connection with the diffusion equation (18), the two boundary conditions (19) are not sufficient to solve the fluvio-deltaic sedimentation problem. An additional relation is required to locate the shoreline position and thus close the initial-boundary-value problem. For the two cases of the bedrock alluvial transition [see (31)] and the overtopping failure of a dam [see (39)], such a third boundary condition was naturally prescribed: at $X = s(t)$, the values for $\hat{\zeta}$ and $\partial\,\hat{\zeta}/\partial\,X$ are given, as is the flux condition far upstream and far downstream, respectively. The additional boundary condition was in both cases a flux (or NEUMANN-type) condition at the shore discontinuity. Physically, the statement emerges from applying the conservation law of sediment mass. Figure 8 is motivated by a figure in [63]. Accordingly, GILBERT-type deltas are characterized by straight forefronts of constant inclination (given as the tangent of the angle of internal friction). Should this straight front be disturbed by external or internal wave activity or by some local effect e.g. of cohesion, it is assumed that the sediment flux from the topset will quickly smooth the surface by the avalanching processes.

To establish a formula for the sediment flux condition, consider Fig. 8 and the area shaded in dark. It is bounded on the left by the coordinate line $X = 0$, from above by the top surface, $Z = \hat{\zeta}(X,t)$ of the moving sediment (in $0 \leqslant X \leqslant s(t)$) and the straight delta front (in $s(t) \leqslant X \leqslant u(t)$), and from below by the basement $Z = b(X,t)$, whose motion on geological time scales is likely governed by subduction processes, but is steady, $Z = b(X)$, on decadal deltaic variations. The lake surface is given by $Z = Z_\ell(t)$, for which annual variations may be of significance. Monitoring the lake level by a weir at the outlet may be used to influence temporal development of delta formation.

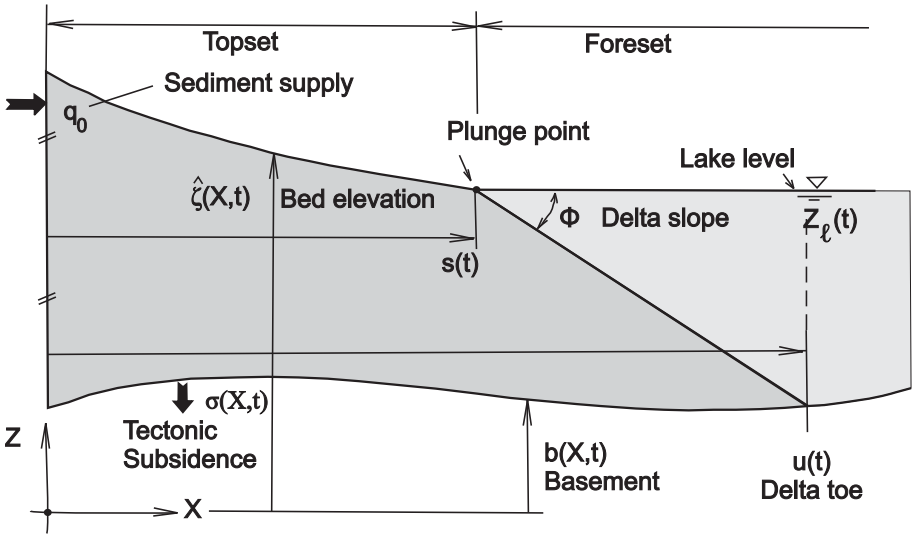

Figure 8: Idealized hypopycnal delta formation. The region is bounded from above by the topset sediment bed $\hat{\zeta}(X,t)$ and the foreset lake surface $Z_\ell(t)$ and from below by the basement $b(X,t)$, subject to a prescribed subsidence rate $\sigma(X,t)$. The delta wedge has constant slope $(-\tan\|\phi\|)$ from the plunge point $s(t)$ to the delta toe $u(t)$. The far upstream boundary is fixed but fed by a prescribed sediment supply q_0, which feeds the delta front surface

The dark-shaded area in Fig. 8 is bounded such that a sediment flux enters it only at $X = 0$; it is

given by q_0. Global sediment conservation then yields[5]

$$q_0 = \frac{\mathrm{d}}{\mathrm{d}\,t}\int_0^{s^-(t)} \Big(\hat{\zeta}(X,t) - b(X,t)\Big)\,\mathrm{d}X + \frac{\mathrm{d}}{\mathrm{d}\,t}\int_{s^+(t)}^{u(t)} \Big((Z_\ell(t) - b(X,t)) - \tan\,\phi\,(X - s(t))\Big)\,\mathrm{d}X. \tag{40}$$

The first integral on the right-hand side represents the shaded area in Fig. 8 between $X = 0$ and $X = s(t)$. The second integral represents the corresponding area (minus the light-shaded triangle of the lake). If the differentiations of the integral terms on the right-hand side are performed (note the LEIBNIZ rule must be applied in this differentiation), and the condition[6]

$$[\hat{\zeta}(X,t) - b(X,t)]_{|X=u(t)} = 0 \tag{41}$$

is used, then the following formula is obtained:

$$(u(t) - s(t))\tan\phi\frac{\mathrm{d}\,s(t)}{\mathrm{d}\,t} = q(s(t),t) - (u(t) - s(t))\frac{\mathrm{d}\,Z_\ell(t)}{\mathrm{d}\,t} + \int_{s(t)}^{u(t)} \sigma(X,t)\mathrm{d}\,X, \tag{42}$$

in which

$$q(s(t)) = -D_1\frac{\partial\hat{\zeta}(X)}{\partial\,X}\Big|_{X=s^-(t)}, \tag{43}$$

$$\sigma(X,t) = -\frac{\partial\,b(X,t)}{\partial\,X}. \tag{44}$$

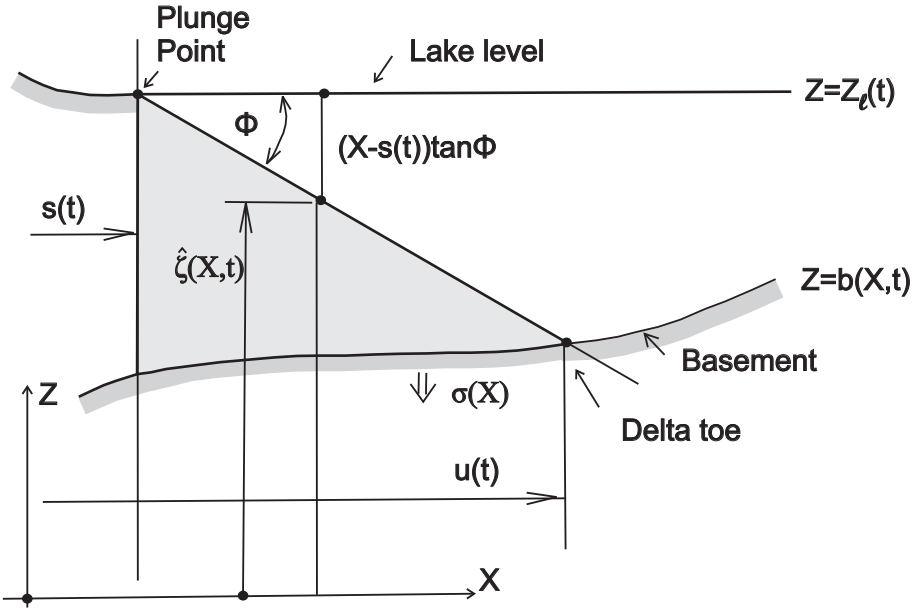

Figure 9: Close-up of the foreset regime of a GILBERT-type delta, explaining how the basement toe position $u(t)$ can be determined from the geometric positions of $s(t), Z_\ell(t), b(X,t)$ and the delta front at slope, $-\tan\|\phi\|$

[5] $s^\pm(t) = s(t) \pm \varepsilon, \varepsilon > 0, \varepsilon \to 0$.

[6] An alternative derivation of formula (42) when $\sigma = 0$ is given in Appendix A

Equation (42) can be viewed as a differential equation for the shore line position, $s(t)$; however, to this end $u(s)$ must be expressed in terms of $s(t)$ and $Z_\ell(t)$. Figure 9 shows that the top surface of the wedge-type delta is given by the equation[7]

$$\begin{aligned}\hat{\zeta}(X,t) &= \hat{\zeta}(s(t)) - \tan\phi\,(X - s(t)) \\ &= Z_\ell(t) - \tan\phi(X - s(t)).\end{aligned} \tag{45}$$

For $X = u(t)$ (and $\hat{\zeta}(u(t),t) = b(u(t),t)$) this equation can be written as

$$\{b(u(t),t) + \tan\,\phi\,u(t)\} = Z_\ell + \tan\,\phi\,s(t). \tag{46}$$

For prescribed lake level $Z_\ell(t)$, plunge point $s(t)$, basement elevation $b(X,t)$ and angle of internal friction, ϕ, (46) can be viewed as a nonlinear equation for $u(t)$. Therefore, (46) must accompany (42) as an additional algebraic equation to determine $u(t)$. Thus, u is obtained in general form a functional equation of the form

$$u = u[s(t), Z_\ell(t), b(u(t),t), \tan\phi].$$

If the basement is immobile, $b = b(X)$, (46) can be replaced by

$$u(t) = s(t) + \frac{1}{\tan\,\phi}\left(Z_\ell(t) - b(X)_{|X=u(t)}\right).$$

Thus,

$$\begin{aligned}&\dot{u}(t) = \dot{s}(t) + \frac{1}{\tan\,\phi}\left\{\dot{Z}_\ell(t) - \frac{\mathrm{d}\,b}{\mathrm{d}X}_{|X=u(t)}\dot{u}(t)\right\} \\ \Longrightarrow \qquad &\left\{1 + \frac{1}{\tan\,\phi}\frac{\mathrm{d}\,b}{\mathrm{d}X}_{|X=u(t)}\right\}\dot{u}(t) = \dot{s}(t) + \frac{1}{\tan\,\phi}\dot{Z}_\ell(t)\end{aligned}$$

or

$$\dot{u}(t) = \left\{1 + \frac{1}{\tan\phi}\frac{\mathrm{d}\,b}{\mathrm{d}\,X}_{|X=u(t)}\right\}^{-1}\left\{\dot{s}(t) + \frac{1}{\tan\,\phi}\dot{Z}_\ell(t)\right\}.$$

This formula shows that $\dot{u}(t) = \dot{s}(t)$ provided $b = const.$ and $Z_\ell = const.$ Lake level rises, $\dot{Z}_\ell > 0$, enhance $\dot{u}(t)$ over $\dot{s}(t)$, but $(\mathrm{d}b/\mathrm{d}X)_{|u(t)} > 0$ decrease $\dot{u}(t)$. All these behaviors are geometrically obvious.

Let us consider the simplest case of steady lake level, $\dot{Z}_\ell = 0$, vanishing subsidence, $\sigma = 0$, and uniform water depth H. In this case the field equations (18), boundary conditions (19), (42) and initial

[7] From now on ϕ is counted as positive

condition $s(0) = 0$ reduce to

$$\begin{aligned}
&\frac{\partial \hat{\zeta}}{\partial t} = D_1 \frac{\partial^2 \hat{\zeta}}{\partial X^2}, \qquad 0 \leqslant X \leqslant s(t), \\
&\frac{\partial \hat{\zeta}}{\partial X}(0,t) = -\frac{q_0}{D_1}, \\
&\hat{\zeta}(s(t),t) = 0, \\
&-H\dot{s}(t) = q(s(t),t) = -D_1 \frac{\partial \hat{\zeta}}{\partial X}(s(t),t), \\
&s(0) = s_0\,(=0) \qquad \text{initial condition},
\end{aligned} \tag{47}$$

where we have set the origin of the coordinates at the intersection point of the lake surface with the basement. $H = (u(t) - s(t)) \tan\phi$ is the uniform water depth. Note that because of the constancy of b, equation (46) is linear in u, can be solved for $u(t)$ and then substituted into (42). The emerging equation is then $(47)_4$ and constitutes an ODE for $s(t)$.

The above equations (47) are not in a form susceptible to similarity solutions; however, they constitute a so-called single phase STEFAN problem, see [8], [9], which, for instance, arises in solidification-melting problems of a heat conducting body reaching the melting temperature. It is, perhaps helpful to quickly look at this problem.

4.1 The classical Stefan problem

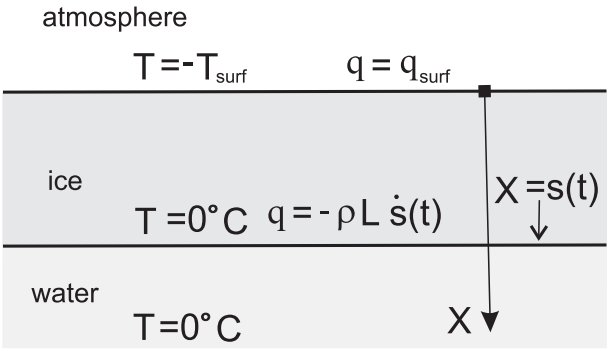

Figure 10: Layer of ice floating on a lake in winter. This is the simplest version of the thermal description of the ice front $s(t)$. At the atmosphere/ice interface, the surface temperature $-T_{surf}$ or the surface heat flux q_{surf} is prescribed

We commence by demonstrating that freezing of a lake and sediment transport into a quiescent ambient fluid are mathematically analogous problems. Consider a lake in winter with an ice cover of a certain thickness, Fig. 10. Assume either that the surface temperature, $-T_{surf}$ (below freezing), or the heat flux into the atmosphere, q_{surf} is prescribed. [Both conditions are thinkable as upper boundary conditions, but neither one is strictly correct in a practical application.] Assume, moreover, that the water layer is at the melting temperature (0°C) and that CLAUSIUS-CLAPEYRON effects (the melting temperature depends on the pressure) and the non-monotonicity of the thermal equation of state are ignored. The initial boundary value problem describing the temperature in the ice is then given by the

following equations

$$\begin{aligned}
&\frac{\partial T}{\partial t} = D_{ice}\frac{\partial^2 T}{\partial X^2}, \qquad 0 \leqslant X \leqslant s(t),\\
&T(0,t) = -T_{surf}, \quad \text{or} \quad \frac{\partial T}{\partial X}(0,t) = -\frac{q_{surf}}{D_{ice}},\\
&T(s(t)) = 0,\\
&-\rho\, L\, \dot{s}(t) = q(s(t),t) = -\kappa_{ice}\frac{\partial T}{\partial X}(s(t),t),\\
&s(0) = 0, \qquad \text{initial condition.}
\end{aligned} \tag{48}$$

In these equations $D_{ice} = \kappa_{ice}/(\rho c_p)_{ice}$ is the thermal diffusivity of ice, c_p its specific heat at constant pressure, κ_{ice} its thermal conductivity, ρ its density and L the latent heat of melting/freezing. The input quantity is either the surface temperature T_{surf} or the heat flow loss, q_{surf}. Equation $(48)_1$ is the heat conduction equation in the ice layer. The two equations in the second line are the driving elements of the problem, leading eventually to two different initial boundary value problems. The equation in the third line is the statement that the temperature at the ice-water interface equals the freezing temperature. The statement in the fourth line of (48) says that the energy, which is withdrawn from the interface and transported through the ice by the heat flow, q, equals the amount of mass of water which freezes per unit time multiplied with the latent heat, L. This latter statement is the STEFAN condition. By simple comparison of (47) and (48), it is seen that the different physical problems of sediment transport into a quiescent ambient fluid and progression of an ice front in a freezing lake are analogous.

Let us demonstrate the solution of the classical STEFAN problem (48) for the case that the surface temperature T_{surf} is prescribed. Construction of this solution is facilitated by introducing the transformation

$$\theta := T + T_{surf}. \tag{49}$$

The initial boundary value problem (48) then transforms into

$$\begin{aligned}
&\frac{\partial \theta}{\partial t} = D_{ice}\frac{\partial^2 \theta}{\partial X^2}, \qquad 0 \leqslant X \leqslant s(t),\\
&\theta(0,t) = 0,\\
&\theta(s(t),t) = T_{surf},\\
&-\frac{L}{c_{ice}}\dot{s}(t) = \hat{q}(s(t),t) = -D_{ice}\frac{\partial \theta}{\partial X}(s(t),t),\\
&s(0) = 0,
\end{aligned} \tag{50}$$

in which $\hat{q}(s(t),t) = q(s(t),t)/(\rho c_{ice})$ is the diffusive heat flux per specific heat. A solution to $(50)_1$ is sought in terms of the similarity variable

$$Y = \frac{X}{\sqrt{2D_{ice}t}} \tag{51}$$

and can be written as (see e. g. KREYSZIG [31], CRANK [9])

$$\theta = A + B\,\mathrm{erf}\left(\frac{X}{2\sqrt{D_{ice}t}}\right), \quad \mathrm{erf}(y) = \frac{2}{\sqrt{\pi}}\int_0^y \exp^{-\xi^2}\,\mathrm{d}\xi, \tag{52}$$

in which A and B are constants of integration. $(50)_{2,3}$ imply $A = 0$ and

$$T_{surf} = B\text{erf}\left(\frac{s(t)}{2\sqrt{D_{ice}t}}\right). \tag{53}$$

Because T_{surf} and B are constants, so must be the argument of erf$(\cdot)$, which we now set equal to λ,

$$\lambda = \frac{s(t)}{2\sqrt{D_{ice}t}} = const. \quad \longrightarrow \quad s(t) = 2\lambda\sqrt{D_{ice}t}. \tag{54}$$

This representation, first, satisfies the initial condition $(50)_5$ and, second, shows that the thickness growth of the ice cover follows a $\sqrt{t}$-law. Obviously, an analogous law also holds for the forward motion of the plunge point of a GILBERT-type delta. To determine the constant λ the remaining STEFAN condition $(50)_4$ is used. With

$$\begin{aligned} \frac{\partial\,\theta}{\partial\,X} &= \frac{2B}{\sqrt{\pi}}\exp\left[-\left(\frac{X}{2\sqrt{D_{ice}}}\right)^2\right]\frac{1}{2\sqrt{D_{ice}t}}, \\ \dot{s}(t) &= \frac{\lambda\sqrt{D_{ice}}}{\sqrt{t}}, \end{aligned} \tag{55}$$

the definition of λ and with (52), equation $(50)_4$ can be written as

$$\lambda\exp(\lambda^2)\text{erf}(\lambda) = \frac{T_{surf}}{\sqrt{\pi}(L/c_{ice})}, \tag{56}$$

which is a transcendental equation for λ. As an approximation, we assume λ to be small, $\lambda \ll 1$; then

$$\exp(\lambda^2) \simeq 1, \qquad \text{erf}(\lambda) \simeq \frac{2}{\sqrt{\pi}}\lambda$$

and (56) becomes

$$\lambda^2 \simeq \frac{T_{surf}}{2(L/c_{ice})}, \tag{57}$$

with the aid of which

$$s(t) \simeq \sqrt{\frac{2D_{ice}T_{surf}}{(L/c_{ice})}t}. \tag{58}$$

If we translate this result into the prograding process of the plunge point of a hypopycnal delta, it reads

$$s(t) \simeq \sqrt{\frac{2D_1\hat{\zeta}_{in}}{H}t}, \tag{59}$$

in which $\hat{\zeta}_{in}$ is the far upstream thickness of the moving sediment layer and H is the constant bottomset depth.

4.2 Prograding deltas

It will be shown now that the analogous problem for the sediment transport differs from the thermal problem only by the 'STEFAN-condition'. An advancing GILBERT-type delta grows into the bottomset region of a lake with a frontal slope of the angle of internal friction ϕ. With reference to Fig. 9 it is clear that

$$\hat{\zeta}_{toe} = \hat{\zeta}_s - \tan\phi\,(u(t) - s(t)) \tag{60}$$

gives the Z-coordinate of the toe of the delta-wedge, irrespective of the exact form of the geometry of the basement. However, if the basement is given as an *inclined plane*, then

$$\hat{\zeta}_{toe} = -u(t)\tan\alpha_1 + \hat{\zeta}_b^0 = -u(t)\tan\alpha_1, \tag{61}$$

where α_1 is the joint slope angle of the basement in the topset and foreset and $\hat{\zeta}_b^0 = 0$ applies, if the origin of the coordinates is shown as indicated in Fig. 36 (see Appendix A). Combining (60) and (61) yields

$$\begin{aligned} -u(t)\tan\alpha_1 &= \hat{\zeta}_s - \tan\phi\,(u(t) - s(t)) \\ \text{or} \qquad u(t)[\tan\phi - \tan\alpha_1] &= \hat{\zeta}_s + \tan\phi\, s(t), \\ \Longrightarrow u(t) &= \frac{\hat{\zeta}_s + \tan\phi\, s(t)}{\tan\phi - \tan\alpha_1}. \end{aligned} \tag{62}$$

If this expression is now substituted into (42), in which $\sigma = 0$ and $\dot{Z}_\ell = 0$, the sediment flux at the plunge point takes the form

$$q(s(t),t) = \left\{ \frac{\hat{\zeta}_s + \tan\phi\, s(t)}{\tan\phi - \tan\alpha_1} - s(t) \right\} \tan\phi \frac{\mathrm{d}\, s}{\mathrm{d}\, t}. \tag{63}$$

Thus, the topset diffusion of a sediment flow on an inclined basement is governed by $(47)_{1,2,3,5}$ with $q_s(s(t),t)$ given by (63), viz.,

$$\begin{aligned} &\frac{\partial\,\hat{\zeta}}{\partial\, t} = D_1 \frac{\partial^2 \hat{\zeta}}{\partial\, X^2}, \qquad 0 \leqslant X \leqslant s(t), \\ &\frac{\partial\,\hat{\zeta}}{\partial\, X} = -\frac{q_0}{D_1}, \qquad X = 0, \quad t \geqslant 0, \\ &\hat{\zeta} = 0, \qquad\qquad X = s(t), \quad t > 0, \\ &\left\{ \frac{\hat{\zeta}(s(t),t) + \tan\phi\, s(t)}{\tan\phi - \tan\alpha_1} - s(t) \right\} \tan\phi \frac{\mathrm{d}s(t)}{\mathrm{d}\, t} \\ &\qquad = q(s(t),t) = -D_1 \frac{\partial\hat{\zeta}}{\partial\, X}_{(s(t),t)}. \end{aligned} \tag{64}$$

The general solution of $(64)_1$ has the form $\hat{\zeta} = A + B\text{erf}(X/(2\sqrt{D_1 t})$. If we write $s(t) = \lambda\sqrt{D_1 t}$ with constant λ, the constants of integration, A and B, can be determined with the aid of $(64)_{2,3}$, so that

$$\hat{\zeta} = \frac{\sqrt{\pi}}{2}\frac{q_0}{D_1}\left\{\text{erf}\left(\frac{\lambda}{2}\right) - \text{erf}\left(\frac{X}{2\sqrt{D_1 t}}\right)\right\}. \tag{65}$$

Now, since $s(t)\dot{s}(t) = D_1\lambda^2/2$ and $\hat{\zeta}(s(t), t) = 0$, the flux boundary condition $(64)_4$ becomes an equation for λ:

$$\begin{aligned} \frac{\lambda^2}{2}\exp\left(-\frac{\lambda^2}{2}\right) &= \frac{q_0}{D_1}\frac{\tan\phi - \tan\alpha_1}{\tan\alpha_1\tan\phi} \\ &\simeq \frac{q_0}{D_1}\frac{1}{\tan\alpha_1}, \quad \text{if} \quad |\alpha_1| \ll \phi. \end{aligned} \tag{66}$$

It is not difficult to become convinced that this analytical solution could only be constructed, because $\hat{\zeta}(s(t), t) = 0$ was imposed as one of the boundary conditions at the plunge point.

4.3 Fluvial 'grade' in river-lake systems

Significant for the fluid mechanical understanding of the formation of GILBERT-type alluvial deltas in a river-lake system are conditions for which neither net deposition nor net erosion arise. A segment of a river where this arises is called **graded**. This terminology was introduced by GILBERT (1877) [18]. According to MUTO & SWENSON (2005) [48], [49] the 'concept of fluvial grade is typically presented as the long-term, equilibrium[8] state of a river system subject to steady allogenic forcing'. They state, quoting SCHUMM (1977) [59], that 'the mechanisms for attaining grade are thought to include adjustments in slope, channel geometry, sinusoidity, bed roughness and grain size.' We add as an important influential factor temporal variations of the free surface of the lake.

Most stretches of alluvial rivers entering a lake are not, or at most approximately 'in a graded state as their long term behavior depends fundamentally on the behavior of its upstream and downstream neighboring environments. Because of this coupling the alluvial river generally cannot attain a graded state with steady boundaries' [49]. This is illustrated in the two panels of Fig. 11, which are motivated by two figures in [48] and PARKER (1977) [53]. Panel (a) shows an idealized fluvio-deltaic GILBERT-type system [19], prograding into a flat-bottomed basin with steady eustatic lake level and constant supply of sediment and water to its upstream boundary. In this case the vertical position of the alluvial-basement transition (the plunge point) is fixed. However, even if the river stretch at time $t = 0$ were in a graded state, the subaqueous avalanching steady sediment flux at the delta front will make the plunge point move lakeward. Consequently, the constant slope delta front will equally move lakeward and therefore lengthen the river stretch and thus decrease its slope thereby forcing aggradation (sediment deposition). The river stretch will thus have its graded state to which it will never return unless an appropriate external control mechanism enforces such conditions. Lake level variations are among such possibilities.

The situation illustrated in panel (b) of Fig. 11, due to PARKER (1977) [53], shows sediment flow into an artificial reservoir bounded by a weir. 'The supplied sediment that progrades and aggrades until the position and elevation of the shoreline coincide with the top of the weir. From this time onward, sediment reaching the shoreline (q_{out}) cannot accumulate on the vertical weir face [. . .]. The alluvial river system continues to expand landward through a combination of aggradation and onlap at the alluvial-basement

[8] I regard the denotation 'equilibrium' as introduced by geologists as a misnomer, since the graded state is not a thermodynamic equilibrium

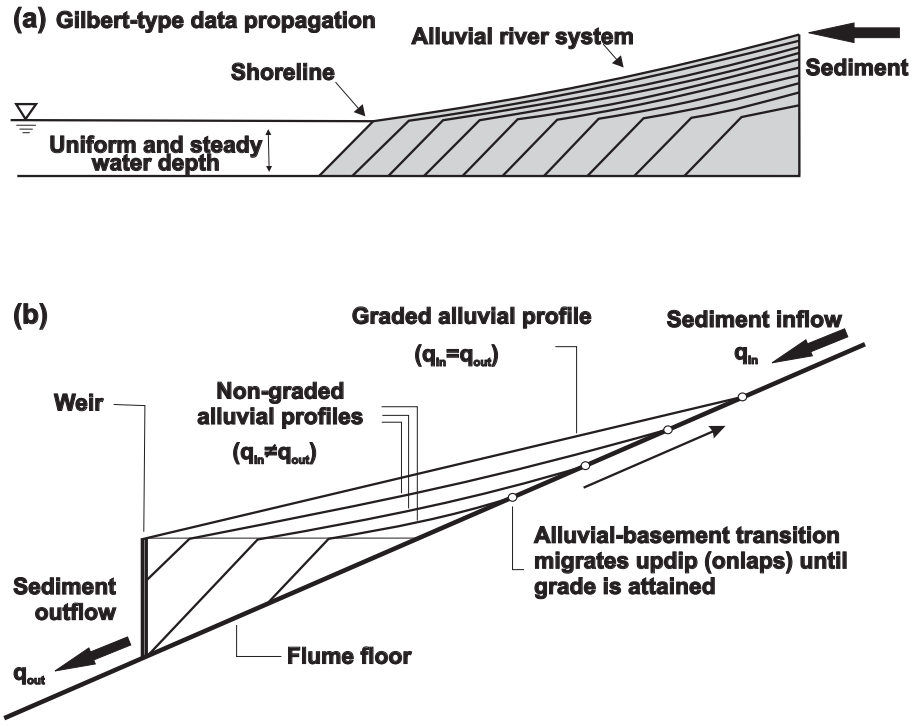

Figure 11: **(a)** Idealized fluvio-deltaic GILBERT-type system prograding into a standing boby of water with uniform and steady depth. Sediment and water supply are steady. Even when the initial state is graded, progression of the wedge delta moves the system away from this graded state into aggravation of sediment, from MUTO & SWENSON [48], [49]. **(b)** sediment flow on an alluvial basement of constant inclination. A weir fixes the free surface of the reservoir. A graded state is attained when aggradation and onlap at the alluvial-basement transition generate a linear profile that allows complete sediment bypass, from PARKER [53]

transition. Eventually, the slope of the alluvial river system becomes constant along its entire length and all sediment is bypassed ($q_{in} = q_{out}$). This graded state, which is characterized by a linear channel profile, will be sustained as long as the fluxes of sediment and water remain unchanged' [48].

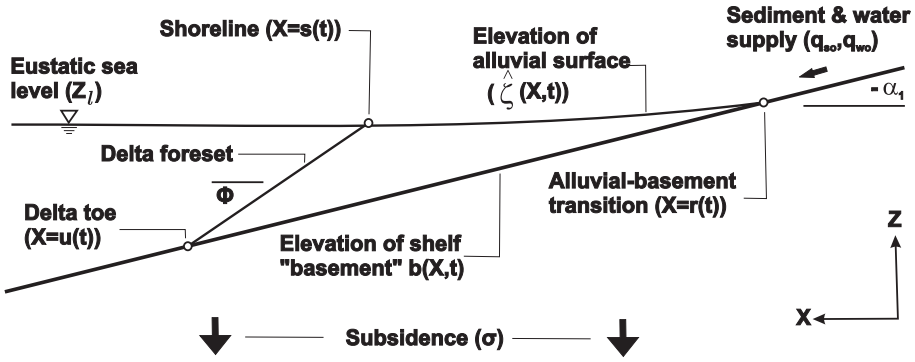

Figure 12: **(a)** Idealized fluvio-deltaic system along a basement of constant inclination ($-\alpha_1$) with a GILBERT-type delta of slope ϕ. Three points are significant: the alluvial-baseement transition, $X = r(t)$; the shoreline or plunge point, $X = s(t)$, and the delta toe, $X = u(t)$, all moving. Courtesy MUTO & SWENSON [48] © *J. Geophys. Res.*

MUTO & SWENSON [48] consider the situation sketched in Fig. 12, where a GILBERT-type delta is formed. This fluvio-deltaic system is prograded across a linear shelf ('basement' $b(X,t)$) in response to a sediment supply q_{s0}. The shelf has a slope $-\alpha_1$ and is subsiding at a spatially uniform rate $\sigma(t)$. The origin of the coordinate system is taken as the intersection of eustatic lake level with the shelf surface at $t = 0$. Let $\zeta(\hat{X},t), b(X,t)$ and $Z_\ell(t)$ be the elevations of the sediment surface, the shelf and eustatic

lake level, respectively. The position of the alluvial-basement transition, shore line (plunge point) and delta toe are $r(t), s(t)$ and $u(t)$, respectively. The initial [. . .] wedge is vanishingly small [. . .] such that at $t = 0$, $r = s = u = 0$ [48].

The diffusion equation in the subaerial regime and boundary conditions at a topset cross-section far upstream, $X = X_1$ and at the plunge point are

$$\begin{aligned} &\frac{\partial\,\hat{\zeta}}{\partial\,t} - D_1\frac{\partial^2\hat{\zeta}}{\partial\,X^2} = -\sigma, && X_1 < X < s(t), \\ &\left.\begin{aligned} &\frac{\partial\,\hat{\zeta}}{\partial\,X} = -(\tan|\alpha_1|)r(t), \\ &D_1\frac{\partial\,\hat{\zeta}}{\partial\,X} = -q_{s0}, \end{aligned}\right\} && X = r(t), \\ &\hat{\zeta} = Z_\ell(t), && X = s(t). \end{aligned} \tag{67}$$

Here, $\sigma = $ const. is the spatially and temporally constant subsidence of the inclined basement. Equation $(67)_2$ expresses that the sediment approaches the up-slope of the basement smoothly, whilst $(67)_3$ prescribes the temporally constant upstream sediment flow. $(67)_4$ sets the level of the sediment surface at the plunge point equal to the level of the lake surface. These conditions must be complemented by a flux jump condition at the plunge point. This is obtained by geometric reasoning. Before turning to that, it is advantageous to introduce the transformed bed elevation

$$\tilde{\zeta} := \hat{\zeta} + \int_0^t \sigma(\tau)\mathrm{d}\tau. \tag{68}$$

Since σ has by assumption no X-dependence, (68) transforms (67) into

$$\begin{aligned} &\frac{\partial\,\tilde{\zeta}}{\partial\,t} = D_1\frac{\partial^2\tilde{\zeta}}{\partial\,X^2}, && 0 < X < s(t), \\ &\left.\begin{aligned} &\frac{\partial\,\tilde{\zeta}}{\partial\,X} = -\tan|\alpha_1|r(t), \\ &D_1\frac{\partial\,\tilde{\zeta}}{\partial\,X} = -q_{s0}, \end{aligned}\right\} && X = r(t), \\ &\tilde{\zeta} = Z_\ell(t) + \int_0^t \sigma(\tau)\mathrm{d}\tau = R_\ell(t), && X = s(t). \end{aligned} \tag{69}$$

The remaining missing boundary condition is the zero jump of sediment flux as the shoreline is crossed: $[\![\, q_s(s(t),t)]\!] = 0$ and will be given here for conditions of non-vanishing subsidence, $\sigma(t) \neq 0$, and non-trivial lake level movements $\dot{Z}_\ell \neq 0$. A first relation is obtained by evaluating the water depth at the delta toe by two different geometric expressions, see Fig. 12,

$$Z_\ell(t) + \int_0^t \sigma(\tau)\mathrm{d}\tau - u(t)\tan|\alpha_1| = (u(t) - s(t))\tan|\phi|,$$

from which we deduce

$$u(t) = \frac{\tan|\phi|s(t) + R_\ell(t)}{\tan|\phi| - \tan|\alpha_1|}, \tag{70}$$

where R_ℓ is defined in $(69)_4$. Next, the sediment flux is given by

$$\begin{aligned} q_s(s(t),t) &= \frac{\mathrm{d}}{\mathrm{d}\,t}\int_s^u \left[\hat{\zeta}(X,t) - b(X,t)\right] \mathrm{d}X \\ &= (u(t)-s(t))\left(\frac{\mathrm{d}\,Z_\ell(t)}{\mathrm{d}\,t} + \tan|\phi|\frac{\mathrm{d}\,s(t)}{\mathrm{d}\,t} + \sigma(t)\right) \\ &= (u(t)-s(t))\left(\frac{\mathrm{d}\,R_\ell(t)}{\mathrm{d}\,t} + \tan|\phi|\frac{\mathrm{d}\,s(t)}{\mathrm{d}\,t}\right) \\ &\overset{(70)}{=} \frac{\tan|\alpha_1|s(t) + R_\ell(t)}{\tan|\phi| - \tan|\alpha_1|}\left(\frac{\mathrm{d}\,R_\ell(t)}{\mathrm{d}\,t} + \tan|\phi|\frac{\mathrm{d}\,s(t)}{\mathrm{d}\,t}\right) \\ &= -D_1\frac{\partial\,\tilde{\zeta}(s(t),t)}{\partial\,X}. \end{aligned} \tag{71}$$

For prescribed $\sigma(t)$ and $Z_\ell(t)$ this formula allows computation of the slope $\partial\,\tilde{\zeta}(s(t),t)/\partial\,X$ at $X = s(t)$ in terms of the basement slope $|\alpha_1|$ and the angle of repose $|\phi|$. We rather wish here to use (71) to determine the temporal evolution of the lake level $R_\ell(t)$, which is necessary to generate graded conditions in the topset. Such conditions prevail, if the slope $\partial\,\tilde{\zeta}/\partial\,X$ is constant throughout the topset river stretch; it implies (see Fig. 12)

$$\begin{aligned} \frac{\partial\,\tilde{\zeta}}{\partial\,X}|_s &= -\frac{q_s}{D_1}|_{X\in[r(t),s(t)]} = -\frac{q_{s0}}{D_1} = \text{const.}, \\ \frac{\partial\,\tilde{\zeta}}{\partial\,X}|_s &= 0. \end{aligned} \tag{72}$$

With the obvious relation

$$\frac{\mathrm{d}\,\tilde{\zeta}}{\mathrm{d}\,t}|_s = \frac{\mathrm{d}R_\ell(t)}{\mathrm{d}\,t} = \underbrace{\frac{\partial\,\tilde{\zeta}}{\partial\,X}|_s}_{-q_{s0}/D_1}\frac{\mathrm{d}\,s(t)}{\mathrm{d}\,t} + \underbrace{\frac{\partial\,\tilde{\zeta}}{\partial\,t}|_s}_{=0}, \tag{73}$$

leading to

$$\frac{\mathrm{d}R_\ell(t)}{\mathrm{d}\,t}|_{\text{graded}} = -\frac{q_{s0}}{D_1}\frac{\mathrm{d}\,s(t)}{\mathrm{d}\,t}, \qquad R_\ell(t)|_{\text{graded}} = -\frac{q_{s0}}{D_1}s(t). \tag{74}$$

Here, the second expression has been obtained by an integration with respect to time. Now, substituting into $(74)_1$ the expression for q_{s0} stated in $(71)_4$, it can be shown that

$$\frac{\mathrm{d}}{\mathrm{d}\,t}\left(R_\ell^2\right) = \mathcal{R}^2\left(\alpha_1,\phi,\frac{D_1}{q_{s0}}\right)q_{s0} \tag{75}$$

with

$$\mathcal{R}^2 := 2(\tan|\phi| - \tan|\alpha_1|)\left\{1 - \tan|\alpha_1|\frac{D_1}{q_{s0}}\right\}^{-1} \times \left\{1 - \tan|\phi|\frac{D_1}{q_{s0}}\right\}^{-1}. \tag{76}$$

Therefore, by integration

$$R_\ell = -\mathcal{R}\sqrt{\int_0^t q_{s0}(\tau)\mathrm{d}\tau} = -\mathcal{R}\sqrt{q_{s0}}\sqrt{t}, \tag{77}$$

in which the expression on the far right holds for $q_{s0} = \text{const}$. Alternatively, in view of the definition of

$R_\ell(t)$ in $(69)_4$

$$Z_\ell = -\mathcal{R}\sqrt{q_{s0}}\sqrt{t} - \sigma\, t, \qquad \text{for} \qquad \sigma = \text{const.} \tag{78}$$

The positive root in (77) would correspond to a lake level rise for which no graded flow exists.

Relation (77) can be made dimensionless by using the reference length $[L]$ and reference time $[T]$ via

$$[L] := q_{s0}|\frac{\mathrm{d}R_\ell}{\mathrm{d}\,t}|_c, \quad [T] = \frac{[L^2]}{D_1} \tag{79}$$

and by scaling R_ℓ and t by

$$R_\ell^* = \frac{R_\ell}{\phi[L]}, \quad t^* = \frac{t}{D_1[L]}. \tag{80}$$

With these, $(77)_2$ takes the form

$$\begin{aligned} R_\ell^* &= \mathcal{R}^*\sqrt{t^*}, \\ \mathcal{R}^* &= -\sqrt{2\left(1-\frac{|\alpha_1|}{|\phi|}\right)\left(\frac{q_{s0}}{|\phi|D_1}\right)^3\left(1-\frac{q_{s0}}{|\phi|D_1}\right)^{-1}\left(1-\frac{q_{s0}}{|\phi|D_1}\frac{|\alpha_1|}{|\phi|}\right)^{-1}} \end{aligned} \tag{81}$$

in which all quantities are dimensionless.

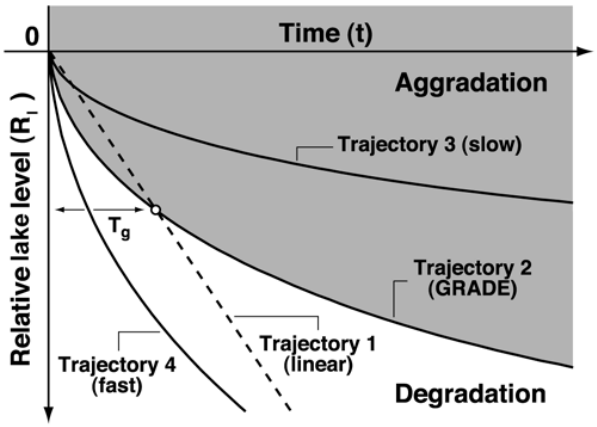

Figure 13: Conceptual partitioning of the $R_\ell - t$ space into regions of global alluvial aggradation (shaded) and degradation. Trajectory 2 is that required for *grade*. For details of the dynamics of trajectories 1 – 4 see the main text. Courtesy MUTO & SWENSON [48] © *J. Geophys. Res.*

MUTO & SWENSON [48] present model predictions of fluvio-deltaic response to the four patterns of R_ℓ – fall, shown conceptually in Fig. 13. Common to all model scenarios are the dimensionless numbers $q_{s0}/(D_1|\alpha_1|) = 0.5$, $|\alpha_1|/|\phi| = 0.2$, and the dimensionless duration of progradation ($0 < t^* < 3$). They consider first the response to a linear R_ℓ history (Fig. 13, dashed trajectory, labeled 1) , which cannot support sustained grade.

Figure 14 shows the evolution of the positions $X = \{r(t), s(t), u(t)\}$, and the corresponding stratigraphic evolution of the fluvio-deltaic system. 'At small times, the constant rate of fall in R_ℓ is less than that required for grade, thereby placing the system in the aggradational regime of $R_\ell - t$ space. During this time interval the position $X = r(t)$ migrates lakeward, and the fluvial system is everywhere aggradational. At $t = T_g$ the linear R_ℓ trajectory intersects the graded trajectory, and the fluvial system attains a state of grade (in an instantaneous sense). The system cannot maintain in this graded state, however [. . .], for $t > T_g$ fluvial incision continuously cannibalizes previously deposited sediments and,

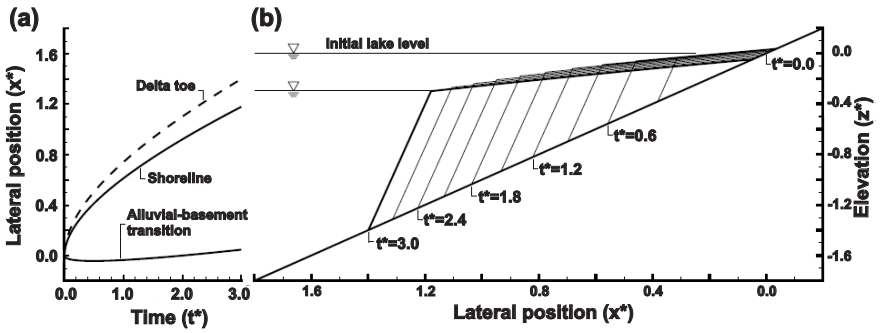

Figure 14: Progradation of a GILBERT-type delta in response to a steady rate of fall in relative lake level. **(a)** Trajectories of the alluvial-basement transition $X = r(t)$; shoreline, $X = s(t)$; delta toe, $X = u(t)$; **(b)** time-lines of the free surface. All quantities are dimensionless. Courtesy MUTO & SWENSON [48] © *J. Geophys. Res.*

correspondingly, the transition point $X = r(t)$ migrates lakeward (offlap)' [49].

Figure 15 shows the graded (top), sub-graded (middle) and super-graded (bottom) states. In panels (a) (left) the evolutions of the alluvial-basement transition, shoreline, and delta toe for the fluvio-deltaic response to a relative lake level curve are shown; panels (b) show the corresponding time lines of the stratal architecture for the indicated dimensionless times. In the top panel the lake level time curve is given by equation (81). 'The alluvial basement transition remains stationary throughout the prograding process. The shoreline and delta toe advance lakeward at a monotonically decreasing rate that reflects the linearly increasing water depth, [48]. Panel (b) is showing the time lines. The alluvial system has a linear profile and shows neither net aggradation nor net erosion. Throughout progradation, the entire sediment supply bypasses the alluvial regime to drive progradation via deposition on the delta' [48].

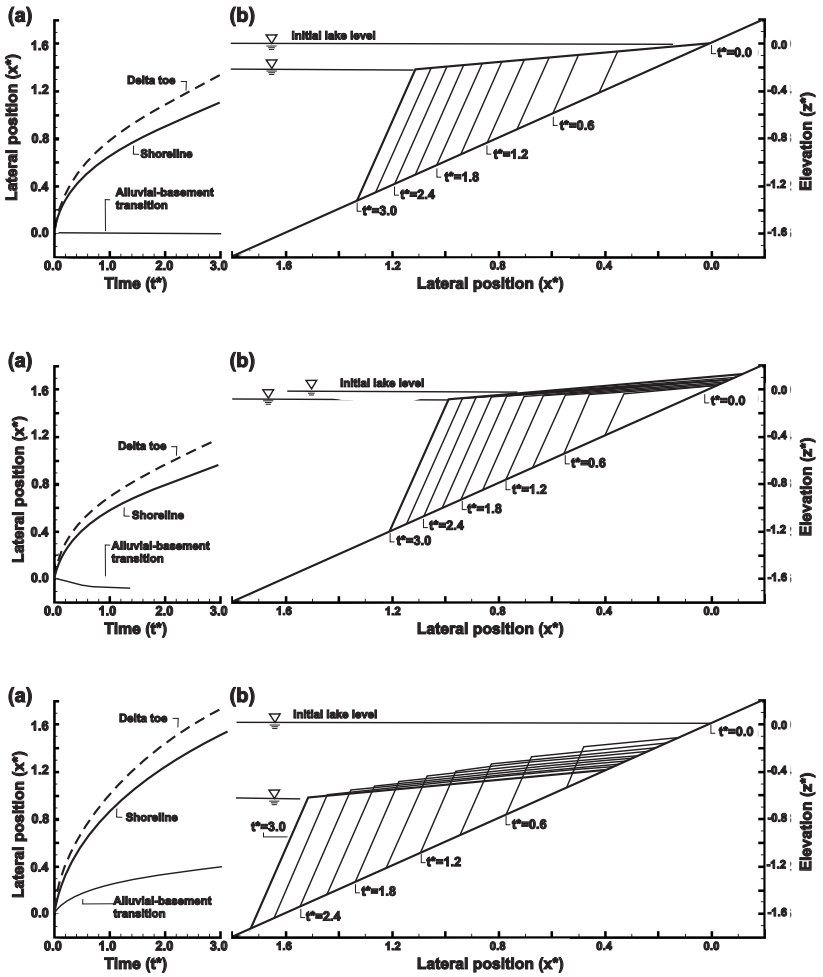

Figure 15: Top: Fluvio-deltaic progradation in a state of grade. Dimensionless relative lake level trajectory, given by equation (81). **(a)** Trajectories of alluvial-basement transition, $X = r(t)$; shoreline $X = s(t)$; delta toe $X = u(t)$; **(b)** resultant stratal architecture (time lines). **Middle**: Same as in the top panel in response to $R^*_\ell \propto -\sqrt{t*}$, but with a leading coefficient, which is half that of the graded value. Note the persistent landward displacement of $X = r(t)$. **Bottom**: Same as in the top and middle panels in response to $R^*_\ell \propto -\sqrt{t*}$, but with a leading coefficient, which is twice that of the graded value. Note the persistent lakeward displacement of all these points $X = \{r(t), s(t), u(t)\}$. Courtesy MUTO & SWENSON [48] © *J. Geophys. Res.*

4.4 Experimental verification

MUTO & SWENSON [48] present laboratory experiments performed at Nagasaki University, which corroborate the correctness of the theoretical model for fluvio-deltaic formations with the outlined specific patterns of relative lake level fall.

A stainless steel tank (4.5 m long $\times$ 1.0 m wide $\times$ 1.3m deep) with a frontal glass wall for photographic recording of the moving sediment mass was filled with water, whose free surface was computer monitored via an electromagnetic flow meter with high accuracy. Inside the tank, a narrow 4.3 m long flume with uniform width (1.0 cm) and longitudinal inclination ($|\alpha_1|$) is placed to mimic the sloping basement. The downslope end of the flume is open. A slurry of 0.2 mm quartz sand and water was fed into the flume from a point above the initial water level, which produced from zero inceptions the desired alluvial deltaic depositions with the typical slope discontinuity at the moving shore line. The sediment flow depth is approximately 1.0 mm thick, and avalanching was the dominant transport mechanism on the subaqueous delta. Among the four experiments in this set-up the significant difference was in doubling and halving of the upstream water supply q_{w0}, which controls diffusivity D_1 and characteristic slope of the fluvial surface q_{s0}/D_1. The dependence of D_1 on q_{w0} was determined by separate flume experiments. Note also that the initial rate of fall in relative lake level according to (77) or (81) has a square root singularity at $t = 0$, which cannot be reproduced in the experiments. Instead, linear initial fall of lake level was used, which intersects the ideal $-\sqrt{t}$ lake level fall curve at $t = T_g$, say, beyond which lake level monitoring followed the $-\sqrt{t}$ curve, for details see MUTO & SWENSON [48]. In the following we report some of their results, see Table 1.

'Figures 16 and 17 document the evolution of the fluvio-deltaic system generated in experimental Run 1, in which the rate of fall in relative lake level was constant. Figure 16 shows the trajectories $X = \{r(t), s(t), u(t)\}$ in $X - t$ space; Figure 17 is a set of sequential photographs of the experiment. With a constant sediment supply in this experiment, the spatial extent of both the alluvial river and the delta foreset increased with time (Fig. 16). Shore line and delta toe migrated basinward throughout the experiment, whereas the alluvial-basement transition migrated first landward ($0 < t < 450$ s) and then basinward ($450 < t < 3736$ s). This transition from net alluvial aggradation to net degradation [...] is clear in Fig. 17. During the degradational phase, material deposited in the previous aggradational state is re-deposited in the formation of the advancing delta front' [48].

In the complementing three experiments the lake level R_ℓ was monitored in the piecewise continuous manner explained previously with data as given in Table 1. Figures 18 and 19 show the moving boundary trajectories and stratigraphic evolution of the fluvio-deltaic system generated in experimental Run 2A (of MUTO & SWENSON [48]), which approximately mimics graded conditions. During the initial steady fall in relative lake level ($0 < t < T_g = 570$ s) the alluvial basement transition migrates landward (Fig. 18), accompanied with sediment deposition in response to the non-graded initial linear lake level drop. This phase was followed by the graded history R_ℓ and re-adjustment into a graded state by degradation and slight lakeward advance of the alluvial-basement transition, $X = r(t)$. This phase terminated at $t = 720$ s beyond which the fluvio-deltaic system was graded. This is clearly seen in Fig. 19, in which the alluvial-basement transition point (∇ in the figure) does not move through time. The small shift between the critical position of this point ($\uparrow$ in the figure) and its position through time (∇) is due to the early time linear lake-level fall (to avoid the $-\sqrt{t}$ singularity as $t \to 0$) and further experimental imperfections (see MUTO & SWENSON [48]). Except for these the maintenance of the graded behavior is well kept in this

Table 1: Experimental parameters for two of the 4 experiments. Courtesy MUTO & SWENSON [48], © *J. Geophys. Res.*

	Run 1	Run 2A
Run time, s	3736	7214
Total R_ℓ fall, cm	-38.9	-16.2
Mode of R_ℓ fall	steady	initially steady, then decelerating
Steady component		
Duration T_g, s	3736	570
Fall rate $\mathrm{d}R_\ell/\mathrm{d}t$ cm/s	-1.04×10^{-2}	-7.78×10^{-3}
Decelerating component		
Duration, s	–	6644
Coefficient in (77) cm $s^{-1/2}$	–	0.197
Coefficient in (81)	–	0.0986
Shelf slope $\lvert\tan\alpha_1\rvert$	0.204	0.196
Foreset slope $\tan\lvert\phi\rvert$	0.739	0.654
Alluvial slope[a]	0.141	0.107
Water discharge ${q_{w0}}^b$, cm^2/s	4.88	3.91
Sediment discharge ${q_{s0}}^b$, cm^2/s	0.351	0.181
Fluvial diffusivity D_1, cm^2/s	2.49	1.69
Length scale, $[L]$, cm	33.7	80.9
Elevation scale, H cm	6.88	15.9
Time scale $[T]$, s	455	3860
Dimensionless numbers		
Alluvial/shelf slope $q_{s0}/(D_1\lvert\alpha_1\rvert)$	0.688	0.545
Shelf/foreset slope $\lvert\tan\alpha_1\rvert/\tan\lvert\phi\rvert$	0.277	0.300

[a] Length-averaged quantity
[b] Width-averaged quantity

experiment.

5 Hyper-pycnal deltas

As already mentioned in the introductory section, hyper-pycnal flows in still ambient waters occur when the inflowing discharge is denser than that of the receiving ambient. This commonly occurs when flood waters, laden with fine sediments enter freshwater lakes. In such cases the denser, particle laden, inflow will plunge down the lake shore in form of a density or turbidity undercurrent as sketched in Fig. 1b. According to ELLISON and TURNER (1959) [12] such flows maintain their identity for long distances because, owing to their relatively large density, mixing with the ambient fluid at their upper boundary is hampered. Their slow secession is primarily due to a gradual settling out of their finer fractions of the suspended sediments (BELL, (1942) [4]) and because of the dying turbulent intensity due to turbulent dissipation.

The boundary layer structure of hyper-pycnal flows down the lake bottom from its shore input to the bottomset far-field generally exerts a significantly different geomorphological influence than do their homo- and hypo-pycnal counterparts. The foresets of hyper-pycnal deltas have much smaller inclinations and, unlike the avalanching processes in GILBERT-type delta fronts, their sediment transport is akin to subaerial bedload transport in the topset river stretches. Such views are supported by studies and

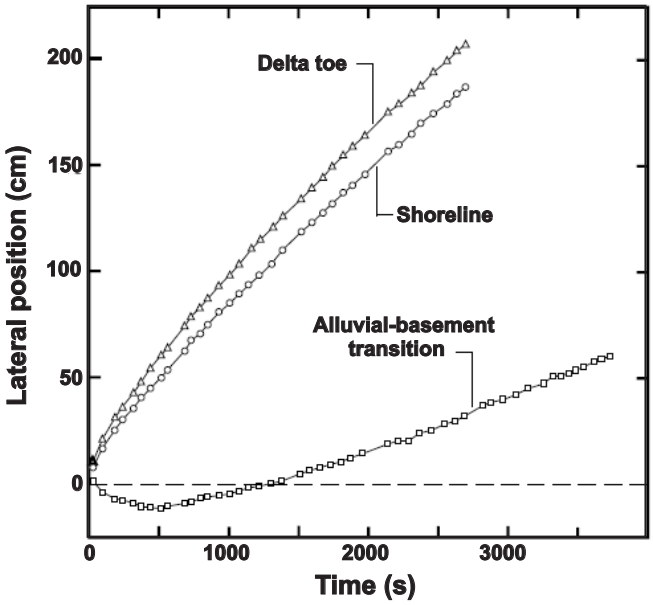

Figure 16: Trajectories of the alluvial-basement transition, $X = r(t)$; shore line, $X = s(t)$; and delta toe, $X = u(t)$; in experimental Run 1, in which R_ℓ falls steadily. Note, $r(t)$ first migrates landward (onlap) until $t = 450$ s, before moving basinward (offlap) for the remainder of the experiment. By contrast, $s(t)$ and $u(t)$ migrate persistently lakeward. The finite slope of all curves is manifestation of the initial linear lake level fall. Courtesy MUTO & SWENSON [48], © *J. Geophys. Res.*

observations in the Alpine Rhine river at Lake Constance (MÜLLER and FÖRSTNER, (1966) [44]; ROTH et al. (2001) [58]), where maximum slopes in the foreset regime are of the order of 5°-10° (ADAMS et al. (2001) [2], 6°) and have further found corroboration e. g. in the Colorado River delta in Lake Mead (GROVER and HOWARD, (1937) [22]; SMITH et al. (1960) [60]) and the Noeik River delta in a fjord of the British Columbia Coast (BORNHOLD and PRIOR, (1990) [5]). Moreover, WRITE et al. (1988) [68] have studied the marine dispersal and deposition of Yellow River silts by gravity driven underflows and FAN and MORRIS (1992) [13] employ such density current concepts to study reservoir sedimentation, all as mentioned by LAI and Capart (2007) [33]. Corresponding laboratory experiments have been conducted, among others, by YU et al. (2000) [69]; KOSTIC and PARKER, (2003) [30]; TONIOLI and SCHULTZ (2005) [64] and LAI, (2006) [32].

In this connection an influential paper by KENYON and TURCOTTE, (1985) [27] should be mentioned. LAI and CAPART emphasize that these authors have foreseen such kind of foreset morphology and its time evolution via a diffusion process. They, 'however, identified bulk transport (creep and landslides) as the geomorphologic agent responsible for the subaqueous diffusion. [. . .] they did not consider the possibility that turbidity undercurrents could be responsible instead.' This under water density current is LAI and CAPART's (2007) [33] suggested mechanism, which is responsible for the formation of hyper-pycnal deltas.

In the ensuing analysis we shall rely upon the diffusive transport model for the topset regime as developed in Sections 2 and 3. This diffusion model will be connected at the plunge point to a similar diffusion model, which will be valid in the foreset regime. This latter model is by itself a simplified description of the realistic sedimenting processes as they occur in hyper-pycnal delta regions. Indeed, 'the turbulent [under]current carries fine sediments which gradually settle out of suspension, and simultaneously they can drive a basal transport of coarser grains. This dual role played by the currents complicates

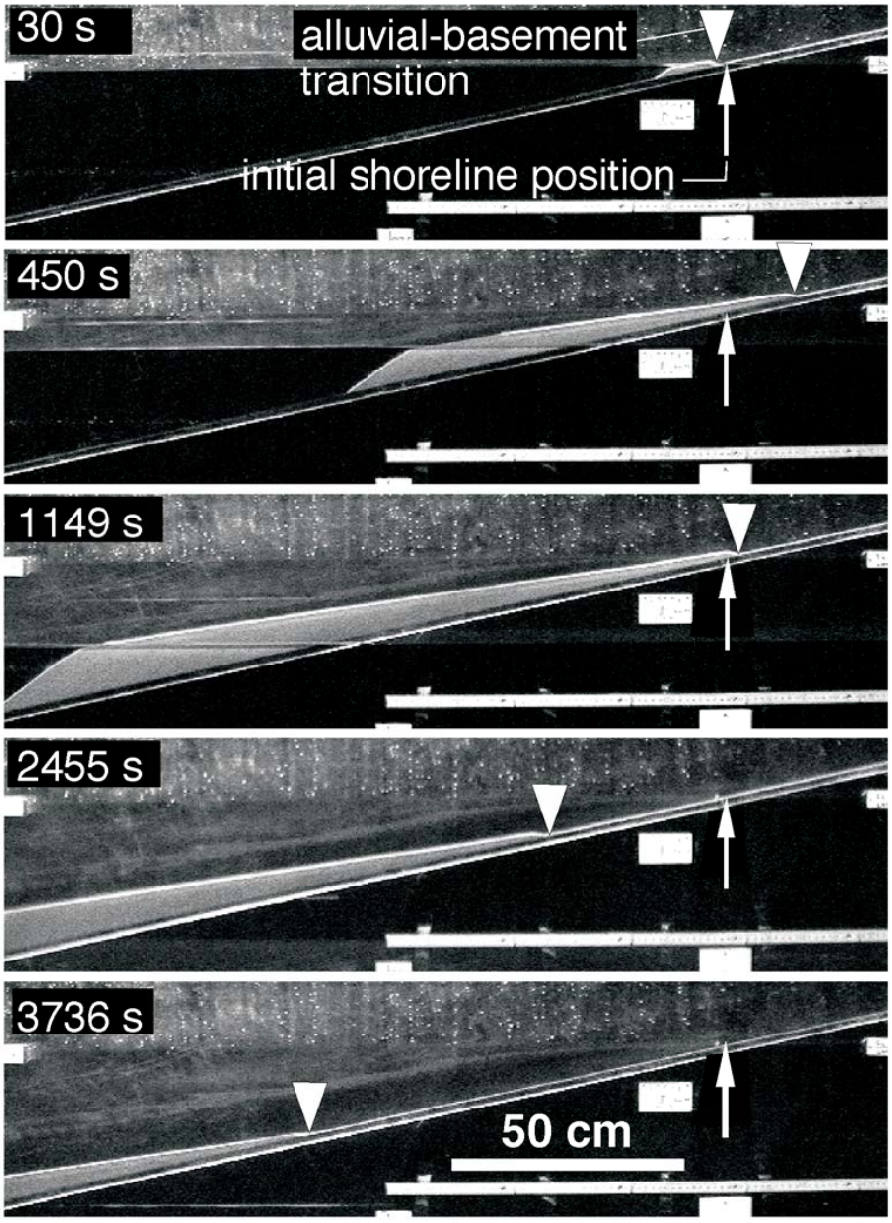

Figure 17: Sequence of photo images of the fluvio-deltaic system in experimental Run 1. Experimental run time (in seconds) is shown in each panel on the left; position of the initial alluvial-basement transition (agreeing with the corresponding theoretical transition position under graded conditions for all time) is shown as $\uparrow$. The evolving experimental alluvial-basement transition point is shown as ∇ and indicates its landward early movement for $t < 450$ s, followed by persistent basinward motion afterwards. Courtesy MUTO & SWENSON [48], © *J. Geophys. Res.*

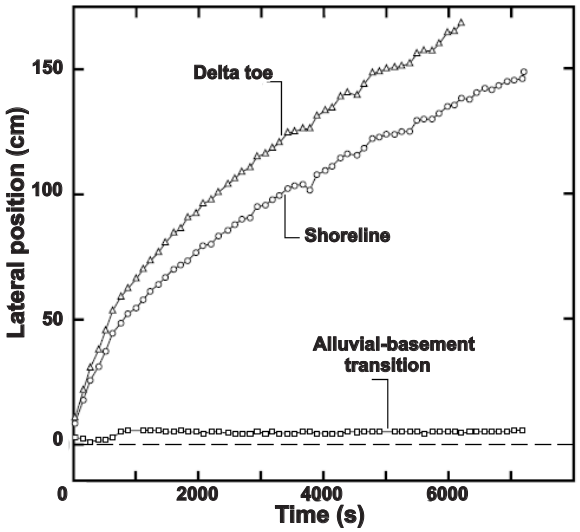

Figure 18: Trajectories of the alluvial-basement transition, $X = r(t)$; shore line, $X = s(t)$; delta toe, $X = u(t)$; in experimental Run 2A. During the early linear lake level fall ($0 < t < T_g = 570$ s) the alluvial-basement transition point retreated somewhat; after $t = 720$ s this transition point remains stationary up to $t = 7200$ s. This experiment mimics graded conditions nearly perfectly as the experimental curve $X = r(t)$ remains practically constant for $t > 720$ s. Note, $X = s(t)$ and $X = u(t)$ show linear initial stretches merging into $-\sqrt{t}$ curves with a slight kink at $t = 720$ s. Courtesy MUTO & SWENSON [48], © *J. Geophys. Res.*

both theoretical developments and experimental interpretations. For this reason, [we will] ignore the first process, and focus only on the second. It will be assumed that the fines fraction of the turbidity current (responsible for the density contrast with the ambient water) settles out of suspension at a very slow rate. As a result, we will not consider the long range delivery or long term settling of these fines, nor consider the resulting formation of bottom set beds. Instead, we will focus exclusively on the upstream geomorphic influence exerted by the turbid underflows on the coarser-grained foresets. This simplified picture is illustrated in Fig. 1b, where it is contrasted with the GILBERT-type delta, Fig. 1a, described earlier', [33].

5.1 Foreset diffusion model

The ensuing derivation follows and complements an analysis by LAI and CAPART (2007) [33]. Accordingly, even though limited entrainment of ambient water into the submerged gravity current gives rise to a growth of mass flow, steady plumes are observed, which corresponds to no growth of mass flow. They correspond to effectively normal subaqueous flow states for which the basal shear stress (TURNER 1973 [65]) is given by

$$\tau_b = \left[(\rho - \rho_\infty)gh + (\rho_0 - \rho)g\delta\right]\sin\beta \simeq (\rho - \rho_\infty)gh\sin\beta, \tag{82}$$

where the approximation holds since $\delta \ll h$. ρ is the density of the turbid water in the density current, and the shear stress τ_b has been reduced due to the ambient buoyancy. Analogously,

$$\sigma_b' = \left[(\rho_\infty h + \rho_0\delta) - (\rho_\infty h + \rho\delta)\right]g\cos\beta = (\rho_0 - \rho)\delta g\cos\beta. \tag{83}$$

Assuming the COULOMB-TERZAGHI relation (9), viz.,

$$\tau_b = \tan\phi\,\sigma_b' \tag{84}$$

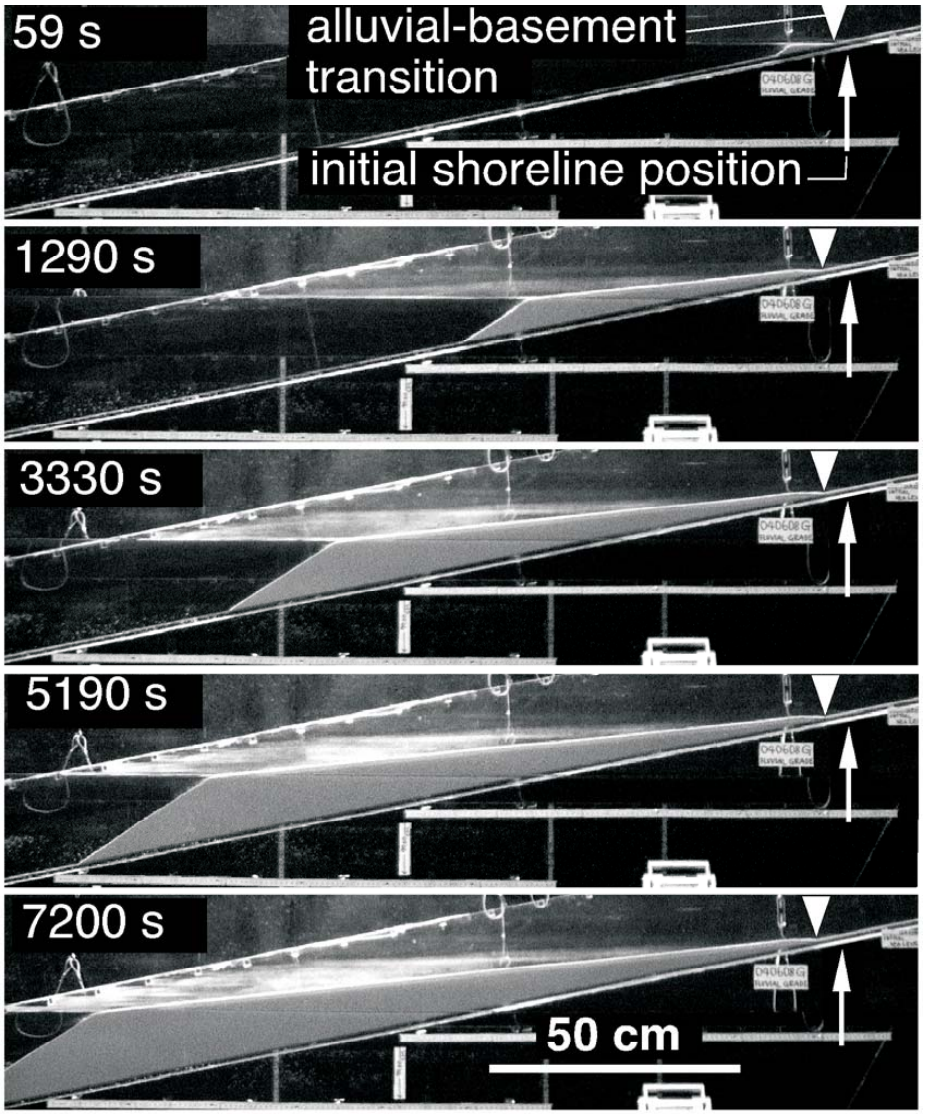

Figure 19: Run 2A, subjected to nearly graded conditions. Sequence of photo images of the fluvio-deltaic system in experimental Run 2A, subjected to nearly graded conditions. ↑ indicates the initial position of the alluvial-basement transition points. ∇'s show these transition points at the indicated times (on the left in each panel); this position remains unchanged after $t = 720$ s and is, together with the plane free surface of the alluvial deposit, reminiscent of graded conditions. Courtesy MUTO & SWENSON [48], © *J. Geophys. Res.*

and substituting (82) and (83) into (84) yields

$$\delta = \frac{(\rho - \rho_\infty)\tan\beta}{(\rho_0 - \rho)\tan\phi}h = \frac{(\rho - \rho_\infty)\tan\beta}{[(1-n_0)\rho_s - \rho]\tan\phi}h, \tag{85}$$

where n_0 is the ponosity. This is the subaqueous analogue to the subaerial representation (11). Note, this result is at variance with that stated in [33]. Next we write

$$v = \alpha_2 u, \tag{86}$$

in which u is the depth averaged downslope velocity of the density current and v is the corresponding average speed of the moving sediment layer. The dimensionless parameter α_2 plays the same role as α_1 in (12) with likely different value, because the velocity profiles in the subaerial flows are not similar to those of subaqueous flows. Now, with $q = \delta\, v$ we obtain

$$q = \delta\, v = \alpha_2 hu \frac{(\rho - \rho_\infty)\tan\beta}{[(1-n_0)\rho_s - \rho]\tan\phi}. \tag{87}$$

With $\tan\beta = -\partial\,\hat{\zeta}/\partial\, X$, the definition

$$\dot{m}' := (\rho - \rho_\infty)hu \tag{88}$$

and the diffusion property

$$q = -D_2 \frac{\partial\,\hat{\zeta}}{\partial\, X}$$

we may alternatively write for the diffusivity

$$D_2 = \frac{\alpha_2 \dot{m}'}{[(1-n_0)\rho_s - \rho]\tan\phi}. \tag{89}$$

Even though the thickness, density and velocity of the current can evolve along the trajectory of the density current, it can be shown that the buoyancy flux (88) remains constant along the trajectory

$$\frac{\mathrm{d}\dot{m}'}{\mathrm{d}\, X} = 0.$$

This is the vanishing entrainment assumption above. In summary, with the conservation of sediment mass equation (5) we obtain the diffusion equation

$$\frac{\partial\,\hat{\zeta}}{\partial\, t} = \frac{\partial}{\partial\, X}\left(D_2 \frac{\partial\,\hat{\zeta}}{\partial\, X}\right) \tag{90}$$

as evolution equation for the position of the upper surface of the sediment layer of hyper-pycnal deltaic formations.

With D_1 and D_2 given by (17) and (89), respectively, we may deduce

$$\frac{D_2}{D_1} = \frac{\alpha_2}{\alpha_1}\frac{(\rho - \rho_\infty)(1-n_0)(\rho_s - \rho_1)}{[(1-n_0)\rho_s - \rho]\rho}. \tag{91}$$

Replacing as an approximation in the braces of the denominator the density ρ by $(1-n_0)\rho_1$, where ρ_1 is the upstream density, the above formula becomes

$$\frac{D_2}{D_1} \simeq \frac{\alpha_2}{\alpha_1}\frac{\rho-\rho_\infty}{\rho} \simeq \frac{\alpha_2}{\alpha_1}\frac{\rho_1-\rho_\infty}{\rho_1}. \tag{92}$$

This formula may serve as an approximation for estimations of the ratio of the foreset and topset diffusivities. With $\alpha_2 \leqslant \alpha_1$ and $\rho_1 \sim \rho$, it is seen that the subaqueous diffusion coefficient is smaller or very much smaller than its subaerial counterpart.[9] This reflects a reduction in transport capacity when the flow transits from subaerial stream flow to subaqueous density current flow.

5.2 Combined topset-foreset diffusion process for hyper-pycnal deltas

According to the above simple formulation of the formation of hyper-pycnal deltas, their evolution is described by the foreset diffusion equation (18), which is solved subject to an upstream boundary condition (either prescription of the moving sediment flux or the Z-coordinate of the moving sediment layer). This topset diffusion problem must be connected to an analogous foreset diffusion problem (90), subject to the far downstream boundary condition that the layer thickness of the density current tends to zero as $X \to \infty$. At the plunge point the two models must be patched together such that the sediment layer thickness at $X = s(t)$ is continuous as is the sediment mass flux across the plunge point. LAI and CAPART [33] write these conditions as

$$\begin{aligned} q(X,t) &= \begin{cases} -D_1\dfrac{\partial\hat{\zeta}}{\partial X}, & \hat{\zeta}(X,t) \geqslant Z_\ell(t), \\ -D_2\dfrac{\partial\hat{\zeta}}{\partial X}, & \hat{\zeta}(X,t) \leqslant Z_\ell(t), \end{cases} \\ \hat{\zeta}(X,t) &- Z_\ell(t) = 0, \end{aligned} \tag{93}$$

where Z_ℓ is the lake level elevation. Equations (18) and (90), combined with upstream and downstream boundary conditions and transition conditions (93) define a so-called double-diffusion problem, which prior to LAI and CAPART [33] was already given by JORDAN and FLEMING (1990) [14] [based on precursory results by BEGIN et al. (1981) [3], KENYON and TURCOTTE (1985) [27], but these authors did not interpret the foreset diffusion problem as emerging from a turbulent density under-current].

a) Topset and bottomset with equal basement slope As a simple but nevertheless mathematically not easy example, consider an infinitely long inclined plane defining the topset-bottomset lower boundary basement with slope $-S = -\tan\beta$, see Fig. 20a. Assume, moreover, a constant lake surface and choose a Cartesian coordinate system as shown in the figure with origin at the intersection of $Z = Z_\ell$ and $Z = -SX$. Let a sediment transport process be started with this configuration at time $t = 0$, and assume a hyper-pycnal delta is being formed for $t > 0$, of which Fig. 20b shows a snapshot. Its plunge point is at $X = s(t), Z = Z_\ell (= 0$ here). The sediment transports in the topset and foreset are then described by the following initial boundary value problems.

[9] With $\alpha_1 = \alpha_2$ and $\rho_1 = 2100$ kg m^{-3} and $\rho_\infty = 1100$ kg m^{-3} one obtains $D_2/D_1 = 0.48$ (foreset conditions). Alternatively, with $\rho_1 = 1200$ kgm^{-3}, $\rho_\infty = 1100$ kgm^{-3}, we get $D_2/D_1 = 0.083$.

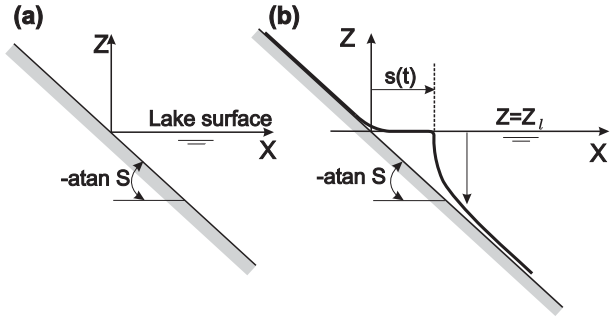

Figure 20: Formation of a hyper-pycnal alluvial delta in a lake with a bottom profile of constant slope $-S$ in the topset and foreset alike. **(a)** Geometry and selection of the coordinates (X, Z) (situation at $t = 0$). **(b)** Delta architecture at $t > 0$

$$\begin{aligned}
&\frac{\partial \hat{\zeta}_1}{\partial t} - D_1 \frac{\partial^2 \hat{\zeta}_1}{\partial X^2} = 0, \quad -\infty < X < s(t), \quad t > 0, \\
&\frac{\partial \hat{\zeta}_1}{\partial X} = -S, \qquad\qquad X \to -\infty, \quad t \geqslant 0, \\
&\hat{\zeta}_1 = 0, \qquad\qquad X = s(t), \quad t \geqslant 0, \\
&\hat{\zeta}_1 = 0, \qquad\qquad -\infty < X < s(t), \quad t = 0,
\end{aligned} \tag{94}$$

as well as

$$\begin{aligned}
&\frac{\partial \hat{\zeta}_2}{\partial t} - D_2 \frac{\partial^2 \hat{\zeta}_2}{\partial X^2} = 0, \quad s(t) < X < \infty, \quad t > 0, \\
&\frac{\partial \hat{\zeta}_2}{\partial X} = -S, \qquad\qquad X \to \infty, \quad t \geqslant 0, \\
&\hat{\zeta}_2 = 0, \qquad\qquad X = s(t), \quad t \geqslant 0, \\
&\hat{\zeta}_2 = 0, \qquad\qquad s(t) < X < \infty, \quad t = 0,
\end{aligned} \tag{95}$$

and these equations must be 'connected' by the transition condition

$$\begin{aligned}
&q_1(s(t), t) - q_2(s(t), t) = -d, \\
&[\![q(s(t), t)]\!] = d.
\end{aligned} \tag{96}$$

Problem (94) describes the sediment transport in the topset as a diffusion process, with vanishing layer thickness at $\hat{\zeta}_1(X, 0), \hat{\zeta}_1(s(t), t)$ and approaching a prescribed slope far upstream. Analogously, the sediment transport in the foreset is also diffusive, starting from a vanishing delta front thickness $\hat{\zeta}_2(X, 0) = 0, \hat{\zeta}_2(s(t), t) = 0$ and approaching the same bottomset slope for $X \to \infty$ as in the topset for $X \to -\infty$. These two solutions are matched at the plunge point by requesting that the moving sediment flux may suffer a jump of size d as given in (96). Its physical significance will be discussed below.

A solution to this problem has been constructed by LAI and CAPART (2007) [33]. The general solution of the diffusion equation has been derived in Section 2, see (20) and is based on the definitions

and assignments

$$\begin{aligned} \hat{\zeta}_1 &= f_1(\Xi_1)\xi_1(t), \qquad \Xi_1 := \frac{X}{\xi_1(t)}, \\ \xi_1(t) &:= 2\sqrt{D_1 t}, \quad s_1(t) := \lambda\sqrt{D_1 t}. \end{aligned} \tag{97}$$

(the index $(\cdot)_1$ stands for 'topset'). It reads [see (27)]

$$f_1(\Xi_1) = -A_1\Xi_1 + B_1\left\{\exp(-\Xi_1^2) + \sqrt{\pi}\Xi_1\left(\mathrm{erf}(\Xi_1) + C_1\right)\right\}, \tag{98}$$

in which A_1, B_1, C_1 are constants of integration. As $\Xi_1 \to -\infty$ we wish to have $\lim_{\Xi_1\to-\infty} f_1(\Xi_1) = -S\Xi_1$ which implies $A_1 = S$ and $C_1 = 1$ (else the second term in braces would violate this condition). Moreover, from $(94)_3$ we deduce

$$B_1 = \frac{S\lambda}{2\exp(-\lambda^2/4) + \lambda\sqrt{\pi}(\mathrm{erf}(\lambda/2) + 1)}. \tag{99}$$

This solution is still incomplete, because the parameter λ is not yet determined. It must await construction of the solution in the foreset.

To find the general solution for $(95)_1$ the procedure is analogous. We write (and use the index $(\cdot)_2$ for the foreset variables)

$$\begin{aligned} \hat{\zeta}_2 &= f_2(\Xi_2)\xi_2(t), \qquad \Xi_2 := \frac{X}{\xi_2(t)}, \\ \xi_2(t) &:= 2\sqrt{D_2 t}, \quad s_2(t) := \lambda\sqrt{D_1 t} \end{aligned} \tag{100}$$

and thus obtain for the function f_2

$$f_2(\Xi_2) = -A_2\Xi_2 + B_2\left\{\exp(-\Xi_2^2) + \sqrt{\pi}\Xi_2\left(\mathrm{erf}(\Xi_2) + C_2\right)\right\}, \tag{101}$$

again with constants of integration A_2, B_2, C_2. As $\Xi_2 \to \infty$, we wish to have $\lim_{\Xi_2\to\infty} f_2(\Xi_2) = -S\Xi_2$, which now implies $C_2 = -1$ and $A_2 = S$. Moreover, from $(95)_3$, since

$$(\Xi_2)^{\mathrm{plungepoint}}_{|X=s(t)} = \frac{s_2(t)}{2\sqrt{D_2 t}} = \frac{\lambda}{2}\sqrt{\frac{D_1}{D_2}}, \tag{102}$$

we obtain

$$B_2 = \frac{S\lambda\sqrt{\dfrac{D_1}{D_2}}}{2\exp\left(\dfrac{-\lambda^2}{4}\sqrt{\dfrac{D_1}{D_2}}\right) + \lambda\sqrt{\pi}\sqrt{\dfrac{D_1}{D_2}}\left\{\mathrm{erf}\left(\dfrac{\lambda}{2}\sqrt{\dfrac{D_1}{D_2}}\right) - 1\right\}}. \tag{103}$$

This solution is incomplete as is the solution for f_1, but an equation for λ follows from the flux jump condition (96), which shall now be derived.

The straightforward approach would be to request in (96) that $d = 0$ and, consequently $q_1 = q_2$ at $X = s(t)$, or

$$-D_2\frac{\partial\,\hat{\zeta}_2}{\partial\,X}|_{X=s(t)} + D_1\frac{\partial\,\hat{\zeta}_1}{\partial\,X}|_{X=s(t)} = 0. \tag{104}$$

In view of (28) [and the formulae immediately before (21): $\partial\hat{\zeta}/\partial X = f'(\Xi)$] (104) is equivalent to

$$\begin{aligned}
&-D_2 f_2'(\Xi_2)_{|\sqrt{\frac{D_1}{D_2}}\frac{\lambda}{2}} + D_1 f_1'(\Xi_1)_{|\frac{\lambda}{2}} = 0,\\
&f_1'(\Xi_1)_{|\frac{\lambda}{2}} = -S + B_1\sqrt{\pi}\left\{\mathrm{erf}(\Xi_1)+1\right\}_{|\Xi_1=\frac{\lambda}{2}},\\
&f_2'(\Xi_2)_{|\sqrt{\frac{D_1}{D_2}}\frac{\lambda}{2}} = -S + B_2\sqrt{\pi}\left\{\mathrm{erf}(\Xi_2)-1\right\}_{|\Xi_2=\sqrt{\frac{D_1}{D_2}}\frac{\lambda}{2}},
\end{aligned} \tag{105}$$

in which B_1 and B_2 are functions of λ as given in (99) and (103).[10] It is now clear that (105) is a transcendental equation for λ.

According to LAI and CAPART (2007) [33] 'the above equations generate profiles which are relatively close in character to the profiles of hyper-pycnal deltas [...]. Qualitative comparisons with small scale experiments [...], however, are rather poor'. They state that substantial improvements of the fit could be obtained at relatively little costs by including the effects of the inclination thresholds. Following MITCHELL (2006) [42], they propose

$$q_{1,2}(X,t) = \begin{cases} \max\left\{-D_1\left(\dfrac{\partial\hat{\zeta}_1}{\partial X} + S_1^{\min}\right), 0\right\}, & \hat{\zeta}_1(X,t) \geqslant Z_\ell,\\ \max\left\{-D_2\left(\dfrac{\partial\hat{\zeta}_2}{\partial X} + S_2^{\min}\right), 0\right\}, & \hat{\zeta}_2(X,t) \leqslant Z_\ell, \end{cases} \tag{106}$$

where $S_{1,2}^{\min}$ are inclination thresholds below which no bedload transport takes place, applicable to the topset and foreset, respectively. Application of (106) at the plunge point to the statement $[\![q]\!] = 0$ yields

$$q_2(s(t),t) - q_1(s(t),t) = -D_1\left(\frac{\partial\hat{\zeta}_1}{\partial X} + S_1^{\min}\right) + D_2\left(\frac{\partial\hat{\zeta}_2}{\partial X} + S_2^{\min}\right) = 0 \tag{107}$$

or

$$\begin{aligned}
&D_2 f_2'(\Xi_2)_{|\sqrt{\frac{D_1}{D_2}}\frac{\lambda}{2}} - D_1 f_1'(\Xi_1)_{|\frac{\lambda}{2}} = -\underbrace{\left(D_2 S_2^{\min} - D_1 S_1^{\min}\right)}_{d},\\
&f_1'(\Xi_1)_{|\frac{\lambda}{2}} = -S + B_1\sqrt{\pi}\left\{\mathrm{erf}(\Xi_1+1\right\}_{|\Xi_1=\frac{\lambda}{2}},\\
&f_2'(\Xi_2)_{|\sqrt{\frac{D_1}{D_2}}\frac{\lambda}{2}} = -S + B_2\sqrt{\pi}\left\{\mathrm{erf}(\Xi_2-1\right\}_{|\Xi_2=\sqrt{\frac{D_1}{D_2}}\frac{\lambda}{2}},
\end{aligned} \tag{108}$$

If $q_1 = 0$ and $q_2 = 0$ at $X = s(t)$, then obviously $d = 0$.

It is worth interpreting these formulae more closely. Formula (106) defines the sediment-mass flux in (93), but still demands continuity of it through the plunge point. This is also the interpretation in (107). However, the differential equations $(94)_1$ and $(95)_1$ are based on flux relations which do not conform with (106) (unless, of course, $S_1^{\min} = S_2^{\min} = 0$). A different interpretation is that the mass flow is uniformly defined by the Fickian relation (93). In this case, the flux of sediment mass suffers a jump as expressed in (96) with d given on the right-hand side of (96). The quantity d can be interpreted as a point production or annihilation rate of sediment mass at the plunge point. It says that the abrupt change of slope from the topset to the foreset regime is achieved by a local pointwise deposition or erosion of sediment. This may correspond to a concentrated action of a process which in reality is a smooth but

[10] Note that the primes in these functions designate differentiations with respect to different variables.

rapid adjustment of the delta slope from the topset to the foreset regime.

It is a fortunate coincidence that the jump condition (108) can be satisfied for

$$d = \begin{cases} \text{constant}, \\ \\ g[(s^2)^{\blacksquare}\,\lambda], \quad s(t) = \lambda\sqrt{Dt}, \quad (s(t)^2)^{\blacksquare} = \lambda^2 D, \end{cases} \tag{109}$$

where D is a diffusivity, e.g. D_1 or D_2 and $g[\cdot]$ is a differentiable function of $[s^2(t)]^{\blacksquare}$ and λ. The jump condition (108) then takes the form

$$\begin{aligned} &\frac{D_2}{D_1}\left[\mathcal{A}\left(\lambda, \frac{D_1}{D_2}\right) - 1\right] - [\mathcal{B}(\lambda) - 1] = \frac{d}{S}, \\ &\mathcal{A}\left(\lambda, \frac{D_1}{D_2}\right) := \frac{\sqrt{\pi}\lambda\sqrt{\frac{D_1}{D_2}}\left\{\text{erf}\left(\frac{\lambda}{2}\sqrt{\frac{D_1}{D_2}}\right) - 1\right\}}{2\exp\left(-\frac{\lambda^2}{4}\frac{D_1}{D_2}\right) + \sqrt{\pi}\lambda\left\{\text{erf}\left(\frac{\lambda}{2}\sqrt{\frac{D_1}{D_2}}\right) - 1\right\}}, \\ &\mathcal{B}(\lambda) := \frac{\sqrt{\pi}\lambda\left\{\text{erf}\left(\frac{\lambda}{2}\right) + 1\right\}}{2\exp\left(-\frac{\lambda^2}{4}\right) + \sqrt{\pi}\lambda\left\{\text{erf}\left(\frac{\lambda}{2}\right) + 1\right\}}, \end{aligned} \tag{110}$$

and

$$d = \begin{cases} D_2\, S_2^{\min} - D_1\, S_1^{\min}, \\ \\ g[(s^2)^{\blacksquare}, \lambda] = g[\lambda^2 D, \lambda]. \end{cases} \tag{111}$$

While $(111)_1$ has univariate variability, $(111)_2$ is very flexible.

Formula (110) provides an additional flexibility to adjust theoretical-computational results to corresponding experimental findings. $(111)_1$ shows that the flexibility is only through the combination $[\![DS^{\min}]\!] = d$. Variation of this parameter therefore only generates a one-parameter family of solutions. Separate selection of $S_{1,2}$ or $D_{1,2}$ does not yield improved matching of experimental results with the theory.[11] Formula $(111)_2$, however, exhibits a broader flexibility through the dependence of g on λ.

b) Sediment intake into a constant depth canal Next, let us consider the flow of sediment with initial level $\hat{\zeta}_0$ at a distance far in the topset (at $X = 0$) into an ambient of constant water depth H_0 (see Fig. 21a, illustrating the situation at $t = 0$). At the initial time the fluid basin, a semi-infinite canal, bounded by a vertical wall at $X = 0$, is free of sediments. The continuous discharge of sediment from this point will diffusively fill the basin and form the alluvial deposit as sketched in Fig. 21b. Hydraulically, this problem is somewhat artificial as the position $(X, Z) = (0, \hat{\zeta}_0)$ is kept fixed, which 'forces' the slope of the topset sediment flow to adjust as the delta formation proceeds. The initial boundary value problem in the topset regime is described by the equations (for the chosen Cartesian coordinates, see Fig. 21; the indices $(\cdot)_{1,2}$ stand again for the 'topset' and 'foreset' regimes, respectively.)

$$\begin{aligned} &\frac{\partial\,\hat{\zeta}_1}{\partial\, t} = D_1 \frac{\partial^2 \hat{\zeta}_1}{\partial\, X^2}, && 0 < X < s(t), \\ &\hat{\zeta}_1 = \hat{\zeta}_0 = \text{const.} \neq 0, && X = 0, \quad t \geqslant 0, \\ &\hat{\zeta}_1 = 0, && X = s(t), \quad t \geqslant 0. \end{aligned} \tag{112}$$

[11] LAI and CAPART [33] choose $d = [\![D]\!]S^{\min}$, assuming that $S_1^{\min} = S_2^{\min}$. They say that this choice may be too restrictive, but it is clear from above that they did not restrict the flexibility of the model by this choice.

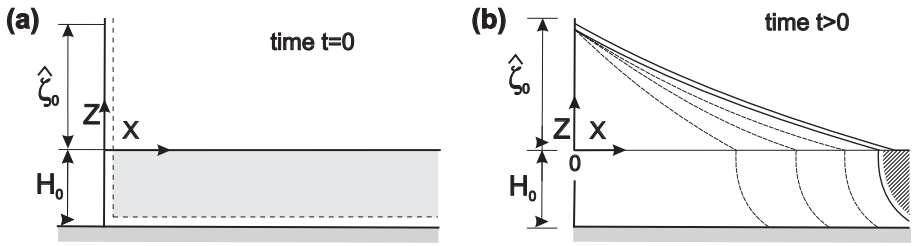

Figure 21: Alluvial deposition into a quiescent ambient channel of constant depth H_0 from a far upstream position $(X, Z) = (0, \hat{\zeta})$. **(a)** Situation at time $t = 0$ with vertical sediment motion down a vertical end wall **(b)** Snapshot of the situation at $t > 0$ with the alluvial architecture at the actual time (dark solid lines) and at a selection of previous times (dashed lines). The early time behavior is hydraulically not realistic. Panel (b) courtesy LAI & CAPART, [33], © *J. Geophys. Res.-Earth Surface*

with the sediment flux $q_1 = -D_1 \partial \hat{\zeta}_1 / \partial X$, in $0 < X < s(t)$. Analogously, the foreset problem is described by

$$\begin{aligned} &\frac{\partial \hat{\zeta}_2}{\partial t} = D_2 \frac{\partial^2 \hat{\zeta}_2}{\partial X^2}, && s(t) < X < \infty, \\ &\hat{\zeta}_2 = 0, && X = s(t), \quad t \geqslant 0, \\ &\hat{\zeta}_2 = -H_0 = \text{const.} \neq 0, && X \to \infty, \quad t \geqslant 0, \\ &\hat{\zeta}_2 = -H_0 = \text{const.} \neq 0, && 0 < X < \infty, \quad t = 0 \quad (\text{initial condition}). \end{aligned} \tag{113}$$

The two initial-boundary value problems are to be connected by the flux jump condition (107)

$$\begin{aligned} &[\![\, q(s(t), t) \,]\!] = d = [\![\, D S^{\min} \,]\!], \quad \text{or} \\ &\left(-D_2 \frac{\partial \hat{\zeta}_2}{\partial X} + D_1 \frac{\partial \hat{\zeta}_1}{\partial X} \right)_{X = s(t)} = D_2 S^{\min} - D_1 S^{\min}. \end{aligned} \tag{114}$$

The problem, described by (112) – (114) is mathematically nearly identical to the STEFAN problem of the formation of an ice cover at the top of a lake. (The problem to be described is the more exact description of the freezing of still water in a lake of which an approximation was described in Sect.4.1). The situation is sketched in Fig. 22, in which it is assumed that the temperature at the ice-atmosphere interface is $T = -T_{surf}$, at the ice-water interface it is the freezing temperature $T = T_f = 0°\text{C}$, and at depth, identified with $X = \infty$ it is $T = T_\infty (= 4°\text{C})$. The heat diffusion problems in the regimes (1) and (2) of Fig. 22 are given by

$$\begin{aligned} &\frac{\partial T_1}{\partial t} = D_1 \frac{\partial^2 T_1}{\partial X^2}, && 0 < X < s(t), \\ &T_1 = -T_{\text{surf}} = \text{const.} \neq 0, && X = 0, \quad t \geqslant 0, \\ &T_1 = 0(°\text{C}), && X = s(t), \quad t \geqslant 0, \end{aligned} \tag{115}$$

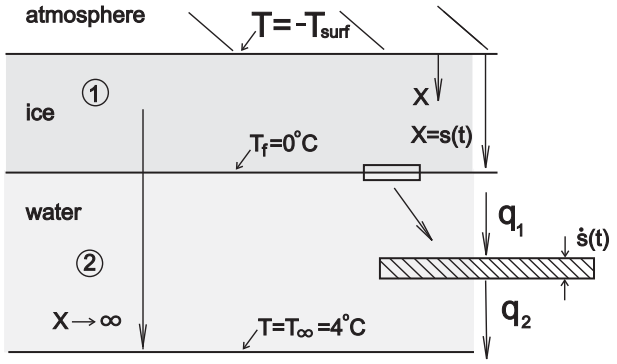

Figure 22: Layer of ice floating on still lake water. The surface temperature $T_{surf} < T_f$, the freezing temperature $T_f = 0^\circ$C and the bottom temperature T_∞ are assumed constant and prescribed. In the regions (1) and (2) the heat conduction describes the temperature distributions. The inset shows the heat flows in and out of the layer of freezing water per unit time and thickness $\dot{s}(t)$

and

$$\begin{aligned} &\frac{\partial T_2}{\partial t} = D_2 \frac{\partial^2 T_2}{\partial X^2}, && s(t) < X < \infty, \\ &T_2 = 0(^\circ\mathrm{C}), && X = s(t), \quad t \geqslant 0, \\ &T_2 = T_\infty (= 4^\circ\mathrm{C}), && X \to \infty, \quad t \geqslant 0, \\ &T_2 = T_\infty && 0 < X < \infty, \quad t = 0 \quad \text{(initial condition)}, \end{aligned} \tag{116}$$

in which $D_{1,2} = \kappa_{1,2}/(c_{1,2}\rho_{1,2})$, where $\kappa_{1,2}, c_{1,2}$ and $\rho_{1,2}$ are heat conductivities, specific heats and densities of ice and water, respectively. Variations of $D_{1,2}$ with X (or T) are ignored. Moreover, $q_{1,2} = -\kappa_{1,2}\partial T_{1,2}/\partial X$ are the heat flows in the ice and water, respectively.

To derive the STEFAN condition at the ice-water interface, consider the thin layer of thickness $\dot{s}(t)$, which freezes onto the ice-water interface per unit time. The heat that flows out from, and into, this layer is $q_2 - q_1$.This heat must equal the latent heat that is released by the water mass $\rho_2 \dot{s}(t)$, which freezes in unit time: $L_2\rho_2\dot{s}(t)$. Therefore,

$$[\![\, q(s(t), t) \,]\!]_{s(t)} = \rho_2 L_2 \dot{s}(t), \quad \dot{s} > 0, \tag{117}$$

where L_2 is the latent heat of freezing water. With the FOURIER heat law, (117) takes the form

$$\left(\kappa_1 \frac{\partial T_1}{\partial X} - \kappa_2 \frac{\partial T_2}{\partial X} \right)_{X=s(t)} = \rho_2 L_2 \dot{s}(t) \tag{118}$$

or when introducing the thermal diffusivities of ice and water, respectively,

$$\left(D_1 \frac{\partial T_1}{\partial X} - D_2 \frac{c_2\rho_2}{c_1\rho_1} \frac{\partial T_2}{\partial X} \right)_{X=s(t)} = \frac{\rho_2 L_2}{c_1\rho_1} \dot{s}(t). \tag{119}$$

Inspection of (112) – (119) shows that the deltaic formation of sediment deposition from a fixed upstream position into a quiescent water channel of constant depth and the freezing of an ice cover on a lake agree mathematically with one another except for the STEFAN conditions (114) and (119). Complete agreement could only be achieved if $c_2\rho_2 = c_1\rho_1$ and if d in (114) would be parameterized as $\mathcal{L}\dot{s}(t)$, where $\mathcal{L}$ is a constant. This has so far not been suggested, but it is a requirement, if the above solution

involving the similarity variables (123) satisfy the STEFAN condition, as we shall indicate below.

To solve equations (112) – (114), it is advantageous to use the transformations

$$\vartheta_{1,2} = \hat{\zeta}_{1,2} - \hat{\zeta}_0, \tag{120}$$

where $\hat{\zeta}_0$ is the constant elevation at $X = 0$. Relations (112) and (113) then reduce to

$$\begin{aligned} &\frac{\partial\,\vartheta_1}{\partial\,t} = D_1 \frac{\partial^2 \vartheta_1}{\partial\,X^2}, && 0 < X < s(t), \\ &\vartheta_1 = 0, && X = 0, \quad t \geqslant 0, \\ &\vartheta_1 = -\hat{\zeta}_0, && X = s(t), \quad t \geqslant 0 \end{aligned} \tag{121}$$

and

$$\begin{aligned} &\frac{\partial\,\vartheta_2}{\partial\,t} = D_2 \frac{\partial^2 \vartheta_2}{\partial\,X^2}, && s(t) < X < \infty, \\ &\vartheta_2 = -\hat{\zeta}_0, && X = s(t), \quad t \geqslant 0, \\ &\vartheta_2 = -(H_0 + \hat{\zeta}_0), && X \to \infty, \quad t \geqslant 0. \end{aligned} \tag{122}$$

Introducing the similarity variables

$$\Xi_{1,2} = \frac{X}{2\sqrt{D_{1,2}t}}, \tag{123}$$

it is straightforward to see, [8], that the general solutions of $(121)_1$ and $(122)_1$ are given by

$$\begin{aligned} \vartheta_1 &= A + B\mathrm{erf}\left(\frac{X}{2\sqrt{D_1 t}}\right), \qquad \mathrm{erf}(x) := \frac{2}{\sqrt{\pi}}\int_0^x \exp(-\xi^2)\mathrm{d}\xi \\ \vartheta_2 &= C + E\mathrm{erfc}\left(\frac{X}{2\sqrt{D_2 t}}\right), \quad \mathrm{erfc}(x) := \frac{2}{\sqrt{\pi}}\int_x^\infty \exp(-\xi^2)\mathrm{d}\xi. \end{aligned} \tag{124}$$

The boundary conditions stated in (121) and (122) imply that $A = C = 0$ and

$$\begin{aligned} B\mathrm{erf}\left(\frac{s(t)}{2\sqrt{D_1 t}}\right) &= -\hat{\zeta}_0 \\ &= -(H_0 + \hat{\zeta}_0) + E\mathrm{erfc}\left(\frac{s(t)}{2\sqrt{D_2 t}}\right). \end{aligned} \tag{125}$$

The first line of this equation implies, since B and $\hat{\zeta}_0$ are constants, that the argument of the error function must also be a constant, which we choose to be

$$\frac{s(t)}{2\sqrt{D_1 t}} = \lambda (= \text{const.}). \tag{126}$$

Similarly, from the second line of (125),

$$\frac{s(t)}{2\sqrt{D_2 t}} = \lambda\sqrt{\frac{D_1}{D_2}}. \tag{127}$$

Therefore, again from (125),

$$B = -\frac{\hat{\zeta}_0}{\operatorname{erf}(\lambda)}, \quad E = \frac{H_0}{\operatorname{erfc}\left(\lambda\sqrt{\frac{D_1}{D_2}}\right)}. \tag{128}$$

The constant λ is still not determined; this is accomplished by satisfying (114), or

$$\left(-D_2\frac{\partial\,\vartheta_2}{\partial\,X} + D_1\frac{\partial\,\vartheta_1}{\partial\,X}\right)_{X=s(t)} = d, \tag{129}$$

$$= \mathcal{L}\dot{s}(t), \tag{130}$$

demonstrating two different parameterizations for the jump $[\![\, q \,]\!]$. With the representations

$$\begin{aligned}\vartheta_1 &= -\frac{\hat{\zeta}_0}{\operatorname{erf}(\lambda)}\operatorname{erf}\left(\frac{X}{2\sqrt{D_1 t}}\right),\\ \vartheta_2 &= -(H_0+\hat{\zeta}_0) + \frac{H_0}{\operatorname{erfc}\left(\lambda\sqrt{\frac{D_1}{D_2}}\right)}\operatorname{erfc}\left(\frac{X}{2\sqrt{D_2 t}}\right),\end{aligned} \tag{131}$$

a somewhat lengthy but straightforward computation shows that the jump condition (129) with constant $d \neq 0$ does not allow determination of λ; the constructed functions (131) are no solution of that double alluvial diffusion problem. If, on the other hand, (130) is chosen with $\mathcal{L} = \text{const.}$, the following transcendental equation for λ is obtained:

$$\frac{\exp(-\lambda^2)}{\operatorname{erf}(\lambda)} - \frac{D_2}{D_1}\sqrt{\frac{D_1}{D_2}}\frac{\exp\left(-\lambda^2\sqrt{\frac{D_1}{D_2}}\right)}{\operatorname{erfc}\left(\lambda\sqrt{\frac{D_1}{D_2}}\right)}\frac{H_0}{\hat{\zeta}_0} = -\frac{\lambda\mathcal{L}\sqrt{\pi}}{\hat{\zeta}_0}. \tag{132}$$

For $\mathcal{L} = 0$, corresponding also to $d = 0$, the sediment flux through the plunge point is continuous. Time slices of the solution in that case are displayed in panel b of Fig. 21.

The above solution corresponds to the classical STEFAN problem, the freezing of water in a lake from its surface. The governing equations are (115), (116). If we write

$$\vartheta_{1,2} = T_{1,2} + T_s$$

and make the identifications $T_{\text{surf}} \leftrightarrow (-\hat{\zeta}_0)$ and $T_\infty \leftrightarrow (-H_0)$, then the solutions (131) remain valid, but the STEFAN condition (119) implies

$$\frac{\exp(-\lambda^2)}{\operatorname{erf}(\lambda)} - \frac{\kappa_2}{\kappa_1}\sqrt{\frac{D_1}{D_2}}\frac{\exp\left(-\lambda^2\frac{D_1}{D_2}\right)}{\operatorname{erfc}\left(\lambda\sqrt{\frac{D_1}{D_2}}\right)}\frac{T_\infty}{T_{surf}} = \frac{\lambda\,L\sqrt{\pi}}{c_{\text{ice}}T_{\text{surf}}}, \tag{133}$$

in which c_{ice} is the heat capacity of ice. Note, the analogy between (132) and (133) is only complete, if $c_{\text{ice}}\rho_{\text{ice}} = c_{\text{water}}\rho_{\text{water}}$. If we ignore in (133) the second term on the left-hand side (e.g. by assuming that $T_\infty = 0°\text{C}$, then (133) reduces to (56) with (58) as $\sqrt{t}$-relation for $s(t)$. The corresponding relation (59) is less realistic, since it is not obvious that the second term on the left-hand side of (132) may be negligible.

Finally, if the parameterization of the jump of the sediment flux d in (129) does not possess the form

Table 2: Reported research on laboratory experiments for hypo- and hyper-pycnal delta formations

Hypo-pycnal	Hyper-pycnal
KOSTIC & PARKER (2003) [29] [30]	LAI (2006) [32]
MUTO (2001) [45]	LAI & CAPART (2007) [33]
MUTO & STEEL(1992) [46]	CAPART et al. (2007) [6]
MUTO & SWENSON (2005) [48]	LORENZO-TRUEBA et al. (2009) [39]

(130), the construction of the solution with functions involving similarity variables (as in this section) breaks down. In such situations one must use numerical techniques to find solutions.

6 Laboratory Experiments

The theory presented in the previous sections has been tested for both GILBERT-type and hyper-pycnal formations of alluvial deltas under the restrictions of two-dimensional motion in a vertical plane, for which the model has so far been developed. Experiments by MUTO & SWENSON (2005) [48] on GILBERT-type delta formations have been reported in Section 4.4. Laboratory experiments on progradation from the topset to the foreset regime on both types of deltas have been conducted by several research teams and are listed (as far as I know) in Table 2. Here, we shall present a brief description of laboratory experiments on hyper-pycnal delta formation and compare results from them with results obtained from the double-diffusive theory. Results are due to LAI and CAPART [32] – [34].

6.1 Progradation of hyper-pycnal deltas

In what follows we shall report on a subset of results, which have been described in greater detail by LAI (2006) [32] and LAI & CAPART (2007) [33]. The experiments were conducted at the Hydro Tech Research Institute of the National Taiwan University. The apparatus, which they constructed was essentially a small scale copy of an experimental set-up by Garcia (1993) [17] for the study of turbidity currents (see Fig. 23 and the description in the figure caption). The flow is photographed with a CCD digital camera from the side perpendicular to the observation window. The bed elevation profile, position of the plunge point and the lake level height are extracted from each digitized photo (note the scale bar on the observation window). Details of this careful analysis of the experiments are available from LAI (2006) [32] and LAI & CAPART (2007) [33].

LAI & CAPART [32] – [35] present results on two experiments, called 'run 1' and 'run 2' which differ by the amount of brine influx

$$Q_1 = 154\text{mm}^2\, s^{-1}, \qquad Q_2 = 229\text{mm}^2\, s^{-1}.$$

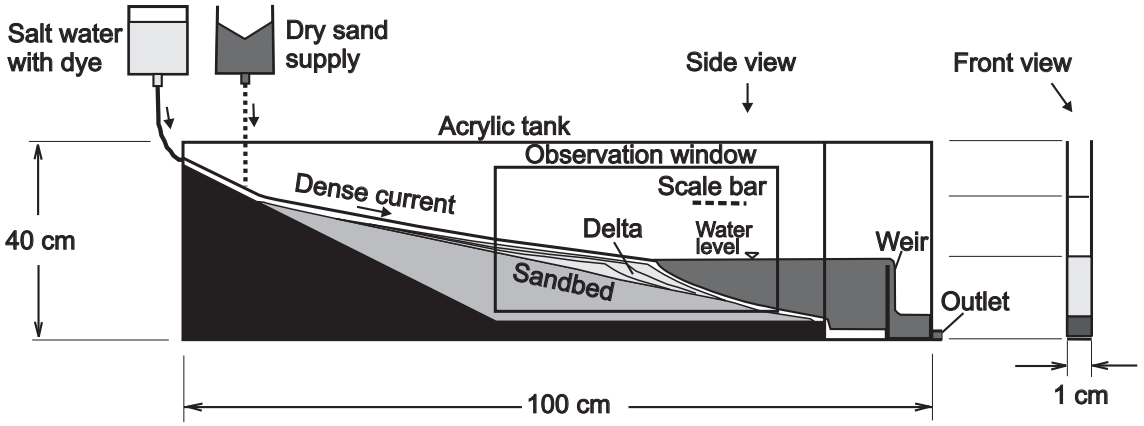

Figure 23: Experimental set-up by LAI & CAPART [32], [33], used for the small scale experiments on prograding hyper-pycnal deltas.
The narrow flume is separately fed by steady streams of salt water at the top left and dry sand from a silo somewhat distant down flow. For material properties of brine and sand and other experimental parameters, see Table 2. This brine-sediment mingling moves down the prefabricated sand-bed with 10°-slope. Initially, subaerial steady flow is established without fresh-water in the basin. Then, freshwater is rapidly added to establish a fresh-water basin with constant water level, kept by a weir. This establishes conditions for delta formation and subaqueous progradation. By adding fluorescent dye to the brine, the subaqueous density current is easily visible. To make the temporal formation of the hyper-pycnal deltas visible, black coal grains are intermittently added to the dripping sand, of which each event leaves imprinted stripes in the deltas, and thus illustrates their architecture. Courtesy LAI & CAPART, [33], © *J. Geophys. Res.-Earth Surface*

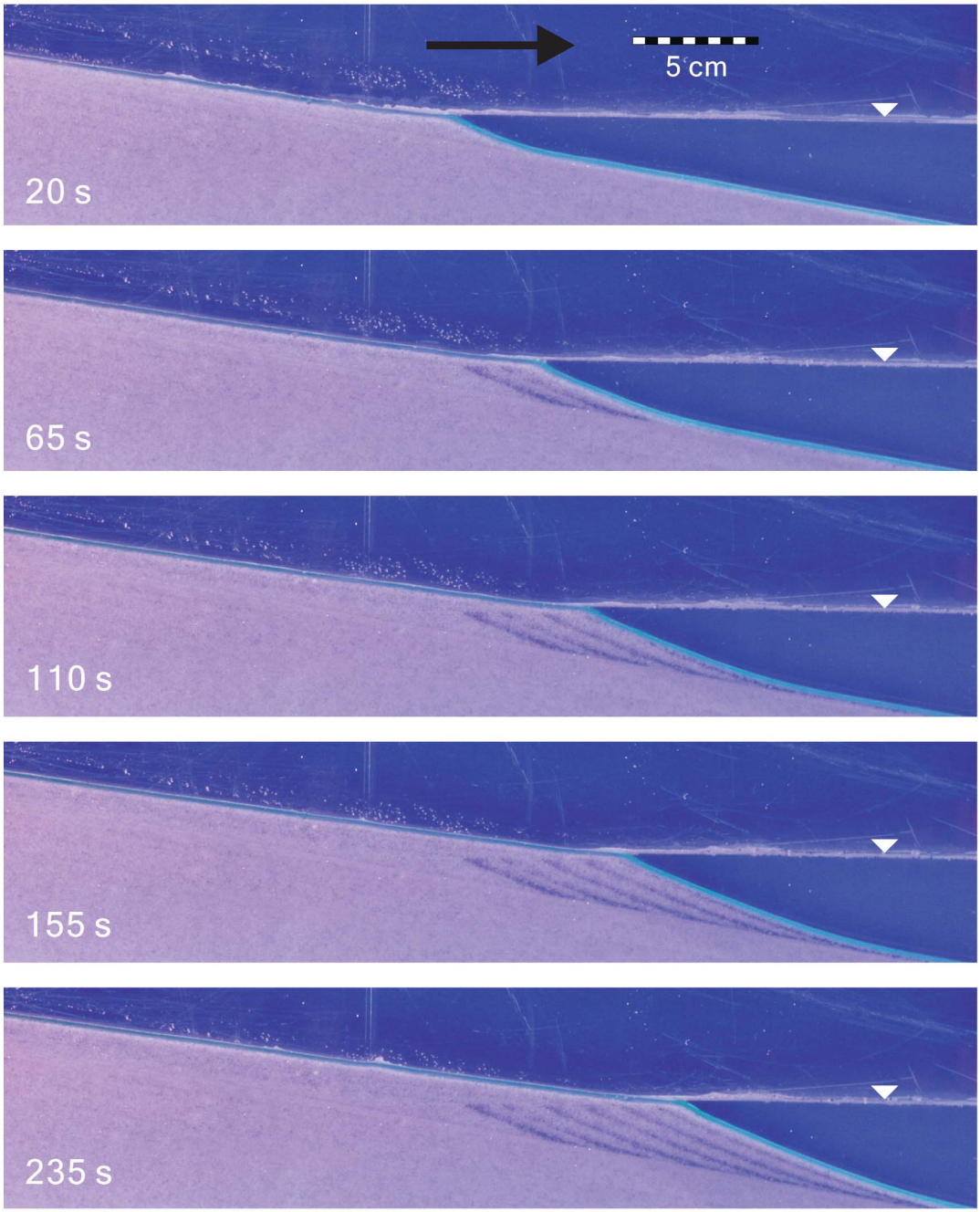

Figure 24: Series of photographs from a laboratory experiment depicting the progradation of a hyper-pycnal delta in a lake of constant water level, starting from a bed of constant inclination. Flow is from left to right (indicated by the arrow). For details, see main text. Photographs courtesy LAI & CAPART [33] © *J. Geophys. Res.-Earth Surface*

A sequence of consecutive snapshots is displayed in Fig. 24, which shows side views of the delta build-up in run 1 with sediment flow from left to right. 'The current is subaerial upstream, plunges into the ambient basin at the shoreline break, and then continues as a subaqeous density current. The delta progrades lakeward by simultaneously building topset and foreset deposits on the two sides of the shoreline. The repeated dark stripes are coal-dust traces bedded into the topset deposit at times corresponding to their intermittent release. As for the observed morphology 'topset and foreset profiles are concave upwards, and everywhere gently curved except for the sharp cusp at the shoreline break, with the topset curvature milder than the foreset curvature. The maximum inclination of the foreset is 24°, well below the measured angle of repose of 37° (see Table 3). At its toe the foreset connects smoothly with the original bed' [33]. Delta profiles at different times are similar to each other; this is shown in Fig. 25, where in panel *a*) measured delta profiles from four time slices ($t = 20, 45, 80, 125$s) are plotted: $\hat{\zeta}_{1,2}$ against X. If, instead the same profiles are plotted as $\hat{\zeta}_{1,2}/\sqrt{Qt}$ against $X/\sqrt{Qt}$, then the graph in panel *b*) is generated. All curves collapse to a single profile, which beautifully demonstrates the self-similarity property. A stronger test of the theory emerges when this same transformation is also performed for ($t = 20, 45, 80, 125$s) for experimental Run 2 with Q_2. This is demonstrated in Fig. 26b, where $\bullet$ and $\circ$ are taken from the respective photographs of Run 1 and Run 2. The two experimental profiles in the scaled plot 'define' a single curve through the foreset and most of the topset. Panel *a*) shows the profiles for the four time slices ($t = 20, 45, 80, 125$s) for the second run. The measured profiles in panels *a*) of Figs. 25 and 26 show as solid curves also the computed profiles of the analytical solutions, derived in Sect. 5.2.

Finally, Fig. 27 displays in physical dimensions the time evolution of the shoreline position for Run 1 and Run 2 (open and full circles) together with the theoretical $\sqrt{t}$-curves (solid lines) based on $s(t) = \lambda\sqrt{D_2}$ with λ as given in Table 3. These values for λ achieve the more rapid shoreline advance for run 2 than for Run 1.

6.2 Reservoir infill by hypo- and hyperpycnal deltas over bedrock

LAI & CAPART (2009) [34] also performed computations along the above lines and extended these by comparing results under homo- and hyperpycnal conditions and sediment loads at different rates. For hyperpycnal conditions the approach of the mathematical solution for the delta formation follows Section 5, and delta configurations are as shown in Figs. 24–27. For homopycnal conditions the foreset diffusivity vanishes (see formulae (89), (88), when $\rho = \rho_\infty$) and the diffusion solution is replaced by a frontal deltaic slope equal to the angle of repose of the sand in water. The topset diffusion equation then still holds with prescribed sediment flux at the bedrock-alluvial transition and a general STEFAN condition as illustrated in App. A, Fig. 36.

The experimental stand used by LAI & CAPART [34] is similar as that shown in Fig. 23. The flume is 1 [m] long and 1 [cm] wide and side-glass walls allow visual inspection. Downstream, the flume is fitted with weirs to control the lake water level and the subaqueous interface. Upstream, a head tank supplies the constant river discharge, and a conveyor belt supplies the bedload sediment. For the river discharge, either freshwater ($\rho = 1000$ [kg m^{-1}]) or brine ($\rho = 1200$[kg m^{-1}]) are used to generate homo- and hyperpycnal inflows into the freshwater lake. The sand characteristics for the bedload sediment are: median diameter $d_{50} = 0.17$ [mm], coefficient of uniformity $d_{60}/d_{10} = 2.3$, angle of repose $\phi = 3^\circ$ (see Table 3). Green fluorescent dye is added to the brine to visualize underflows, and black ash is

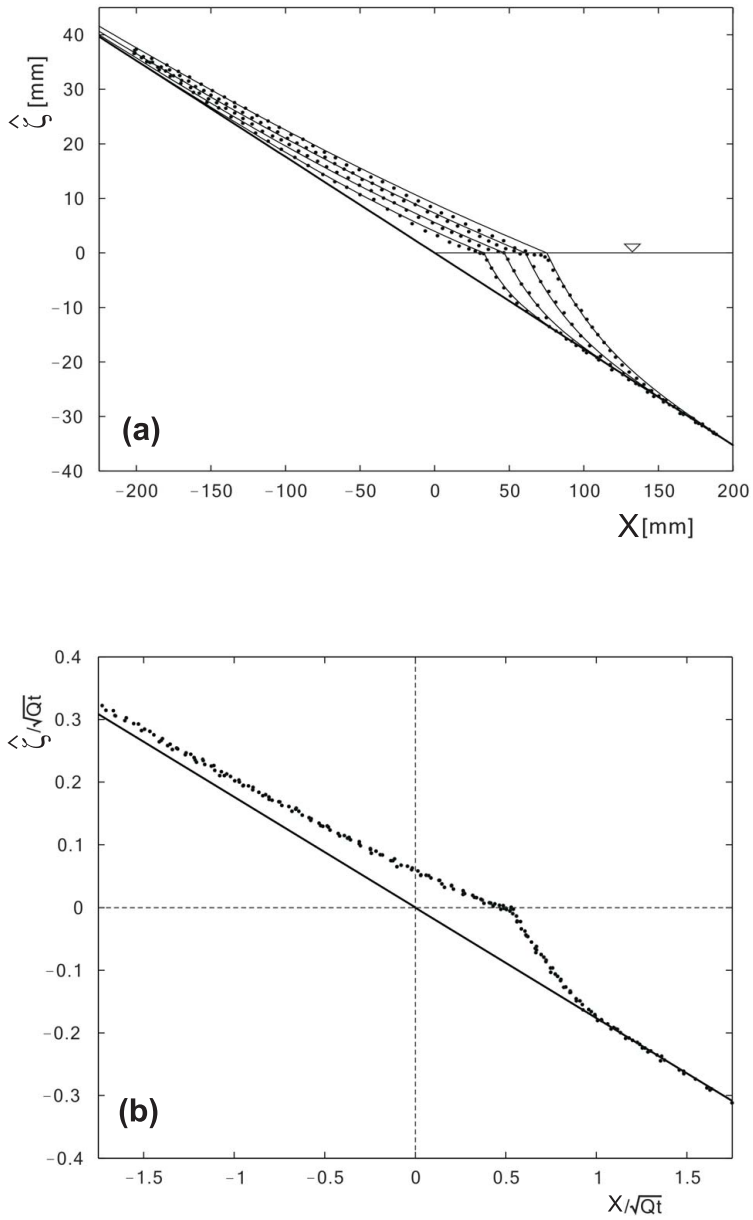

Figure 25: Results for hyper-pycnal delta progradation for Run 1 with $Q = 154\text{mm}^2\,\text{s}^{-1}$. Panel **(a)** shows four snapshots at times ($t = 20, 45, 80, 125$s), $\hat{\zeta}$ plotted against X. Points represent topset and foreset profiles as read from photographs at the above times, solid lines depict the computed profiles of the double diffusive model as explained in the main text. Panel **(b)** shows the same experimental data now rescaled by the inverse square root: $\hat{\zeta}/\sqrt{Q\,t}$ versus $X/\sqrt{Q\,t}$. Courtesy LAI & CAPART [33], © *J. Geophys. Res.-Earth Surface*

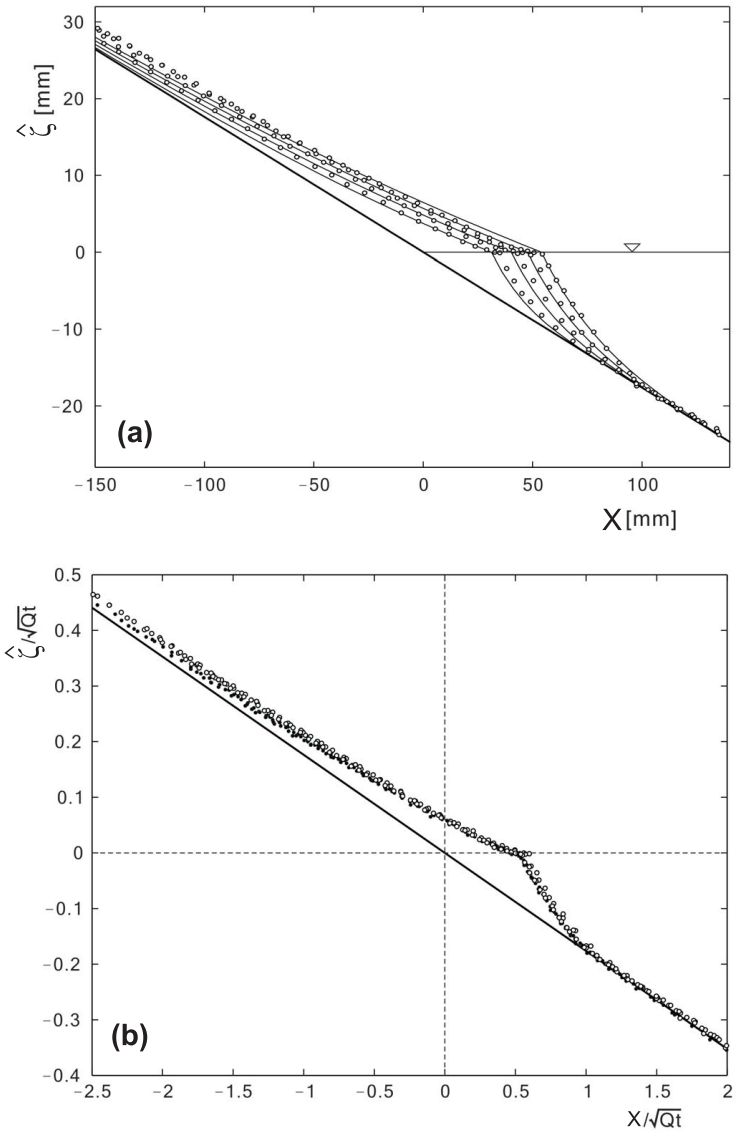

Figure 26: **(a)** Hyper-pycnal delta progradation for Run 2 with $Q = 229\text{mm}^2\,\text{s}^{-1}$. Measured data (circles) are compared with results from analytical solutions (solid lines) of the double diffusion model. Panel **(b)** combines the data of both Runs 1 and 2 in rescaled fashion: $\hat{\zeta}/\sqrt{Q\,t}$ plotted against $X/\sqrt{Q\,t}$ for ($t = 20, 45, 80, 125$s) and $Q_{(1)} = 154\text{mm}^2 s^{-1}$ (full circles), $Q_{(2)} = 229\text{mm}^2\text{s}^{-1}$ (open circles). Courtesy LAI & CAPART [33], © *J. Geophys. Res.-Earth Surface*

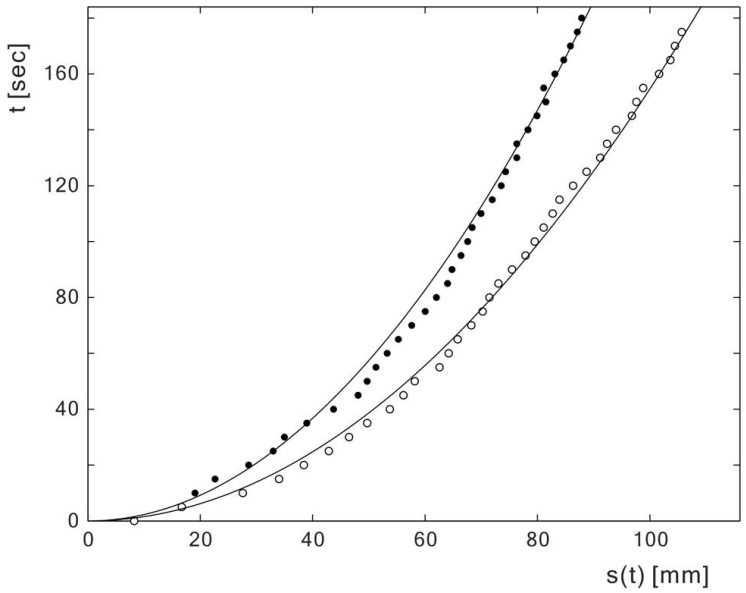

Figure 27: Comparison of experimental and analytical results for the time varying shoreline position of hyper-pycnal deltas. Full circles show results for the sediment flux $Q_1 = 154\text{mm}^2\text{s}^{-1}$, open circles for $Q_2 = 229\text{mm}^2\text{s}^{-1}$. Solid lines represent the theoretical results. Courtesy LAI & CAPART, [33], © *J. Geophys. Res.-Earth Surface*

sprinkled at repeated intervals to visualize the stratigraphy of the deposits. Photography is taken as in earlier reported experiments. 'Figures 28a,b,c,d show deltaic morphologies resulting from homo- and hyperpycnal river inflows, respectively, over bedrock forms of moderate inclination ($\theta = 10°$)'. The experiment A (Fig. 28a) shows typical GILBERT-type behaviour. 'To examine the effect of inclination, experiment C is conducted under the same hyperpycnal conditions as experiment B with the steepness of the bedrock floor increased twofold to $\theta = 20°$. Experiment D shows what happens under the same conditions when the bedload supply is decreased by a factor of approximately 5.5, and the hyperpycnal current ponds into a subaqueous pool at the downstream end of the flume [. . .]. All tests are performed under the same river discharge, held steady at a volumetric flow rate per unit width, $q = 80.6$ [mm^2 s^{-1}]', [34].

'The experiment photographed in panel A and performed under homopycnal conditions and $\theta = 10°$ bedrock slope leads to a GILBERT delta with a topset of mild inclination, a steep foreset, inclined at the angle of repose and sharp slope breaks at the shore line and at the delta toe. This behaviour is contrasted in experiment of panel B, which was performed under hyperpycnal conditions; it has again a topset of mild inclination and slope break at the shoreline, but smaller now, well below the angle of repose. The concave foreset profile changes smoothly, is therefore longer than for GILBERT-type deltas and reaches the base theoretically at an infinite distance from the shoreline. Qualitatively, whereas the foresets in panels A and B are different, the topset geometries are qualitatively very similar. This is quite different in the experiments of panels C and D, of which both have a basal bedrock inclined by 20° and are subjected to hyperpycnal conditions. In panel C the upstream sediment flux is the same as in panels A and B, but owing to the increased bedrock slope, this flow drives a greater proportion of the sediment load into the lake. The delta foreset is highly elongated, nearly straight but still concave-curved, with a small topset forming the subaerial delta. The fluorescent trace indicates the sediment flow very clearly. The experiment in panel D, in which the water flow and bedrock slope are the same as in panel C, but the upstream sediment inflow q_0 is reduced by a factor of 5.5. The entire river sediment load is now driven

Table 3: Properties of the sand material and brine solution used in the experiments and values of parameters for the double diffusion problem, which fit the illustrated experiment (after [33], [34])

Property	Value
Median sand diameter d_{50} [mm]	0.17
Sand uniformity coefficient $C_u = d_{60}/d_{10}$	2.3
Sand density ρ_s[kg m^{-3}]	2670
Porosity of uncompacted sand bed $n_0 = V_{\text{void}}/V$ [–]	0.507
Angle of repose ϕ [deg]	37°
Upstream brine density [kg m^{-3}]	1200
Water density in receiving ambient [kg m^{-3}]	1000
$Q_{(1)}$. Discharge in experimental Run 1:[mm^2 s^{-1}]	0.59
$Q_{(2)}$. Discharge in experimental Run 2 [mm^2 s^{-1}]	0.30
α_1 Velocity ratio (topset) [-]	0.59
α_2 Velocity ratio (foreset) [-]	0.30
$D_1^{(1)}$ Diffusivity (topset) [mm^2 s^{-1}]	199
$D_2^{(1)}$ Diffusivity (foreset) [mm^2 s^{-1}]	16.9
$D_1^{(2)}$ Diffusivity (topset) [mm^2 s^{-1}]	295
$D_2^{(2)}$ Diffusivity (foreset) [mm^2 s^{-1}]	25.1
$\lambda^{(1)}, \lambda^{(2)}$	0.468

into the lake without formation of a subaerial delta but building a subaqueous delta, prograding into the turbid pool. Evidently, the subaqueous delta of experiment A and the subaerial delta of experiment D are quite similar in their morphology. Both exhibit short, straight foresets, inclined at the angle of repose, and long topsets with small curvature. Their difference is in the topset inclination. Panels C and D on the other hand, demonstrate that it is possible for lake deposits to exhibit very different patterns, even at the same bedrock slopes' [34]. The theoretical profiles, corresponding to the four different experiments displayed in Fig. 28 possess similarity structure (as one would expect). So, if in each experiment $\hat{\zeta}/\sqrt{q_0 t}$ is plotted against $X/\sqrt{q_0 t}$ the results in all experiments should fall onto one curve. LAI and CAPART [34] have done this and present Fig. 29, in which the panels A to D correspond to the panels A to D of the experiments shown in Fig. 28. Figure 29 shows as solid heavy lines the computed similarity solutions, and as coloured symbols the digitized experimental profiles from photographs taken at four different times. The shapes of the sediment bed and the elevations are well predicted with only slight errors in phase for the positions of the delta fronts. Most important, the theory is able to reproduce the wide range of the experimental deltas. This range includes the production of straight and curved foresets (A versus B), contrasted ratios of foreset to topset lengths (B versus C), and the formation of topset - foreset deposits of opposite extents (C versus D). The theory may obviously help explaining depositional

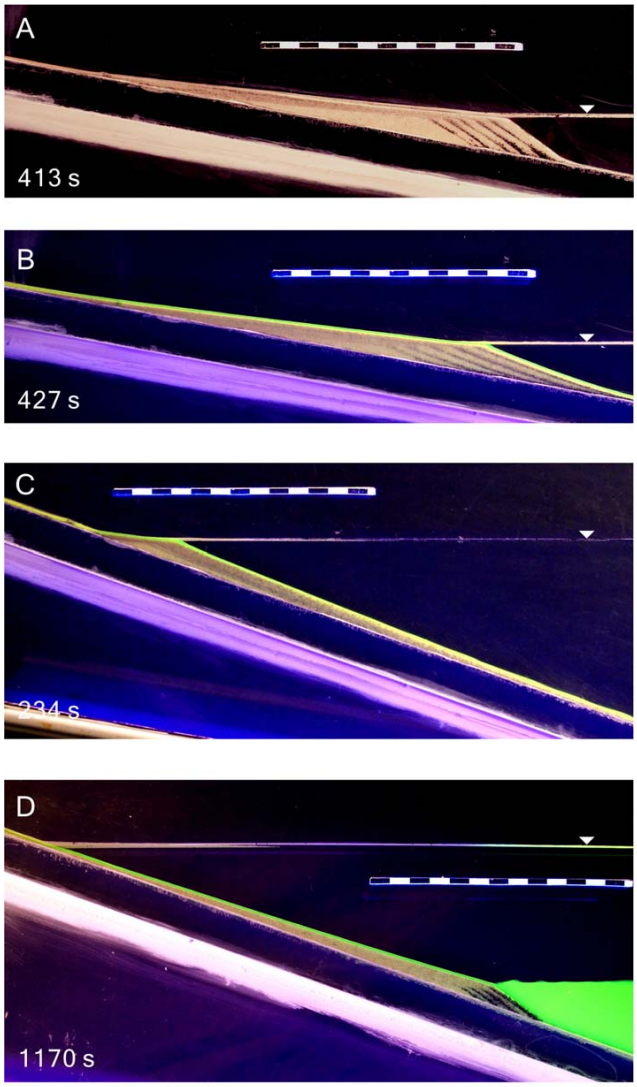

Figure 28: Experimental deltas over bedrock: **(a)** homopycnal delta (bedload influx $q_0 = 5.7[\mathrm{mm}^2\,\mathrm{s}^{-1}]$, bedrock inclination $\theta = 10^\circ$); **(b)** hyperpycnal delta ($q_0 = 5.2[\mathrm{mm}^2\,\mathrm{s}^{-1}]$, $\theta = 10^\circ$); **(c)** hyperpycnal delta over steeper bedrock slope ($q_0 = 5.2[\mathrm{mm}^2\,\mathrm{s}^{-1}]$, $\theta = 20^\circ$);**(d)** hyperpycnal delta with smaller rate of sediment influx ($q_0 = 0.94[\mathrm{mm}^2\,\mathrm{s}^{-1}]$, $\theta = 20^\circ$), from LAI & CAPART, [34], © *Geophys. Res. Letters*

patterns that have been documented in mountain reservoirs, [34].

LAI & CAPART [34] list a number of field sites, where the situations displayed in Fig. 28 have been observed. A GILBERT-type delta similar to panel A of Fig. 28 has led to the recent infill of the small Ronghua reservoir, upstream of the large Shihmen reservoir (CAPART et al., 2007 [6]) in Taiwan. In this reservoir, the river inflow is highly turbid during floods (LEE et al. [38]) yet, homopycnal conditions prevail because this small reservoir rapidly becomes turbid itself, blurring the density contrast between inflow and lake waters. The Shihmen reservoir, on the other hand, shows deposits similar to case D. Well known hyperpycnal deltas having morphologies matching cases B and C are the deltas of the Upper Rhine at Lake Constance (HINDERER, 2001 [23]) and the Colorado river at Lake Mead (GRAF 1971 [21]). A first step into this direction has been taken by CAPART et al. (2011) in a study of the formation and decay of a tributary-dammed Lake in the Laonong River [7].

At the research forefront the next urgent steps should now be the application of the illustrated theo-

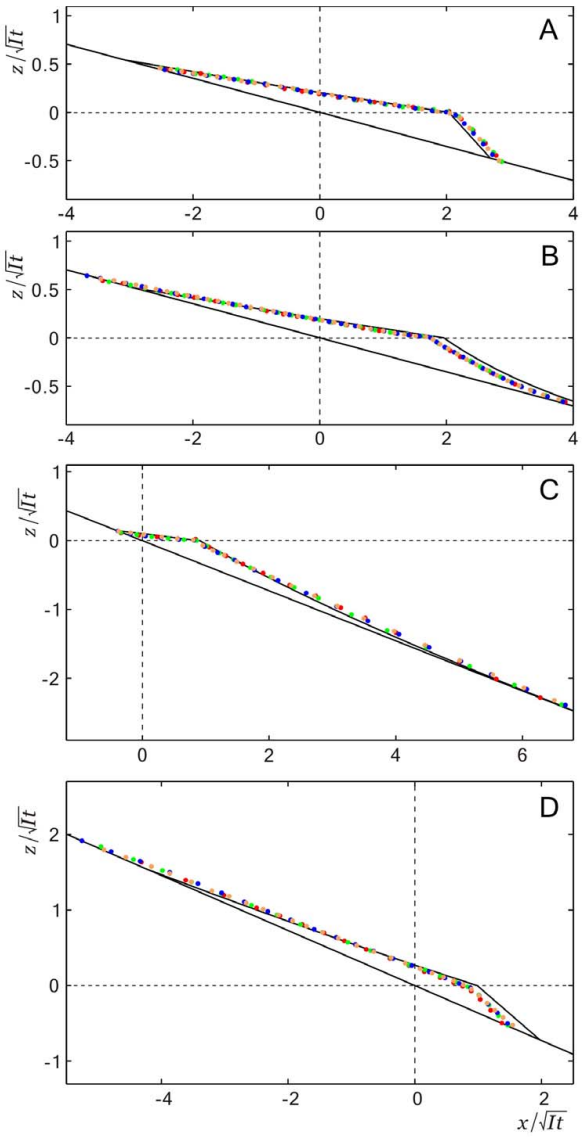

Figure 29: Comparison of measured (symbols) and theoretical (solid lines) profiles for the experimental deltas of Fig. 28. Data points coloured red, green, blue and orange denote delta profiles measured at evenly spaced time t_1 to t_4. Normalized coordinates are used to demonstrate self-similarity, from LAI & CAPART, [34], © *Geophys. Res. Letters*

retical concepts to the sediment infill of artificial lakes in mountainous areas during floods and the release of deposited sediments through the bottom or side outlet of the reservoir barrage.

7 Formation and Evolution of Tributary Dammed Lakes

7.1 Introduction

In this section a dynamical description of 'onset and growth of tributary dammed lakes' due to HSU and CAPART (2008) [24] is presented. In mountainous regions many natural lakes have been formed by glacial retreats at the termination of the last Ice Age. Apart from this glaciogenic formation natural lakes have also been created by river obstruction due to landslides, which may occur during heavy rainfall events. Sudden sediment deposits at a localized restricted region of a valley from a side tributary may block the continuous flow of sediments down the valley, whilst the water flow, after a short interruption

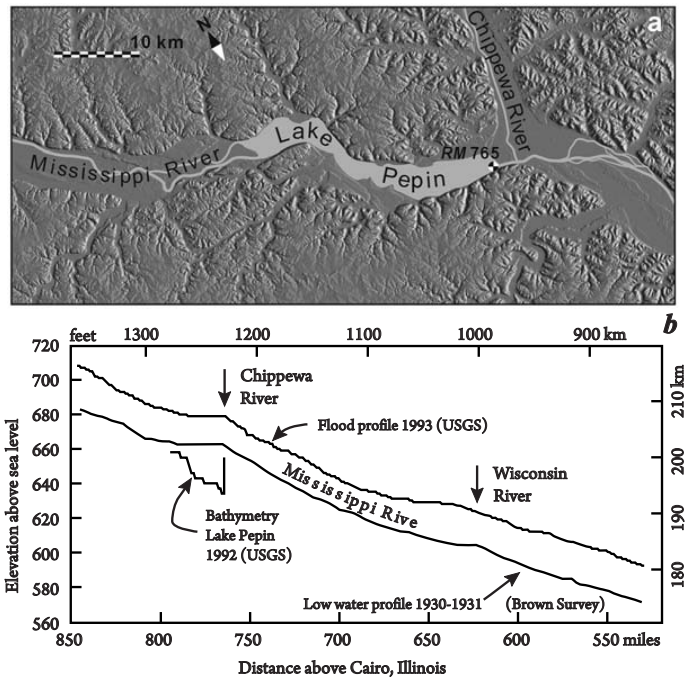

Figure 30: Tributary-dammed Lake Pepin, formed across the Mississippi River because of sediment influx from the Chippewa River: **(a)** Map showing the local relief (digital elevation data from the Upper Mississippi Basin Stackholder Network, St. Mary's University of Minnesota) and watercourse (bathymetry from the USGS Upper Midwest Environmental Sciences Centre) and **(b)** elevation plot showing the influence of the Chippewa and Wisconsin rivers on the long profile of the Upper Mississippi (source of the data, USGS). The marker at river mile 765 has latitude 44°24'49"N and longitude 92°06'54"W, from HSU & CAPART (2008) [24] © *Water Resources Research, American Geophysical Union*

may continue, once the lake level has reached the crown of the dam of the sediment deposit. Early descriptions of such tributary dammed lakes are by DAVIS (1933) [11] and LANE (1955) [37] and examples are reported by GALAY et al. (1983) [16]. HSU & CAPART report that the 'Upper Mississippi River, where postglacial outwash deposits supplied by the tributary Chippewa River caused the formation of Lake Pepin (ZUMBERGE, (1952) [71]; WRIGHT et al. (1998) [67])', Fig. 30. Two different regimes of river morphology may ensue from such tributary sediment depositions. 'When this influx is moderate, the main river can deposit sediment upstream of the aggrading tributary junction to maintain a down-valley bed inclination. The result is a cuspate profile [Fig. 31a]. When the influx from the side is large, by contrast, the deposition rate in the main river cannot keep pace with [the] confluence aggradation because of insufficient sediment load. This causes the formation of a natural lake upstream of the tributary mouth, as in the case of Lake Pepin upstream of the Chippewa confluence', HSU & CAPART (2008) [24].[12]

In the ensuing analysis a simplified situation will be considered, in which the sediment flow in the principal valley is one-dimensional and defined by the classical diffusion equation. Moreover, the sediment influx from a tributary is represented by a *steady*[13] point source, and the origin of the horizontal-

[12]Similar, somewhat reminiscent alterations of sediment regimes have frequently occurred in the Alps during the Middle Ages when ice avalanches, formed from hanging glaciers, dammed riverine valleys, ROETHLIBERGER (1978) [57]. As long as the ice deposit existed, an ice-dammed lake formed and changed the upslope and downslope sediment flows. More significantly, floods due to sudden dam break caused devastating debris flows. Other, related processes are artificially formed when barrages are built for valley reservoirs. They change the upstream sediment regimes and slowly fill the reservoir, thereby reducing the power-generating capacity. Through a base opening in the barrage or side channel and judicious flushing operations, in which the discharge and the lake level are monitored, the sediment deposit is partly removed, a process which affects the sediment regimes in the lake and its topset as well as the sediment flow in the river stretch below the barrage.

[13]Unsteady situations can also be analysed, but may need pure numerical solution techniques.

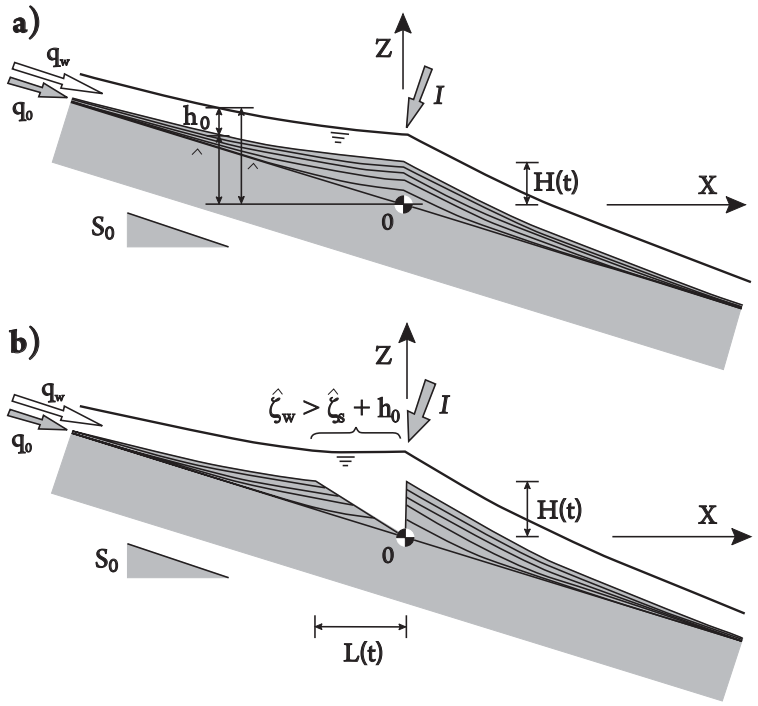

Figure 31: Self-similar alluvial responses to sediment supply from a tributary: **(a)** tributary-induced cuspate aggradation and **(b)** tributary-dammed lake, forming when the tributary supply exceeds twice the original sediment transport rate in the river ($I > 2q_0$), from [24] © *Water Resources Research, American Geophysical Union*

vertical coordinate system (X, Z) is chosen to be the location of the point source. With the notation of Section 1, the sediment diffusion equation takes the form

$$\frac{\partial \hat{\zeta}_s}{\partial t} + \frac{\partial q}{\partial X} = \sigma = I\delta(X), \tag{134}$$

in which $\hat{\zeta}_s$ is the vertical coordinate of the upper surface of the sediment layer, q is the sediment flux in the main river and I is the (here) steady point sediment source from the tributary river (a change of the amount of water in the river stretch below the source point is ignored). $\delta(X)$ is the HEAVISIDE function.

We further assume that the longitudinal sediment motion is driven by a *steady* uniform water discharge (per unit width), q_w, flowing down valley ($q_w > 0$). Variations in the evolution of the sediment profile are assumed to be sufficiently slow as the water surface reacts quasi-statically. This implies that $Z = \hat{\zeta}_s$ and $Z = \hat{\zeta}_w$ are varying 'in parallel', so that with sufficient accuracy

$$\frac{\partial \hat{\zeta}_w}{\partial t} = \frac{\partial \hat{\zeta}_s}{\partial t}, \quad \frac{\partial \hat{\zeta}_w}{\partial X} = \frac{\partial \hat{\zeta}_s}{\partial X}. \tag{135}$$

Finally, $\hat{\zeta}_w$ and $\hat{\zeta}_s$ are subject to the following inequalities:

$$\hat{\zeta}_w \geqslant \hat{\zeta}_s + h_0, \quad -\frac{\partial \hat{\zeta}_w}{\partial X} \geqslant 0, \quad \left(\hat{\zeta}_w - \hat{\zeta}_s - h_0\right) \frac{\partial \hat{\zeta}_w}{\partial X} = 0. \tag{136}$$

Theses inequalities subdivide the river course into stretches of running water and sediments for which

$$\frac{\partial \hat{\zeta}_w}{\partial X} = \frac{\partial \hat{\zeta}_s}{\partial X} > 0, \quad \hat{\zeta}_w - \hat{\zeta}_s = h_0, \tag{137}$$

where steady (normal) flow is assumed, and segments with standing water for which

$$\frac{\partial\,\hat{\zeta}_w}{\partial\,X} = \frac{\partial\,\hat{\zeta}_s}{\partial\,X} = 0, \qquad \hat{\zeta}_w > \hat{\zeta}_s + h_0. \tag{138}$$

In other words, these regions are the lake-pools, where the water surface is horizontal and larger than $Z = \hat{\zeta}_s + h_0$, and where the sediment flux vanishes.

We also follow HSU & CAPART (2008) [24] and postulate the sediment flux in the form

$$q = D_{\max}\left\{-\frac{\partial\,\hat{\zeta}_w}{\partial\,X} - S_{\min}, 0\right\}, \tag{139}$$

in which D is the alluvial diffusivity, defined in Section 1, formula (17), and $S_{\min}$ is the minimum slope required for sediment transport. Note that (135) contains $\partial\,\hat{\zeta}_w/\partial\,X$, but it can be replaced by $\partial\,\hat{\zeta}_s/\partial\,X$, if (135) is satisfied. For segments where $-\partial\,\hat{\zeta}_w/\partial\,X > S_{\min}$ and with $S_{\min} = \text{constant}$ and D = constant, we have $\partial\,q/\partial\,X = -D\partial\hat{\zeta}_w/\partial\,X = -D\partial\hat{\zeta}_s/\partial\,X$; in this restricted case (134) takes the form

$$\frac{\partial\,\hat{\zeta}_s}{\partial\,t} + D\frac{\partial^2\,\hat{\zeta}_s}{\partial\,X^2} = I\delta(X). \tag{140}$$

There remains to establish the initial and boundary conditions, for which (140) is to be solved. HSU & CAPART (2008) [24] assume that the process starts from initial conditions $\hat{\zeta}_s(X,0) = -S_0X$, representing a linear profile of constant inclination S_0 exceeding the transport threshold ($S_0 > S_{\min}$). The background sediment transport rate is then

$$Q_0 = D(S_0 - S_{\min}). \tag{141}$$

7.2 Theory

The solution for the partial differential equation (140) is determined by constructing it intuitively from independent functions which satisfy the boundary conditions at $X = 0$ and $X = \pm\infty$. We shall construct solutions in $-\infty < X \leqslant 0$ and in $0 \leqslant X < \infty$, independently and then will match the two solutions at $X = 0$. Linearity is a crucial element of this approach. For mathematical properties of the involved functions, see Appendix B.

- The linear function

$$\hat{\zeta}_s^{(1)} = -S_0X \tag{142}$$

satisfies (140) with $I = 0$ trivially and matches the asymptotic requirement that the full solution approaches $-S_0X$ as $X \to \pm\infty$.

It follows that any further solution which is added to (142) must satisfy the asymptotic limit $\hat{\zeta}_s^{(2)}(X,t) \to 0$ as $X \to \infty$ and $\hat{\zeta}_s^{(3)}(X,t) \to 0$ as $X \to -\infty$.

- The function

$$\hat{\zeta}_s^{(2)} = \frac{A}{D}\sqrt{Dt}\,\text{ierfc}\left(\frac{X}{2\sqrt{Dt}}\right), \quad X > 0 \tag{143}$$

is equally a solution of the homogeneous equation (140) (with $I = 0$) in $X > 0$ with the properties

that

$$\hat{\zeta}_s^{(2)} \to 0 \quad \text{as} \quad X \to \infty,$$
$$\frac{\partial\, \hat{\zeta}_s^{(2)}}{\partial\, X}\Big|_{X=0^+} = -\frac{A}{2D}. \tag{144}$$

- The function

$$\hat{\zeta}_s^{(3)} = \frac{A}{D}\sqrt{Dt}\,\mathrm{ierfc}\left(\frac{|X|}{2\sqrt{Dt}}\right), \quad X < 0 \tag{145}$$

is also a solution of the homogeneous diffusion equation (140) (with $I = 0$) and with the properties that

$$\hat{\zeta}_s^{(3)} \to 0 \quad \text{as} \quad X \to -\infty,$$
$$\frac{\partial\, \hat{\zeta}_s^{(3)}}{\partial\, X}\Big|_{X=0^-} = \frac{A}{2D}. \tag{146}$$

These properties, claimed for $\hat{\zeta}_s^{(2)}$ and $\hat{\zeta}_s^{(3)}$ are collected in Appendix B and can be verified by elementary computation. The complete solution of the inhomogeneous partial differential equation (140) may now be written as

$$\hat{\zeta}_s = \begin{cases} -S_0 X + \dfrac{A}{D}\sqrt{Dt}\,\mathrm{ierfc}\left(\dfrac{X}{2\sqrt{Dt}}\right), & 0 \leqslant X < \infty, \\ -S_0 X + \dfrac{A}{D}\sqrt{Dt}\,\mathrm{ierfc}\left(\dfrac{|X|}{2\sqrt{Dt}}\right), & -\infty < X \leqslant 0. \end{cases} \tag{147}$$

The free constant A follows by patching the two solutions (147) at $X = 0$. A first condition is that $\hat{\zeta}_s(0^-, t) = \hat{\zeta}_s(0^+, t)$, which is already satisfied. A follows by integration of (140) from $X = -\varepsilon$ to $X = +\varepsilon$ for arbitrarily small $\varepsilon > 0$. Indeed,

$$\underbrace{\int_{-\varepsilon}^{+\varepsilon} \frac{\partial\, \hat{\zeta}_s}{\partial\, t}\mathrm{d}X}_{\to 0} - \underbrace{\int_{-\varepsilon}^{+\varepsilon} D\frac{\partial^2\, \hat{\zeta}_s}{\partial\, X^2}}_{[\![D\frac{\partial\, \hat{\zeta}_s}{\partial\, X}]\!]} = \underbrace{I\int_{-\varepsilon}^{+\varepsilon} \delta(X)\mathrm{d}X}_{I},$$

in which $[\![f]\!] = f(0^+) - f(0^-)$ is the jump of f across the discontinuity. Therefore, using the results of items 2 and 3 above, we obtain $-[\![D\partial\hat{\zeta}_s/\partial X]\!]_{|X=0} = I$ or

$$\left(S_0 D + \frac{A}{2}\right) - \left(S_0 D - \frac{A}{2}\right) = A = I. \tag{148}$$

Consequently, a compact form of the solution of (147) is

$$\hat{\zeta}_s = -S_0 X + \frac{I}{D}\sqrt{Dt}\,\mathrm{ierfc}\left(\frac{|X|}{2\sqrt{Dt}}\right), \quad -\infty < X < \infty, \tag{149}$$

which is the form reported by HSU & CAPART [24]. This solution represents conditions of aggradation during which the sediment bed maintains its cuspate shape of Fig. 31a. The self-similarity of the profile becomes evident, if (149) is written as

$$\mathfrak{z}_s = -S_0\xi + \frac{I}{D}\mathrm{ierfc}(|\xi|), \quad \xi = \frac{X}{2\sqrt{Dt}}, \quad \mathfrak{z} = \frac{\hat{\zeta}_s}{2\sqrt{Dt}}, \tag{150}$$

which demonstrates that for fixed S_0, I the similarity variables in the horizontal and vertical directions are subjected to the same scaling.

The solution (149) is, however, not valid for unrestricted values of the flux I from the side tributary. Its limitation for the validity of (149) follows from the slope of the river channel immediately upstream of the tributary junction

$$S_{0^-} = S_0 - \frac{I}{2D} \tag{151}$$

(see Appendix B and (148)). In order that sediment flux $q_s > 0$ occurs at $X = 0^-$, we must have $S_0 > S_{\min}$, implying with (151)

$$I \leqslant 2D(S_0 - S_{\min}) = 2q_0, \tag{152}$$

where q_0 is the sediment flux far upstream at $X \to -\infty$. If the inequality (152) is violated, i.e. if $I > 2q_0$, the sediment flow at $X = 0^-$ ceases and all upstream sediments are deposited. In HSU & CAPART's [24] words 'the sediment infill upstream of the junction cannot keep up with the aggrading confluence, and a tributary channel lake forms, Fig. 31b. The point of minimum inclination $S = S_{\min}$ at the downstream end of the upstream alluvial reach is forced to retreat up-valley, producing a migrating slope break at [the] evolving position $X = -L(t)$. The resulting gap $-L(t) < X < 0$ is filled by a pool of standing water, across which sediment transport is suppressed', [24].

Under these conditions two separate mathematical problems of sediment transport must now be solved,

(i) the sediment transport for the downstream part of the river, which is fed at $X = 0^+$ with a sediment flux of the side tributary only, whose upper Z-coordinate at $X = 0^+$ is given by the moving lake level, and

(ii) the upstream sediment flow with vanishing flux (and thus slope) at the lake end $X = -L(t)$ and flux q_0 far upstream at $X = -\infty$.

Sediment flow below the lake: $0^+ < X < \infty$. With a constant sediment flux at $X = 0^+$ and a basal slope of magnitude $-S_0$ as $X \to \infty$, it is easy to see on the basis of the previous analysis that the function

$$\hat{\zeta}_s(X,t) = -S_0 X + \frac{A}{D}\sqrt{Dt}\,\mathrm{ierfc}(\xi), \quad \xi := \frac{X}{2\sqrt{Dt}} \tag{153}$$

solves the diffusion equation for which

$$q_{0^+} = -D\left(\frac{\partial\,\hat{\zeta}_s}{\partial\,X} - S_{\min}\right) = D(S_0 - S_{\min}) - \frac{A}{D}[\mathrm{erf}(\xi) - 1] \tag{154}$$

describes the flux. At $X = 0^+$, we have

$$q_{0^+} \overset{(154)}{=} D(S_0 - S_{\min}) + \frac{A}{2} = I$$

$$\Longrightarrow \quad A = 2[I - \underbrace{D(S_0 - S_{\min})}_{q_0}] = 2(I - q_0). \tag{155}$$

Consequently, the sediment flow below the lake is described by the equation

$$\hat{\zeta}_s(X,t) = -S_0 X + \frac{2(I-q_0)}{D}\sqrt{Dt}\,\mathrm{ierfc}\left(\frac{X}{2\sqrt{Dt}}\right), \quad 0 < X < \infty. \tag{156}$$

At $X = 0^+$ this becomes

$$\hat{\zeta}_s(0^+,t) = \frac{2(I-q_0)}{D\sqrt{\pi}}\sqrt{Dt}, \tag{157}$$

which is positive, since $I > 2q_0$ according to (152) and the text following it. On the other hand, if no lake is formed, (149) applies and $\hat{\zeta}_s(0^-,t)$ takes the form

$$\hat{\zeta}_s(0^-,t) = \frac{I}{D\sqrt{\pi}}\sqrt{Dt}. \tag{158}$$

The thickness of the sediment deposit at the tributary mouth is thus given by

$$H := \hat{\zeta}_s(0,t) = \frac{1}{\sqrt{\pi}}\max\left\{\frac{2(I-q_0)}{D}, \frac{I}{D}\right\}\sqrt{Dt}. \tag{159}$$

With (157) the lake level at $X = 0^{\pm}$ then follows as[14]

$$\hat{\zeta}_w(0^+,t) = \hat{\zeta}_s(0^+,t) + h_0. \tag{160}$$

Because of (159) 'the dependence of the deposit thickness on the tributary influx I is nonlinear. A break of trend occurs at the onset of lake formation ($I = 2q_0$), beyond which aggradation is enhanced at the tributary junction. When the influx exceeds this threshold, a lake of rising level and increasing length develops (Fig. 31b) [...]. Water continues to flow past the dam and only sediment transit is interrupted across the lake. The up-valley transgression of the lake leaves a characteristic bathymetric signature with a lake bed that acquires a downstream facing slope of constant inclination. Unlike avalanching [GILBERT-type] delta foresets, for which the slope is determined by the angle of repose, here the lake bed inclination is set by the rate of aggradation of the tributary dam. A faster aggradation [by an increased value of I] yields more rapid lake transgression, hence a lake of milder downstream-facing slope [...]', [24]. Analogous shoreline transgressions for deltas responding to sea level rise are due to MUTO & STEEL (1992) [46] and PARKER & MUTO (2003) [54].

Sediment flow above the lake: $-\infty < X < -L(t)$. Under standing water conditions, $\partial\hat{\zeta}_w/\partial X = 0$, the upstream edge of the lake rises in lockstep with the aggrading 'dam crest', defined by (157) (Fig. 31b). The initial boundary value problem again possesses the solution

$$\hat{\zeta}_s(X,t) = -S_0 X + \frac{A}{D}\sqrt{Dt}\,\mathrm{ierfc}\left(-\frac{X}{2\sqrt{Dt}}\right). \tag{161}$$

Indeed, this function satisfies the homogeneous diffusion equation (with constant diffusivity) and the asymptotic boundary condition that $q_0 = S_0 D$. Additional conditions must be satisfied at the upper edge

[14] h_0 is the water depth on the assumption that the water flux leaving the lake is the same as the in-flux.

of the lake. *First*, we have with $L(t) = \lambda\sqrt{Dt}$

$$\begin{aligned}\hat{\zeta}_s(-L(t),t) &\overset{!}{=} \hat{\zeta}_s(0^-,t) \overset{(161)}{=} \frac{2(I-q_0)}{D\sqrt{\pi}}\sqrt{Dt} \\ &\overset{(161)}{=} S_0\lambda\sqrt{Dt} + \frac{A}{D}\sqrt{Dt}\,\mathrm{ierfc}\left(\frac{\lambda\sqrt{Dt}}{2\sqrt{Dt}}\right),\end{aligned}$$

from which one may deduce

$$\frac{\lambda}{2} + \frac{A\,\mathrm{ierfc}(\lambda/2)}{2q_0} - \frac{I-q_0}{\sqrt{\pi}q_0} = 0, \quad q_0 := S_0 D. \tag{162}$$

Once A is determined, this is an algebraic equation for λ. *Second*, at $X = -L(t)$, the sediment flux is given by $S_{\min}$, which together with (161) yields

$$S_0 + \frac{A}{2D}\left[\mathrm{erf}\left(-\frac{\lambda}{2}\right) + 1\right] = S_{\min}, \tag{163}$$

from which one obtains

$$A = \frac{2D(S_0 - S_{\min})}{\mathrm{erfc}(\lambda/2)} = \frac{2q_0}{\mathrm{erfc}(\lambda/2)}. \tag{164}$$

Finally, substitution of (164) into (161) and (162) yields

$$\begin{aligned}&\hat{\zeta}_s(X,t) = -S_0 X + \frac{2q_0}{D}\frac{\sqrt{Dt}}{\mathrm{erfc}(\lambda/2)}\,\mathrm{ierfc}\left(\frac{-X}{2\sqrt{Dt}}\right), \quad -\infty < X < -L(t), \\ &\frac{\lambda}{2} + \frac{q_0\,\mathrm{ierfc}(\lambda/2)}{DS_0\mathrm{erfc}(\lambda/2)} - \frac{I-q_0}{\sqrt{\pi}DS_0} = 0\end{aligned} \tag{165}$$

as the sediment transport equation and lake length $L(t) = \lambda\sqrt{Dt}$.

7.3 Experiments

As a test the above model approach, HSU & CAPART (2008) [24] performed laboratory experiments. The experimental set-up is sketched in Fig. 32. It consists of a 250 [cm] long, 1 [cm] wide channel of adjustable inclination angle. The water flow, q_w far upstream enters the flume from a constant back tank and the sand is dropped onto the steady upstream water flow from two feeders whose fluxes, q_0 and I, are adjustable. A sink tank at the lower end collects the sediment and water outflow. The most important data are collected in Table 4.

Calibration runs with the tributary influx I turned off and the bed brought to equilibrium grade under steady upstream inflows of water and sand were first performed to characterize the relation $q_0(q_w, S)$ between upstream water discharge q_w, inclination $S = -\partial\hat{\zeta}_s/\partial X$ and sediment flux q_0. The resulting data (Fig. 33) are well approximated by the power law

$$\begin{aligned}&q_0 = k q_w^\alpha S^\beta, \\ &k = 1.03[\mathrm{mm^2 s^{-1}}]^{1-\alpha}, \quad \alpha = 1.39, \quad \beta = 2.28\end{aligned} \tag{166}$$

(and root-mean-square residual $= 4$ [$\mathrm{mm^2 s^{-1}}$] for sediment fluxes in the range $0 < q < 130$ [$\mathrm{mm^2 s^{-1}}$]).

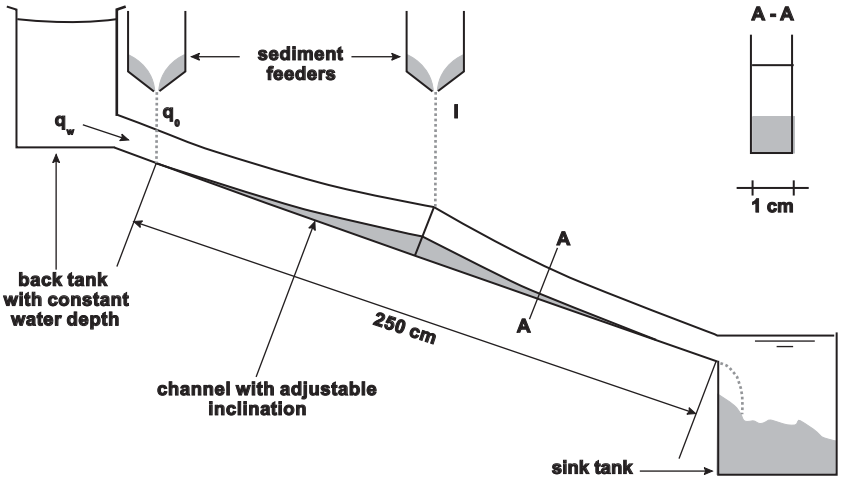

Figure 32: Sketch of the laboratory experiment to check the theoretical model, performed by HSU & CAPART (2008) [24], © *Water Resources Research, American Geophysical Union*

Table 4: Key properties of the laboratory experimental stand and the physical parameters of the sand used

Channel length	250 [cm]
Channel width	1 [cm]
Flume inclination angle	adjustable
Submerged angle of repose	36 [$^\circ$]
Sand median diameter d_{50}	0.32 [cm]
Sand coefficient of uniformity d_{60}/d_{10}	1.84 [-]

'Tributary experiments were conducted for different values of water discharge and tributary sediment influx. All experiments were started from the same initial grade $S_0 = 0.11$, obtained by adjusting the upstream sand supply q_0 to the corresponding water discharge. At $t = 0$, the tributary sand supply is turned on at prescribed rate of influx I. The ensuing response of the sand bed is observed through the transparent side wall using time-lapse photography', [24]. HSU & CAPART performed a total of 27 runs with water discharges $q_w = \{280, 470, 730\}$ [mm^{2}s^{-1}] subject to various tributary influxes I such that $1 < I/q_0 < 5$. For comparison with the theory, which is not built on a functional relation (166), the power law (166) must first be approximated by the simplified form of equation (139). This was done by cross calibrating the coefficients D and $S_{\min}$ against k, α and β (using least squares over range $0 \leqslant S/S_{\min} \leqslant 2$, yielding $D/q_0 = 30$ and $S_{\min}/S = 0.7$, and the precise relation represented by the bold line in Fig. 33.) Once the two coefficients have been determined, all other results can be calculated from the theory, and thus present testable predictions.

Comparison of theory and experimental results. Figures 34a,b show in dimensionless representation the lake length LS_0/H and sediment deposition thickness $H/\sqrt{S_0 q_0 t}$ against I/q_0. The solid curve in Fig. 34a represents the results of the theory, symbols those of the experiments. As shown theoretically, a lake is formed only when $I > 2q_0$, which explains the onset of non-vanishing values for L at $I/q_0 < 2$. The curve in this latter range of I/q_0 follows from solutions of (165) for λ and (159) and grows sharply for I/q_0 slightly larger than 2, but quickly tapers with a decelerating growth. The experimental

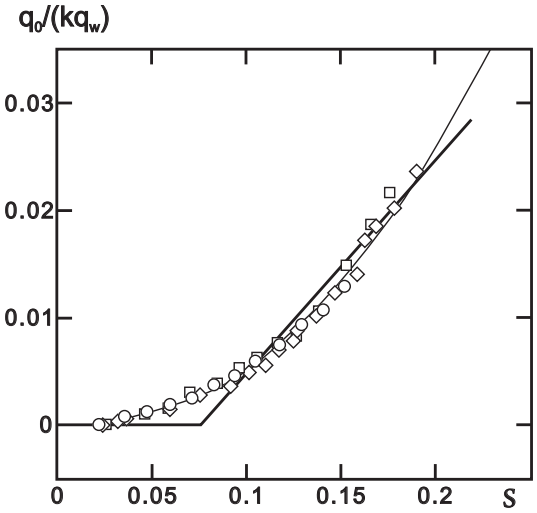

Figure 33: Calibrated sediment transport relation (thin curve power law; thick curve, approximate diffusion flux). Symbols represent experimental data for water discharges $q_1 = 283$ [mm^{2}s^{-1}] (squares), $q_2 = 467$ [mm^{2}s^{-1}] (diamonds), and $q_3 = 733$ [mm^{2}s^{-1}] (circles), from HSU & CAPART (2008) [24], © *Water Resources Research, American Geophysical Union*

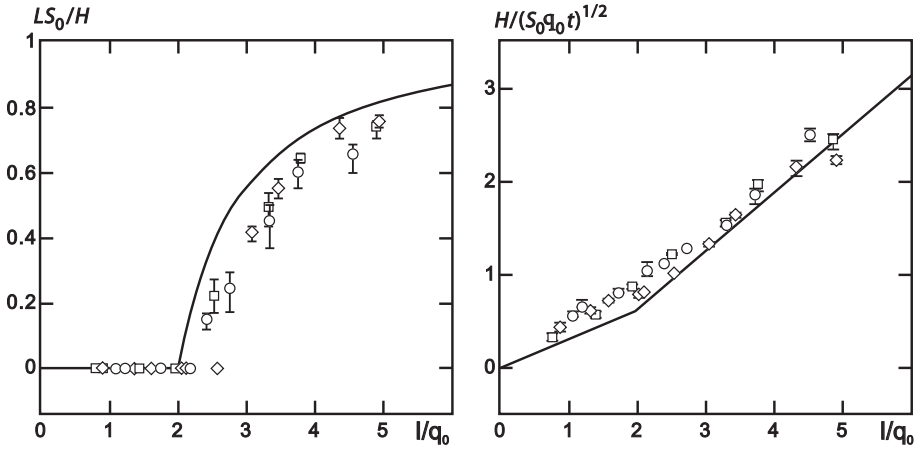

Figure 34: **(a)** Normalized lake length versus ratio of tributary sediment supply I to undisturbed sediment transport q_0 ,with lake formation predicted to occur when $I > 2q_0$. **(b)** Dependence of the normalized sediment deposit thickness at the tributary on the ratio I/q_0. The thick curves in the two panels are the theoretical predictions, and symbols represent experimental data for water discharges $q_1 = 283$ [mm^{2}s^{-1}] (squares), $q_2 = 467$ [mm^{2}s^{-1}] (diamonds), and $q_3 = 733$ [mm^{2}s^{-1}] (circles), from HSU & CAPART (2008) [24], © *Water Resources Research, American Geophysical Union*

lake length $L(t)$ is represented for each run with a data point and error bar for $q_0 = \{283, 467, 733\}$ [mm^{2}s^{-1}], represented by {squares, diamonds, circles}, respectively. Evidently, even though the observed onset of the lake formation is slightly delayed, and the measured data fall slightly below the theoretical curve, the experimental data and the theory follow the same trend. Results for the theoretical dimensionless sediment deposit thickness $H/\sqrt{S_0 q_0 t}$ follow two linear (I/q_0)-dependences, given mathematically by (159), Fig. 34. The experimental points follow the same trend, but a kink at $I/q_0 = 2$ is not clearly identifiable.

Longitudinal profiles for two experimental runs below ($I/q_0 = 1.6$, Fig. 35a) and above ($I/q_0 = 4.4$, Fig. 35b) the lake-formation threshold are presented in Fig. 35. As profiles $\hat{\zeta}_s(X, t)$ are geometrically self-similar, they collapse together when plotted in the normalized coordinates of Fig. 35. Below the threshold $I/q_0 = 2$, a cuspate aggradation is observed. 'The deposit thickness [then] exhibits mirror symmetry about the tributary mouth, and the bed profile maintains an elevation that monotonically de-

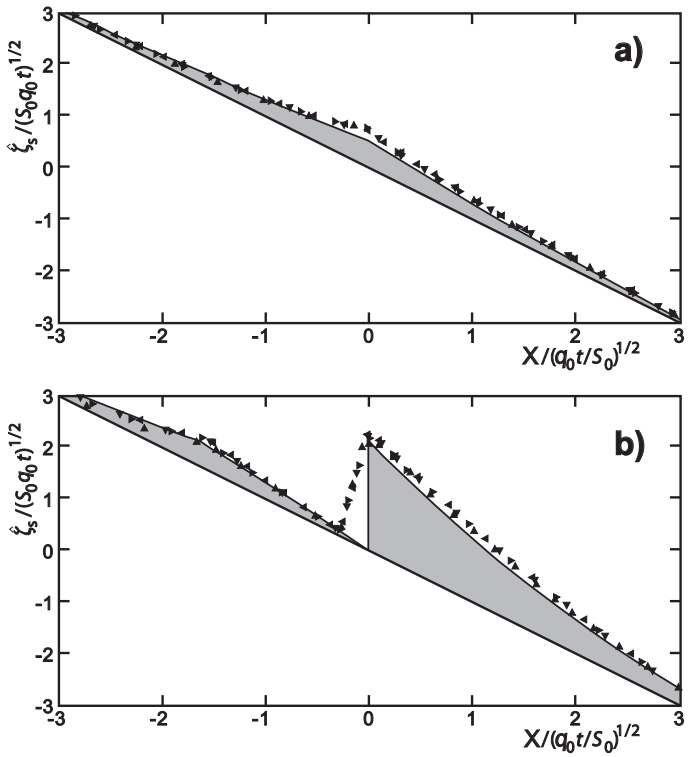

Figure 35: Self-similar river and lake bed profiles produced by steady sediment influx from a tributary: **(a)** cuspate aggradation ($I/q_0 = 1.6$) and **(b)** tributary-dammed lake ($I/q_0 = 4.4$). Lines are the theoretical predictions, and rotated triangles represent measured profiles approximately 1, 2, 3, 4 minutes after the start of the tributary influx. Both experimental runs correspond to water discharge $q_2 = 467$ [mm^{2}s^{-1}], from HSU & CAPART (2008) [24], © *Water Resources Research, American Geophysical Union*

creases down valley [Fig. 35a]. Above the threshold [. . .], the alluvial profile is no longer monotonically decreasing, and a lake forms upstream of a tributary dam [. . .]. The downstream deposit accumulates more sediment (received from the strong tributary influx) than the upstream deposit (which traps the weaker background sediment flux). Overall the theoretical and experimental profiles match well, [except] for a slightly underestimated cuspate deposit thickness in Fig. 35a, and for the upstream dam face in Fig. 35b, assumed vertical in the theory (no up-valley sediment motion is allowed), but which relaxes to the angle of repose in the experiments [. . .]. The other features of the tributary-dammed lake of Fig. 35 show good agreement between theory and experiment. This includes the predicted retreat of the upstream lake edge along a line of constant inclination (well below the angle of repose), the shallow deposit upstream of the lake, and the half-cusp profile of the river bed downstream of the tributary mouth', [24]. Qualitatively this is reminiscent of the recorded profile of the Upper Mississippi River (Fig. 30b) with the convex segments upstream and downstream of the Wisconsin junction, and the existence of Lake Pepin with its triangular bathymetry.

8 Discussion and Conclusions

A review has been given in this article on sediment transport from an alluvial river stretch into a quiescent ambient. Depending upon whether the river-water density is lighter than, the same or heavier than that of the water of the lake, two kinds of delta formations could be distinguished: for $\rho_{\text{river}} \leqslant \rho_{\text{lake}}$ (hypo-pycnal delta formations) the coarser sediments tend to separate from the suspended fines and form deltas with constant frontal slopes generated by the angle of repose. For $\rho_{\text{river}} > \rho_{\text{lake}}$ (hyper-pycnal delta formation) the subaerial river current plunges down into the still ambient water and forms a turbulent subaqueous density current with moving coarse sediment load. For hypo-pycnal deltas, the alluvial river transport can be described by a sediment diffusion equation, generally subject to upstream flux and downstream lake level prescriptions. The positions of the shore line as a function of time is obtained from a generalized STEFAN condition relating the sediment flux to the basement geometry and basement deformation processes. For hyper-pycnal deltas the subaerial and subaqueous sediment transports are both governed by diffusion equations with different diffusivities ($D_{\text{subaerial}} \neq D_{\text{subaqueous}}$). Far upstream and far downstream boundary conditions in the topset and foreset and lake level prescription at the temporally varying shore line complete the problem formulation except for the determination of the shore line position via a generalized STEFAN condition. This condition is formulated as a jump condition of sediment flux across the shore line position, in which the jump of sediment flux is given as a phenomenological statement for the turbulent mixing processes induced in the transition region of the abrupt flow changes. Numerous analytical solutions for both delta types have been presented and some have been compared with results from laboratory experiments. Moreover, the close mathematical connection is demonstrated of the single and double sediment diffusion problems with freezing of lake water in winter when being subject to constant freezing atmospheric temperature.

The presented model is limited because several simplifying assumptions both in the physical and mathematical descriptions have been imposed. Among such assumptions are the following restrictions.

- The subaerial and subaqueous sediment flows are restricted to motions taking place in a vertical plane. This is particularly restrictive as soon as the river water enters the lake environment. A generalization to a three-dimensional set-up of the concept is likely possible if one is satisfied with increased phenomenology in place of physics. A step towards this end has been undertaken by VOLLER et al. [66].

- The suspended matter in the turbid water has been ignored as have been the particle size separation and the segregational depositions in the bottomset. Memoirs, which include these processes in a two-dimensionally restricted setting are given by KOSTIC et al. [28], [29], [30].

- All applications, which have been presented, have so been chosen that mathematical solutions could be constructed analytically. More generally, (generalized) STEFAN problems are moving boundary value problems and therefore require care, when numerical integrations have to be performed. If sedimentary processes are strictly prograding or strictly transgrading, the time t can be replaced as an independent variable by $s(t)$, the shore line position, and a *fixed-domain formulation* without moving boundaries be constructed.
  For GILBERT-type deltas numerical solutions have been constructed by VOLLER et al. (2006) [66], and for hyper-pycnal deltas by LAI & CAPART (2011) [35].

- The focus in the present paper has been sediment transport and deployment in a quiescent ambient on decadal and centennial time scales, but it must have become clear that the formulation is equally applicable to geological time scales of millennia and multi millennia through the Holocene. In this connection the term 'graded' river stretch was introduced (see Section 4 and [48]), and it became clear that graded sediment flow was the exception rather than the rule. The concept is important in long term sedimentary processes as a special response to lake level fall, which generates alluvial aggradations, whereas lake level rise leads to shore line transgression. Such hydro-geological processes are studied in detail by MUTO et al. [49], [50], [55].

- Applications to river-reservoir hydraulics have been given by LAI & CAPART (2009) [34], and CAPART et al. (2010) [7] and LAI & CAPART [35].

Acknowledgments This work has been self-supported. I thank E. VASILIEVA for her teχpertise and I. CHUBARENKO, Russian Academy of Sciences, Kaliningrad, Russia for figure drawings. T. MUTO, University of Nagasaki, Japan, J. B. SWENSON of the University of Minnesota, Duluth, USA, and H. CAPART, National Taiwan University, Taipei, Taiwan, have granted copyright permission of many figures and originals of photographs as identified in the figure captions. I have tremendously profited from all of their works, which I appreciate very much. An earlier, shorter, unpublished, version of this paper has been dedicated to Prof. W. H. HAGER on the occasion of his 60^{th} birthday.
I am grateful to Prof. PETER RUTSCHMANN from the Lehrstuhl und Versuchsabstalt für Wassserbau und Wasserwirtschaft of the Technische Universität München to publish this version of the "Tutorial. . . " in his 'Mitteilungen' as a contribution to sediment transport. I equally thank Stephan Hötzl for his help in the editorial procedures.

Appendix A: Derivation of the sediment flux boundary condition at the plunge point of a Gilbert-type delta

In this appendix an explicit derivation of the flux boundary condition (42) at the plunge point of a hypopycnal delta will be given. The derivation follows KOSTIC & PARKER [29] but in the notation of this article.

Consider Fig. 36. With reference to this figure the front surface of the foreset delta can be described as

$$\hat{\zeta}(X,t) = \hat{\zeta}_s - \tan\phi\,(u(t) - s(t))\,, \quad \text{where} \quad \hat{\zeta}_s = \zeta(s(t),t). \tag{167}$$

If this is evaluated at the toe of the alluvial deposit,

$$\hat{\zeta}_b = \hat{\zeta}_s - \tan\phi\,(u(t) - s(t)) \tag{168}$$

is obtained.

If conservation of mass is formulated for a sediment element as shown in the inset of Fig. 36, then one may deduce

$$\begin{aligned} n_s \frac{\partial\,\hat{\zeta}}{\partial\,t}\mathrm{d}X &= \bar{q}_s(X) - \bar{q}_s(X+\mathrm{d}X) \\ &\simeq \bar{q}_s(X) - \bar{q}_s(X) - \frac{\partial\,\bar{q}_s}{\partial\,X}\mathrm{d}X = -\frac{\partial\,\bar{q}_s}{\partial\,X}\mathrm{d}X, \end{aligned}$$

or, since the solid volume fraction is assumed to be constant,

$$\frac{\partial\,\hat{\zeta}}{\partial\,t} = -\frac{\partial(\bar{q}_s/n_s)}{\partial\,X} = -\frac{\partial\,q_s}{\partial\,X}. \tag{169}$$

In the above, $\bar{q}_s$ is the sediment flux at a certain volume fraction, whereas q_s is the corresponding effective flux.

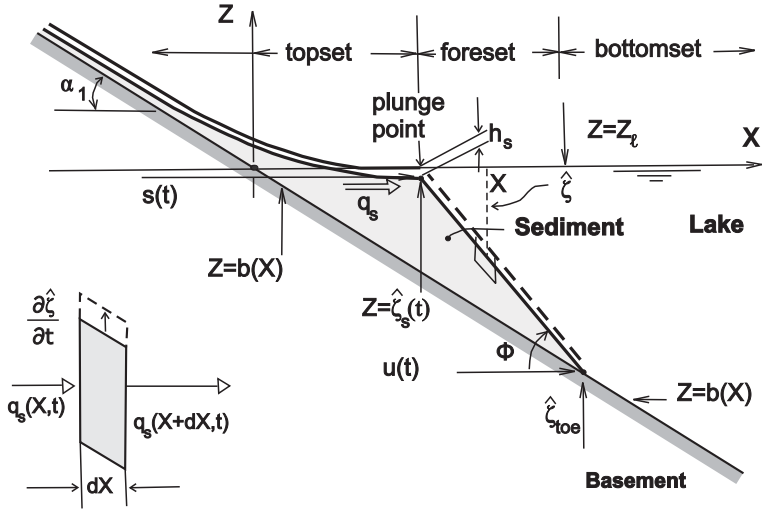

Figure 36: Definition sketch for a GILBERT-type deltaic deposition on a non-erodible basement of slope angle α_1. The origin of the (X, Z)-coordinates is at the intersection of the basement, $Z = b(X)$ and the lake surface at time $t = 0, Z = Z_\ell(0)$, the plunge point is at $[X = s(t), Z = \hat{\zeta}_s(t)]$ and the front of the wedge is at $[X = u(t), Z = \hat{\zeta}_{toe}(t)]$. The sediment flow through the plunge point from the topset is $q_s(s(t), t)$ and the conservation of mass of the sediment, expressed in formula (169) is explained in the inset. The river water depth at the plunge point is $h_s(t)$ and the level of the lake may vary with time, $Z = Z_\ell(t)$

An explicit expression for q_s is obtained, if equation (169) is integrated from $X = s^-$ to $X = u(t)$. This integration is composed of an 'integration' from $X = s^-(t)$ to $X = s^+(t)$ plus the integration from $X = s^+(t)$ to $X = u(t)$. Thus,

$$q_s|_{s^-(t)}^{s^+(t)} = q_s(s^+(t)) - q_s(s^-(t)) = -\int_{s^-(t)}^{s^+(t)} \frac{\partial\,\hat{\zeta}}{\partial\,t}\,\mathrm{d}\,X = 0.$$

Here, the integral on the far right vanishes because of continuity requirements for $\hat{\zeta}(\cdot)$. It follows that the flux q_s is continuous across the plunge point. Therefore, we may write

$$\begin{aligned}\int_{s^-(t)}^{u(t)} \frac{\partial\,q_s}{\partial\,X}\mathrm{d}X = \underbrace{q_{s_{|u(t)}}}_{=0} - q_{s^-|s(t)} &= \int_{s^-(t)}^{u(t)} \frac{\partial\hat{\zeta}}{\partial\,t}\mathrm{d}\,X \\ = -q_{s|s^-(t)} &= -\int_{s^-(t)}^{u(t)} \frac{\partial\,\hat{\zeta}}{\partial\,t}\mathrm{d}X,\end{aligned} \tag{170}$$

in which integration can now be restricted to $X > s(t)$. Moreover, it was assumed that the sediment flux at the toe of the frontal surface of the delta vanishes, which is realistic. With $\hat{\zeta}$ as given in (167) one may

write

$$\begin{aligned}\frac{\partial\,\hat{\zeta}}{\partial\,t} &= \frac{\mathrm{d}}{\mathrm{d}\,t}\hat{\zeta}\left(s^{-}(t),t\right) - \frac{\partial}{\partial\,t}\left(\tan\phi(X-s(t))\right)\\ &= \frac{\mathrm{d}}{\mathrm{d}\,t}\hat{\zeta}\left(s^{-}(t),t\right) + \tan\phi\frac{\mathrm{d}s}{\mathrm{d}\,t} - (\tan\phi)^{\blacksquare}(X-s(t))\end{aligned} \tag{171}$$

in which

$$\begin{aligned}\frac{\mathrm{d}}{\mathrm{d}\,t}\left(\hat{\zeta}(s^{-}(t),t)\right) &= \frac{\partial\,\hat{\zeta}}{\partial t}\,|_{s(t)} + \frac{\partial\,\hat{\zeta}}{\partial X}\dot{s}(t)\\ &= \frac{\partial\,\hat{\zeta}}{\partial t}\,|_{s(t)} - \tan\alpha_1|_{s^{-}(t)}\,\dot{s}(t).\end{aligned} \tag{172}$$

Here, $\tan\alpha_1$ is the slope of the sediment bed in the topset of the plunge point. Substituting (172) into (171) and the resulting expression for $\partial\,\hat{\zeta}/\partial\,t$ into (170) yields

$$\begin{aligned}q_s|_{s^{-}(t)} &= \int_{s(t)}^{u(t)}\left\{\frac{\partial\,\hat{\zeta}}{\partial\,t}\,|_{s(t)} - (\tan\alpha_1-\tan\phi)\dot{s}(t) - (\tan\phi)^{\cdot}(X-s(t))\right\}\mathrm{d}X\\ &= \left\{\frac{\partial\,\hat{\zeta}}{\partial\,t}\,|_{s(t)} + (\tan\phi-\tan\alpha_1)\frac{\mathrm{d}s}{\mathrm{d}\,t}\right\}(u(t)-s(t)) - \tfrac{1}{2}(\tan\phi)^{\cdot}(u(t)-s(t))^2.\end{aligned} \tag{173}$$

The surface point $\hat{\zeta}_{|s(t)}$ is given by the level of the lake surface and the water depth above the sediment as follows: $\hat{\zeta}_{|s(t)} = Z_\ell(t) - h_{|s(t)}$. Consequently,

$$\frac{\partial\hat{\zeta}}{\partial\,t}|_{s(t)} = \frac{\partial}{\partial\,t}\left(Z_\ell - h\right)|_{s(t)} = \dot{Z}_\ell(t) - \frac{\partial\,h}{\partial\,t}\,|_{s(t)}. \tag{174}$$

Substituting this into (173) yields a first variant of the final formulae for q_s:

$$\begin{aligned}q_s|_{s(t)} = \Bigg\{\Bigg[\left(\dot{Z}_\ell - \frac{\partial\,h}{\partial\,t}\,|_{s(t)}\right) &+ (\tan\phi-\tan\alpha_1)\,\frac{\mathrm{d}s}{\mathrm{d}\,t}\Bigg](u(t)-s(t))\\ &- \tfrac{1}{2}(\tan\phi)^{\blacksquare}\,(u(t)-s(t))^2\Bigg\}.\end{aligned} \tag{175}$$

Sometimes it is more convenient to additionally use the trigonometric relation

$$(u(t)-s(t)) = \frac{\hat{\zeta}-\hat{\zeta}_{toe}}{\tan\phi}. \tag{176}$$

We then obtain

$$\begin{aligned}q_{s\,|\,s(t)} = \Bigg\{\Bigg[\left(\frac{\dot{Z}_\ell(t) - \frac{\partial\,h}{\partial\,t}\,|_{s(t)}}{\tan\phi}\right) &+ \left(1-\frac{\tan\alpha_1}{\tan\phi}\right)\frac{\mathrm{d}s}{\mathrm{d}\,t}\Bigg]\left(\hat{\zeta}_s-\hat{\zeta}_{toe}\right)\\ &- \tfrac{1}{2}(\tan\alpha_1)^{\cdot}\,\frac{\left(\hat{\zeta}_s-\hat{\zeta}_{toe}\right)^2}{(\tan\phi)^2}\Bigg\}.\end{aligned} \tag{177}$$

Even though $\tan\alpha_1 < (<) \tan\phi$, it is not justified in general, to ignore $\tan\alpha_1/\tan\phi$ in the above formulae. However, it is justified to ignore the term associated with $(\tan\phi)^{\blacksquare}$. Ignoring also $(\partial\, h/\partial\, t)_{|s(t)}$ and $\dot{Z}_\ell(t)$ yields

$$q_{s|s(t)} = \left(\hat{\zeta}_s - \hat{\zeta}_{toe}\right) \frac{\mathrm{d}\, s(t)}{\mathrm{d}\, t}. \tag{178}$$

Formula (42) with $\sigma = 0$ is obtained from (175), if the river water depth is ignored, $(\partial\, h/\partial\, t)_{|s(t)} \simeq 0$ and $\tan\alpha_1$ is ignored in comparison to $\tan\phi$.

Appendix B: Characteristics of error functions

In this Appendix we collect a number of properties of mathematical expressions which are connected to the error function. These have been collected and/or derived in CARLSLAW & JAEGER (1959) [8]

- Definition of the *error function* and *complementary error function*

$$\mathrm{erf}(x) = \frac{2}{\sqrt{\pi}} \int_0^x \exp(-\xi^2)\mathrm{d}\xi, \tag{179}$$

$$\mathrm{erfc}(x) = 1 - \mathrm{erf}(x) = \frac{2}{\sqrt{\pi}} \int_x^\infty \exp(-\xi^2)\mathrm{d}\xi, \tag{180}$$

- The above definitions imply

$$\begin{aligned} &\mathrm{erf}(0) = 0, \quad \mathrm{erf}(\infty) = 1, \quad \mathrm{erf}(-x) = -\mathrm{erf}(x), \\ &\mathrm{erfc}(0) = 1, \quad \mathrm{erfc}(\infty) = 0, \quad \mathrm{erfc}(-x) = 2 - \mathrm{erfc}(x). \end{aligned} \tag{181}$$

- Both,

$$\mathrm{erf}\left(\frac{x}{2\sqrt{Dt}}\right) \quad \text{and} \quad \mathrm{erfc}\left(\frac{x}{2\sqrt{Dt}}\right)$$

  satisfy the diffusion equation

$$\frac{\partial\, f}{\partial\, t} - D\frac{\partial^2 f}{\partial\, x^2} = 0.$$

- The n-th *integral complementary error functions* are defined as

$$\mathrm{i}^n\mathrm{erfc}(x) = \int_x^\infty \mathrm{i}^{n-1}\mathrm{erfc}\,\xi\mathrm{d}\xi, \quad n = 2, 3, 4, \ldots$$

$$\mathrm{i}^0\mathrm{erfc}(x) = \mathrm{erfc}(x), \tag{182}$$

$$\mathrm{ierfc}(x) = \int_x^\infty \mathrm{erf}\,\xi\,\mathrm{d}\xi$$

$$\overset{\text{integr. by parts}}{=} \xi\mathrm{erfc}(\xi)|_x^\infty - \frac{1}{\sqrt{\pi}} \int_x^\infty \underbrace{(-2\xi)\exp(-\xi^2)}_{\frac{\mathrm{d}}{\mathrm{d}\xi}(\exp(-\xi^2))}\,\mathrm{d}\xi \tag{183}$$

$$= -x\,\mathrm{erfc}(x) + \frac{\exp(-x^2)}{\sqrt{\pi}}. \tag{184}$$

- The function $\mathrm{erfc}(x)$ exhibits the following properties:

(1)

$$\hat{\zeta}_s^{(2)}(x,t) = \frac{A}{D}\sqrt{Dt}\,\mathrm{ierfc}\left(\frac{x}{2\sqrt{Dt}}\right), \quad x \geqslant 0,$$

– $\lim_{x\to\infty} \hat{\zeta}_s^{(2)}(x,t) \to 0,$

– $$\frac{\partial\,\hat{\zeta}_s^{(2)}}{\partial\,x} = \frac{A}{2D}\left(\mathrm{erf}\left(\frac{x}{2\sqrt{Dt}}\right) - 1\right) \tag{185}$$

– $\zeta_s^2(x,t)$ satisfies the diffusion equation

$$\frac{\partial\,\hat{\zeta}_s^{(2)}(x,t)}{\partial\,t} - D\frac{\partial^2\,\hat{\zeta}_s^{(2)}(x,t)}{\partial\,x^2} = 0,$$

(2)

$$\hat{\zeta}_s^{(3)}(x,t) = \frac{A}{D}\sqrt{Dt}\,\mathrm{ierfc}\left(\frac{|x|}{2\sqrt{Dt}}\right), \quad x \leqslant 0,$$

– $\lim_{x\to-\infty} \hat{\zeta}_s^{(3)}(x,t) \to 0,$

– $$\frac{\partial\,\hat{\zeta}_s^{(3)}(x,t)}{\partial\,x} = \frac{A}{2D}\left(-\mathrm{erf}\left(\frac{|x|}{2\sqrt{Dt}}\right) + 1\right) \tag{186}$$

– $\hat{\zeta}_s^{(3)}(x,t)$ satisfies the diffusion equation

$$\frac{\partial\,\hat{\zeta}_s^{(3)}(x,t)}{\partial\,t} - D\frac{\partial^2\,\hat{\zeta}_s^{(3)}(x,t)}{\partial\,x^2} = 0.$$

Appendix C: Notation

Roman Symbols

A	Constant of integration in the construction of similarity solutions of the diffusion equation
B	Constant of integration in the construction of similarity solutions of the diffusion equation
b(X,t)	Basement function, defining the solid bed below the lake and alluvial deposits, see e.g. Fig. 8
C	Constant of integration in the construction of similarity solutions of the diffusion equation
c_p, c_{ice}	Specific heat of ice at constant pressure or constant volume
D_1	Topset diffusivity of the subaerial moving bed load
D_2	Topset diffusivity for hyper-pycnal sediment processes
$D_{ice} = \frac{\kappa_{ice}}{\rho\, c_p\, _{ice}}$	Diffusivity of ice
d	Point production/annihilation rate of sediment mass at the plunge point

E	Constant of integration in the construction of similarity solutions of the diffusion equation
f(Ξ), $f_{1,2}(\Xi)$	Similarity functions for the detritus surface
g	Gravity constant ($g = 9.81 m\, s^{-2}$)
H	Constant thickness/depth of a channel of still water
h	Thickness of the moving slurry-layer of water above the detritus layer at the basement
I	Sediment source to the main bed load from a side tributary
L	Latent heat of freezing/melting of water/ice
= $\rho_1 Q$	Downslope (horizontal) subaerial total sediment mass flow
$' = (\rho - \rho_\infty)hu$	Downslope (horizontal) subaqueous total mass flow
n_0	Porosity in the moving subaerial bed load
p_b	Normal pressure at the sediment bed.
Q	Volumetric discharge = specific volume flux
q	Specific downslope sediment flux
q_0	Specific down-slope sediment flux at far upstream position - constant value of q at graded conditions
q_{surf}	Heat flow through the free surface of a lake
$R_\ell(t)$	Relative lake level $\left(R_\ell(t) = Z_\ell(t) + \int_0^t \sigma t' \mathrm{d}t' \text{ at } X = s(t)\right)$
$R_\ell(t), \mathcal{R}_\ell^*$	Dimensionless relative lake level
r(t)	Alluvial-basement transition ($X = r(t)$)
$S_{1,2}$	Far up-stream and far-down-stream bed slopes
$S_{1,2}^{min}$	Inclination thresholds below which no bed load transport is possible
s(t)	X-position of the shore point (plunge point) as a function of time
T	Temperature
T_{surf}	Temperature (of the water) at the free surface of a lake
T_∞	Temperature of the lake water at the deep bottom
t	Time
u	Mean downslope velocity in the turbid layer water (possibly with suspended sediments)
u(t)	Position of the toe of a hypo-pycnal delta
v	Mean down-slope detritus velocity in the sediment layer
X	Horizontal Cartesian coordinates
$X/\sqrt{Q}t$	Similarity variable
x	Downslope Cartesian coordinate in the topset tangential to the basement
$Y = \sqrt{2D_{ice}t}$	Similarity variable [see (51)]
Z	Vertical Cartesian coordinate
$Z = Z_\ell(t)$	Position of the lake level as a function of time

z Cartesian coordinate perpendicular to the inclined sediment bed

Greek symbols

$\alpha_1 = \left(\frac{v}{u}\right)_1$ Ratio of the subaqueous down-slope sediment velocity to the down-slope density current velocity, $\frac{1}{2} < \alpha_1 < 1$

$\alpha_2 = \left(\frac{v}{u}\right)_2$ Ratio of the subaerial down-slope sediment velocity to the down-slope slurry velocity

β Inclination (slope) angle of the subaerial sediment layer

δ Thickness of the moving sediment layer - DIRAC Delta-function

ε Small parameter $(0 < \varepsilon << 1)$

Vertical position of the upper surface of the moving sediment

$\zeta = \zeta(x,t)$ as a function of (x,t) measured perpendicular to the basement

= (X, t) as a function of (X,t) , measured vertically

= (t) or $= \mathrm{Z}_\ell(t)$ Z-coordinate of the lake level

$_s = \hat{\zeta}(s(t))$ Upper surface of the moving sediment layer at the plunge point

$_{toe} = \hat{\zeta}(u(t))$ Detritus level at the delta fore front

$/\sqrt{Qt}$ Similarity variable

$\theta = T + T_{surf}$ Temperature variable

$\vartheta_{1,2} = \hat{\zeta}_{1,2} - \hat{\zeta}_0$ [see (120)]

κ, κ_{ice} Heat conductivity of ice

$\Lambda(\lambda) = \omega$ [see (38)]

λ Separation constant, introduced in the generalized STEFAN conditions arising as $s(t) = \lambda\xi(t)$

$\xi, \Xi/\xi(t)$ Similarity variable for the sediment position [see (20)]

π = 3.14159

ρ Mass density of water or slurry (due to wash load)

ρ_0 Mass density of the moving sediment layer

ρ_w, ρ_s True density of water, – of sediment

ρ_1 Buoyancy corrected detritus density in the top set

ρ_∞ Density of the particle laden lake water at the upper edge of the subaqueous turbidity current

σ Supply rate of moving sediment mass

$\sigma_b\prime$ Effective stress (pressure) at the top of the moving sediment layer

τ_b Shear traction at the upper surface of the bed load layer

ϕ Angle of internal friction (angle of repose measured under water)

ω Ratio of slopes, defining the parameter λ in the generalized STEFAN condition [see e.g. (38)]

Miscellaneous Symbols

$\mathrm{d}/\mathrm{d}\,t$	Total time derivative operator
$\partial/\partial\,t$	Partial time derivative operator
∇	Nabla (gradient operator)
erf	Error function
erfc	Complementary error function
ierf	Integrated error function [see (183) and (184)]

References

[1] Abramowitz, M. and Stegun, I. A.: *Handbook of Mathematical Functions* Dover Publ. Inc, New York, (1964)

[2] Adams, E. W., Schlager, W. and Anselmetti, F. S.: Morphology and curvature of delta slopes in Swiss lakes: Lessons for the interpretation of clinoforms in seismic data. *Sedientology*, **48**, 661-679 (2001)

[3] Begin, Z. B., Meyer, D. F. and Schumm, S. A.: Development of longitudinal profiles of alluvial channels in reponse to base level lowering. *Earth Surface Processes & Landforms*, **6**, 49-68 (1981)

[4] Bell, H. S.: Density currents as agents for transporting sediments. *J. Geology*, **50**, 512-547 (1942)

[5] Bornhold, B. D. and Prior, D. B.: Morphology and sedimentary processes on the subaqeous Noeick River delta, British Columbia, Canada. In: *Coarse-Grained Deltas, Spec. Publs. Int. Ass. Sediment.,* (Collela, A. and Prior, D. B, Eds.) **10**, 169-181 (1960)

[6] Capart, H., Bellal, M. and Young, D. L.: Self-similar evolution of semi-infinite alluvial channels with moving boundaries. *J. Sedimentary Research*, **77**, 13-22, (2007)

[7] Capart, H., Hsu, J. P. C., Lai, S. Y. J. and Hsieh, M.-L.: Formation and decay of a tributary-dammed lake, Laonong River, Taiwan *Water Resources Res.*, doi: 10.1029/2010WR009159 (2010)

[8] Carlslaw, H. S. and Jaeger, J. C.: *Conduction of Heat in Solids* Oxford University Press, Oxford (1946)

[9] Crank, J.: *Free and Moving Boundary Problems*, Cambridge University Press, Cambridge (1984)

[10] Culling, W. E. H.: Analytical theory of erosion. *J. Geology*, **68**, 336-344

[11] Davis, W.M.: The lakes of California. *Calif. J. Mines*, **29**, 175-236 (1933)

[12] Ellison, T. H. and Turner, J. S.: Turbulent entrainment in stratified flows *J. Fluid Mech.* **6**, 423-448 (1959)

[13] Fan, J. and Morris G.L.: Reservoir sedimentation VI: Delta and density current deposits. *J. Hydraul. Eng* bf 118(3), 354-369 (1992)

[14] Fleming, P. B. and Jordan, T. E.: A synthetic stratigraphic model of foreland basin development. *Geophys,. Res.*, **94**, 3851-3866 (1989)

[15] Fracarollo, L. and Capart, H.: Riemann wave description of erosional dam-break flows. *J. Fluid Mech.*, **461**, 183-228 (2002)

[16] Galay, V. J., Tutt, D. B. and Kellerhals, R.: The meandering distributary channels of the upper Columbia river. In: *River Meandering*, edited by Eliott, C. M., pp 113-125, Am. Soc. Civil. Engr., New York (1983)

[17] Garcia, M. H.: Hydraulic jumps in sediment-driven bottom currents. *J. Hydraul. Eng.*, **119**, (10), 1094-1117 (1993)

[18] Gilbert, G. K.: *Geology of the Henri Mountains* 170 pp. U.S. Government Print. Office, Washington, D. C. (1877)

[19] Gilbert, G. K.: *Lake Bonneville* U.S. Geological Survey Monograph, no. 1, 438 p. (1890)

[20] Gill, M. A.: Diffusion model for degrading channels *J. Hydraul. Res.*, **21**, 369-378 (1983)

[21] Graf, W. H.: *Hydraulics of Sediment transport*, McGraw-GHill, New York (1971)

[22] Grover, N. C. and Howard, C. S.: The passage of turbid water through Lake Mead. *Transactions ASCE*, Paper No. 1994, 720-732, (1937)

[23] Hinderer, M.: Late quarternary denudation of the Alps, valley and lake fillings and modern river loads. *Geodinamica Acta*, **14**, 231-263 (2001)

[24] Hsu, J. P. C. and Capart, H.: Onset and growth of tributary dammed lakes. *Water Resources Research*, **44**, W11201 (2008)

[25] Hydon, P. E.: *Symmetry methods for differential equations*, Cambridge University press, Cambridge

[26] Jordan, T. E. and Fleming, P. B.: From geodynamic models to basin fill, a stratigraphic perspective. In: *Quantitative Dynamic Stratigraphy* (Ed.: T.A. Cross), 149-163 (1990)

[27] Kenyon, P. M. and Turcotte, D. L.: Morphology of a delta prograding by bulk sediment transport. *Geol. Soc. Amer. Bull.*, **96**, 1457-1465 (1985)

[28] Kostic, S. Parker, G. and Marr, J. G.: Role of turbidity currents in setting the foreset slope of clinoforms prograding into standing fresh water. *J. Sedimentary Res.*, **72** (3), 353-362 (2002)

[29] Kostic, S. and Parker, G.: Progradational sand mud deltas in lakes and reservoirs. Part I. Theory and numerical modeling. *J. Hydr. Res.* **41**(2), 127-140 (2003)

[30] Kostic, S. and Parker, G.: Progradational sand-mud deltas in lakes and reservoirs. Part II. Experiment and numerical simulation, *J. Hydr. Res.* **41**(2), 141-152 (2003)

[31] Kreyszig, E.: *Advanced Engineering Mathematics*, Wiley (2006)

[32] Lai, S. Y. J.: *Self-similar delta formation by hyperpycnal flows: theory and experiments.* M. S. Thesis, Graduate Institute of Civil Engineering, Natl. Taiwan University, Taiwan, June 2006

[33] Lai, S. Y. J. and Capart, H.: Two-diffusion description of hypopycnal deltas. *J. Geophys Res. Earth Surface*, **112**, art F05005, 1-20 (2007) doi: 10.1029/2006JF00617

[34] Lai, S. Y. J. and Capart, H.: Reservoir infill by hyperpycnal deltas over bedrock. *Geophys. Res. Lett.*, **36** (2009) L08402, doi:10.1029/2008GL037139 (2009)

[35] Lai, S. Y. J. and Capart, H.: Response of hyperpycnal deltas to steady rise in base level. *5^{th} IAHR Symposium on River, Coastal and Estuarine Morphodynamics* in press (2011)

[36] Lambert. A.: Turbidity currents from the Rhine River on the bottom of Lake Constance. *Wasserwirtschaft*, **72**(4), 14 (in German), (1982)

[37] Lane, E. W.: The importance of fluvial morphology in hydraulic engineering. *Proceedings Am. Soc. Civ. Eng.* **81**, 745-1-745-17 (1955)

[38] Lee, H.-Y, Lin, Y.-T, Chiu, Y. J. Quantitative estimation of reservoir sedimentation from three typhoon events. *J. Hydraul. Eng.* **11**, 362-370 (2006)

[39] Lorenzo-Trueba, J., Voller, V. R., Muto, T., Kim, W., Paola, C. and Swenson, J. B.: A similarity solution for a dual moving boundary problem associated with a coastal-plain depositional system. *J. Fluid Mech.*, **628**, 427-443 (2009)

[40] Mackin, J. H.: Concept of the graded river. *Bulletin Geol. Soc. America* **59**, 463-512 (1948)

[41] Meyer-Peter, E. and Müller, R.: Formulas for bedload transport. *2nd Meeting, Int. Hydraul. Structures Research, Stockholm*, 39-64 (1948)

[42] Mitchell, N. C.: Morphologies of kinkpoints in submarine canyons. *Geol. Soc. Amer. Bull.*, **118**, 589-605 (2006)

[43] Müller, G.: The new Rhine delta in Lake Constance. In: *Deltas in their geologic framework*, Shirley, M.L. and Ragsdale, J. E., eds. Houston Geological Society, 107-124 (1966)

[44] Müller, G. and Förstner, U.: General relationship between suspended sediment concentration and water discharge in the Alpenrhein and some other rivers. Nature **217**, 244-245 (1966)

[45] Muto, T. Shoreline autoretreat substantiated in flume experiments. *J. Sedimentary Res.*, **71**(2), 246-254 (2001)

[46] Muto, T., and Steel, R. J.: Retreat of the front in a prograding delta. *Geology*, **20**, 967-970 (1992)

[47] Muto, T. and Steel, R. J.: Autogenic attainment of large-scale alluvial grad with steady sea-level fall. Implications from flume-tank experiments. *Geology*, **32**(5), 401-404; doi:10.1130/G20269 (2004)

[48] Muto, T. and Swenson, J. B.: Large-scale fluvial grade as a non-equilibrium state in linked depositional systems: Theory and experiment. *J. Geophys. Res.*, **110**(F3), art.no F03002 (2005)

[49] Muto, T. and Swenson, J. B.: Autogenic attainment of large-scale alluvial grad with steady sea-level fall. An analog tank-flume experiment *Geology*, **34**(3), 161-164; doi: 10.1130/G21923.1 (2006)

[50] Muto, T., Steel, R. J. and Swenson, J. B.: Autostratigraphy: A framework norm for genetic stratigraphy *J. Sedimentary Res.*, **77**, 2-12, doi:10.2110/JSR2007.005 (2007)

[51] Paola, C.: Subsidence and gravel transport in alluvial basins. In: *New Perspectives in Basin Analysis* (K. L. Kleinsphen and C. Paola, eds), 231-243 (1988)

[52] Paola, G., Heller, P. L. and Angevine, C. L.: The large scale dynamics of grain-size variations in alluvial basins. 1: Theory. *Basin Res.* **4**, 73-90 (1992)

[53] Parker, G.: Basic principles of river hydraulics. *Hydraul. Div. ASCE* **103**, 1077-1087 (1977)

[54] Parker, G., Muto, T.: One-dimensional numerical model of delta response to rising sea-level. In: *Proceedings third IAHR Symposium on River, Coastal and Estuarine Morphodynamics* Editors: A Sánches-Arcilla and A. Bateman, pp. 558-570. *Int Assoc. for Hydraulic Research, Madrid* (2003)

[55] Petter, A. L. and Muto, T.: Sustained alluvial aggradation and autogenic detachment of the alluvial river from the shoreline in response to steady fall of relative sea level. *J. Sedimentary Res.*, **78**, 98-111; doi: 10.2110/JRS.2008.012 (2008)

[56] Pitman, W. C.: Relationship between eustacy and stratigraphic sequences on passive margins. *Geol. Soc. Am. Bull.* **89**, 1389-1403 (1978)

[57] Roethlisberger, H.: Eislawinen und Ausbrüche von Gletscherseen. *Jahrbuch der Schweizerischen Naturforschenden Gesellschaft, wissenschaftlicher Teil*, 170-211 (1978)

[58] Roth, M. M., Weber, M. and Bezzola, G. R.: Physical modeling of sediment deposits in a river delta: The Alpenrhein Delta in Lake Constance. *Proc. XXIX IAHR Congress, Beijing, China, Theme E.*, 187-194 (2001)

[59] Schumm, S. A.: *The Fluvial System*, 338 pp. John Wiley, Hoboken, N. J. (1977)

[60] Smith, W. O., Vettere, C. P. and Cummings, G. B.: Comprehensive survey of sedimentation in Lake Mead, 1948-1949. *U.S Geol. Survey Prof.* Papier 295, 253 p. (1960)

[61] Sokolnikoff, I. S. and Redheffer, R. M.: *Mathematics of Physics and Modern Engineering*, McGraw Hill Book Company, New York, etc. (1966)

[62] Soni, J. P.: Unsteady sediment teransport law and prediction of aggradation parameters *Water Resour. Res.*, **17**, 33-40 (1981)

[63] Swenson, J. B., Voller, V. R., Paola, C., Parker, G. and Marr, J. G.: Fluvio-deltaic sedimentation: A generalized Stefan problem. *Euro J. of Applied Mathematics*, **11**, 433-452 (2000)

[64] Tonioli, H. and Schultz, J.: Experiments on sediment trap efficiency in reservoirs. *Lakes and Reservoirs* **10**, 13-24 (2005)

[65] Turner, T. H.: *Buoyancy effects in fluids*. Cambridge University Press, Cambridge UK (1973)

[66] Voller, V. R., Swenson, J. B., Kim, W. and Paola, C.: An enthalpy method for moving boundary problems on the Earth's surface. *Int. J. Numerical Methods for Heat & Fluid Flow*, **16**(5), 641-654, (2006)

[67] Wright, H. E., Jr., Lease, K. and Johnson, S. *Glacier River Warren, Lake Pepin, and the environmental history of southeastern Minnesota*. In: *Contributions to Quarternary Studies in Minnesota, Minn. Geol. Surv. Rep. Invest.* Vol **49**, (C.J. Patterson and H.E. Wright, Jr., eds., pp. 131-140, Univ. of Minn. Press, Minneapolis, Minn (1998)

[68] Write, L. D., Wiseman, W. J., Bornhold, B. D., Prior, D. B., Suhayda, J. N., Keller, G. H. Yang, Z.-S. and Fan, J. B.: Marine dispersal and deposition of Yellow River silts by gravity driven underflows. *Nature*, **332**, 629-632 (1988)

[69] Yu, W.-S., Lee, H.-Y. and Hsu, S. M.: Experimental study on delta formation in a reservoir. *J. Chin. Inst. Civ. Hydraul. Eng.*, **12**(1), 171-177 (2000) [in Chinese]

[70] Zhang, H. and Kahawita, R.: Nonlinear model for aggradation in alluvial channels *J. Hydraul Res.*, **113**, 353-369 (1987)

[71] Zumberge, J. H.: *The lakes of Minnesota, their Origin and Classification* Univ. of Minn. Press, Minneapolis, Minn. (1952)

Manuscript received: 09. May 2012

A Global View of Sediment Transport in Alluvial Systems

Kolumban Hutter* Ioana Luca†

*Bergstrasse 5, 8044 Zürich, Switzerland, hutter@vaw.baug.ethz.ch,

†Dept. Math. Methods and Models, Univ. Politehnica of Bucharest,

Splaiul Independentei 313, 060042 Bucharest, Romania, iolucaro@yahoo.com

Abstract

Sediment transport arises in alluvial lake-river systems in two different forms: (i) as bed load, comprising the moving detritus of the river bed and of the shallow, often only near-shore regions, and (ii) the suspended sediment load of the finer fractions. In river hydraulics the latter are often neglected; so, the bed load transport is treated without back-coupling with the wash-load. This is justified on decadal time scales. In the deeper parts of lakes wind-induced shearing in the benthic boundary layer hardly mobilizes the bed material, which stays immobile for most time and may be set in motion only interruptedly. However, the particle laden fluid transports the suspended material, which is advected and may on longer time scales settle in deposition-prone regions. In general, the deposition to and erosion from the basal surface occur concurrently. This environmental interplay is studied in this article.

The slurry - a mixture of the bearer fluid and particles of various sizes – is treated as a mixture of class I, in which mass, momentum and energy balances for the mixture as a whole are formulated to describe the geophysical fluid mechanical setting, whilst the suspended solid particles move through the bearer medium by diffusion. The governing equations of this problem are formulated, at first for a compressible, better non-density preserving, mixture. They thus embrace barotropic and baroclinic processes. These equations, generally known as NAVIER-STOKES-FOURIER-FICK (NSFF) fluids[1], are subjected to turbulent filter operations and complemented by zeroth and first order closure schemes. Moreover, simplified versions, e.g. the (generalized) BOUSSINESQ, shallow water and hydrostatic pressure assumptions are systematically derived and the corresponding equations presented in both conservative and non-conservative forms. Beyond the usual constitutive postulates of NSFF–fluids and turbulent closure schemes the non-buoyant suspended particles give rise to settling velocities; these depend on the particle size, expressed by a nominal particle diameter. A review of the recent hydraulic literature of terminal settling velocities is given. It shows that the settling velocity depends on the particle diameter and on the particle Reynolds number.

A separate section is devoted to the kinematic and dynamic boundary conditions on material and non-material singular surfaces as preparation for the mathematical-physical description of the sediment transport model, which follows from an analysis of jump transition conditions at the bed.

The simplest description of detritus transport does not use the concept of the motion of a thin layer of sediments. It treats it as a singular surface, which is equipped with surface grains of various grain size diameters. Such a simplified theoretical level is also used in this article; it implies that solid mass exchange, as erosion and deposition of different particle size fractions, is the only physical quantity relevant in the description of the sediment transport. It entails formulation of surface mass balances of an infinitely thin detritus layer for the sediment and surface momentum balance of

[1] Stress tensor, heat flux vector and mass flux vectors are given as proposed by Navier&Stokes, Fourier and Fick, respectively.

the mixture. The deposition rate of the various grain fractions, expressed as grain classes, follows from a parameterization of the free fall velocity of isolated particles in still water, but is in general coupled with the local flow and then follows from the solution of the hydrodynamic equations and the processes at the basal surface. The erosion rate is governed by two statements, (a) a fracture criterion determining the threshold value of a stress tensor invariant at the basal surface, which separates existence and absence regimes of erosion, and (b) determination of the amount of erosion beyond the threshold value of the mentioned stress invariant.

Contents

1 Description of the sediment transport model

The spatially one-dimensional model for the formation of deltas due to alluvial sediment progradation from straight rivers provides enlightening insight into the physical behaviour of the interacting processes which are exhibited by the sedimentary erosion and deposition in river-lake systems. Laboratory experiments demonstrated excellent agreement between the theoretical predictions of the two limiting forms of the evolving deltas - GILBERT-type 'triangular subaqeous slopes' under hypo- and homo-pycnal conditions and smoothly evolving weakly curved foreset depositions so generated by turbulent density-under currents. The laboratory experiments reflect realistic flow states, but the theory was shown to equally reproduce realistic conditions, when in a linear valley an elongated lake is formed by steady sediment deposits from a side tributary and when, under special conditions, it may relatively quickly again disintegrate. Practically of significance is also the development of the sediment regime in an elongated reservoir after its construction; large sediment input through the decades after dam erection may fill the reservoir and make flushing scenarios necessary through a bottom outlet or a side-pass tunnel. Qualitatively, these scenarios can also be described by the model.

It is, however, clear that multi-dimensionality of the sedimentary processes generally prevails in a river mouth and its vicinity, especially in mountainous lakes of complex geometry, see Figs. 1, 2. Moreover, the sediment loads generally occur in two different forms, as (i) bed load, comprising the moving grains of the alluvial river bed or the frontal part of the delta, formed and evolved by the coarser sediment fractions of the prograding processes, and (ii) the suspended sediment load of the finer fractions (usually clay and silt). Both participate in the formation of the bottom boundary and its evolution in time and space, on the one hand by deposition or settling processes of the suspended, non-buoyant fines according to the local water current, which they are exposed to, and, on the other hand, by motion cessation, re-suspension of the sliding, rolling and saltation particles of the bed load and their consequential transports in suspension.

It transpires that the settling and re-suspension of particles depend upon (i) the state of the water flow above the sediment bed and the wind induced barotropic or baroclinic current in the wider vicinity of the river mouth, and (ii) the grain size distribution of the alluvial sediments. In deposition processes of the suspension load, often also called *wash load*, the coarser grains will settle out first, followed by the smaller ones. So, the slurry-like upper water layer will be subject to persistent particle size segregation and consequential alteration and steepening of the grain size curve. It is evident that an adequate model for the suspended sediment load must be formulated as a mixture of a pure fluid with a number of solid constituents, each representative of a specific grain size range, and expressed as a balance of mass of its size-range with FICKian parameterization of its flux and vanishing production rate.[2]

In much the same way the moving sediment bed is equally composed of grains of different sizes, generally coarser than those of the suspended load. The material in this moving layer may again be interpreted as a mixture of a number of particles in very narrow size ranges plus an interstitial fluid. Except for eruptive intermittent bursts over which an averaging of the particle motions and the fluid might be justified on time scales relevant for sediment transport, all these components have nearly the same velocity, but it turns out that nevertheless balance laws of mass and momenta for the constituents need to be formulated. Because of its small thickness the moving sediment layer may then be viewed as a singular surface equipped with mass and momentum for which two-dimensional mass and momentum

[2]It is assumed that no fragmentation of particles into sizes other than those in the own size-range occurs.

Figure 1: Channelized entrance of the river Rhine (Alpen-Rhein) into Lake Constance at Fussach, near Bregenz, showing alternating sandbanks within the artificial channel and a large patch of suspended sediments in front of the river mouth. The island on the right frame is Lindau. Copyright: 'Tino Dietsche - airpics4you.ch'

balances are to be formulated. Its mass density changes by deposition of fines from the wash load and re-suspension of the eroded components from the moving bed.

The likely computational procedures for the moving sediment bed can be either a continuum approach as stipulated above, or application of molecular dynamics of the particles interacting with each other and with the fluid, better and more adequately known as **D**iscrete **E**lement **M**ethod (DEM). This approach has been carefully studied in a Ph.-D. thesis by VETSCH (2011) [49], but the method is presently not sufficiently advanced to warrant a detailed presentation here. Consequently, the text below will be based on the continuum approach, but, of course, with implementation of additional simplifying assumptions. One is the complexity of the mixture formulation. The most detailed situation prevails when each component is equipped with its own density, velocity and temperature. For each of them balances of mass, momenta and energy must then be accounted for. HUTTER & JÖHNK (2004) [17], p. 255, call this a *mixture of class III*. When heat exchange between the constituents is rapid, all constituents possess (nearly) the same temperature; then it suffices to only consider the energy balance of the mixture as a whole, involving a single temperature field, while balances of mass and momentum of all the constituents are kept. This defines a *mixture of class II*. Still a further simplification is possible, if for some reason all constituents except one arise in small concentrations and have nearly the same velocity as the dominant bearer fluid. Such conditions prevail for the salts defining the mineralisation or salinity of lake or ocean water. In this case it may suffice to formulate also momentum balance for the mixture as a whole and to account for the variation of the concentrations of the constituent masses by their mass balances. This defines a *mixture of class I*. This is the principal conceptual formulation of the sediment transport as wash and bed loads for which the balances of momentum and energy are formulated for the mixture as a whole, but balances of mass for each tracer individually and for the mixture as a whole.

Figure 2: Close-up to the mouth of the river Rhine (Alpen-Rhein) at Fussach, near Bregenz, showing the right river dam and the suspended sediments (wash-load) with the strong spatial variation of its concentration. Copyright: 'Tino Dietsche - airpics4you.ch'

Which mixture class ought to be applied depends on the sort and scale of application in focus. For hydraulic and possibly also geologic applications bed-load is likely restricted to near shore zones and the vicinity of river mouths. [Exceptions are, of course, large, very shallow lakes of, say, less than 5 m maximum depth (Neusiedler See, Austria/Hungary; Lake Taihu China; Northern part of Caspian Sea).] On the other hand, the suspended particle phase can be ignored in most interior parts of less shallow lakes for shorter, hydraulically relevant, e.g. decadal time scales, but ought to be considered for variations over geologically relevant time scales over centuries and millennia. In near shore zones and close to river mouths, particle laden mixtures will likely govern the wash and bed load transports.

The above description indicates that for certain questions, bed load movement or relatively rapid depositing or erosive detritus rates are localized to sub-regions of, but not subject to, the entire lake. In such cases application of *sub-structuring* or *nesting* is suggested, of which the use is as follows: Global, e.g. wind induced processes of the entire homogeneous or stratified lake are investigated with a judiciously simplified model (e.g. in which bed load movement is ignored) and a discretisation allowing determination of the current, (temperature and particle concentration[3]) fields within the entire lake, however, with values of the field variables only at the grid points of the relatively large meshes of the lake-scale global problem. A sub-region of the lake in the vicinity of the river mouth and the lowest part of the river is subsequently selected and the governing equations describing the dynamics of the upper-layer and the bed load are then discretized with a much finer net than the equations of the global, whole lake analysis. At the open, lake-ward boundaries the flux conditions must then be properly transferred as boundary values for the boundary value problem, valid in the sub-region within which the evaluation of the bottom topography in the river mouth region is determined.

[3]Often these fields may even be dropped and simply assumed to be frozen to the fluid particles.

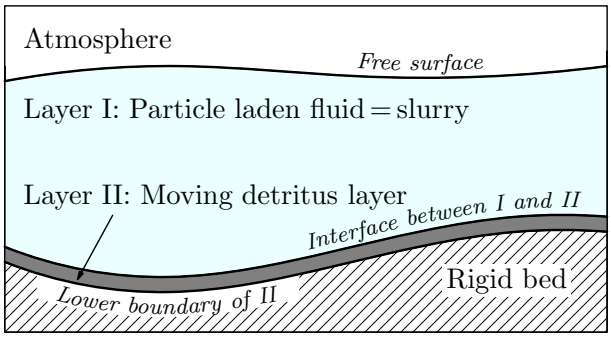

Figure 3: Lake domain divided into the large particle laden fluid part, I, and the moving detritus layer, II, with indicated boundaries: free surface, interface between I & II, and the lower boundary of the detritus layer where no grains move.

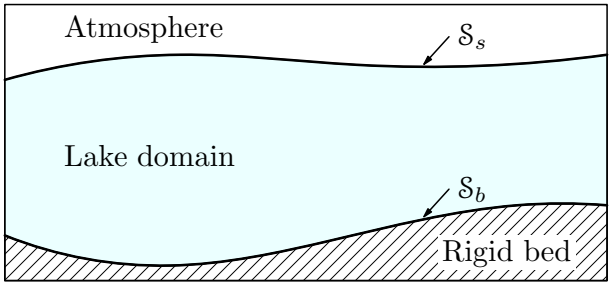

Figure 4: Lake domain bounded by the free surface $\mathcal{S}_s$ and the basal surface $\mathcal{S}_b$. The surface $\mathcal{S}_b$ incorporates also domain II.

In the subsequent analysis the lake domain will at least be subdivided into two layers, see Fig. 3. In the upper layer the lake water will be treated as a particle laden, possibly turbulent BOUSSINESQ fluid subject to the shallow water approximation.[4] This layer may, at a later stage be further sub-divided into sub-layers for computational reasons or in order to model stratification. The second layer is the domain of the sliding, rolling and saltating sediment, saturated by fluid. Its upper boundary will, in general, move or deform, and it defines the bathymetric profile of the lake bottom as a function of time and space. Its lower boundary marks the upper boundary of the rigid immobile solid bed. In comparison to the upper layer, this second layer is very thin, and it may well be thought to be describable by an infinitely thin sheet of which the physical properties must account for its finite thickness.[5] We will conceive layer II as a singular surface $\mathcal{S}_b$ separating the rigid bed and layer I (lake domain), see Fig. 4, being equipped with its own material properties and balance laws.

Layer I is interacting at its upper surface with the atmosphere; wind-shear transfers momentum to it, and solar irradiation may give rise to changes in the stratification. The interface between the two layers is non-material in general unless neither suspended material from layer I is deposited nor certain fractions of the bed-load in layer II are (re)-suspended into layer I. This fact makes adequate definition of the interface between the two layers difficult. Experience with laboratory experiments, however, shows that under given dynamical conditions immediately above the interface, grains above the corresponding minimum grain diameter do not erode, i.e. are not lifted into layer I (for a substantial amount of time), but stay within the detritus layer. This implies that an erosion inception condition which depends on the

[4]The focus is not on strong internal baroclinic motion but rather on the reproduction of the current near the basal surface (e.g. the benthic boundary layer).

[5]In the theory of interfaces such sheets are called *diffuse interfaces*.

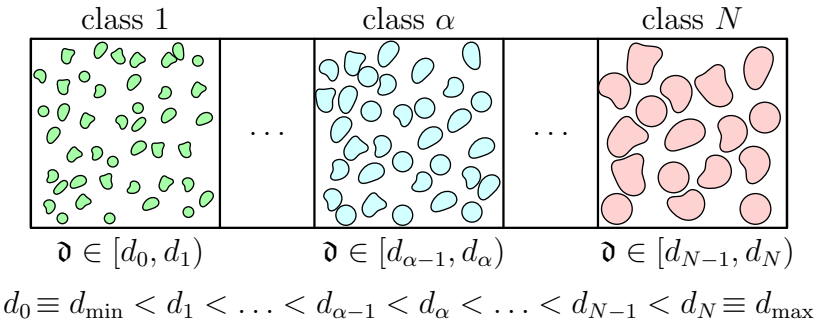

Figure 5: Partition of the interval $[d_{\min}, d_{\max})$, in which the nominal particle diameters range, into N disjoint subsets, each of them defining a particle class; $\mathfrak{d}$ is the nominal particle diameter.

particle diameter must be established.

2 Governing equations in lake domain

The field equations in lake domain are formulated at this general level as those for turbulent motion of a BOUSSINESQ fluid of a mixture of class I. We briefly explain the derivation of these equations.

2.1 NSFF flow

The solid particles surrounded by the bearer fluid possess nominal diameters in the interval $[d_{\min}, d_{\max})$, $d_{\min} < d_{\max}$. This interval is partitioned into N subintervals, and so particles in $[d_{\alpha-1}, d_\alpha)$ define the α-th particle class, see Fig. 5.[6] Such a class is modelled as a continuous body with its own motion and rheology. Thus, at the level of fine resolution (at which methods of direct numerical simulation are applicable) the slurry is modelled as a continuous mixture consisting of a fluid and N solid constituents (classes). Moreover, since the solid particles are dragged on by the fluid with nearly the same velocity as that of the fluid, a mixture of class I is an appropriate concept to be applied for the description of the slurry flow. The equations describing this flow take then the forms

- Balance of mass for the mixture

$$\frac{\mathrm{d}\,\rho}{\mathrm{d}\,t} + \rho \operatorname{div} \boldsymbol{v} = 0\,; \tag{1}$$

- Balance of momentum for the mixture

$$\rho \left\{ \frac{\mathrm{d}\,\boldsymbol{v}}{\mathrm{d}t} + 2\boldsymbol{\Omega} \times \boldsymbol{v} \right\} = -\operatorname{grad} p + \operatorname{div} \boldsymbol{\sigma}_E + \rho \boldsymbol{g}\,; \tag{2}$$

- Balance of mixture energy

$$\begin{aligned} \rho \frac{\mathrm{d}\epsilon}{\mathrm{d}\,t} &= -\operatorname{div} \boldsymbol{q} - p \operatorname{div} \boldsymbol{v} + \operatorname{tr} \left(\boldsymbol{\sigma}_E \boldsymbol{D} \right), \text{[7]} \quad \text{or[8]} \\ \rho \frac{\mathrm{d}h}{\mathrm{d}\,t} - \frac{\mathrm{d}\,p}{\mathrm{d}\,t} &= -\operatorname{div} \boldsymbol{q} + \operatorname{tr} \left(\boldsymbol{\sigma}_E \boldsymbol{D} \right), \end{aligned} \tag{3}$$

[6] This is motivated by sieve experiments: one has a whole column of sieves, numbered $0, \ldots, \alpha, \ldots, N-1$, with the largest mesh size on top and the smallest at the bottom; class α ($\alpha = 1, \ldots, N$) consists of those particles which are collected by sieve $\alpha - 1$. It is tacitly understood that the sieve with number '0' is impermeable for all particles of sizes larger than a chosen minimum (say for clay and silt fractions which cannot pass very small holes simply because of cohesion coalescence).

in which h is the mixture enthalpy,

$$h \equiv \epsilon + \frac{p}{\rho}\,; \tag{4}$$

- Balance of tracer mass of constituent α

$$\rho\,\frac{\mathrm{d}\,c_\alpha}{\mathrm{d}\,t} = -\mathrm{div}\,\{\boldsymbol{j}_\alpha - \rho\,c_\alpha \boldsymbol{w}_\alpha^s\} + \phi^{(c_\alpha)}, \quad \alpha = 1,\ldots,N\,. \tag{5}$$

In these equations ρ is the mixture density, $\boldsymbol{v}$ is the barycentric velocity, p, $\boldsymbol{\sigma}_E$, ϵ, $\boldsymbol{q}$, are the pressure, the extra stress tensor, the internal energy and the heat flux vector, respectively, all referring to the mixture as a whole, $\boldsymbol{g}$ is the gravity vector, and $\boldsymbol{\Omega}$ ($|\boldsymbol{\Omega}| = 7.272 \times 10^{-5}\,[\mathrm{s}^{-1}]$) is the angular velocity of the rotation of the Earth. (As customary in Geophysical Fluid Dynamics, the EULER acceleration is ignored and the centripetal acceleration is thought to be incorporated in the gravity term.) Moreover, we use the notation

$$\frac{\mathrm{d}\,(\cdot)}{\mathrm{d}\,t} \equiv \frac{\partial\,(\cdot)}{\partial\,t} + (\mathrm{grad}\,(\cdot))\,\boldsymbol{v}\,, \quad \boldsymbol{D} \equiv \mathrm{sym}\,(\mathrm{grad}\,\boldsymbol{v}) = \tfrac{1}{2}(\boldsymbol{L} + \boldsymbol{L}^T) \;\text{ with }\; \boldsymbol{L} \equiv \mathrm{grad}\,\boldsymbol{v}\,, \tag{6}$$

as the substantive derivative following the barycentric motion, and the strain rate or rate of strain or stretching tensor $\boldsymbol{D}$ of the barycentric velocity, respectively. Finally, the balance law of tracer mass of constituent α, (5), requires special justification. It is easy to show that the mass balance law of constituent α, $\partial\rho_\alpha/\partial\,t + \mathrm{div}\,(\rho_\alpha \boldsymbol{v}_\alpha) = \phi^{(c_\alpha)}$, where ρ_α, $\boldsymbol{v}_\alpha$ and $\phi^{(c_\alpha)}$ are the density, the velocity and the mass production rate density of constituent α, can be written as

$$\rho\,\frac{\mathrm{d}\,c_\alpha}{\mathrm{d}\,t} = -\mathrm{div}\,\boldsymbol{\mathfrak{J}}_\alpha + \phi^{(c_\alpha)}\,, \tag{7}$$

in which $c_\alpha, \boldsymbol{\mathfrak{J}}_\alpha$ are the mass fraction or concentration and the diffusive-advective mass flux of constituent α, respectively:

$$c_\alpha \equiv \frac{\rho_\alpha}{\rho}\,, \quad \boldsymbol{\mathfrak{J}}_\alpha \equiv \rho c_\alpha(\boldsymbol{v}_\alpha - \boldsymbol{v})\,. \tag{8}$$

We recall that the constituent α is composed of particles of various diameters ranging in $[d_{\alpha-1}, d_\alpha)$. Thus, one may think of class α as a continuous mixture of a finite number of constituents. A possibility to account for this fact is to introduce the decomposition

$$\boldsymbol{\mathfrak{J}}_\alpha = \underbrace{\rho c_\alpha(\boldsymbol{v}_\alpha - \boldsymbol{v}_\alpha^s)}_{\equiv\,\boldsymbol{j}_\alpha} + \underbrace{\rho\,c_\alpha(\boldsymbol{v}_\alpha^s - \boldsymbol{v})}_{\equiv\,-\rho\,c_\alpha \boldsymbol{w}_\alpha^s}\,, \tag{9}$$

[7] tr is the trace operator: $\mathrm{tr}\,\boldsymbol{A} = A_{ii}$, where $\boldsymbol{A}$ is a second order tensor.

[8] Consider the term $p\,\mathrm{div}\,\boldsymbol{v}$ on the right-hand side of $(3)_1$. With the aid of (1) this takes the form

$$-p\,\mathrm{div}\,\boldsymbol{v} = \frac{p}{\rho}\frac{\mathrm{d}\,\rho}{\mathrm{d}\,t} = -\rho\frac{\mathrm{d}}{\mathrm{d}\,t}\left(\frac{p}{\rho}\right) + \frac{\mathrm{d}\,p}{\mathrm{d}\,t}\,.$$

Therefore, the balance of mixture energy may also be written as

$$\rho\frac{\mathrm{d}}{\mathrm{d}\,t}\left(\epsilon + \frac{p}{\rho}\right) - \frac{\mathrm{d}\,p}{\mathrm{d}\,t} = -\,\mathrm{div}\,\boldsymbol{q} + \mathrm{tr}\,(\boldsymbol{\sigma}_E \boldsymbol{D})\,,$$

suggesting the definition of the mixture enthalpy (4). In almost density preserving materials the term $p\,\mathrm{div}\,\boldsymbol{v}$ in $(3)_1$ and the term $\mathrm{d}\,p/\mathrm{d}\,t$ in $(3)_2$ are generally ignored, which implies $\mathrm{d}\epsilon/\mathrm{d}\,t \approx \mathrm{d}h/\mathrm{d}\,t$, which is the reason why one can often see in the literature both formulations using ϵ or h.

where $\boldsymbol{v}_\alpha^s$ is the velocity of a *representative* granular constituent (perhaps that one with greatest concentration or that with the mean diameter) of the mixture class α. Thus, $\boldsymbol{j}_\alpha$ is now the diffusive flux of the constituent α with respect to the representative particle in the class α. For this flux term a gradient type constitutive relation will be postulated in the spirit of FICK's law. The second term expresses the advected flux of the representative particle relative to the barycentric motion. For this advected flux a constitutive relation is postulated. In sediment transport work a rather restricted but courageous statement is made:

$$\boldsymbol{w}_\alpha^s = w_\alpha^s \boldsymbol{e}_z \iff \rho c_\alpha (\boldsymbol{v}_\alpha^s - \boldsymbol{v}) = -\rho c_\alpha w_\alpha^s \boldsymbol{e}_z \,, \tag{10}$$

where $w_\alpha^s > 0$ is the terminal free falling velocity of the selected representative particle in still water, and $\boldsymbol{e}_z$ is the unit vector against the gravity vector.[9] This is how $w_\alpha^s \boldsymbol{e}_z$ would enter formula (5). Of course, in reality this is not correct; perhaps as an approximation, non-vanishing horizontal components of $\boldsymbol{w}_\alpha^s$ are expected. A likely better choice may be

$$\boldsymbol{w}_\alpha^s = w_\alpha^s \left\{ \tan\theta \frac{\boldsymbol{v}_H}{\|\boldsymbol{v}_H\|} + \boldsymbol{e}_z \right\} , \tag{11}$$

where

$$\boldsymbol{v}_H \equiv \{\boldsymbol{v} - (\boldsymbol{v}\cdot\boldsymbol{e}_z)\boldsymbol{e}_z\}_{\mathcal{S}_b} \tag{12}$$

is the horizontal velocity at the basal surface $\mathcal{S}_b$, see Fig. 3, and θ is a tilt angle (approx. 0° or somewhat larger) to be determined. More generally, determination of the motion of a solid particle immersed in a moving fluid is a difficult specialized topic of interaction dynamics.

The above balance equations can also easily be transformed to *conservative form* by judiciously combining them with the balance equation of mass (1). Often these forms are better suited to numerical implementation. This yields[10]

- Balance of mass for the mixture

$$\frac{\partial\,\rho}{\partial\,t} + \operatorname{div}(\rho\boldsymbol{v}) = 0\,; \tag{13}$$

- Balance of momentum for the mixture

$$\frac{\partial(\rho\boldsymbol{v})}{\partial\,t} + \operatorname{div}(\rho\boldsymbol{v}\otimes\boldsymbol{v}) + 2\rho\boldsymbol{\Omega}\times\boldsymbol{v} = \operatorname{div}(-p\boldsymbol{I} + \boldsymbol{\sigma}_E) + \rho\boldsymbol{g}\,; \tag{14}$$

- Balance of mixture energy

[9] For a non-buoyant particle α falling in still water we have $\boldsymbol{w}_\alpha^s \equiv -(\boldsymbol{v}_\alpha^s - \boldsymbol{v}) = w_\alpha^s \boldsymbol{e}_z$; here $\boldsymbol{v}_\alpha^s$ is the velocity of the solid particle, and $\boldsymbol{v} \approx \boldsymbol{0}$ is the velocity of the surrounding fluid at rest. When the grain stops to decelerate it has attained the so-called terminal settling velocity or free fall velocity.

[10] (a) Using (1) yields for the left-hand side of (2)

$$\rho\frac{\mathrm{d}\boldsymbol{v}}{\mathrm{d}\,t} = \frac{\mathrm{d}\,\rho\boldsymbol{v}}{\mathrm{d}\,t} - \frac{\mathrm{d}\,\rho}{\mathrm{d}\,t}\boldsymbol{v} \overset{(1)}{=} \frac{\mathrm{d}\,\rho\boldsymbol{v}}{\mathrm{d}\,t} + (\rho\operatorname{div}\boldsymbol{v})\boldsymbol{v} = \frac{\partial\,\rho\boldsymbol{v}}{\partial\,t} + \operatorname{div}(\rho\boldsymbol{v}\otimes\boldsymbol{v}),$$

whilst the right-hand side remains unchanged.

(b) Using (1), for a scalar function f we obtain

$$\rho\frac{\mathrm{d}f}{\mathrm{d}\,t} = \frac{\mathrm{d}\,\rho f}{\mathrm{d}\,t} - \frac{\mathrm{d}\,\rho}{\mathrm{d}\,t} f \overset{(1)}{=} \frac{\mathrm{d}\,\rho f}{\mathrm{d}\,t} + (\rho\operatorname{div}\boldsymbol{v})f = \frac{\partial\,\rho f}{\partial\,t} + \operatorname{div}(\rho f\boldsymbol{v}),$$

which turns (3) and (5) into (15) and (16), respectively.

$$\frac{\partial(\rho\epsilon)}{\partial t} + \operatorname{div}(\rho\epsilon\boldsymbol{v}) = -\operatorname{div}\boldsymbol{q} - p\operatorname{div}\boldsymbol{v} + \operatorname{tr}(\boldsymbol{\sigma}_E\boldsymbol{D}) \quad \text{or}$$
$$\frac{\partial(\rho h)}{\partial t} + \operatorname{div}(\rho h\boldsymbol{v}) - \left\{\frac{\partial p}{\partial t} + \operatorname{grad} p\cdot\boldsymbol{v}\right\} = -\operatorname{div}\boldsymbol{q} + \operatorname{tr}(\boldsymbol{\sigma}_E\boldsymbol{D})\,; \tag{15}$$

- Balance of tracer mass α

$$\frac{\partial(\rho\, c_\alpha)}{\partial t} + \operatorname{div}(\rho\, c_\alpha\boldsymbol{v}) = -\operatorname{div}(\boldsymbol{j}_\alpha - \rho\, c_\alpha\boldsymbol{w}_\alpha^s) + \phi^{(c_\alpha)}\,, \quad \alpha = 1,\ldots,N. \tag{16}$$

In (16), $\rho\, c_\alpha\boldsymbol{w}_\alpha^s$ could be incorporated into the div-term on the left-hand side, but will not be done here.

2.2 Turbulent motion

For the turbulent motion it is common usage to average equations (13)–(16) by applying adequate filter operations to the balance laws. If the filter operation is denoted by $\langle\cdot\rangle$, any field variable f can be composed of its average $\langle\, f\,\rangle$ and fluctuation f' according to

$$f = \langle\, f\,\rangle + f'\,, \quad f' \equiv f - \langle\, f\,\rangle\,. \tag{17}$$

If this decomposition is applied to all field variables and a statistical filter with the property $\langle\langle\cdot\rangle\rangle = \langle\cdot\rangle$ is chosen, the filter operation is called REYNOLDS averaging. For example, the averaged balance law of mass (13) takes the form

$$\frac{\partial\langle\,\rho\,\rangle}{\partial t} + \operatorname{div}(\langle\,\rho\,\rangle\langle\boldsymbol{v}\rangle) = -\operatorname{div}(\langle\,\rho'\boldsymbol{v}'\rangle)\,. \tag{18}$$

Evidently, the correlation $\langle\,\rho'\boldsymbol{v}'\,\rangle$ only arises because of density variations due to turbulence. The turbulent mass flux on the right-hand side of (18) is the only place of all averaged balance laws, where such a term arises. It is small for nearly density preserving fluids and will then be ignored.[11]

Rather than referring to the general balance laws (13)–(16) we consider the balance laws (i) corresponding to a generalized BOUSSINESQ fluid and (ii) those obtained with the assumption that the density fluctuations are negligibly small.

2.2.1 Model 1: Generalized BOUSSINESQ fluid

A BOUSSINESQ *fluid* is defined as a fluid for which density variations are ignored except in the gravity term of the momentum equation. Balance of mass then reduces to $\operatorname{div}\,\boldsymbol{v} = 0$, agreeing with the continuity equation of density preserving continua. A somewhat more general assumption is as follows, see e.g.

[11] If for the velocity the so-called FAVRE averaging operator is employed,

$$\{\boldsymbol{v}\} \equiv \frac{\langle\rho\boldsymbol{v}\rangle}{\langle\rho\rangle}\,, \tag{19}$$

then the averaged mass balance takes the form

$$\frac{\partial\langle\rho\rangle}{\partial t} + \operatorname{div}(\langle\,\rho\rangle\{\boldsymbol{v}\}) = 0\,. \tag{20}$$

So, Favre averaging would preserve the conservative form of the balance of mass under filtering. However, this would also imply consequences in the remaining balance laws. A complete derivation using FAVRE averaging is e.g. given in LUCA et al. (2004) [26]. We prefer to stay with (18).

Hutter et al. [18]:

$$\begin{aligned} &\text{(i) } \rho = \rho_0(z) + \rho_d(\boldsymbol{x}, t), \\ &\text{(ii) } \rho_d(\boldsymbol{x}, t) \text{ is everywhere ignored except in the gravity term.} \end{aligned} \tag{21}$$

We call this the *generalized* BOUSSINESQ *assumption*. In (21), $\rho_0(z)$ is a static density field, which in a lake usually represents the stable stratification induced by radiation. For $\rho_0(z) =$ constant, (21) reduces to the classical BOUSSINESQ assumption. Owing to $(21)_{\text{(i)}}$, with

$$p = p_d + p_{st}, \quad p_{st} \equiv g \int_0^z \rho_0(\xi) \mathrm{d}\xi \,, \tag{22}$$

where g is the gravity constant, we introduce the dynamic, p_d, and the 'quasi-static', p_{st}, pressures, which implies

$$-\mathrm{grad}\ p = -\mathrm{grad}\ p_d - \rho_0(z)\, \boldsymbol{g} \,. \tag{23}$$

With (21)–(23), the physical balance laws (1)–(3), (5) subjected to the generalized BOUSSINESQ assumption take the forms

- Balance of mass for the mixture

$$\mathrm{div}\, \rho_0 \boldsymbol{v} = 0 \,; \tag{24}$$

- Balance of momentum for the mixture

$$\rho_0 \left\{ \frac{\mathrm{d}\, \boldsymbol{v}}{\mathrm{d}\, t} + 2\boldsymbol{\Omega} \times \boldsymbol{v} \right\} = -\mathrm{grad}\ p_d + \mathrm{div}\, \boldsymbol{\sigma}_E + (\rho - \rho_0)\boldsymbol{g} \,; \tag{25}$$

- Balance of mixture energy

$$\rho_0 \frac{\mathrm{d}\, \epsilon}{\mathrm{d}\, t} = -\mathrm{div}\, \boldsymbol{q} - p\, \mathrm{div}\, \boldsymbol{v} + \mathrm{tr}\, (\boldsymbol{\sigma}_E \boldsymbol{D}) \quad \text{or} \quad \rho_0 \frac{\mathrm{d}\, h}{\mathrm{d}\, t} - \frac{\mathrm{d}\, p}{\mathrm{d}\, t} = -\mathrm{div}\, \boldsymbol{q} + \mathrm{tr}\, (\boldsymbol{\sigma}_E \boldsymbol{D}) \,; \tag{26}$$

- Balance of tracer mass of constituent α

$$\rho_0 \frac{\mathrm{d}\, c_\alpha}{\mathrm{d}\, t} = -\mathrm{div}\, \{\boldsymbol{j}_\alpha - \rho_0\, c_\alpha \boldsymbol{w}_\alpha^s\} + \phi^{(c_\alpha)}, \quad \alpha = 1, \ldots, N \,, \tag{27}$$

or in the alternative, conservative forms, see (13)–(16),

- Balance of mass for the mixture

$$\mathrm{div}\, \rho_0 \boldsymbol{v} = 0 \,; \tag{28}$$

- Balance of momentum for the mixture

$$\frac{\partial\, (\rho_0 \boldsymbol{v})}{\partial\, t} + \mathrm{div}\, (\rho_0 \boldsymbol{v} \otimes \boldsymbol{v}) + 2\rho_0 \boldsymbol{\Omega} \times \boldsymbol{v} = \mathrm{div}\, (-p_d \boldsymbol{I} + \boldsymbol{\sigma}_E) + (\rho - \rho_0)\boldsymbol{g} \,; \tag{29}$$

- Balance of mixture energy

$$\begin{aligned} \frac{\partial\,(\rho_0\epsilon)}{\partial\,t} + \operatorname{div}(\rho_0\epsilon\boldsymbol{v}) &= -\operatorname{div}\boldsymbol{q} - p\operatorname{div}\boldsymbol{v} + \operatorname{tr}(\boldsymbol{\sigma}_E\boldsymbol{D}) \quad \text{or} \\ \frac{\partial\,(\rho_0 h)}{\partial\,t} + \operatorname{div}(\rho_0 h\boldsymbol{v}) - \left\{\frac{\partial\,p}{\partial t} + \operatorname{grad} p\cdot\boldsymbol{v}\right\} &= -\operatorname{div}\boldsymbol{q} + \operatorname{tr}(\boldsymbol{\sigma}_E\boldsymbol{D})\,; \end{aligned} \tag{30}$$

- Balance of tracer mass of constituent α

$$\frac{\partial(\rho_0\,c_\alpha)}{\partial\,t} + \operatorname{div}(\rho_0\,c_\alpha\boldsymbol{v}) = -\operatorname{div}(\boldsymbol{j}_\alpha - \rho_0 c_\alpha\boldsymbol{w}_\alpha^s) + \phi^{(c_\alpha)}, \quad \alpha = 1,\ldots,N\,. \tag{31}$$

We mention that for relatively shallow basins the term involving $\mathrm{d}\,p/\mathrm{d}\,t$ in $(26)_2$ and $(30)_2$ is ignored in the enthalpy formulations.

The turbulent analogues to the balance laws (24)–(31) are obtained if these laws are subjected to the filter operation $\langle\cdot\rangle$. In this process, $\rho_0, \boldsymbol{g}, \boldsymbol{\Omega}$ do not possess fluctuations, so that $\langle\rho_0\rangle = \rho_0$, $\langle\boldsymbol{g}\rangle = \boldsymbol{g}$, $\langle\boldsymbol{\Omega}\rangle = \boldsymbol{\Omega}$. When omitting the angular brackets, the REYNOLDS averaged equations then take the forms

- Balance of mass for the mixture

$$\operatorname{div}\rho_0\boldsymbol{v} = 0\,; \tag{32}$$

- Balance of momentum of the mixture

$$\begin{aligned} \rho_0\,\frac{\mathrm{d}\boldsymbol{v}}{\mathrm{d}\,t} + 2\rho_0\boldsymbol{\Omega}\times\boldsymbol{v}\left(= \frac{\partial\,(\rho_0\boldsymbol{v})}{\partial\,t} + \operatorname{div}(\rho_0\boldsymbol{v}\otimes\boldsymbol{v}) + 2\rho_0\boldsymbol{\Omega}\times\boldsymbol{v}\right) = \\ -\operatorname{grad}\,p_d + \operatorname{div}\boldsymbol{R} + (\rho-\rho_0)\boldsymbol{g}\,; \end{aligned} \tag{33}$$

- Balance of mixture energy

$$\begin{aligned} \rho_0\frac{\mathrm{d}\,\epsilon}{\mathrm{d}\,t}\left(= \frac{\partial(\rho_0\epsilon)}{\partial\,t} + \operatorname{div}(\rho_0\epsilon\boldsymbol{v})\right) &= -p\operatorname{div}\boldsymbol{v} - \operatorname{div}\boldsymbol{Q}_\epsilon + \phi^{(T)}, \\ \rho_0\frac{\mathrm{d}\,h}{\mathrm{d}\,t} - \frac{\mathrm{d}\,p}{\mathrm{d}\,t}\left(= \frac{\partial(\rho_0 h)}{\partial\,t} + \operatorname{div}(\rho_0 h\boldsymbol{v}) - \frac{\mathrm{d}\,p}{\mathrm{d}\,t}\right) &= -\operatorname{div}\boldsymbol{Q}_h + \phi^{(T)} + \operatorname{div}\boldsymbol{\mathcal{P}}\,; \end{aligned} \tag{34}$$

- Balance of tracer mass of constituent α

$$\rho_0\frac{\mathrm{d}\,c_\alpha}{\mathrm{d}\,t}\left(= \frac{\partial(\rho_0 c_\alpha)}{\partial\,t} + \operatorname{div}(\rho_0 c_\alpha\boldsymbol{v})\right) = -\operatorname{div}\{\boldsymbol{J}_\alpha - \rho_0 c_\alpha\boldsymbol{w}_\alpha^s\} + \phi^{(c_\alpha)}. \tag{35}$$

In these equations $\mathrm{d}f/\mathrm{d}\,t$ is the substantive derivative of f following the averaged turbulent velocity. Furthermore, the non-conservative and conservative forms have been written together to save space. The quantities[12]

$$\begin{aligned} \boldsymbol{R} &\equiv \langle\boldsymbol{\sigma}_E\rangle - \rho_0\langle\boldsymbol{v}'\otimes\boldsymbol{v}'\rangle\,, \quad \boldsymbol{Q}_\epsilon \equiv \langle\boldsymbol{q}\rangle + \rho_0\langle\epsilon'\boldsymbol{v}'\rangle\,, \quad \boldsymbol{Q}_h \equiv \langle\boldsymbol{q}\rangle + \rho_0\langle h'\boldsymbol{v}'\rangle\,, \\ \phi^{(T)} &\equiv \operatorname{tr}(\langle\boldsymbol{\sigma}_E\rangle\langle\boldsymbol{D}\rangle) + \operatorname{tr}\langle\boldsymbol{\sigma}_E'\boldsymbol{D}'\rangle - \langle p'\operatorname{div}\boldsymbol{v}'\rangle\,, \quad \boldsymbol{\mathcal{P}} \equiv \langle p'\boldsymbol{v}'\rangle\,, \\ \boldsymbol{J}_\alpha &\equiv \langle\boldsymbol{j}_\alpha\rangle + \rho_0\langle c_\alpha'\boldsymbol{v}'\rangle - \rho_0\langle c_\alpha'\boldsymbol{w}_\alpha^{s'}\rangle\,, \end{aligned} \tag{36}$$

[12]For these formulae we employ the symbol $\langle\cdot\rangle$ of filter operation to emphasize the role of the averaged laminar quantities and averages of turbulent correlation quantities.

represent

(i) the total stress $\boldsymbol{R}$ (modulo the pressure) as a combination of the averaged extra stress tensor $\langle \boldsymbol{\sigma}_E \rangle$ and the REYNOLDS stress tensor $-\rho_0 \langle \boldsymbol{v}' \otimes \boldsymbol{v}' \rangle$ due to turbulence;

(ii) the total heat flux $\boldsymbol{Q}_\epsilon$, $\boldsymbol{Q}_h$ as the sum of the averaged 'laminar' heat flux $\langle\, \boldsymbol{q} \,\rangle$ and the energy flux due to turbulence in the internal energy, $\rho_0 \langle \epsilon' \boldsymbol{v}' \rangle$, and the enthalpy, $\rho_0 \langle h' \boldsymbol{v}' \rangle$ formulation, respectively;

(iii) the averaged internal energy/enthalpy production rate density $\phi^{(T)}$ due to the power of working $\operatorname{tr} \langle \boldsymbol{\sigma}_E \rangle \langle \boldsymbol{D} \rangle$ of the mean motion and the correlations $\operatorname{tr} \langle \boldsymbol{\sigma}_E' \boldsymbol{D}' \rangle$, $\langle p' \operatorname{div} \boldsymbol{v}' \rangle$;

(iv) the average pressure work $\mathcal{P}$ (note that it only arises in the enthalpy formulation of the energy equation and that it can in principle be combined with the heat flux term $\boldsymbol{Q}_h$);

(v) the total mass flux of constituent α comprising the averaged laminar mass flux $\langle \boldsymbol{j}_\alpha \rangle$, turbulent mass flux $\rho_0 \langle c_\alpha' \boldsymbol{v}' \rangle$ and turbulent mass flux due to non-buoyant particle flow $\rho_0 \langle c_\alpha' \boldsymbol{w}_\alpha^{s'} \rangle$.

It is the goal of turbulence theory to propose closure relations for the quantities (36). We refrain to do this here and pass to the presentation of another model, for which, however, we give closure relations.

2.2.2 Model 2: Small density fluctuation assumption

One can find in the literature yet another set of averaged field equations which are stated as such but without any or little motivation. It can be motivated by considering the density fluctuation ρ' in the decomposition $\rho = \langle \rho \rangle + \rho'$ so small, that it is everywhere ignored. Of course, this strictly requires that $|\rho'| \ll \langle \rho \rangle$ and that any correlation $|\langle \rho' a' \rangle|$ is smaller than $|\langle a' b' \rangle|$ $(b' \neq \rho')$. We therefore propose the following

Small density-fluctuation-turbulence assumption: *Consider a non-density preserving fluid subjected to turbulent motions for which turbulent density fluctuations ρ' are negligibly small,*

$$\big|\rho'\big| \ll \big\langle \rho \big\rangle\,, \quad \big|\big\langle \rho' a' \big\rangle\big| \ll \big|\big\langle a' b' \big\rangle\big| \quad (b' \neq \rho') \tag{37}$$

can be dropped from the equations.

With this assumption the density function $\rho(\mathbf{x}, t)$ can be everywhere approximated by

$$\rho(\mathbf{x}, t) \approx \big\langle \rho(\mathbf{x}, t) \big\rangle\,. \tag{38}$$

Omitting the angular brackets $\langle \cdot \rangle$, with this approximation applied to the mixture mass density, the averaged balance laws as deduced from (13)–(16) can be written as

- Balance of mass for the mixture
$$\frac{\partial\, \rho}{\partial\, t} + \operatorname{div}(\rho \boldsymbol{v}) = 0\,; \tag{39}$$
- Balance of momentum for the mixture
$$\frac{\partial (\rho \boldsymbol{v})}{\partial\, t} + \operatorname{div}(\rho \boldsymbol{v} \otimes \boldsymbol{v}) + 2\rho \boldsymbol{\Omega} \times \boldsymbol{v} = -\operatorname{grad} p + \operatorname{div} \boldsymbol{R} + \rho \boldsymbol{g}\,; \tag{40}$$

- Balance of mixture energy

$$\begin{aligned} \frac{\partial(\rho\epsilon)}{\partial t} + \operatorname{div}(\rho\epsilon\boldsymbol{v}) &= -p\operatorname{div}\boldsymbol{v} - \operatorname{div}\boldsymbol{Q}_\epsilon + \phi^{(T)} \quad \text{or} \\ \frac{\partial(\rho h)}{\partial t} + \operatorname{div}(\rho h\boldsymbol{v}) - \frac{\mathrm{d}p}{\mathrm{d}t} &= -\operatorname{div}\boldsymbol{Q}_h + \operatorname{div}\boldsymbol{\mathcal{P}} + \phi^{(T)}; \end{aligned} \tag{41}$$

- Balance of tracer mass of constituent α

$$\frac{\partial(\rho c_\alpha)}{\partial t} + \operatorname{div}\rho c_\alpha\boldsymbol{v} = -\operatorname{div}(\boldsymbol{J}_\alpha - \rho c_\alpha\boldsymbol{w}_\alpha^s) + \phi^{(c_\alpha)}, \tag{42}$$

with the definitions

$$\begin{gathered} \boldsymbol{R} \equiv \langle\boldsymbol{\sigma}_E\rangle - \rho\langle\boldsymbol{v}'\otimes\boldsymbol{v}'\rangle, \quad \boldsymbol{Q}_\epsilon \equiv \langle\boldsymbol{q}\rangle + \rho\langle\epsilon'\boldsymbol{v}'\rangle, \quad \boldsymbol{Q}_h \equiv \langle\boldsymbol{q}\rangle + \rho\langle h'\boldsymbol{v}'\rangle, \\ \phi^{(T)} \equiv \operatorname{tr}(\langle\boldsymbol{\sigma}_E\rangle\langle\boldsymbol{D}\rangle) + \operatorname{tr}\langle\boldsymbol{\sigma}_E'\boldsymbol{D}'\rangle - \langle p'\operatorname{div}\boldsymbol{v}'\rangle, \quad \boldsymbol{\mathcal{P}} \equiv \langle p'\boldsymbol{v}'\rangle, \\ \boldsymbol{J}_\alpha \equiv \langle\boldsymbol{j}_\alpha\rangle + \rho\langle c_\alpha'\boldsymbol{v}'\rangle - \rho\langle c_\alpha'\boldsymbol{w}_\alpha^{s'}\rangle. \end{gathered} \tag{43}$$

In the subsequent analysis we will use equations (39)–(42), for which we assume the following closure relations:

(i) As in physical limnology, we take

$$\begin{gathered} \epsilon = c_v(T - T_0) + \epsilon_0, \quad h = c_p(T - T_0) + h_0, \\ c_v = \text{specific heat at constant volume}, \quad c_p = \text{specific heat at constant pressure}, \end{gathered} \tag{44}$$

where T is the absolute temperature, as expressions for the internal energy and enthalpy in the respective formulations; the specific heats c_v, c_p are assumed constant. For a thermodynamic justification of (44) or its generalization, see Appendix A.

(ii) The density ρ is taken as

$$\rho = \left(1 - \sum_{\alpha=1}^{N}\nu_\alpha\right)\rho_w(T,s) + \left(\sum_{\alpha=1}^{N}\nu_\alpha\right)\rho_s, \tag{45}$$

in which ν_α is the volume fraction of sediment α, $\rho_w(T,s)$ is the water density at temperature T and constant salinity s, and $\rho_s \approx 2100\,\mathrm{kg\,m^{-3}}$ is the buoyancy corrected density of the suspended sediment. Explicit formulae are e.g. given in (I, 10, p. 344ff)[13]. If the contribution of the mineralization is negligibly small, then

$$\begin{gathered} \rho_w = \rho_w(T) = \rho^*\left(1 - \tilde{\alpha}(T - T^*)^2\right), \\ \rho^* = 1000\,\mathrm{kg\,m^{-3}}, \quad T^* = 277^\circ\,\mathrm{K}, \quad \tilde{\alpha} = 6.493\times10^6\,\mathrm{K^{-2}}, \end{gathered} \tag{46}$$

is a useful quadratic approximation; ρ^* is the reference density of water at 4°C.

It was already mentioned that in very deep lakes of depth larger than approximately 500 m (Lake Baikal, Lake Tanganijka, Caspian Sea) the pressure dependence in the thermal equation of state should

[13] We shall refer to specific pages of [18] as (I, . . .).

not be ignored. This implies that (45) is replaced by

$$\rho = \left(1 - \sum_{\alpha=1}^{N} \nu_\alpha\right) \rho_w(T,s,p) + \left(\sum_{\alpha=1}^{N} \nu_\alpha\right) \rho_s\,, \tag{47}$$

in which the contribution of the pressure to ρ_w requires that the energy equation is used in the enthalpy formulation.

(iii) The specific energy production $\phi^{(T)}$, also called dissipation rate density, is deduced by assuming the Newtonian law for the dissipative stresses $\boldsymbol{\sigma}_E$. Thus, with $\boldsymbol{\sigma}_E = 2\rho\nu_\ell \boldsymbol{D}$, where ν_ℓ is the 'laminar' kinematic viscosity, $(43)_4$ yields

$$\begin{aligned}\phi^{(T)} = \quad & \underbrace{4\rho\nu_\ell\, II_{\langle \boldsymbol{D}\rangle}}_{\substack{\text{dissipation rate due}\\ \text{to the mean velocity}}} \quad + \quad \underbrace{4\rho\nu_\ell \langle II_{\boldsymbol{D}'}\rangle}_{\substack{\text{turbulent dissipation}\\ \text{rate } \rho\varepsilon}} \quad - \langle p' \mathrm{div}\, \boldsymbol{v}'\rangle \;= \\ & = \rho\left(4\nu_\ell II_{\langle \boldsymbol{D}\rangle} + \varepsilon\right) - \langle p' \mathrm{div}\, \boldsymbol{v}'\rangle\,,\end{aligned} \tag{48}$$

in which $II_{\boldsymbol{A}} \equiv \frac{1}{2}(\boldsymbol{A}\cdot\boldsymbol{A})$ is the second invariant of $\boldsymbol{A}$. Moreover, for $\langle p' \mathrm{div}\, \boldsymbol{v}'\rangle$ we assume

$$\langle p' \mathrm{div}\, \boldsymbol{v}'\rangle = \zeta_p \langle p\rangle \mathrm{div}\, \langle \boldsymbol{v}\rangle\,, \quad \zeta_p \approx 0\,, \tag{49}$$

while the turbulent dissipation rate ε will be later discussed, see (vii) below in this section.

(iv) For suspended particles of size range α we ignore fragmentation into other size ranges, so that we assume $\phi^{(c_\alpha)} = 0$.

(v) The second order tensor $\boldsymbol{R}$, and vectors $\boldsymbol{Q}_\epsilon$, $\boldsymbol{Q}_h$, $\boldsymbol{J}_\alpha$ $(\alpha = 1,\ldots,N)$ are combinations of the averaged laminar and the turbulent fluxes of momentum, energy and species masses, given by the following gradient type parameterizations:[14]

$$\begin{aligned}\frac{1}{\rho}\boldsymbol{R} &= 2\nu_\ell \boldsymbol{D} - \langle \boldsymbol{v}' \otimes \boldsymbol{v}'\rangle = -\tfrac{2}{3}k\boldsymbol{I} + 2\left(\nu_\ell + \nu_t\right)\boldsymbol{D},\\ \frac{1}{\rho^*[c_v]}\boldsymbol{Q}_\epsilon &= -\chi_\ell^{(T)} \mathrm{grad}\, T + \frac{\rho\, c_v}{\rho^*[c_v]}\langle T'\boldsymbol{v}'\rangle = -\left(\chi_\ell^{(T)} + \frac{\nu_t}{\sigma_T}\right)\mathrm{grad}\, T,\\ \frac{1}{\rho^*[c_p]}\boldsymbol{Q}_h &= -\chi_\ell^{(T)} \mathrm{grad}\; T + \frac{\rho\, c_p}{\rho^*[c_p]}\langle T'\boldsymbol{v}'\rangle = -\left(\chi_\ell^{(T)} + \frac{\nu_t}{\sigma_T}\right)\mathrm{grad}\; T\,,\\ \frac{1}{\rho^*}\boldsymbol{J}_\alpha &= -\chi_\ell^{(c_\alpha)} \mathrm{grad}\, c_\alpha + \frac{\rho}{\rho^*}\langle c'_\alpha \boldsymbol{v}'\rangle - \frac{\rho}{\rho^*}\langle c'_\alpha \boldsymbol{w}^{s'}_\alpha\rangle = \\ &\quad - \left(\chi_\ell^{(c_\alpha)} + \frac{\nu_t}{\sigma_{c_\alpha}}\right)\mathrm{grad}\, c_\alpha - \frac{\rho}{\rho^*}\langle c'_\alpha \boldsymbol{w}^{s'}_\alpha\rangle, \quad \alpha = 1,\ldots,N\,.\end{aligned} \tag{50}$$

[14] Parameterization $(50)_4$ does not account for cross dependences of the form

$$-\sum_{\beta=1}^{N} \lambda_{\alpha\beta}\left(\chi_\ell^{(c_\beta)} + \frac{\nu_t}{\sigma_{c_\beta}}\right)\mathrm{grad}\; c_\beta\,, \quad \alpha = 1,\ldots,N\,,$$

with $\lambda_{\alpha\beta} < 1$. Our selection in $(50)_4$ is $\lambda_{\alpha\beta} = \delta_{\alpha\beta}$. In principle the more general case is possible.

In $(50)_1$, k is the turbulent kinetic energy per unit mass[15] and ν_t is the turbulent kinematic viscosity; they will be parameterized below in this section. The quantities $[c_v]$ and $[c_p]$ arising in $(50)_{2,3}$ are typical values of the specific heats c_v, c_p. Then, in $(50)_{2-4}$ the FOURIER law for the heat flux $\boldsymbol{q}$ and the FICK law for the diffusive flux $\boldsymbol{j}_\alpha$ are understood, which explains the 'laminar' difussivities $\chi_\ell^{(T)}$, $\chi_\ell^{(c_\alpha)}$. Moreover, σ_T and σ_{c_α} are turbulent PRANDTL and SCHMIDT numbers; they are always assumed to be constant, which expresses a certain similarity between the diffusive processes of momentum, heat and species masses, which is generally not borne out experimentally. The coefficient of $\operatorname{grad} T$ in the representations $(50)_{2,3}$ is supposed to be the same; this choice is exact if $[c_v] = [c_p]$ is selected. Additionally, to differentiate the viscosities from the diffusivities in $(50)_{2,3,4}$ one often makes use of the replacements

$$\begin{aligned} \left(\chi_\ell^{(T)} + \frac{\nu_t}{\sigma_T}\right) \quad &\longrightarrow \quad D^{(T)} \\ \left(\chi_\ell^{(c_\alpha)} + \frac{\nu_t}{\sigma_{c_\alpha}}\right) \quad &\longrightarrow \quad D^{(c_\alpha)} \end{aligned} \tag{51}$$

and calls $D^{(T)}$ the thermal diffusivity and $D^{(c_\alpha)}$ the species diffusivities. We shall follow this custom. We will also use the interpretation

$$\nu_\ell + \nu_t \quad \longrightarrow \quad \nu_t$$

in $(50)_1$ and call the new ν_t – the kinematic turbulent viscosity. Finally, in the parameterization $(50)_4$ of $\boldsymbol{J}_\alpha$ we may assume

$$\langle c'_\alpha \boldsymbol{w}_\alpha^{s'} \rangle = \zeta \langle c_\alpha \rangle \langle \boldsymbol{w}_\alpha^s \rangle , \quad \zeta \approx 0 ,$$

as is the custom in the literature. Summarizing, for $\boldsymbol{R}$, $\boldsymbol{Q}_\epsilon$, $\boldsymbol{Q}_h$, $\boldsymbol{J}_\alpha$ we have the following closure relations:

$$\begin{aligned} \boldsymbol{R} &= -\tfrac{2}{3}\rho k \boldsymbol{I} + 2\rho\nu_t \boldsymbol{D} , \\ \boldsymbol{Q}_\epsilon = -\rho^* [c_v] D^{(T)} \operatorname{grad} T , \quad \boldsymbol{Q}_h &= -\rho^* [c_p] D^{(T)} \operatorname{grad} T , \\ \boldsymbol{J}_\alpha = -\rho^* D^{(c_\alpha)} \operatorname{grad} c_\alpha - \zeta \rho \langle c_\alpha \rangle \langle \boldsymbol{w}_\alpha^s \rangle , \quad &\zeta \approx 0 , \quad \alpha = 1, \ldots, N . \end{aligned} \tag{52}$$

(vi) For $\boldsymbol{w}_\alpha^s$ we assume (10), where expressions of the particle settling velocity w_α^s are discussed below in (vii).

(vii) Now, given numerical values for the laminar viscosity ν_ℓ, specific heats c_v, c_p, and diffusivities $D^{(T)}$, $D^{(c_\alpha)}$, the above model equations (39) - (52) must still be complemented by closure relations for ν_t, k, ε, w_α^s. The way of approach how this is done depends on the sophistication which is applied to the turbulent parameterization. When applying classical zeroth order closure schemes, algebraic parameterization for ν_t, k and ε are given; for higher order closure relations one or two equation models or full REYNOLDS models are suggested. Next we refer to such closure relations for ν_t, k and ε and then we review parameterizations for the particle settling velocity w_α^s.

Zeroth order, algebraic parameterization for ν_t, k and ε In (I, 6.2.6, p. 201ff), PRANDTL's eddy viscosity formula [34] was generalized and a proposal for the turbulent kinetic energy was given. Moreover, since dimensionally $[\varepsilon] = [k^{3/2}]/[\ell]$, where ℓ is a mixing length introduced by PRANDTL, the

[15] For a solenoidal velocity field it is often customary to incorporate the contribution of the turbulent kinetic energy k in relation $(50)_1$ into the pressure term, or to ignore it.

following propositions may be meaningful:

$$\begin{aligned} &\text{(I, 6.55)} \quad \nu_t = 2\ell^2\sqrt{II_{\boldsymbol{D}}}, \\ &\text{(I, 6.56)} \quad k = c_k 4\ell^2 II_{\boldsymbol{D}}, \\ &\text{(I, 6.57)} \quad \varepsilon = c_\varepsilon 8\ell^2 II_{\boldsymbol{D}}^{3/2}, \end{aligned} \tag{53}$$

where the third expression follows from $\varepsilon = \text{ const } \times k^{3/2}/\ell$. PRANDTL added a balance equation of the form (54), below, but this would correspond to a first order closure scheme. At zeroth order closure, ℓ is an adjustable constant scalar coefficient.

First order parameterization – the $(k-\varepsilon)$-model The most popular first order turbulence model is the so-called $(k-\varepsilon)$ *model*. Its full derivation is e.g. given by HUTTER & JÖHNK [17], Chap. 11, and a summary is given in I, 6. Here we give a short presentation of this model.

The most simple first order turbulent closure model is based on a differential equation for ℓ and was proposed by PRANDTL [34] as

$$\frac{\partial\,\ell}{\partial\,t} + \operatorname{div}\ell\boldsymbol{v} + 2\ell\sqrt{2} + \cdots = 0\,, \tag{54}$$

including the unspecified '$\cdots$', but was not pursued any further by him. We shall neither elaborate on this and will directly pass on to the standard turbulent two-equation model, which is the $(k-\varepsilon)$ model. It uses evolution equations for the specific turbulent kinetic energy k and the specific turbulent dissipation rate ε, and is based on the fact that $\nu_t,\ k$ and ε fulfil the dimensional identity $[\nu_t] = [k^2]/[\varepsilon]$, suggesting the parameterization

$$\nu_t = c_\mu \frac{k^2}{\varepsilon}\,, \tag{55}$$

in which c_μ is a dimensionless scalar, determined by inverse methods from experiments, but interpreted as a 'universal' constant. For k and ε balance laws are established,

$$\frac{\partial\,k}{\partial\,t} + \operatorname{div}(k\boldsymbol{v}) = -\operatorname{div}\boldsymbol{\phi}^k + \pi^k\,, \quad \frac{\partial\,\varepsilon}{\partial\,t} + \operatorname{div}(\varepsilon\boldsymbol{v}) = -\operatorname{div}\boldsymbol{\phi}^\varepsilon + \pi^\varepsilon\,,$$

in which the flux, $\boldsymbol{\phi}^k,\ \boldsymbol{\phi}^\varepsilon$, and production, $\pi^k,\ \pi^\varepsilon$, quantities must be parameterized. For a BOUSSINESQ fluid, these are proposed and adequately justified e.g. by HUTTER & JÖHNK [17] and also listed in I, 6, equations (I, 6.63)–(I, 6.65), to which the reader is referred. The fluxes have gradient closure form

$$\boldsymbol{\phi}^k = -\frac{\nu_t}{\sigma_k}\operatorname{grad}\,k, \quad \boldsymbol{\phi}^\varepsilon = -\frac{\nu_t}{\sigma_\varepsilon}\operatorname{grad}\,\varepsilon\,, \tag{56}$$

and the production terms are given by

$$\begin{aligned} \pi^k &= \operatorname{div}(\nu_\ell \operatorname{grad} k) + 4\nu_t II_{\boldsymbol{D}} - \varepsilon + \frac{\rho\alpha_T}{\rho^*}\frac{\nu_t}{\sigma_T}\,\boldsymbol{g}\cdot\operatorname{grad} T\,, \\ \pi^\varepsilon &= \operatorname{div}(\nu_\ell \operatorname{grad}\varepsilon) + 4c_1 k II_{\boldsymbol{D}} - c_2\frac{\varepsilon^2}{k} + c_3\frac{\rho\alpha_T}{\rho^*}\frac{c_\mu}{\sigma_T}\,k\,\boldsymbol{g}\cdot\operatorname{grad} T\,, \end{aligned} \tag{57}$$

in which α_T is the coefficient of thermal expansion of water and c_3 is small but not well constrained. Numerical values for the various closure constants are given in Table 1.

Table 1: Numerical values for the closure constants of the $(k-\varepsilon)$ model

$c_\mu = 0.09$	$c_1 = 0.126$	$c_2 = 1.92$	$c_3 \approx 0$	$\sigma_k = 1.4$	$\sigma_\varepsilon = 1.3$

Historically, the $(k-\varepsilon)$ model has originally been developed in the 1970s by HANJALIC & LAUNDER [14], JONES & LAUNDER [21] and LAUNDER & SPALDING [24]. RODI [35],[36] describes its applicability in geophysics and hydraulic engineering. Apart from the $(k-\varepsilon)$ model, other two-equation models have also been proposed. The $(k-\ell)$ and $(k-\omega)$ models use, besides the turbulent kinetic energy, a length – the PRANDTL mixing length, or the turbulent vorticity, ω, with dimension $[k/\ell^2]$. Expositions on these latter models are given by ROTTA [37] and WILCOX [51], [52]. For REYNOLDS stress parameterization by Large Eddy Simulation (LES), see Appendix B.

Particle settling velocity The fall velocity w_α^s is the remaining quantity of the above model, which has not been specified so far. It is an exhaustively treated subject of hydraulic research and still a topic of active on-going work. Its introduction in (42) and earlier equations, e.g. (10), is the fall velocity of particles in a specified size range under dynamic conditions of laminar or turbulent flow. Studies on the settling velocity are generally restricted to spherical particles in still water; but it is well known that the fall velocity of a non-buoyant particle in a fluid depends on both the particle shape and the flow state in the ambient fluid. This complex non-linear interaction is out of reach and physically too difficult for our purposes. Consequently, authors on this subject identify w_α^s with the terminal velocity of a free falling particle in still water, generally restricted to spheres or (unspecified) natural sediment particles. Here, we adopt this restricted view as well.

The ensuing description is based on the study by SONG et al. (2008) [42], who summarize earlier work and replace the different formulae by their own one. For an isolated spherical particle in a fluid at rest the settling velocity can be estimated by balancing the net gravitational force and the drag resistance,

$$\Delta\rho g\,\frac{\pi}{6}\,\mathfrak{d}_\alpha^3 = \frac{1}{2}\,\rho C_{\mathfrak{d}_\alpha}\,\frac{\pi}{4}\,\mathfrak{d}_\alpha^2 (w_\alpha^s)^2, \qquad \Delta \equiv \frac{\rho_s}{\rho} - 1, \tag{58}$$

where $\rho_s, \rho, g, \mathfrak{d}_\alpha, C_{\mathfrak{d}_\alpha}$ are the densities of the particle and the fluid, the acceleration due to gravity, the (nominal) diameter of a representative element in the sediment class α[16], and $C_{\mathfrak{d}_\alpha}$ is the drag coefficient; (58) can be written as

$$C_{\mathfrak{d}_\alpha} = \frac{4}{3}\,\frac{\Delta\, g\, \mathfrak{d}_\alpha}{(w_\alpha^s)^2}\,, \tag{59}$$

which is used to deduce the settling velocity w_α^s once the drag coefficient $C_{\mathfrak{d}_\alpha}$ is given as function of w_α^s. Thus, it is well known that, depending on the particle REYNOLDS number

$$Re_\alpha \equiv \frac{w_\alpha^s \mathfrak{d}_\alpha}{\nu}\,, \tag{60}$$

there are two asymptotic limits for the settling velocity: $C_{\mathfrak{d}_\alpha} = A/Re_\alpha$ when $Re_\alpha < 1$ (STOKES flow), and $C_{\mathfrak{d}_\alpha} = B$ when $10^5 < Re_\alpha < 2\times 10^5$ (turbulent flow), where A and B are constants, see any book

[16] Such a representative element in class α has already been used when defining the advected mass flux $\rho c_\alpha \boldsymbol{w}_\alpha^s$. To simplify the notation, we use $\mathfrak{d}_\alpha$ for the diameter of this grain particle; note that $\mathfrak{d}_\alpha \in [d_{\alpha-1}, d_\alpha)$, so that $\mathfrak{d}_\alpha$ should not be confused with d_α.

on fluid dynamics of viscous flow. Substituting these expressions into (59) implies

$$\begin{aligned} w_\alpha^s &= \frac{4}{3A}\,\frac{\Delta g\,\mathfrak{d}_\alpha^2}{\nu} \quad \text{for STOKES flow}\,, \\ w_\alpha^s &= \sqrt{\frac{4}{3B}\Delta g\,\mathfrak{d}_\alpha} \quad \text{for turbulent flow}\,. \end{aligned} \tag{61}$$

According to SONG et al. [42] most of the existing quasi-theoretical or semi-empirical formulae are based on the asymptotic solutions (61).[17] A smooth connection between the two asymptotic representations for $C_{\mathfrak{d}_\alpha}$ is e.g. reached by

$$C_{\mathfrak{d}_\alpha} = \left\{ \left(\frac{A}{Re_\alpha} \right)^{1/n} + B^{1/n} \right\}^n \tag{62}$$

(CHENG (1997) [8]). Indeed, as $Re_\alpha \to 0$, relation (62) implies $C_{\mathfrak{d}_\alpha} \approx A/Re_\alpha$; similarly, for $Re_\alpha \to \infty$, $C_{\mathfrak{d}_\alpha} \approx B$. Introducing the dimensionless particle diameter

$$\mathfrak{d}_\alpha^* \equiv \left(\frac{\Delta g}{\nu^2} \right)^{1/3} \mathfrak{d}_\alpha \tag{63}$$

into (59) and using the definition (60) for Re_α yields

$$C_{\mathfrak{d}_\alpha} = \frac{4}{3}\,\frac{(\mathfrak{d}_\alpha^*)^3}{(Re_\alpha)^2}\,. \tag{64}$$

Equating (62) to (64) leads to a quadratic equation for $(Re_\alpha)^{1/n}$, which can be solved; subsequently an explicit formula for w_α^s can be found via the definition of the REYNOLDS number. This is done by SONG et al [42]. Their formula reads

$$w_\alpha^s = \frac{\nu}{\mathfrak{d}_\alpha} \left\{ \sqrt{\frac{1}{4}\left(\frac{A}{B}\right)^{2/n} + \left(\frac{4}{3}\,\frac{(\mathfrak{d}_\alpha^*)^3}{B} \right)^{1/n}} - \frac{1}{2}\left(\frac{A}{B}\right)^{1/n} \right\}^n . \tag{65}$$

Various values for A, B and n that have been used by different authors for spherical particles and natural sediments are given. However, comparison of results with experiments is not satisfactory, and the disparate values for A, B and n, obtained by different authors make application of (65) cumbersome.

As an alternative, SONG et al. [42] restrict consideration to STOKES flow and choose $(61)_1$ to evaluate

$$Re_\alpha = \frac{w_\alpha^s \mathfrak{d}_\alpha}{\nu} = \frac{4}{3A}\,(\mathfrak{d}_\alpha^*)^3\,. \tag{66}$$

Somewhat surprisingly[18], they substitute this into (62), obtain

$$C_{\mathfrak{d}_\alpha} = \left\{ \left(\frac{\sqrt{3}A}{2(\mathfrak{d}_\alpha^*)^{3/2}} \right)^{2/n} + B^{1/n} \right\}^n , \tag{67}$$

[17] MCGAUHEY [27], ZANKE [56], CONCHA and ALMENDRA [9], TURTON & CLARK [45], ZHANG [58], JULIEN [22], SOULSBY [43], CHENG [8], AHRENS [1], GUO [13], JIMENEZ and MADSEN [20], BROWN & LAWLER [6], SHE et al. [38], CAMENEN [7].

[18] Formula (62) was proposed by CHENG [8] to match both asymptotic limits for STOKES *and* turbulent flows.

and using (64) deduce the settling velocity

$$w_\alpha^s = \frac{\nu}{\mathfrak{d}_\alpha}\mathfrak{d}_\alpha^* \left\{ \left(\frac{3A}{4}\right)^{2/n} + \left(\frac{3B}{4}\,(\mathfrak{d}_\alpha^*)^3\right)^{1/n} \right\}^{-n/2} . \tag{68}$$

SONG et al. [42] take experimental data by EGLUND and HANSEN [10] and CHENG [8] and determine A, B and n by least square error minimization; they found

$$A = 32.2\,, \quad B = 1.17\,, \quad n = 1.75\,,$$

and then, on substituting these into (68), obtained the following formula for w_α^s,

$$w_\alpha^s = \frac{\nu}{\mathfrak{d}_\alpha}\,(\mathfrak{d}_\alpha^*)^3 \left\{ 38.1 + 0.93\,(\mathfrak{d}_\alpha^*)^{12/7} \right\}^{-7/8} , \tag{69}$$

and listed alternative formulae of settling velocities by other scholars, viz.,

- ZHU & CHENG (1993) [59]

$$w_\alpha^s = \frac{\nu}{\mathfrak{d}_\alpha}(\mathfrak{d}_\alpha^*)^3 \left\{ \frac{1}{\sqrt{144\cos^6\beta + \left(4.5\cos^3\beta + 0.9\sin^2\beta\right)(\mathfrak{d}_\alpha^*)^3} + 12\cos^3\beta} \right\} ,$$
$$\beta = \begin{cases} 0\,, & \mathfrak{d}_\alpha^* \leqslant 1\,, \\ \pi\{2 + 2.5(\log \mathfrak{d}_\alpha^*)^{-3}\}^{-1}\,, & \mathfrak{d}_\alpha^* > 1\,. \end{cases} \tag{70}$$

- CHENG (1997) [8]

$$w_\alpha^s = \frac{\nu}{\mathfrak{d}_\alpha}\left(\sqrt{25 + 1.2(\mathfrak{d}_\alpha^*)^2} - 5\right)^{3/2} . \tag{71}$$

- AHRENS (2000) [1]

$$w_\alpha^s = \frac{\nu}{\mathfrak{d}_\alpha}(\mathfrak{d}_\alpha^*)^{3/2}\left(C_1(\mathfrak{d}_\alpha^*)^{3/2} + C_2\right) ,$$
$$C_1 = 0.055\tanh\left[12(\mathfrak{d}_\alpha^*)^{-1.77}\exp\left(-0.0004(\mathfrak{d}_\alpha^*)^3\right)\right] , \tag{72}$$
$$C_2 = 1.06\tanh\left[0.01(\mathfrak{d}_\alpha^*)^{1.5}\exp\left(-120/(\mathfrak{d}_\alpha^*)^3\right)\right] .$$

- GUO (2002) [13]

$$w_\alpha^s = \frac{\nu}{\mathfrak{d}_\alpha}(\mathfrak{d}_\alpha^*)^3\left[24 + \frac{\sqrt{3}}{2}(\mathfrak{d}_\alpha^*)^{3/2}\right]^{-1} . \tag{73}$$

- SHE et al. (2005) [38]

$$w_\alpha^s = 1.05\frac{\nu}{\mathfrak{d}_\alpha(\mathfrak{d}_\alpha^*)^{3/2}}\left[1 - \exp\left(-0.315(\mathfrak{d}_\alpha^*)^{0.765}\right)\right]^{2.2} . \tag{74}$$

Table 2 presents a comparison of calculated settling velocities using formulae (69)–(74) with the experimental data of ENGLUND & HANSEN (1972) [10] and CHENG (1997) [8]. The average value of

the relative error E and the standard deviation σ, defined as[19]

$$E = \frac{1}{N}\sum_{i=1}^{N}\left|\frac{(w_\alpha^s)^{\text{comp}}}{(w_\alpha^s)^{\text{exp}}} - 1\right| \times 100\%\,, \quad \sigma = \sqrt{\frac{1}{N}\sum_{i=1}^{N}\left|\frac{(w_\alpha^s)^{\text{comp}}}{(w_\alpha^s)^{\text{exp}}} - 1\right|^2} \times 100\%\,,$$

are listed in columns 2 and 3 of Table 2. It corroborates the best performance for (69). Even more convincing results are shown in the graphs of [42]. We therefore recommend to use (69).

Table 2: Fit accuracy of formulae (69)–(74) against experimental data by EGLUND & HANSEN [10], CHENG [8].

Equation Nr	*Error* $E(\%)$	*Standard deviation* $\sigma(\%)$
(69)	6.36	9.10
(70)	7.02	11.30
(71)	6.96	10.96
(72)	16.93	16.84
(73)	6.87	10.56
(74)	16.34	16.49

All these parameterizations enjoy the property that w_α^s does not depend on the flow dynamics of the slurry. It is, however, intuitively clear that the turbulent intensity may inhibit the free fall velocity. A bold account of this property may be the following choice

$$w_\alpha^s = \exp\left[-\left(\frac{k}{\sigma_k}\right)^2\right] \frac{\nu}{\mathfrak{d}_\alpha^*}(\mathfrak{d}_\alpha^*)^3 \left\{38.1 + 0.93(\mathfrak{d}_\alpha^*)^{12/7}\right\}^{-7/8}, \tag{75}$$

in which k is the turbulent kinetic energy and σ_k a standard deviation, chosen to be sufficiently small. This reduces the value of w_α^s whenever k is large, which is the case close to the free surface, in the metalimnion and immediately above the moving detritus. A dependence on the RICHARDSON number would be a competing alternative.

2.3 BOUSSINESQ and shallow water approximations in Model 2

In this section we simplify the equations characterizing Model 2 by using the Boussinesq assumption or/and the shallow water assumption. Thus, when written with respect to a Cartesian coordinate system with horizontal (x, y)-axes and vertical z-axis, the REYNOLDS averaged equations (39)–(42), are as follows:

- Balance of mass

$$\frac{\partial\,\rho}{\partial\,t} + \frac{\partial\,\rho\,u}{\partial\,x} + \frac{\partial\,\rho\,v}{\partial\,y} + \frac{\partial\,\rho\,w}{\partial\,z} = 0\,; \tag{76}$$

[19] N is the number of experimental points where values for $(w_\alpha^s)^{\text{exp}}$ have been measured.

- Balance of momentum

$$\begin{aligned}
\rho\left(\frac{\partial u}{\partial t}+u\frac{\partial u}{\partial x}+v\frac{\partial u}{\partial y}+w\frac{\partial u}{\partial z}+\tilde{f}w-fv\right) &= -\frac{\partial p}{\partial x}+\frac{\partial R_{xx}}{\partial x}+\frac{\partial R_{xy}}{\partial y}+\frac{\partial R_{xz}}{\partial z}\,;\\
\rho\left(\frac{\partial v}{\partial t}+u\frac{\partial v}{\partial x}+v\frac{\partial v}{\partial y}+w\frac{\partial v}{\partial z}+fu\right) &= -\frac{\partial p}{\partial y}+\frac{\partial R_{yx}}{\partial x}+\frac{\partial R_{yy}}{\partial y}+\frac{\partial R_{yz}}{\partial z}\,;\\
\rho\left(\frac{\partial w}{\partial t}+u\frac{\partial w}{\partial x}+v\frac{\partial w}{\partial y}+w\frac{\partial w}{\partial z}-\tilde{f}u\right) &= -\frac{\partial p}{\partial z}+\frac{\partial R_{zx}}{\partial x}+\frac{\partial R_{zy}}{\partial y}+\frac{\partial R_{zz}}{\partial z}-\rho g\,;
\end{aligned} \tag{77}$$

- Balance of energy

$$\begin{aligned}
\rho c_v\left(\frac{\partial T}{\partial t}+u\frac{\partial T}{\partial x}+v\frac{\partial T}{\partial y}+w\frac{\partial T}{\partial z}\right) &= -p\left(\frac{\partial u}{\partial x}+\frac{\partial v}{\partial y}+\frac{\partial w}{\partial z}\right)\\
&\quad -\left(\frac{\partial Q_x^\epsilon}{\partial x}+\frac{\partial Q_y^\epsilon}{\partial y}+\frac{\partial Q_z^\epsilon}{\partial z}\right)+\phi^{(T)}\,;
\end{aligned} \tag{78}$$

$$\begin{aligned}
&\rho c_p\left(\frac{\partial T}{\partial t}+u\frac{\partial T}{\partial x}+v\frac{\partial T}{\partial y}+w\frac{\partial T}{\partial z}\right)-\frac{\mathrm{d}p}{\mathrm{d}t}\\
&\quad=-\left(\frac{\partial Q_x^h}{\partial x}+\frac{\partial Q_y^h}{\partial y}+\frac{\partial Q_z^h}{\partial z}\right)+\left(\frac{\partial \mathcal{P}_x}{\partial x}+\frac{\partial \mathcal{P}_y}{\partial y}+\frac{\partial \mathcal{P}_z}{\partial z}\right)+\phi^{(T)}\,;
\end{aligned} \tag{79}$$

- Balance of species mass[20]

$$\begin{aligned}
\rho\left(\frac{\partial c_\alpha}{\partial t}+u\frac{\partial c_\alpha}{\partial x}+v\frac{\partial c_\alpha}{\partial y}+w\frac{\partial c_\alpha}{\partial z}\right) &= -\frac{\partial J_{\alpha x}}{\partial x}-\frac{\partial J_{\alpha y}}{\partial y}-\frac{\partial J_{\alpha z}}{\partial z}+\\
&\quad \frac{\partial}{\partial z}(\rho\, c_\alpha w_\alpha^s)+\phi^{(c_\alpha)}\,,\quad \alpha=1,\ldots,N\,.
\end{aligned} \tag{80}$$

In these equations u, v, w are the Cartesian velocity components in the x, y, z directions, $Q_x^{\epsilon,h}, Q_y^{\epsilon,h}, Q_z^{\epsilon,h}$ are the Cartesian components of the heat flux vectors in the internal energy and enthalpy formulations, respectively; moreover, $J_{\alpha x}, J_{\alpha y}, J_{\alpha z}$ are the Cartesian components of $\boldsymbol{J}_\alpha$, and f, $\tilde{f}$ are the first and second CORIOLIS parameters,

$$f = 2\Omega\,\sin\varphi,\quad \tilde{f} = 2\Omega\,\cos\varphi, \tag{81}$$

in which $\Omega \equiv \|\boldsymbol{\Omega}\|$ is the angular velocity of the Earth ($\Omega = 7.272\times10^{-5}$ [s^{-1}]) and φ is the latitude angle. Writing (76)–(80) one has made use of the closure assumptions (10), (44).

It is now assumed that the typical processes have large horizontal but small vertical scales. For instance, typical horizontal scales of water disturbances are often many kilometers, while the corresponding depth variations are generally tens of meters and less; similarly, horizontal velocity components are generally large, while corresponding vertical velocity components are a factor of 10^{-3} smaller. This

[20]This equation holds with $\boldsymbol{w}_\alpha^s = w_\alpha^s \boldsymbol{e}_z$. If $\boldsymbol{w}_\alpha^s$ is parameterized as in equation (11), then

$$\frac{\partial}{\partial x}(\rho\, c_\alpha w_\alpha^s \tan\theta\cos\xi)+\frac{\partial}{\partial y}(\rho\, c_\alpha w_\alpha^s \tan\theta\sin\xi)$$

must be added to the right-hand side of equation (80). Here, ξ is the angle between the x-axis and $\boldsymbol{v}_H$.

suggests to introduce the aspect ratios [21]

$$\mathcal{A}_L \equiv \frac{\text{typical vertical length scale}}{\text{typical horizontal length scale}} = \frac{[H]}{[L]},$$
$$\mathcal{A}_V \equiv \frac{\text{typical vertical velocity scale}}{\text{typical horizontal velocity scale}} = \frac{[W]}{[V]},$$

to substitute these into the governing field equations, to suppose that

$$0 < \mathcal{A}_L = \mathcal{A}_V \equiv \mathcal{A} \ll 1,$$

and to look at the governing equations in the limit as $\mathcal{A} \to 0$.

To compare the various terms arising in the governing equations, each quantity, say Ψ, is written in the form $\Psi = [\Psi]\overline{\Psi}$, where $[\Psi]$ is the scale for Ψ (and has the physical units of Ψ) and $\overline{\Psi}$ is dimensionless and of the order of unity if the value for $[\Psi]$ is correctly selected. The procedure is well known and is e.g. demonstrated in [18], p. 150–154. We shall select the scales according to

$$\begin{gathered}
(x,y,z) = ([L]\,\overline{x},\ [L]\,\overline{y},\ [H]\,\overline{z}\,), \quad (t,f,\tilde{f}) = \left(\frac{1}{[f]}\,\overline{t}\,,\ [f]\overline{f},\ [f]\overline{\tilde{f}}\right), \\
(u,v,w,w_\alpha^s) = \left([V]\,\overline{u},\ [V]\,\overline{v},\ \frac{[H]}{[L]}[V]\,\overline{w},\ \frac{[H]}{[L]}[V]\,\overline{w_\alpha^s}\right), \\
\rho = \rho^*\,(1 + [\sigma]\,\overline{\sigma}\,), \quad p = -\rho^* g z + \rho^*[f][V][L]\,\overline{p}\,, \\
T = T_0 + [\Delta T]\,\overline{T}\,, \quad c_\alpha = [c_\alpha]\,\overline{c_\alpha}\,, \quad c_v = [c_v]\,\overline{c_v}\,, \quad c_p = [c_p]\,\overline{c_p}\,, \\
\phi^{(T)} = [\phi^{(T)}]\overline{\phi^{(T)}}\,, \qquad \phi^{(c_\alpha)} = [\phi^{(c_\alpha)}]\overline{\phi^{(c_\alpha)}}\,, \quad \boldsymbol{\mathcal{P}} = \rho^*[c_p][f][H][\Delta T]\,\overline{\boldsymbol{\mathcal{P}}}\,.
\end{gathered} \tag{82}$$

Moreover, we introduce the kinematic turbulent viscosity, $\mathcal{N}$, heat diffusivity, $\mathcal{D}^{(T)}$, and species mass diffusivity, $\mathcal{D}^{(c_\alpha)}$, by

$$\nu_t = [f][H^2]\mathcal{N}\,, \quad D^{(T)} = [f][H^2]\mathcal{D}^{(T)}\,, \quad D^{(c_\alpha)} = [f][H^2]\mathcal{D}^{(c_\alpha)}\,. \tag{83}$$

After some lengthy but straightforward calculations and with the assumption $\boldsymbol{R} = 2\rho\,\nu_t\,\boldsymbol{D}$ for the turbulent REYNOLDS stress[22], the field equations (76)–(80) take the following forms (the overbars characterizing dimensionless quantities are omitted):

- Balance of mass

$$\frac{[\sigma]}{\mathcal{R}o}\frac{\partial\,\sigma}{\partial\,t} + \operatorname{div}\boldsymbol{v} + [\sigma]\operatorname{div}(\sigma\boldsymbol{v}) = 0\,; \tag{84}$$

[21] The symbol $[f]$ denotes an order of magnitude for the quantity f within the range of values which f may assume (in the physical dimensions in which it is expressed) in the processes under consideration.

[22] We neglect the contribution of the turbulent kinetic energy in $(52)_1$.

Table 3: Physical parameters and typical orders of magnitude for the scales in (82)

Parameter	*Order of magnitude*	*Nomenclature*
ρ^*	$10^3\,\mathrm{kg\,m^{-3}}$	Reference density at 4°C
$[\sigma]$	$\approx 10^{-3}$	Density anomaly
$[L]$	$\approx 10^4 - 10^6\,\mathrm{m}$	Horizontal length scale
$[H]$	$\approx 10^1 - 10^3\,\mathrm{m}$	Vertical length scale
$[V]$	$\approx 10^{-2} - 10^1\,\mathrm{m\,s^{-1}}$	Horizontal velocity scale
$[f]$	$\approx 10^{-4}\,\mathrm{s^{-1}}$	CORIOLIS parameter
T_0	$\approx 10^\circ\,\mathrm{C}$	Reference temperature
$[\Delta T]$	$\approx 10^\circ\,\mathrm{C}$	Temperature range
$[c_v]$	$\approx 4200\,\mathrm{m^2\,s^{-2}\,K^{-1}}$	Specific heat at constant volume
$[c_p]$	$\approx 4200\,\mathrm{m^2\,s^{-2}\,K^{-1}}$	Specific heat at constant pressure
$[c_\alpha]$	$\approx 10^{-3} - 10^{-1}$	Scale for mass fraction of tracer α
$[\phi^{(T)}]$		Scale for energy production
$[\phi^{(c_\alpha)}]$		Scale for production of tracer α

- Balance of momentum

$$
\begin{aligned}
(1+[\sigma]\sigma)\left\{\frac{\partial u}{\partial t}+\mathcal{R}o\,(\mathrm{grad}\ u)\cdot\boldsymbol{v}+\mathcal{A}\tilde{f}w-fv\right\} &= -\frac{\partial p}{\partial x}+\\
\mathcal{A}^2\left\{2\frac{\partial}{\partial x}\left[(1+[\sigma]\sigma)\mathcal{N}\frac{\partial u}{\partial x}\right]+\frac{\partial}{\partial y}\left[(1+[\sigma]\sigma)\mathcal{N}\left(\frac{\partial u}{\partial y}+\frac{\partial v}{\partial x}\right)\right]\right\}+&\\
\frac{\partial}{\partial z}\left[(1+[\sigma]\sigma)\mathcal{N}\left(\frac{\partial u}{\partial z}+\mathcal{A}^2\frac{\partial w}{\partial x}\right)\right],&
\end{aligned}
\tag{85}
$$

$$
\begin{aligned}
(1+[\sigma]\sigma)\left\{\frac{\partial v}{\partial t}+\mathcal{R}o\,(\mathrm{grad}\ v)\cdot\boldsymbol{v}+fu\right\} &= -\frac{\partial p}{\partial y}+\\
\mathcal{A}^2\left\{\frac{\partial}{\partial x}\left[(1+[\sigma]\sigma)\mathcal{N}\left(\frac{\partial u}{\partial y}+\frac{\partial v}{\partial x}\right)\right]+2\frac{\partial}{\partial y}\left[(1+[\sigma]\sigma)\mathcal{N}\frac{\partial v}{\partial y}\right]\right\}+&\\
\frac{\partial}{\partial z}\left[(1+[\sigma]\sigma)\mathcal{N}\left(\frac{\partial v}{\partial z}+\mathcal{A}^2\frac{\partial w}{\partial y}\right)\right],&
\end{aligned}
\tag{86}
$$

$$
\begin{aligned}
(1+[\sigma]\sigma)\left\{\mathcal{A}^2\left[\frac{\partial w}{\partial t}+\mathcal{R}o\,(\mathrm{grad}\ w)\cdot\boldsymbol{v}\right]-\mathcal{A}\tilde{f}u\right\} &= -\frac{\partial p}{\partial z}+\\
\mathcal{A}^2\frac{\partial}{\partial x}\left[(1+[\sigma]\sigma)\mathcal{N}\left(\frac{\partial u}{\partial z}+\mathcal{A}^2\frac{\partial w}{\partial x}\right)\right]+&\\
\mathcal{A}^2\frac{\partial}{\partial y}\left[(1+[\sigma]\sigma)\mathcal{N}\left(\frac{\partial v}{\partial z}+\mathcal{A}^2\frac{\partial w}{\partial y}\right)\right]+2\mathcal{A}^2\frac{\partial}{\partial z}\left[(1+[\sigma]\sigma)\mathcal{N}\frac{\partial w}{\partial z}\right]-\mathcal{B}\sigma\,;&
\end{aligned}
\tag{87}
$$

- Balance of energy

$$c_v(1+[\sigma]\sigma)\left\{\frac{\partial T}{\partial t}+\mathcal{R}o\,(\mathrm{grad}\,T)\cdot\boldsymbol{v}\right\}=-\mathcal{F}\left(-\frac{\mathcal{B}}{[\sigma]}\,z+p\right)\mathrm{div}\,\boldsymbol{v}+ \\ \mathcal{A}^2\left[\frac{\partial}{\partial x}\left(\mathcal{D}^{(T)}\frac{\partial T}{\partial x}\right)+\frac{\partial}{\partial y}\left(\mathcal{D}^{(T)}\frac{\partial T}{\partial y}\right)\right]+\frac{\partial}{\partial z}\left(\mathcal{D}^{(T)}\frac{\partial T}{\partial z}\right)+\mathcal{P}_\epsilon^{(T)}\phi^{(T)}\,, \tag{88}$$

$$c_p(1+[\sigma]\sigma)\left\{\frac{\partial T}{\partial t}+\mathcal{R}o(\mathrm{grad}\;T)\cdot\boldsymbol{v}\right\}-\Pi\left\{\frac{\partial p}{\partial t}+\mathcal{R}o(\mathrm{grad}\;p)\cdot\boldsymbol{v}-\mathcal{G}\,w\right\} \\ =\mathcal{A}^2\left[\frac{\partial}{\partial x}\left(\mathcal{D}^{(T)}\frac{\partial T}{\partial x}\right)+\frac{\partial}{\partial y}\left(\mathcal{D}^{(T)}\frac{\partial T}{\partial y}\right)\right]+\frac{\partial}{\partial z}\left(\mathcal{D}^{(T)}\frac{\partial T}{\partial z}\right) \\ +\mathcal{A}\left[\frac{\partial\mathcal{P}_x}{\partial x}+\frac{\partial\mathcal{P}_y}{\partial y}\right]+\frac{\partial\mathcal{P}_z}{\partial z}+\mathcal{P}_h^{(T)}\phi^{(T)}\,; \tag{89}$$

- Balance of tracer mass

$$(1+[\sigma]\sigma)\left\{\frac{\partial c_\alpha}{\partial t}+\mathcal{R}o\,(\mathrm{grad}\,c_\alpha)\cdot\boldsymbol{v}\right\}=\mathcal{A}^2\left[\frac{\partial}{\partial x}\left(\mathcal{D}^{(c_\alpha)}\frac{\partial c_\alpha}{\partial x}\right)+\frac{\partial}{\partial y}\left(\mathcal{D}^{(c_\alpha)}\frac{\partial c_\alpha}{\partial y}\right)\right] \\ +\frac{\partial}{\partial z}\left(\mathcal{D}^{(c_\alpha)}\frac{\partial c_\alpha}{\partial z}\right)+\mathcal{R}o\frac{\partial}{\partial z}\left\{(1+[\sigma]\sigma)\,c_\alpha w_\alpha^s\right\}+\mathcal{P}^{(c_\alpha)}\phi^{(c_\alpha)}\,. \tag{90}$$

In these equations all variables, including the operators, are dimensionless. The dimensionless parameters arising in equations (84)–(90) are listed in Table 4 together with their nomenclature and (some) together with their orders of magnitude as obtained with the scales of Table 3. Note that the buoyancy parameter may also be written as

$$\mathcal{B}=\frac{\mathcal{A}[\sigma]g}{[f][V]}\,,$$

and thus depends linearly on the aspect ratio $\mathcal{A}$, but it is not thought to take the limit value 0 as $\mathcal{A}\to 0$. It is rather assumed that $\mathcal{B}$ assumes a finite value as $\mathcal{A}$ becomes vanishingly small. This is indeed the only correct limit as long as gravity is acting as one of the driving mechanism. This is also the reason why $\mathcal{A}$ has not been put in evidence in the expression of $\mathcal{B}$ in Table 4. Special attention should also be devoted to certain combinations of the dimensionless quantities of Table 3 as they occur in the energy equations (88) and (89). One of these is

$$\frac{\mathcal{B}\mathcal{F}}{[\sigma]}=\frac{g\mathcal{A}[V]}{[f][c_v][\Delta T]}\approx 0.25\times(10^3-10^5)\,. \tag{91}$$

Note that, while $\mathcal{B}$ arises together with $[\sigma]$, the combination $\mathcal{B}\mathcal{F}/[\sigma]$ is free of $[\sigma]$. On the other hand, $\mathcal{F}$ by itself is much smaller than (91). This shows (see the term multiplied with $\mathrm{div}\,\boldsymbol{v}$ on the right-hand side of (88)) that the power of working due to the dynamic pressure is much smaller than the corresponding power due to the hydrostatic pressure. An analogous inference also follows from the corresponding term in (89). Here, it can be shown that $\Pi=\mathcal{O}(10^{-7}-10^{-2})$, while $\mathcal{G}\Pi=\mathcal{O}(10^{-7}-10^{-1})$ is generally somewhat larger, but it is not so clear whether the dynamic or the static pressure or both or none ought to be kept in the equation.

In the present context, our interest is in orders of magnitude of numerical values for the parameters $[\sigma]$ and $\mathcal{A}$. This information suggests derivation of approximate models:

Table 4: Dimensionless parameters

Parameter	*Order of magnitude*	*Name*
$\mathcal{A} = \dfrac{[H]}{[L]}$	$10^{-5} - 10^{-2}$	Aspect ratio
$\mathcal{B} = \dfrac{g[\sigma][H]}{[f][L][V]}$	$10^{-2} - 10^{2}$	Buoyancy parameter
$\mathcal{D}^{(T)} = \dfrac{D^{(T)}}{[f][H^2]}$	$10^{-4} - 10^{0}$	Heat diffusivity
$\mathcal{D}^{(c_\alpha)} = \dfrac{D^{(c_\alpha)}}{[f][H^2]}$	$10^{-4} - 10^{0}$	Species mass diffusivity
$\mathcal{F} = \dfrac{[V^2]}{[c_v][\Delta T]}$	$10^{-7} - 10^{-1}$	Pressure work parameter
$\mathcal{G} = \dfrac{g[H]}{[f^2][L^2]}$	$10^{0} - 10^{3}$	Squared velocity ratio
$\mathcal{N} = \dfrac{\nu_t}{[f][H^2]}$	$10^{-6} - 10^{1}$	Dimensionless kinematic turbulent viscosity
$\Pi = \dfrac{[f][L][V]}{[c_p][\Delta T]}$	$10^{-7} - 10^{-2}$	Pressure work parameter
$\mathcal{P}_{\epsilon}^{(T)} = \dfrac{[\phi^{(T)}]}{\rho^*[f][c_v][\Delta T]}$		Power working parameter
$\mathcal{P}_{h}^{(T)} = \dfrac{[\phi^{(T)}]}{\rho^*[f][c_p][\Delta T]}$		Power working parameter
$\mathcal{P}^{(c_\alpha)} = \dfrac{[\phi^{(c_\alpha)}]}{\rho^*[f][c_\alpha]}$		Constituent mass production parameter
$\mathcal{R}o = \dfrac{[V]}{[f][L]}$	$10^{-4} - 10^{0}$	ROSSBY number

BOUSSINESQ **approximation** The BOUSSINESQ approximation obtains if the limiting equations are used for which $[\sigma] \to 0$. Inspection of (84)–(90) shows that in this case the variable density is set equal to a constant except in the gravity term. The only term of concern is the combination (91) which shows that the limit $[\sigma] \to 0$ does not affect the values for $\mathcal{BF}/[\sigma]$. Nevertheless the value for (91) is generally large, a fact which explicitly indicates that the power of working due to the hydrostatic pressure may not be negligible at large depths, whereas the corresponding dynamic contribution may be negligible. In any case, these terms can only contribute when the velocity field is not solenoidal, i. e., when

$$\lim_{[\sigma]\to 0} \frac{[\sigma]}{\mathcal{R}o} = \mathcal{O}(1)\,,$$

for which the first term of (84) survives. Except for these cases the mass balance equation reduces to $\operatorname{div} \boldsymbol{v} = 0$, which agrees with the continuity equation of a density preserving fluid even though density variations are accounted for.

Shallow water approximation The shallow water approximation is obtained if equations (84)–(90) are applied in the limit as $\mathcal{A} \to 0$. Inspection of (84)–(90) then implies the following inferences:

- The second CORIOLIS parameter drops out of the equations. It enters the equations only when $\mathcal{O}(\mathcal{A})$-terms are kept.
- The vertical momentum balance reduces to a force balance between the vertical pressure gradient and the gravity force (in dimensionless formulation):

$$\frac{\partial\, p}{\partial\, z} + \mathcal{B}\sigma = 0\,, \tag{92}$$

  or, in dimensional coordinates,

$$\frac{\partial\, p}{\partial\, z} + \rho\, g = 0\,, \tag{93}$$

  equivalent to the hydrostatic pressure assumption. This equation is violated provided $\mathcal{O}(\mathcal{A})$ or higher order terms are accounted for.
- In the balance equations of momentum, energy and species masses, only the vertical gradients of the flux terms survive. This means:

$$\begin{aligned}
\frac{\partial}{\partial\, z}\left[(1+[\sigma]\sigma)\,\mathcal{N}\,\frac{\partial\, u}{\partial\, z}\right] &\quad\longleftrightarrow\quad \frac{\partial R_{xz}}{\partial\, z}\,,\\
\frac{\partial}{\partial\, z}\left[(1+[\sigma]\sigma)\,\mathcal{N}\,\frac{\partial\, v}{\partial\, z}\right] &\quad\longleftrightarrow\quad \frac{\partial R_{yz}}{\partial\, z}\,,\\
\frac{\partial}{\partial\, z}\left(\mathcal{D}^{(T)}\,\frac{\partial\, T}{\partial\, z}\right) &\quad\longleftrightarrow\quad \frac{\partial Q_z^{\varepsilon}}{\partial\, z}\\
\frac{\partial}{\partial\, z}\left(\mathcal{D}^{(c_\alpha)}\,\frac{\partial\, c_\alpha}{\partial\, z}\right) + \mathcal{R}o\frac{\partial}{\partial z}\left\{(1+[\sigma]\sigma)\,c_\alpha w_\alpha^s\right\} &\quad\longleftrightarrow\quad \frac{\partial}{\partial\, z}\left(-J_{\alpha z} + \rho c_\alpha w_\alpha^s\right)\,,
\end{aligned}$$

  are the only flux terms which contribute in the shallow water approximation to the field equations. This is a well-established result in Geophysical Fluid Mechanics.

BOUSSINESQ **and shallow water approximation** The governing equations in both the BOUSSINESQ assumption, $[\sigma] \to 0$, and the shallow water assumption, $\mathcal{A} \to 0$, are obtained from (84) – (90) and have the following forms in dimensional notation:

- Balance of mass (continuity equation)

$$\operatorname{div} \boldsymbol{v} = 0\,; \tag{94}$$

- Balance of momentum

$$\begin{aligned} \frac{\partial u}{\partial t} + (\operatorname{grad} u)\cdot\boldsymbol{v} - fv &= -\frac{1}{\rho^*}\frac{\partial p}{\partial x} + \frac{\partial}{\partial z}\left(\nu_t \frac{\partial u}{\partial z}\right), \\ \frac{\partial v}{\partial t} + (\operatorname{grad} v)\cdot\boldsymbol{v} + fu &= -\frac{1}{\rho^*}\frac{\partial p}{\partial y} + \frac{\partial}{\partial z}\left(\nu_t \frac{\partial v}{\partial z}\right), \\ 0 &= \frac{1}{\rho^*}\frac{\partial p}{\partial z} + g\,; \end{aligned} \tag{95}$$

- Balance of energy (heat conduction equation)

$$\rho^* c_v \left\{\frac{\partial T}{\partial t} + (\operatorname{grad} T)\cdot\boldsymbol{v}\right\} = \rho^*[c_v]\frac{\partial}{\partial z}\left(D^{(T)}\frac{\partial T}{\partial z}\right) + \phi^{(T)}\,, \tag{96}$$

$$\begin{aligned} \rho^* c_p \left\{\frac{\partial T}{\partial t} + (\operatorname{grad} T)\cdot\boldsymbol{v}\right\} = -\left\{\frac{\partial p}{\partial t} + \operatorname{grad} p\cdot\boldsymbol{v}\right\} + \\ \rho^*[c_p]\frac{\partial}{\partial z}\left(D^{(T)}\frac{\partial T}{\partial z}\right) + \frac{\partial \mathcal{P}_z}{\partial z} + \phi^{(T)}\,; \end{aligned} \tag{97}$$

- Balance of tracer mass

$$\begin{aligned} \rho^*\left\{\frac{\partial c_\alpha}{\partial t} + (\operatorname{grad} c_\alpha)\cdot\boldsymbol{v}\right\} = \rho^*\frac{\partial}{\partial z}\left(D^{(c_\alpha)}\frac{\partial c_\alpha}{\partial z}\right) + \rho^*\frac{\partial}{\partial z}(c_\alpha w_\alpha^s) + \phi^{(c_\alpha)}\,, \\ \alpha = 1,\ldots,N\,. \end{aligned} \tag{98}$$

In the above equations, ν_t stands for the sum of the laminar plus turbulent viscosities, the former can in general be ignored in comparison to the latter, but is better included when the turbulent viscosity should become small; c_v is the heat capacity of water at constant volume and c_p is the heat capacity of water at constant pressure, while $D^{(c_\alpha)}$ is the mass diffusivity of the suspended particles of the size range α. Moreover, $\phi^{(T)}$ is the dissipative work power and $\phi^{(c_\alpha)}$ the mass production rate of the particles of size range α. Both are generally ignored in sedimentation processes in lakes.[23]

2.4 BOUSSINESQ and hydrostatic pressure assumption in Model 2

In a comparison with (84)–(90) equations (94)–(98) show that in the shallow water approximation the horizontal diffusive flux terms are all dropped in a zeroth order shallowness approximation ($\mathcal{A} \to 0$). Inspection of (84)–(90) further shows that these terms are $\mathcal{O}(\mathcal{A}^2)$. Resurrection of the horizontal flux terms in the balance laws of momentum, energy and constituent masses therefore strictly means that the

[23] $\phi^{(c_\alpha)}$ could consist of fragmentation and abrasion of suspended particles, which, however, are unlikely processes.

full equations (84)–(90) must be kept and only be reduced by the BOUSSINESQ approximation $[\sigma] \to 0$. However, as shown by (87), the hydrostatic pressure assumption can not be maintained if the $\mathcal{O}(\mathcal{A}^2)$-terms are kept in the remaining field equations. Moreover, since the Coriolis terms in (85)–(87) are of $\mathcal{O}(\mathcal{A})$, these terms should also be kept (the $\tilde{f}$ term in (85) and (87)!). Nevertheless, in the literature equations are used in which the BOUSSINESQ approximation is combined with the hydrostatic pressure assumption. A derivation from a systematic scaling analysis is not known to us, but the following suppositions lead to the very popular system of field equations in the BOUSSINESQ and hydrostatic pressure approximations:

Hydrostatic pressure assumption: Ignore in the vertical momentum equation (87) all acceleration and diffusive terms and keep only those of zeroth order in $\mathcal{A}$.

This hypothesis reduces (87) to (92) or, in dimensional form, to equation (93). Writing the latter as

$$\frac{\partial p}{\partial z} = -\rho^{**} g + g(\rho^{**} - \rho) = -\rho^{**} g - \rho^{**} g \sigma(x,y,z,t)\,, \quad \sigma(x,y,z,t) \equiv \frac{\rho(x,y,z,t)}{\rho^{**}} - 1\,, \tag{99}$$

after integration we obtain

$$p(x,y,z,t) = \underbrace{\rho^{**} g\,(\zeta(x,y,t) - z) + p^{\text{atm}}(x,y,t)}_{p^{\text{ext}}} + \underbrace{\rho^{**} g \int_z^{\zeta(x,y,t)} \sigma(\cdot,\bar{z})\, d\bar{z}}_{p^{\text{int}}}\,. \tag{100}$$

Here, ρ^{**} is a constant density (smaller than any density in the lake, e.g., $\rho^{**} = \rho(30^\circ\text{C})$, so that $\sigma > 0$), $z = \zeta(x,y,t)$ defines the deformed free surface, and p^{atm} is the atmospheric pressure. In lake applications one usually assumes that p^{atm} is spatially constant. The derivatives of (100),

$$\begin{aligned} \frac{\partial p}{\partial x} &= \rho^{**} g \frac{\partial \zeta}{\partial x} + \frac{\partial p^{\text{atm}}}{\partial x} + \rho^{**} g \frac{\partial}{\partial x} \int_z^{\zeta(x,y,t)} \sigma(x,y,\bar{z},t)\, d\bar{z}\,, \\ \frac{\partial p}{\partial y} &= \rho^{**} g \frac{\partial \zeta}{\partial y} + \frac{\partial p^{\text{atm}}}{\partial y} + \rho^{**} g \frac{\partial}{\partial y} \int_z^{\zeta(x,y,t)} \sigma(x,y,\bar{z},t)\, d\bar{z}\,, \end{aligned} \tag{101}$$

may then be substituted into (85), (86) to eliminate the pressure formally as a variable from the horizontal momentum equations.

In oceanography the hydrostatic pressure assumption is often combined with other ad hoc assumptions, which can not be motivated by the shallow water assumption. These assumptions are the following:

- Assume the horizontal diffusivities in the horizontal momentum equations to be large of $\mathcal{O}(\mathcal{A}^{-2})$ and *constant*, and the vertical diffusivities to be variable and of $\mathcal{O}(1)$:
  - horizontal momentum diffusivities: $\mathcal{N} \to \mathcal{N}_{\text{hor}}/\mathcal{A}^2$ and constant;
  - vertical momentum diffusivities: $\mathcal{N} \to \mathcal{N}_{\text{vert}}(x,y,z,t)$.
- Assume in the energy and constituent mass balances the horizontal diffusivities to be large of $\mathcal{O}(\mathcal{A}^{-2})$:
  - horizontal energy diffusivities: $\mathcal{D}^{(T)} \to \mathcal{D}^{(T)}_{\text{hor}}/\mathcal{A}^2$;

– vertical energy diffusivities: $\mathcal{D}^{(T)} \to \mathcal{D}^{(T)}_{\text{vert}}$;

– horizontal constituent mass diffusivities: $\mathcal{D}^{(c_\alpha)} \to \mathcal{D}^{(c_\alpha)}_{\text{hor}}/\mathcal{A}^2$;

– vertical constituent mass diffusivities: $\mathcal{D}^{(c_\alpha)} \to \mathcal{D}^{(c_\alpha)}_{\text{vert}}$.

If these assumptions are substituted into (84)–(90) and the limits $\mathcal{A} \to 0$ and $[\sigma] \to 0$ are taken, the following system of equations (in physical dimensions) emerges:

- Balance of mass:

$$\operatorname{div} \boldsymbol{v} = 0\,; \tag{102}$$

- Balance of momentum:

$$\begin{aligned}\frac{\partial u}{\partial t} + (\operatorname{grad} u)\cdot \boldsymbol{v} - fu = -\frac{1}{\rho_*}\frac{\partial p}{\partial x} + \\ \nu_{\text{hor}}\left[\left(\frac{\partial^2 u}{\partial x^2} + \frac{\partial^2 u}{\partial y^2}\right) + \underbrace{\frac{\partial}{\partial x}\left(\frac{\partial u}{\partial x} + \frac{\partial u}{\partial y}\right)}\right] + \frac{\partial}{\partial z}\left(\nu_{\text{vert}}\frac{\partial u}{\partial z}\right),\end{aligned} \tag{103}$$

$$\begin{aligned}\frac{\partial v}{\partial t} + (\operatorname{grad} v)\cdot \boldsymbol{v} - fv = -\frac{1}{\rho_*}\frac{\partial p}{\partial y} + \\ \nu_{\text{hor}}\left[\left(\frac{\partial^2 v}{\partial x^2} + \frac{\partial^2 v}{\partial y^2}\right) + \underbrace{\frac{\partial}{\partial y}\left(\frac{\partial v}{\partial x} + \frac{\partial v}{\partial y}\right)}\right] + \frac{\partial}{\partial z}\left(\nu_{\text{vert}}\frac{\partial v}{\partial z}\right);\end{aligned} \tag{104}$$

- Balance of energy:

$$\begin{aligned}\rho^\star c_v\left(\frac{\partial T}{\partial t} + (\operatorname{grad} T)\cdot \boldsymbol{v}\right) = \\ \rho^\star [c_v] D^{(T)}_{\text{hor}}\left(\frac{\partial^2 T}{\partial x^2} + \frac{\partial^2 T}{\partial y^2}\right) + \rho^\star [c_v]\frac{\partial}{\partial z}\left(D^{(T)}_{\text{vert}}\frac{\partial T}{\partial z}\right) + \phi^{(T)},\end{aligned} \tag{105}$$

$$\begin{aligned}\rho^\star c_p\left(\frac{\partial T}{\partial t} + (\operatorname{grad} T)\cdot \boldsymbol{v}\right) = -\left(\frac{\partial p}{\partial t} + (\operatorname{grad} p)\cdot \boldsymbol{v}\right) + \\ \rho^\star [c_p] D^{(T)}_{\text{hor}}\left(\frac{\partial^2 T}{\partial x^2} + \frac{\partial^2 T}{\partial y^2}\right) + \rho^\star [c_p]\frac{\partial}{\partial z}\left(D^{(T)}_{\text{vert}}\frac{\partial T}{\partial z}\right) + \phi^{(T)};\end{aligned} \tag{106}$$

- Balance of tracer mass:

$$\begin{aligned}\rho^\star\left(\frac{\partial c_\alpha}{\partial t} + (\operatorname{grad} c_\alpha)\cdot \boldsymbol{v}\right) = \rho^\star D^{(c_\alpha)}_{\text{hor}}\left(\frac{\partial^2 c_\alpha}{\partial x^2} + \frac{\partial^2 c_\alpha}{\partial y^2}\right) + \\ \rho^\star \frac{\partial}{\partial z}\left(D^{(c_\alpha)}_{\text{vert}}\frac{\partial c_\alpha}{\partial z}\right) + \rho^\star \frac{\partial}{\partial z}(c_\alpha w - \alpha^s) + \phi^{(c_\alpha)}.\end{aligned} \tag{107}$$

These equations are to be complemented by the pressure equation (100). We further remark, that physical values for ν_{hor} are $1\,\text{m}^2\text{s}^{-1}$, while those for ν_{vert} are $10^{-4} - 10^{-2}\,\text{m}^2\text{s}^{-1}$. Similar order of magnitude differences also exist for the horizontal and vertical diffusivities $D^{(T)}_{\text{hor}}$, $D^{(T)}_{\text{vert}}$, $D^{(c_\alpha)}_{\text{hor}}$, and $D^{(c_\alpha)}_{\text{vert}}$.

However, the underbraced terms are omitted in the oceanographic and limnological literature. In that reduced form the momentum equations were first presented by MUNK in 1950 [31]. We also note

that there is no rational justification of the above laws which would be based on continuum mechanical principles of an anisotropic viscous stress-stretching relation. Wang (1996) [50], however, presents in his dissertation a derivation based on such principles and delimits the conditions under which equations (102)–(107) hold true. This derivation is also given in Hutter et al. (2011) [18].

3 A primer on boundary and transition conditions

The free surface, the transition surface between regions I and II (Fig. 3) and the lower boundary separating the detritus region from the immobile rigid bed are *singular surfaces*; these are so called, since physical quantities may suffer a jump discontinuity from values on one side to the other side when the surface is crossed. For instance, from region I in Fig. 3, to the atmosphere, the density changes by a factor of 10^{-3}; likewise the velocity changes from that of the lake water to that of the air. Depending on specific conditions such surfaces may be occupied by the same material particles for all times, or may be simply discontinuity surfaces for some fields; they are then called *material* and *non-material* surfaces, respectively. Two kinds of mathematical statements can be derived for such surfaces: (i) those of geometric-kinematic nature and (ii) those of dynamic meaning. They are used to formulate boundary conditions for the equations in the bulk adjacent bodies. Our derivation will be brief and partly incomplete. The reader is directed to the specialized literature e.g. MÜLLER (1985) [30], HUTTER (1992) [15], SLATTERY et al. (2007) [40]. In order to present these conditions we need some basics from the geometry and kinematics of a moving surface.

First, we consider *geometric* properties of a (stagnant) surface $\mathcal{S}$, given parametrically in a Cartesian reference system $Ox^1x^2x^3$ by

$$\boldsymbol{r} = \boldsymbol{x}(\xi^1, \xi^2) = x^k(\xi^1, \xi^2)\, \boldsymbol{e}_k\,, \quad (\xi^1, \xi^2) \in \Delta_0\,, \tag{108}$$

where $\{\boldsymbol{e}_1, \boldsymbol{e}_2, \boldsymbol{e}_3\}$ is the Cartesian basis. It is supposed that the function $\boldsymbol{r}$ is such that the vectors

$$\boldsymbol{\tau}_\mathfrak{a} \equiv \frac{\partial \boldsymbol{r}}{\partial \xi^\mathfrak{a}} = \frac{\partial x^k}{\partial \xi^\mathfrak{a}}\, \boldsymbol{e}_k\,, \quad \mathfrak{a} = 1,\, 2\,, \tag{109}$$

satisfy the condition

$$\boldsymbol{\tau}_1 \times \boldsymbol{\tau}_2 \neq \boldsymbol{0}\,, \quad \forall\ (\xi^1, \xi^2) \in \Delta_0\,,$$

implying, in particular, that $\boldsymbol{\tau}_1$, $\boldsymbol{\tau}_2$ are not zero. At $\boldsymbol{r}(\xi^1, \xi^2)$ the vectors $\boldsymbol{\tau}_1$ and $\boldsymbol{\tau}_2$ are tangent vectors (generally not perpendicular to one another and neither necessarily of unit length) to the coordinate lines $\xi^2 =$ constant and $\xi^1 =$ constant, respectively. Their span defines the tangent space to $\mathcal{S}$ at $\boldsymbol{r}(\xi^1, \xi^2)$, and

$$\boldsymbol{n} \equiv \frac{\boldsymbol{\tau}_1 \times \boldsymbol{\tau}_2}{\|\boldsymbol{\tau}_1 \times \boldsymbol{\tau}_2\|} \tag{110}$$

is a unit vector normal to this tangent space. This way one obtains a basis, $\{\boldsymbol{\tau}_1, \boldsymbol{\tau}_2, \boldsymbol{n}\}$, for the space of three-dimensional vectors, and hence we may write[24]

$$\frac{\partial \boldsymbol{\tau}_\mathfrak{a}}{\partial \xi^\mathfrak{b}} = \Gamma^\mathfrak{c}_{\mathfrak{a}\mathfrak{b}}\, \boldsymbol{\tau}_\mathfrak{c} + b_{\mathfrak{a}\mathfrak{b}}\, \boldsymbol{n}\,,$$

[24] We employ the summation convention from 1 to 2 over doubly repeated coefficients of contra and covariant tensor components: $A^\mathfrak{c}_{\mathfrak{a}\mathfrak{b}} v_\mathfrak{c}$ or $A^{\mathfrak{a}\mathfrak{b}}_\mathfrak{c} v^\mathfrak{c}$, etc.

which is the representation of $\partial\boldsymbol{\tau}_{\mathfrak{a}}/\partial\xi^{\mathfrak{b}}$ with respect to this basis. The coefficients $\Gamma^{\mathfrak{c}}_{\mathfrak{a}\mathfrak{b}}$ are called CHRISTOFFEL symbols and are proved to be given by

$$\Gamma^{\mathfrak{c}}_{\mathfrak{a}\mathfrak{b}} = \tfrac{1}{2} g^{\mathfrak{c}\mathfrak{d}} \left(\frac{\partial g_{\mathfrak{d}\mathfrak{a}}}{\partial \xi^{\mathfrak{b}}} + \frac{\partial g_{\mathfrak{d}\mathfrak{b}}}{\partial \xi^{\mathfrak{a}}} - \frac{\partial g_{\mathfrak{a}\mathfrak{b}}}{\partial \xi^{\mathfrak{d}}} \right) , \tag{111}$$

where $g_{\mathfrak{a}\mathfrak{b}}$ are the *coefficients of the first fundamental form* of $\mathcal{S}$,

$$g_{\mathfrak{a}\mathfrak{b}} \equiv \boldsymbol{\tau}_{\mathfrak{a}} \cdot \boldsymbol{\tau}_{\mathfrak{b}} ,$$

and $g^{\mathfrak{a}\mathfrak{b}}$ are defined as

$$g^{\mathfrak{a}\mathfrak{b}} \equiv \boldsymbol{\tau}^{\mathfrak{a}} \cdot \boldsymbol{\tau}^{\mathfrak{b}} ,$$

with $\{\boldsymbol{\tau}^1, \boldsymbol{\tau}^2\}$ the reciprocal basis of the *natural basis* $\{\boldsymbol{\tau}_1, \boldsymbol{\tau}_2\}$ of the tangent space, i.e.,

$$\boldsymbol{\tau}^{\mathfrak{a}} \cdot \boldsymbol{\tau}_{\mathfrak{b}} = \delta^{\mathfrak{a}}{}_{\mathfrak{b}} ,$$

where $\delta^{\mathfrak{a}}{}_{\mathfrak{b}}$ is the KRONECKER delta; the matrix $(g^{\mathfrak{a}\mathfrak{b}})$ is the matrix inverse of $(g_{\mathfrak{a}\mathfrak{b}})$: $(g^{\mathfrak{a}\mathfrak{b}}) = (g_{\mathfrak{a}\mathfrak{b}})^{-1}$. On the other hand, $b_{\mathfrak{a}\mathfrak{b}}$ are the so-called *coefficients of the second fundamental form* of $\mathcal{S}$, and they can be calculated as

$$b_{\mathfrak{a}\mathfrak{b}} = \frac{\partial \boldsymbol{\tau}_{\mathfrak{a}}}{\partial \xi^{\mathfrak{b}}} \cdot \boldsymbol{n} = -\boldsymbol{\tau}_{\mathfrak{a}} \cdot \frac{\partial \boldsymbol{n}}{\partial \xi^{\mathfrak{b}}} = b_{\mathfrak{b}\mathfrak{a}} , \tag{112}$$

once the functions $x^k(\xi^1, \xi^2)$, $k = 1, 2, 3$ (see (108)) are known. Since

$$\frac{\partial \boldsymbol{n}}{\partial \xi^{\mathfrak{b}}} = -b_{\mathfrak{a}\mathfrak{b}}\, \boldsymbol{\tau}^{\mathfrak{a}} , \quad \mathfrak{b} = 1, 2 ,$$

it is clear that the scalars $b_{\mathfrak{a}\mathfrak{b}}$ give an insight on how much the surface is 'curved'. An intrinsic (i.e., independent of the parameterization (108) for $\mathcal{S}$) quantity measuring the curvature of $\mathcal{S}$ is the *mean curvature*

$$K \equiv \tfrac{1}{2}\, g^{\mathfrak{a}\mathfrak{b}}\, b_{\mathfrak{a}\mathfrak{b}} . \tag{113}$$

Now, we refer to the *kinematic* properties of a moving surface $\mathcal{S}$. Thus, now $\mathcal{S}$ denotes a one-parameter family $\{\mathcal{S}_t\}_{t\in I}$, with $I \subset \mathbb{R}$ an open (time) interval, of surfaces $\mathcal{S}_t$ given by

$$\boldsymbol{x} = \boldsymbol{r}(\xi^1, \xi^2, t) = x^k(\xi^1, \xi^2, t)\, \boldsymbol{e}_k , \quad (\xi^1, \xi^2) \in \Delta_0 , \quad t \in I . \tag{114}$$

The vector

$$\boldsymbol{w} \equiv \frac{\partial \boldsymbol{r}}{\partial t} \tag{115}$$

is the *velocity of the surface point* (ξ^1, ξ^2) at the moment t. With respect to the basis $\{\boldsymbol{\tau}_1, \boldsymbol{\tau}_2, \boldsymbol{n}\}$ it has the representation

$$\boldsymbol{w} = w^{\mathfrak{a}}\, \boldsymbol{\tau}_{\mathfrak{a}} + \mathcal{U}\boldsymbol{n} . \tag{116}$$

The normal component $\mathcal{U}$ of $\boldsymbol{w}$ is independent of the choice of the parametric representation (114), and is called the speed of displacement of that point on $\mathcal{S}_t$ for which the position vector is $\boldsymbol{r}(\xi^1, \xi^2, t)$, or simply, the *speed of displacement of* $\mathcal{S}$.

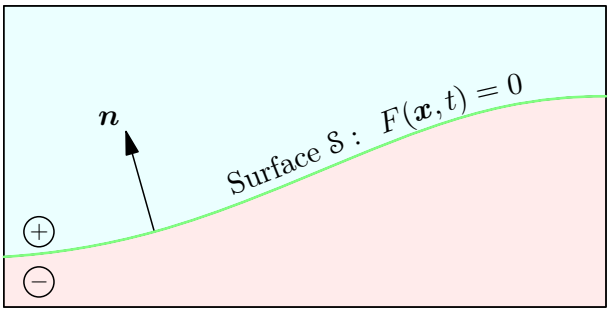

Figure 6: A surface $\mathcal{S}$, given by the equation $F = 0$, separates the three-dimensional space into the semi-spaces on the (+)- and (–)-sides of $\mathcal{S}$. The (+)-side is on that side into which the unit normal vector points.

3.1 Kinematic surface condition

The moving surface $\mathcal{S}$ may be given implicitly, that is, by an equation of the form

$$F(\boldsymbol{x},t) = 0\,. \tag{117}$$

Choosing a local parameterization for $\mathcal{S}$, say in the form (114), we have

$$F(\boldsymbol{r}(\xi^1,\xi^2,t),t) = 0$$

for all $(\xi^1,\xi^2) \in \Delta_0$ and for all $t \in I$. Differentiating this relation with respect to t and recalling definition (115) of $\boldsymbol{w}$, we obtain

$$\frac{\partial F}{\partial t} + \operatorname{grad} F \cdot \boldsymbol{w} = 0\,, \tag{118}$$

which is called the *kinematic condition* for F. Now, if the surface parameters are conveniently ordered, the unit normal vector (110) is $\boldsymbol{n} = \operatorname{grad} F/\|\operatorname{grad} F\|$, and so with (116) we rewrite (118) in the form

$$\underbrace{\frac{\partial F/\partial t}{\|\operatorname{grad} F\|} + \underbrace{\frac{\operatorname{grad} F}{\|\operatorname{grad} F\|}}_{=\boldsymbol{n}} \cdot \boldsymbol{w}}_{=\mathcal{U}} = 0 \iff \mathcal{U} = -\frac{\partial F/\partial t}{\|\operatorname{grad} F\|}\,, \tag{119}$$

which serves to calculate the speed of displacement $\mathcal{U}$ if the function F is known, or stands as a partial differential equation for F if the normal velocity $\mathcal{U}$ is known. It is customary to denote the semi-space to which $\boldsymbol{n}$ is directed the positive side of the surface and the other semi-space the negative side of it, see Fig. 6. Altering the orientation from (+) to (–) is possible by replacing F with $-F$.

It may happen that the surface $\mathcal{S}$ is a material surface, that is, it is always occupied by the same bodily particles identified with their position vectors $\boldsymbol{X}$ in a reference configuration and having their own motion on $\mathcal{S}$. Thus, if

$$\boldsymbol{x} = \boldsymbol{\chi}(\boldsymbol{X},t)$$

represents the motion of the particle $\boldsymbol{X}$, since for all times t the particle lies on $\mathcal{S}$, we have

$$F(\boldsymbol{\chi}(\boldsymbol{X},t),t) = 0\,.$$

Differentiating this relation with respect to t and defining the velocity $\boldsymbol{v}_{\mathcal{S}}$ of the surface particle $\boldsymbol{X}$ as

$$\boldsymbol{v}_{\mathcal{S}} \equiv \frac{\partial \boldsymbol{\chi}}{\partial t}\,, \tag{120}$$

we obtain the *kinematic condition for the material surface* $\mathcal{S}$:

$$\frac{\partial F}{\partial t} + \operatorname{grad} F \cdot \boldsymbol{v}_{\mathcal{S}} = 0\,. \tag{121}$$

This gives

$$\boldsymbol{v}_{\mathcal{S}} \cdot \boldsymbol{n} = -\frac{\partial F}{\partial t} / \|\operatorname{grad} F\|\,,$$

which, when comparing with (119), shows that for material surfaces equality $\boldsymbol{v}_{\mathcal{S}} \cdot \boldsymbol{n} = \mathcal{U}$ holds (for details see Fig. 9). If $\mathcal{S}$ consists of particles of a three-dimensional continuum body $\mathcal{B}$, then $\boldsymbol{v}_{\mathcal{S}} = \boldsymbol{v}$, where $\boldsymbol{v}$ is the velocity field corresponding to $\mathcal{B}$, and (121) takes the form

$$\frac{\partial F}{\partial t} + \operatorname{grad} F \cdot \boldsymbol{v} = 0\,. \tag{122}$$

3.2 Dynamic surface jump conditions

Consider a bodily region, in which the physical fields are continuously differentiable (smooth), except for singular surface(s) $\mathcal{S}$ across which some fields may suffer jump discontinuities; $\mathcal{S}$ is supposed to not have its own physical properties. Figure 7 and its caption explain the situation. Applying the balance law

$$\frac{d}{dt}\int_{\mathcal{B}=\mathcal{B}^+\cup\mathcal{B}^-} f\,dv = -\int_{\partial\mathcal{B}=\partial\mathcal{B}^+\cup\partial\mathcal{B}^-} \boldsymbol{\phi}^f \cdot \boldsymbol{n}\,da + \int_{\mathcal{B}^+\cup\mathcal{B}^-} (s^f + \pi^f)\,dv \tag{123}$$

to the pillbox volume $\mathcal{B}$ (Fig. 7 b) and performing the limit $\varepsilon \to 0$ in the emerging statement such that $\mathcal{S}$ stays between lid and bottom, leads to the expression

$$[\![f\,(\boldsymbol{v} - \boldsymbol{w}) \cdot \boldsymbol{n}]\!] + [\![\boldsymbol{\phi}^f \cdot \boldsymbol{n}]\!] = 0\,. \tag{124}$$

In the above equations, f, $\boldsymbol{\phi}^f$, s^f and π^f denote the physical quantity inside $\mathcal{B} = \mathcal{B}^+ \cup \mathcal{B}^-$, its flux across the outer surface $\partial\mathcal{B} = \partial\mathcal{B}^+ \cup \partial\mathcal{B}^-$, the supply and the production rates within $\mathcal{B} = \mathcal{B}^+ \cup \mathcal{B}^-$, respectively. Moreover, with $\psi^{\pm}$ the values of a quantity ψ immediately on the (+)- and (–)-side of $\mathcal{S}$, respectively, $[\![\,\psi\,]\!] \equiv \psi^+ - \psi^-$ is the jump of ψ across $\mathcal{S}$. The derivation of (124) from (123) is given in books on continuum mechanics, e.g. HUTTER and JÖHNK (2004) [17].

In the balance statement (123) it is assumed that the integral $\int_{\mathcal{B}}(s^f + \pi^f)\,dv$ vanishes as $\varepsilon \to 0$, so that s^f and π^f do not arise in (124). Similarly, it is also assumed that $\int_{\mathcal{B}} f\,dv$ vanishes as $\varepsilon \to 0$. The relevant quantities f and $\boldsymbol{\phi}^f$ are collectively summarized in Table 5 for the physical laws (76)–(80).

For instance, when referred to the physical laws (76)–(80), to which the entries of Table 5 correspond, the jump condition (124) takes the forms

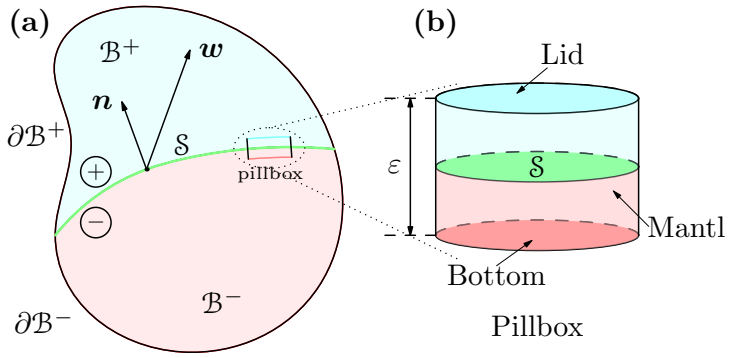

Figure 7: (a) Body $\mathcal{B} = \mathcal{B}^+ \cup \mathcal{B}^-$ whose physical fields may suffer jump discontinuities across $\mathcal{S}$, but are smooth in the vicinity of $\mathcal{S}$. **(b)** Pillbox, zoomed from panel (a). Its total surface consists of the lid on the (+)-side of $\mathcal{S}$ and the bottom on the (–)-side; its mantle surface has thickness ε. Balance laws (124) for this bodily surface will be formulated in the limit as $\varepsilon \to 0$. The unit normal vector to $\mathcal{S}$ points into $\mathcal{B}^+$ and $\boldsymbol{w}$ is the velocity of surface coordinates on $\mathcal{S}$, but only $\mathcal{U} = \boldsymbol{w} \cdot \boldsymbol{n}$ is kinematically relevant for $\mathcal{S}$.

Table 5: Expressions for the quantity f and its flux $\boldsymbol{\phi}^f$ in the physical balance laws[a]

Quantity f	f	$\boldsymbol{\phi}^f$
Mixture mass balance	ρ	$\boldsymbol{0}$
Constituent mass balance	ρc_α	$\boldsymbol{J}_\alpha - \rho c_\alpha \boldsymbol{w}_s^\alpha$
Mixture momentum balance	$\rho\,\boldsymbol{v}$	$p\boldsymbol{I} - \boldsymbol{R}$
Mixture energy balance	$\rho(\epsilon + \frac{1}{2}\boldsymbol{v}\cdot\boldsymbol{v})$	$\boldsymbol{Q}_\epsilon + (p\boldsymbol{I} - \boldsymbol{R})\boldsymbol{v}$
Mixture energy balance	$\rho(h + \frac{1}{2}\boldsymbol{v}\cdot\boldsymbol{v})$	$\boldsymbol{Q}_h + (p\boldsymbol{I} - \boldsymbol{R})\boldsymbol{v}$

[a] ρ is the mixture density, c_α – the mass fraction of tracer α, $\boldsymbol{J}_\alpha$ – the constituent laminar and turbulent mass flux vector, $\boldsymbol{w}_s^\alpha$ – the settling velocity of constituent α, $\boldsymbol{v}$ – the barycentric velocity, p – the mixture pressure, $\boldsymbol{R}$ – the turbulent REYNOLDS stress tensor, ϵ – the internal energy, h – the enthalpy, $\boldsymbol{Q}_\epsilon$, $\boldsymbol{Q}_h$ – turbulent heat flux vectors.

$$
\begin{aligned}
&[\![\rho(\boldsymbol{v}-\boldsymbol{w})\cdot\boldsymbol{n}]\!] = 0\,,\\
&[\![\rho\, c_\alpha(\boldsymbol{v}-\boldsymbol{w})\cdot\boldsymbol{n}]\!] + [\![\boldsymbol{J}_\alpha - \rho c_\alpha \boldsymbol{w}_s^\alpha]\!]\cdot\boldsymbol{n} = 0\,,\quad \alpha = 1,\dots,N\,,\\
&[\![\rho((\boldsymbol{v}-\boldsymbol{w})\cdot\boldsymbol{n})\boldsymbol{v}]\!] - [\![-p\boldsymbol{I}+\boldsymbol{R}]\!]\boldsymbol{n} = \boldsymbol{\theta}\,,\\
&[\![\rho(\epsilon+\tfrac{1}{2}\boldsymbol{v}\cdot\boldsymbol{v})(\boldsymbol{v}-\boldsymbol{w})\cdot\boldsymbol{n}]\!] + [\![\boldsymbol{Q}_\epsilon + (p\boldsymbol{I}-\boldsymbol{R})\boldsymbol{v}]\!]\cdot\boldsymbol{n} = 0\,,\\
&[\![\rho(h+\tfrac{1}{2}\boldsymbol{v}\cdot\boldsymbol{v})(\boldsymbol{v}-\boldsymbol{w})\cdot\boldsymbol{n}]\!] + [\![\boldsymbol{Q}_h + (p\boldsymbol{I}-\boldsymbol{R})\boldsymbol{v}]\!]\cdot\boldsymbol{n} = 0\,.
\end{aligned}
\tag{125}
$$

These describe the jump conditions of the mass of the mixture as a whole and of the tracer masses, of the mixture momentum and mixture energy balances. All are written by using the mass fraction c_α and the barycentric velocity as basic fields. In the BOUSSINESQ approximation ρ may be replaced by ρ^*. Of special interest is the situation when $\boldsymbol{w}\cdot\boldsymbol{n} = \boldsymbol{v}\cdot\boldsymbol{n}$. In this case only the second terms on the left-hand sides of (125) survive. Even though this does not exactly define the physical jump conditions for a *material* surface, it is customary to call such surfaces material. The better denotation is to say that such *surfaces follow the barycentric motion*.

Note that, due to the jump condition $(125)_1$, explicitly

$$
\underbrace{\rho^+(\boldsymbol{v}^+-\boldsymbol{w})\cdot\boldsymbol{n}}_{\equiv\mathcal{M}^+} = \underbrace{\rho^-(\boldsymbol{v}^--\boldsymbol{w})\cdot\boldsymbol{n}}_{\equiv\mathcal{M}^-}\,,
\tag{126}
$$

in fluid mechanical applications the kinematic surface relation (118) is often written as

$$
\frac{\partial F/\partial t}{\|\operatorname{grad} F\|} + \boldsymbol{v}^\pm\cdot\boldsymbol{n} = \frac{\mathcal{M}}{\rho^\pm}\,,
\tag{127}
$$

where $\mathcal{M}\equiv\mathcal{M}^+ = \mathcal{M}^-$. We emphasize that (118) is a pure kinematic statement, while (127) is a mixed kinematic-dynamic statement.

3.3 Surface balance laws

The above jump conditions are obtained on the assumption that the singular surface $\mathcal{S}$ does not possess its own physical properties. We shall now relax this assumption and request that $\mathcal{S}$ contributes to the balance law of the pillbox with a surface density $f_\mathcal{S}$, having a production $\pi^{f_\mathcal{S}}$ and a supply $s^{f_\mathcal{S}}$ per unit area of $\mathcal{S}$, and a flux $\boldsymbol{\phi}^{f_\mathcal{S}}$ per unit length and tangential to $\mathcal{S}$ through the boundary $\mathcal{C}$ of $\mathcal{S}$ (see Fig. 8):

$$
\begin{aligned}
\frac{d}{dt}\left\{\int_{\mathcal{B}=\mathcal{B}^+\cup\mathcal{B}^-} f\,dv + \int_\mathcal{S} f_\mathcal{S}\,da\right\} = &-\int_{\partial\mathcal{B}=\partial\mathcal{B}^+\cup\partial\mathcal{B}^-}\boldsymbol{\phi}^f\cdot\boldsymbol{n}\,da - \int_{\mathcal{C}=\partial\mathcal{S}}\boldsymbol{\phi}^{f_\mathcal{S}}\cdot\boldsymbol{h}\,ds +\\
&\int_{\mathcal{B}^+\cup\mathcal{B}^-}(\pi^f + s^f)\,dv + \int_\mathcal{S}(\pi^{f_\mathcal{S}} + s^{f_\mathcal{S}})\,da\,.
\end{aligned}
\tag{128}
$$

Here, ds is the line element along the closed loop $\mathcal{C}$ (without double point), generated by the intersection of $\mathcal{S}$ with the mantle surface of the pillbox; $\boldsymbol{h}$ is the unit tangent vector to $\mathcal{S}$, exterior to the pillbox mantle and normal to $\mathcal{C}$ (thus, $\boldsymbol{h}$ together with the positive direction of $\mathcal{C}$ and the orientation of the unit normal

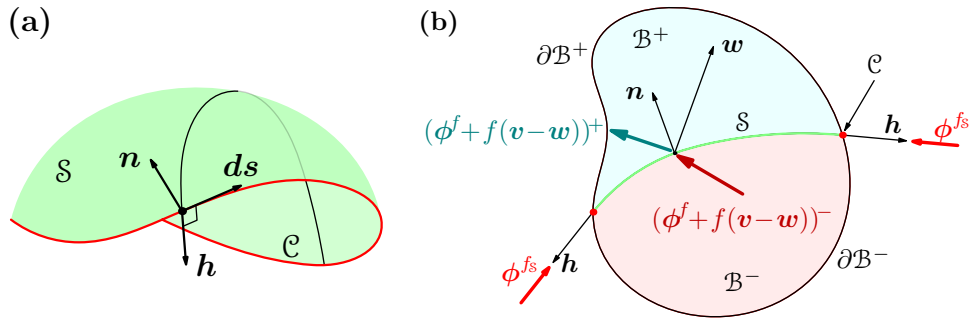

Figure 8: **(a)** Surface $\mathcal{S}$ spanned over a simple double-point free closed loop $\mathcal{C}$; $\boldsymbol{n}$ is the unit normal vector on $\mathcal{S}$ at a point on $\mathcal{C}$; $\boldsymbol{ds}$ is the incremental tangent vector to the curve $\mathcal{C}$; $\boldsymbol{h}$ is the unit vector normal to $\mathcal{C}$ and tangential to $\mathcal{S}$; $\boldsymbol{h}$, $\boldsymbol{ds}$, and $\boldsymbol{n}$ form a right-handed orthogonal triad. **(b)** Two-dimensional sketch of the singular surface $\mathcal{S}$ with unit normal vector $\boldsymbol{n}$ and spanned by the closed loop $\mathcal{C}$. The panel shows positive ($\mathcal{B}^+$) and negative ($\mathcal{B}^-$) regions separated by $\mathcal{S}$, the surface flux $\boldsymbol{\phi}^{f_\mathcal{S}}$ into $\mathcal{S}$ along $\mathcal{C}$, the vector $\boldsymbol{h}$ (compare panel (a)) and the conductive and convective fluxes from the bulk region.

vector $\boldsymbol{n}$ of $\mathcal{S}$ form a counterclockwise skrew, Fig. 8 a).

The derivation from the global balance law (128) of the local balance law valid on $\mathcal{S}$ can be found, e.g., in the book by SLATTERY et al. [40] (2007). Here we sketch the proof. Thus, letting the thickness of the pillbox approaching zero ($\varepsilon \to 0$ as in Fig. 7b) turns (128) into

$$\frac{d}{dt}\int_\mathcal{S} f_\mathcal{S}\, da = \underbrace{-\int_\mathcal{C} \boldsymbol{\phi}^{f_\mathcal{S}} \cdot \boldsymbol{h}\, ds}_{(1)} + \underbrace{\int_\mathcal{S} \left(\pi^{f_\mathcal{S}} + s^{f_\mathcal{S}}\right) da}_{(2)} \underbrace{- \int_\mathcal{S} [\![\boldsymbol{\phi}^f + f(\boldsymbol{v}-\boldsymbol{w})]\!] \cdot \boldsymbol{n}\, da}_{(3)} . \tag{129}$$

The three underlined terms represent

(1) the flux of $f_\mathcal{S}$ out of $\mathcal{S}$ and tangential to $\mathcal{S}$ along the loop $\mathcal{C}$,

(2) the production and supply of $f_\mathcal{S}$ on $\mathcal{S}$,

(3) the conductive plus convective flow of the bulk quantity f through $\mathcal{S}$.

The term on the left-hand side of (129) will be transformed with the aid of the transport theorem for a material surface (see Fig. 9),

$$\frac{d}{d\,t}\int_{\Sigma_t} f_\mathcal{S}(\boldsymbol{x},t)\, da = \int_{\Sigma_t} \left\{ \frac{\partial f_\mathcal{S}}{\partial t} + \frac{\partial f_\mathcal{S}}{\partial \xi^\mathfrak{a}}\,\dot{\xi}^\mathfrak{a} + f_\mathcal{S}\left(v^\mathfrak{a}_{\mathcal{S};\mathfrak{a}} - 2\mathcal{U}K\right)\right\} da = \int_{\Sigma_t} \left\{ \frac{\partial f_\mathcal{S}}{\partial t} + \mathrm{Div}(f_\mathcal{S}\boldsymbol{v}_\mathcal{S}) - \frac{\partial f_\mathcal{S}}{\partial \xi^\mathfrak{a}}\, w^\mathfrak{a}\right\} da\,. \tag{130}$$

Here $\dot{\xi}^\mathfrak{a}$ is explained in Fig. 9, $\boldsymbol{v}_\mathcal{S}$ is the velocity of a surface material point (see (120)), $w^\mathfrak{a}$ and $\mathcal{U}$ are the components of the surface velocity, see (116), $\psi^\mathfrak{a}_{;\mathfrak{b}}$ denotes the covariant derivative of a tangent surface vector field $\boldsymbol{\psi} = \psi^\mathfrak{a}\boldsymbol{\tau}_\mathfrak{a}$,

$$\psi^\mathfrak{a}_{;\mathfrak{b}} \equiv \frac{\partial \psi^\mathfrak{a}}{\partial \xi^\mathfrak{b}} + \Gamma^\mathfrak{a}_{\mathfrak{c}\mathfrak{b}}\,\psi^\mathfrak{c}$$

(see (111) for the definition of CHRISTOFFEL symbols $\Gamma^\mathfrak{a}_{\mathfrak{c}\mathfrak{b}}$), K is the mean curvature, and $\partial f_\mathcal{S}/\partial t$ and

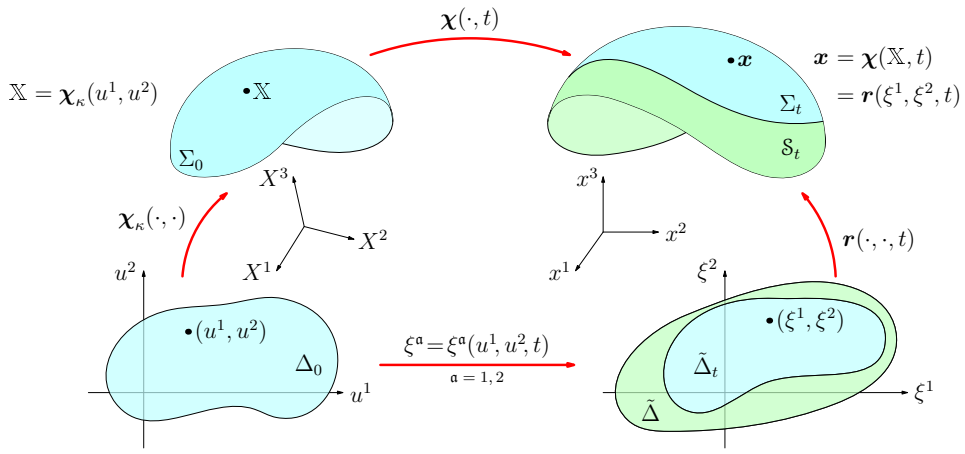

Figure 9: $\mathcal{S}\equiv\{\mathcal{S}_t\}$ is a moving ('geometric') surface; it is given parameterically by $\boldsymbol{x}=\boldsymbol{r}(\xi^1,\xi^2,t)$, $(\xi^1,\xi^2)\in\tilde{\Delta}$ and moves with the velocity $\boldsymbol{w}\equiv\partial\boldsymbol{r}(\xi^1,\xi^2,t)/\partial t$. $\Sigma\equiv\{\Sigma_t\}$ is a moving material surface: $\Sigma_t=\boldsymbol{\chi}(\Sigma_0,t)$, where Σ_0 is the material surface in a reference configuration. The velocity $\boldsymbol{v}_\mathcal{S}$ of $\mathbb{X}\in\Sigma_0$ is $\boldsymbol{v}_\mathcal{S}\equiv\partial\boldsymbol{\chi}(\mathbb{X},t)/\partial t$. Σ is so moving that $\Sigma_t\subset\mathcal{S}_t$ at each instant t. Therefore, $\Sigma_t=\boldsymbol{r}(\tilde{\Delta}_t,t)$, for a some $\tilde{\Delta}_t\subset\tilde{\Delta}$, and for $\boldsymbol{x}\in\Sigma_t$, $\boldsymbol{x}=\boldsymbol{\chi}(\mathbb{X},t)=\boldsymbol{r}(\xi^1,\xi^2,t)$, which can be written as $\boldsymbol{x}=\boldsymbol{\chi}(\boldsymbol{\chi}_\kappa(u^1,u^2),t)=\boldsymbol{r}(\xi^1(u^1,u^2,t),\xi^2(u^1,u^2,t),t)$. Differentiation of this relation with respect to t yields $\boldsymbol{v}_\mathcal{S}=\dot{\xi}^\alpha\boldsymbol{\tau}_\alpha+\boldsymbol{w}$, where $\dot{\xi}^\alpha\equiv\partial\xi^\alpha(u^1,u^2,t)/\partial t$, showing, in particular, that $\boldsymbol{v}_\mathcal{S}\cdot\boldsymbol{n}=\boldsymbol{w}\cdot\boldsymbol{n}\equiv\mathcal{U}$.

the surface divergence operator Div are defined by

$$\frac{\partial f_\mathcal{S}}{\partial t}\equiv\frac{\partial}{\partial t}\,f_\mathcal{S}(\xi^1,\xi^2,t)\,,\quad \mathrm{Div}\,(f_\mathcal{S}\boldsymbol{v}_\mathcal{S})\equiv\frac{\partial f_\mathcal{S}\boldsymbol{v}_\mathcal{S}}{\partial\xi^\alpha}\,\boldsymbol{\tau}^\alpha\,. \tag{131}$$

For the term (1) on the right-hand side of (129) the GAUSS' law will be used. This process yields the local, point form of the *surface balance law* as

$$\frac{\partial f_\mathcal{S}}{\partial t}+\mathrm{Div}(f_\mathcal{S}\boldsymbol{v}_\mathcal{S}+\boldsymbol{\phi}^{f_\mathcal{S}})-\frac{\partial f_\mathcal{S}}{\partial\xi^\alpha}\,w^\alpha=-[\![\boldsymbol{\phi}^f+f(\boldsymbol{v}-\boldsymbol{w})]\!]\cdot\boldsymbol{n}+(\pi^{f_\mathcal{S}}+s^{f_\mathcal{S}})\,. \tag{132}$$

Apparently, due to the tangential components w^α of the surface velocity $\boldsymbol{w}$, relation (132) would depend on the parameterization of $\mathcal{S}$. However, this is not so, since the combination $\partial f_\mathcal{S}/\partial t-w^\alpha\partial f_\mathcal{S}/\partial\xi^\alpha$, representing the delta-time derivative (THOMAS [44] (1961)), is independent of the parameterization of $\mathcal{S}$. Relation (132) is the extension of the classical jump condition (124) if smooth surface fields $f_\mathcal{S}$, $\boldsymbol{\phi}^{f_\mathcal{S}}$, $\pi^{f_\mathcal{S}}$, $s^{f_\mathcal{S}}$ are occupying the singular surface $\mathcal{S}$; (132) reduces to (124) if all surface fields vanish.

If $f_\mathcal{S}$ is a scalar field, the balance law (132) reads

$$\frac{\partial f_\mathcal{S}}{\partial t}+\left(f_\mathcal{S}\boldsymbol{v}_\mathcal{S}+\boldsymbol{\phi}^{f_\mathcal{S}}\right)^\alpha_{\ ;\alpha}-\frac{\partial f_\mathcal{S}}{\partial\xi^\alpha}\,w^\alpha-2f_\mathcal{S}\mathcal{U}K=-[\![\boldsymbol{\phi}^f+f(\boldsymbol{v}-\boldsymbol{w})]\!]\cdot\boldsymbol{n}+(\pi^{f_\mathcal{S}}+s^{f_\mathcal{S}})\,. \tag{133}$$

Let us discuss special cases:

(a) *No curvature effects*. The curvature effects are contained explicitly in K, the mean curvature, in the last term on the left-hand side of (133). When such effects are negligible and the coordinate cover is Cartesian, we have

$$\frac{\partial\boldsymbol{\tau}_\alpha}{\partial\xi^\beta}=\boldsymbol{0}\Longrightarrow\Gamma^\gamma_{\alpha\beta}=0\,,\quad K=0\,,\quad(\cdot)_{;\alpha}=(\cdot)_{,\alpha}\,,$$

so that the balance law (133) takes the form

$$\frac{\partial f_{\mathcal{S}}}{\partial t} + \left(f_{\mathcal{S}} \boldsymbol{v}_{\mathcal{S}} + \boldsymbol{\phi}^{f_{\mathcal{S}}} \right)^{\mathfrak{a}}{}_{,\mathfrak{a}} - \frac{\partial f_{\mathcal{S}}}{\partial \xi^{\mathfrak{a}}} w^{\mathfrak{a}} = -[\![\boldsymbol{\phi}^{f} + f(\boldsymbol{v} - \boldsymbol{w})]\!] \cdot \boldsymbol{n} + (\pi^{f_{\mathcal{S}}} + s^{f_{\mathcal{S}}}) \,. \tag{134}$$

Still further simplified versions of surface jump conditions are possible by ignoring some of the surface terms $f_{\mathcal{S}}$, $\boldsymbol{\phi}^{f_{\mathcal{S}}}$, $\pi^{f_{\mathcal{S}}}$, $s^{f_{\mathcal{S}}}$.

(b) *Surface following the bulk motion.* If $\boldsymbol{w} \cdot \boldsymbol{n} = \boldsymbol{v} \cdot \boldsymbol{n}$, the jump term in (133) reduces to the jump in volume flux, $[\![\boldsymbol{\phi}^{f}]\!] \cdot \boldsymbol{n}$. For mass balance this term is absent and only surface mass fields interact with one another in this case.

(c) *Reduced surface balance law.* Some of the surface fields in (133) may be small in comparison to others. When $f_{\mathcal{S}} = 0$, (133) reduces to

$$(\boldsymbol{\phi}^{f_{\mathcal{S}}})^{\mathfrak{a}}{}_{;\mathfrak{a}} = -[\![\boldsymbol{\phi}^{f} + f(\boldsymbol{v} - \boldsymbol{w})]\!] \cdot \boldsymbol{n} + (\pi^{f_{\mathcal{S}}} + s^{f_{\mathcal{S}}}) \,. \tag{135}$$

This variant (usually with $s^{f_{\mathcal{S}}} = 0$) accounts for surface tension effects if (135) is a reduced momentum balance.

4 Boundary conditions; a simple model of detritus layer

The simplest model for the detritus transport (thin layer II in Fig. 3) is obtained if the layer concept for the detritus transport is collapsed to zero thickness, see Fig. 4. Thus, the field equations presented in Sect. 2 must be complemented by boundary conditions at the free surface $\mathcal{S}_s$ and at the basal surface $\mathcal{S}_b$. At this level two procedures are principally possible: (i) One may assume the basal surface $\mathcal{S}_b$ to be equipped with surface masses and surface momenta for all constituents α, but treat these as a mixture of class I. This then means that mass balance laws must be formulated for the solid constituents and the mixture as a whole and momentum balance is only formulated for the mixture as a whole. (ii) A full mixture formulation of class II is formulated for all constituent mass and momentum balances. In this process the interaction of the bulk fields with the surface fields from the $(+)$- and $(-)$-sides of the singular surface must be accounted for. We adopt the simpler case (i). Moreover, the time evolution of the basal surface is governed by the kinematic equation (119) and the erosion and sedimentation rates are incorporated in the surface mass balances for the N sediment classes.

4.1 Boundary conditions at the free surface

We shall treat the free surface as a surface following the barycentric motion, with

$$F(\boldsymbol{x}, t) \equiv z - s(x, y, t) = 0 \,, \tag{136}$$

where $s(x, y, t)$ describes its z-position. With u, v, w the mixture 'material' velocity components in the x, y and z directions of the Cartesian coordinate system, the kinematic surface condition (122) takes the form[25]

$$\frac{\partial s}{\partial t} + \frac{\partial s}{\partial x} u + \frac{\partial s}{\partial y} v - w = 0 \,, \quad \text{at} \quad z = s(x, y, t) \,. \tag{137}$$

Now we refer to the dynamic jump conditions (125), in which $\boldsymbol{v} \cdot \boldsymbol{n} = \boldsymbol{w} \cdot \boldsymbol{n}$:

[25] If barotropic surface waves are ignored, i.e., the *rigid lid* approximation is imposed, then (137) is replaced by $z = 0$, where the origin of the coordinate system is at the undeformed free surface and the x and y axes are horizontal.

(i) Condition $(125)_1$ is identically satisfied.

(ii) The *stress boundary condition* $(125)_3$ emerges as $[\![-p\boldsymbol{I}+\boldsymbol{R}]\!]\boldsymbol{n}=\boldsymbol{0}$, or, explicitly,

$$(-p\boldsymbol{I}+\boldsymbol{R})\boldsymbol{n}_s=\boldsymbol{\sigma}^{\text{atm}}\boldsymbol{n}_s \quad \text{at} \quad z=s(x,y,t)\,.$$

Projections of this equation perpendicular and tangential to $\mathcal{S}_s$ reveal the following statements at $z=s(x,y,t)$:

$$\begin{aligned} &\text{normal to } \mathcal{S}_s: && -p+\boldsymbol{n}_s\cdot\boldsymbol{R}\boldsymbol{n}_s=-p^{\,\text{atm}}\,,\\ &\text{tangential to } \mathcal{S}_s: && \boldsymbol{R}\boldsymbol{n}_s-(\boldsymbol{n}_s\cdot\mathbf{R}\boldsymbol{n}_s)\boldsymbol{n}_s=\boldsymbol{\tau}^{\text{wind}}\,, \end{aligned} \tag{138}$$

where

$$p^{\,\text{atm}}\equiv-\boldsymbol{\sigma}^{\text{atm}}\boldsymbol{n}_s\cdot\boldsymbol{n}_s\,,\quad \boldsymbol{\tau}^{\text{wind}}\equiv\boldsymbol{\sigma}^{\text{atm}}\boldsymbol{n}_s+p^{\,\text{atm}}\boldsymbol{n}_s\,.$$

In the shallow water approximation formulae (138) can easily be shown to reduce to

$$\begin{aligned} &\text{normal to } \mathcal{S}_s: && p=p^{\,\text{atm}}\,,\\ &\text{tangential to } \mathcal{S}_s: && R_{xz}=\tau_x^{\text{wind}},\quad R_{yz}=\tau_y^{\text{wind}}\,, \end{aligned} \tag{139}$$

at $z=s(x,y,t)$. The atmospheric input of the surface tractions $p^{\,\text{atm}}$, $\boldsymbol{\tau}_H^{\text{wind}}\equiv(\tau_x^{\text{wind}},\tau_y^{\text{wind}})$ is generally implemented by the parameterizations[26]

$$\begin{aligned} p^{\,\text{atm}}&=\text{constant (often = 0)}\,,\\ \boldsymbol{\tau}_H^{\text{wind}}&=\rho^{\text{atm}}C_d^{\text{wind}}\,\|\boldsymbol{v}_H^{\text{wind}}(x,y,t)\|\,\boldsymbol{v}_H^{\text{wind}}(x,y,t)\,, \end{aligned} \tag{140}$$

with dimensionless drag coefficient $C_d^{\text{wind}}\approx 2\times10^{-3}$, and $\boldsymbol{v}_H^{\text{wind}}\equiv(v_x^{\text{wind}},v_y^{\text{wind}})$; v_x^{wind}, v_y^{wind} are the Cartesian components in the x, y directions of the wind velocity $\boldsymbol{v}^{\text{wind}}$ at the free surface $\mathcal{S}_s$.

(iii) If also temperature evolutions are in focus, the heat flow from the atmosphere into the lake must be prescribed. Relation $(125)_4$ together with the stress traction continuity and the closure law $(52)_2$ then states that

$$\rho^*[c_v]D^{(T)}\,(\text{grad}\;T)\cdot\boldsymbol{n}_s\underbrace{-((-p\boldsymbol{I}+\boldsymbol{R})\,\boldsymbol{n}_s)\cdot[\![\boldsymbol{v}]\!]}_{\substack{\text{power of working of the}\\ \text{surface tractions}}}=Q_\perp^{\text{atm}}\,. \tag{141}$$

Here, $Q_\perp^{\text{atm}}$ is the energy input from the atmosphere into the water: $Q_\perp^{\text{atm}}\equiv-\boldsymbol{Q}^{\text{atm}}\cdot\boldsymbol{n}_s$, with $\boldsymbol{Q}^{\text{atm}}$ the heat flux in the atmosphere. The power of working of the surface tractions is often ignored or computed by assuming that $[\![\boldsymbol{v}]\!]=\boldsymbol{v}^{\text{wind}}-\boldsymbol{v}^{\text{water}}\approx\boldsymbol{v}^{\text{wind}}$. With this last assumption in the shallow

[26] The right-hand side of $(140)_2$ should involve the difference $(\boldsymbol{v}_H^{\text{wind}}-\boldsymbol{v}_H^{\text{water}})_{\mathcal{S}}$, but the water velocity is very much smaller than the wind velocity, which justifies the approximation.

water approximation, (141) reduces to

$$\rho^*[c_v]D^{(T)}\frac{\partial T}{\partial z} - \boldsymbol{\tau}_H^{\text{wind}}\cdot\boldsymbol{v}_H^{\text{wind}} = Q_\perp^{\text{atm}}\,. \tag{142}$$

The contributions to the energy input $Q_\perp^{\text{atm}}$ are written as $Q_\perp^{\text{atm}} = Q_{ir}^{\text{atm}} - Q_{ir}^{\text{water}} + Q_\ell + Q_s$, with

$Q_{ir}^{\text{atm}} \equiv$ (black body) radiation of air,

$Q_{ir}^{\text{water}} \equiv$ (black body) radiation of water,

$Q_\ell \equiv$ latent heat flow between water and air,

$Q_s \equiv$ sensible heat flow between water and air.

Parameterizations of the latent and sensible heats are given by HUTTER & JÖHNK (2004) [17].

(iv) The free surface is not only assumed to follow the barycentric motion, it is here simultaneously supposed to be *impermeable to the suspended sediments* of all fractions. This implies that $(125)_2$ reduces to

$$(\boldsymbol{J}_\alpha - \rho c_\alpha \boldsymbol{w}_\alpha^s)\cdot\boldsymbol{n}_s = 0 \quad \text{at} \quad z = s(x,y,t)\,, \quad \alpha = 1,\ldots,N\,, \tag{143}$$

expressing vanishing mass flow of tracer α through the free surface. With gradient-type closures (see (52), (51)), (143) takes the form

$$\rho^* D^{(c_\alpha)}\frac{\partial c_\alpha}{\partial \boldsymbol{n}_s} + \rho\, c_\alpha \boldsymbol{w}_\alpha^s\cdot\boldsymbol{n}_s = 0 \quad \text{at} \quad z = s(x,y,t)\,, \quad \alpha = 1,\ldots,N\,, \tag{144}$$

or, in the shallow water and BOUSSINESQ approximations,

$$D^{(c_\alpha)}\frac{\partial c_\alpha}{\partial z} + c_\alpha w_\alpha^s = 0, \quad \alpha = 1,\ldots,N\,, \quad \text{at} \quad z = s(x,y,t)\,. \tag{145}$$

With this the discussion of the dynamic jump conditions (125) is completed.

Remark The parameterization of w_α^s in (144) and (145) with the final free fall velocity (69) seems rather inappropriate at the free surface, where the turbulent intensity is generally large and falling distances for particles are restricted. When k is parameterized by $(53)_2$ or the $(k-\varepsilon)$ model is employed, (75) ought to be used instead.

If the $(k-\varepsilon)$ model for turbulent closure is employed, physically acceptable postulations for the boundary conditions of the turbulent kinetic energy and its dissipation are

$$\frac{\partial k}{\partial \boldsymbol{n}_s} = \boldsymbol{0}, \quad \frac{\partial \varepsilon}{\partial \boldsymbol{n}_s} = \boldsymbol{0}\,, \quad \text{at } z = s(x,y,t)\,, \tag{146}$$

or in the shallow water approximation,

$$\frac{\partial k}{\partial z} = 0, \quad \frac{\partial \varepsilon}{\partial z} = 0\,, \quad \text{at} \quad z = s(x,y,t)\,. \tag{147}$$

In this case, the rigid lid assumption, $s(x,y,t) = 0$, is often justified.

4.2 Boundary conditions at the rigid bed

The simplest description of detritus transport does not use the concept of the motion of a thin layer of sediments. The existence of this layer is negated and the lower boundary of the lake domain is directly the singular surface between the slurry layer and the rigid bed of alluvial detritus. We treat this surface as having its own physical properties in the context of a mixture of class I, and so the surface balance law (132) will be now used. Moreover, the surface moves and deforms with time owing to the removal of grains from the bed, their incorporation in the particle laden water, and the deposition of some components of the washload from the slurry above the bottom surface. Therefore, in these simple models essentially only two physically significant statements are made:

- A criterion, or more generally, some criteria are established, which define the onset of erosion of sediments of grain class α. It is expected that a characteristic variable will act as a threshold measure. Below a certain value of this variable only sediments of classes α will be lifted, for which the grain size is smaller than for class α_{thres}[27].
- For those components α which are eroded and incorporated in the slurry, the amount of eroded material per unit time for each grain class, i.e., the mass flow for each component from the rigid bed to the ambient water must be quantified.

For the ensuing developments it is perhaps advantageous, if the classical approach to sediment transport is briefly illustrated. Thus, the next two sections are devoted to this issue.

4.2.1 Erosion inception

In the words of KRAFT et al. (2011) [23], 'the erosion of sediment begins when the shear stress on the bed surface, τ_w, exceeds the critical wall shear stress of the corresponding sediment material, τ_c'. A widely used procedure for the determination of the beginning of entrainment of cohesionless particles is represented by the SHIELDS curve (1936) [39]; see also VAN RIJN (1984) [47], which is based on the results of numerous laboratory measurements with different grain sizes, densities and wall shear stresses. A critical SHIELDS parameter (the dimensionless critical shear stress) is defined by

$$\tau_c^*\,(=\theta_c) \equiv \frac{\tau_c}{\Delta\rho\, g\, \mathfrak{d}}\,, \qquad \Delta \equiv \frac{\rho_s}{\rho} - 1\,, \tag{148}$$

where $\mathfrak{d}$ is the mean particle diameter for class α of particles with a range of particle diameters in the interval $[d_{\alpha-1}, d_\alpha)$; we suggest to take this mean value to be $\mathfrak{d} = \frac{1}{2}(d_{\alpha-1} + d_\alpha)$. Moreover, ρ_s is the true density of the sediment and ρ is the mixture density.

A large number of laboratory experiments has been conducted (for a review, see VETSCH (2012) [49]) and identified the critical dimensionless shear stress τ_c^* or θ_c for a grain size $\mathfrak{d}$ as a function of the critical particle REYNOLDS number

$$Re_c^* \equiv \frac{u^*\mathfrak{d}}{\nu}, \quad \text{where} \quad u^* \equiv \left(\frac{g\,\nu}{\Delta}\right)^{1/3}. \tag{149}$$

[27] If $\mathfrak{d}_\alpha$ and $\mathfrak{d}_{\alpha_{\text{thres}}}$ are the nominal grain diameters of the grain size classes α and α_{thres}, respectively, then all grains with $\mathfrak{d}_\alpha < \mathfrak{d}_{\alpha_{\text{thres}}}$ are mobilized, whilst those with $\mathfrak{d}_\alpha > \mathfrak{d}_{\alpha_{\text{thres}}}$ are still at rest.

Thus,

$$\tau_c^* = f(Re_c^*)\,. \tag{150}$$

Re_c^* is sometimes also called 'dimensionless particle diameter' and is then identified with

$$\mathfrak{d}^\star \equiv \mathfrak{d}\left(\frac{g}{\nu^2\Delta}\right)^{1/3} (= Re_c^*)\ , \tag{151}$$

see KRAFT et al. [23]. This formula can be motivated by dimensional analysis, see Appendix C. A great number of representations of $f(Re_c^*) = f(\mathfrak{d}^\star)$ have been proposed, see again VETSCH for a review; he lists, among many others, expressions by VAN RIJN (1984, 2007) [47], [48], viz.,

$$\tau_c^* = \begin{cases} 0.115(\mathfrak{d}^\star)^{-0.5}, & \text{for} \quad 1 < \mathfrak{d}^\star < 4\,, \\ 0.14(\mathfrak{d}^\star)^{-0.64}, & \text{for} \quad 4 \leqslant \mathfrak{d}^\star < 10\,, \\ 0.04(\mathfrak{d}^\star)^{-0.1}, & \text{for} \quad 10 \leqslant \mathfrak{d}^\star < 20\,, \\ 0.013(\mathfrak{d}^\star)^{0.29}, & \text{for} \quad 20 \leqslant \mathfrak{d}^\star < 150\,, \\ 0.055, & \text{for} \quad 150 \leqslant \mathfrak{d}^\star\,. \end{cases} \tag{152}$$

This automatically suggests a possible division of the grain size distribution into five regimes. Again according to VETSCH, YALIN and DA SILVA (2001) [55] approximate the VAN RIJN data by a continuous functional relation

$$\tau_c^* = 0.13(\mathfrak{d}^\star)^{-0.392}\exp(-0.015(\mathfrak{d}^\star)^2) + 0.045\left(1 - \exp\left(-0.068(\mathfrak{d}^\star)^2\right)\right)\ . \tag{153}$$

There are also a number of other formulae for the critical shear stress τ_c^*. For instance, KRAFT et al. (2011) [23] list a formula due to ZANKE (2001) [57],

$$\tau_c^* = \psi_Z \tan(\varphi) - \theta_w'\,, \tag{154}$$

in which φ is the angle of internal friction of the sediment and θ_w' is the root mean square turbulent fluctuation of the wall shear stress. For natural sediments the coefficient ψ_Z takes the value $\psi_Z = 0.7$.

This is about the appropriate place where a clarifying remark about the critical shear stress should be made. Formulae (148) to (154) are expressed in terms of a shear stress τ_c, since the stress distribution in river flow is close to *simple shearing* plus a hydrostatic pressure,

$$\boldsymbol{\sigma} = \begin{pmatrix} 0 & 0 & \tau_c \\ 0 & 0 & 0 \\ \tau_c & 0 & 0 \end{pmatrix} - p \begin{pmatrix} 1 & 0 & 0 \\ 0 & 1 & 0 \\ 0 & 0 & 1 \end{pmatrix} \Longrightarrow \boldsymbol{\sigma}_E = \begin{pmatrix} 0 & 0 & \tau_c \\ 0 & 0 & 0 \\ \tau_c & 0 & 0 \end{pmatrix}, \tag{155}$$

in which $\boldsymbol{\sigma}_E$ is the stress deviator of $\boldsymbol{\sigma}$. In a more general flow, the actual basal criterion describing the

onset of sediment motion cannot so simply be described. A likely adequate definition of the onset of the sediment movement, which subsequently will systematically be used, is to identify τ_c in (148) as

$$\tau_c \equiv (II_{\boldsymbol{\sigma}_E})^{1/2}_{\text{crit}} \,, \tag{156}$$

where $II_{\boldsymbol{\sigma}_E} \equiv \frac{1}{2}\text{tr}\left((\boldsymbol{\sigma}_E)^2\right)$ is the second invariant of the stress deviator $\boldsymbol{\sigma}_E$ evaluated just below the sediment bed. For simple shearing this is just the shear stress. Thus, a stress state invariant definition of θ_c or τ_c^* is[28]

$$\theta_c = \frac{(II_{\boldsymbol{\sigma}_E})^{1/2}_{\text{crit}}}{\Delta\rho\, g\, \mathfrak{d}} \,. \tag{157}$$

4.2.2 Erosion amount

The second statement, which is needed, is the parameterization of the *entrainment amount*. The literature again knows a large number of formulations for determining the erosion rate. KRAFT et al. (2011) [23] quote three formulae which here are briefly outlined as well:

- VAN RIJN (1984) [46] conducted laboratory experiments to determine the sediment erosion rate for various particle sizes and flow velocities and proposed for the pick-up rate per unit mass, area and time the function

$$\phi_p = \frac{E}{\rho_s\,(\Delta g \mathfrak{d})^{0.5}} = 0.0003(\mathfrak{d}^\star)^{0.3}\tilde{T}^{1.5}, \quad \tilde{T} \equiv \mathcal{H}\left(\left(\frac{u_{\tau_w}}{u_{\tau_c}}\right)^2 - 1\right)\left(\left(\frac{u_{\tau_w}}{u_{\tau_c}}\right)^2 - 1\right) \,, \tag{158}$$

  where $\mathcal{H}$ is the Heaviside function and

$$u_{\tau_c} \equiv \sqrt{\frac{\tau_c}{\rho}} \quad \text{and} \quad u_{\tau_w} \equiv \sqrt{\frac{\tau_w}{\rho}} \tag{159}$$

  denote the critical and actual wall shear velocities, defined as suggested in (156).

- The approach of EINSTEIN (1950) [11] is stochastic. A statistically averaged wall shear stress is not considered here, it is rather assumed that turbulent fluctuations will push the particles in motion. The pick-up rate is expressed as

$$E = \psi_E\, \rho_s\, (\Delta g \mathfrak{d})^{0.5}\; P \,, \tag{160}$$

  in which ψ_E is a universal constant, and P is the fraction of time during which a sediment particle is suspended by the flow. Note that this relation contains no critical shear stress. While for small wall shear stress P is negligibly small, for sufficiently large wall shear stress P will rapidly reach

[28] More generally, a criterion marking the onset of erosion is an equation of the form

$$f(I_{\boldsymbol{\sigma}},\, II_{\boldsymbol{\sigma}_E},\, III_{\boldsymbol{\sigma}_E}) = 0 \quad (*)$$

between the first stress invariant and the second and third stress deviator invariants at the basal surface. A dependence on $I_{\boldsymbol{\sigma}}$ describes a possible influence of the (mean) pressure; that on $II_{\boldsymbol{\sigma}_E}$ accounts for the significance of shearing, but the role of $III_{\boldsymbol{\sigma}_E}$ is presently not clear. In the form $(*)$ the erosion inception is very much reminiscent of the onset criterion of yield in the theories of plasticity.

its saturation value. In the present application we consider P simply a constant (for a given grain size range α) and the erosion will occur just as the shear stress exceeds its critical value.

- YALIN [53] determined the erosion rate from statistically averaged flow parameters. If the critical shear stress is exceeded, particles are entrained. The number of eroded particles rises linearly with the wall shear velocity. The erosion rate is computed by

$$E = \psi_Y \rho_s u_{\tau_w}. \tag{161}$$

  The constant ψ_Y should be determined by experiment.

It is evident from the above formulae that VAN RJIN's and EINSTEIN's erosion rates depend on the particle size, and for this reason can and should be restricted for a given grain size distribution curve to a single α-class of grain sizes. This makes YALIN's formula inapplicable to mathematical erosion processes which differentiate α-classes by grain size. KRAFT et al. [23] also remark that 'YALIN and VAN RJIN assumed in their formula that the number of eroded particles increases with increasing wall shear velocity'. ALAN and KENNEDY (see e.g. YALIN (1985) [54]) in their experiments demonstrated that the flow near the sediment bed is fully saturated when a certain wall shear velocity is reached, and the erosion rate converges to a certain value and does not rise further. With this in mind, only the approach of EINSTEIN does justice to these observations.

The above formulae have formally been written for a single particle diameter. Here, we interpret them as being applicable to the narrow range of particle diameters of class α. Let us summarize the salient formulae with this identification:

- Dimensionless α-particle diameter (see (151))

$$\mathfrak{d}_\alpha^\star = \mathfrak{d}_\alpha \left(\frac{g}{\nu^2 \Delta}\right)^{1/3} ; \tag{162}$$

- Dimensionless critical shear stress according to YALIN and DA SILVA [55] for class α and interpreted in the spirit of formula (156),

$$(\tau_c^*)_\alpha = Y_\alpha^* = 0.13(\mathfrak{d}_\alpha^\star)^{-0.392} \exp(-0.015(\mathfrak{d}_\alpha^\star)^2) + 0.045\left[1 - \exp(-0.068(\mathfrak{d}_\alpha^\star)^2)\right] ; \tag{163}$$

- The pick-up rate for class α is given, according to VAN RIJN [46], by

$$E_\alpha = 0.0003(\mathfrak{d}_\alpha^\star)^{0.3} \tilde{T}_\alpha^{1.5} \rho_s \left(\Delta\, g \mathfrak{d}_\alpha\right)^{0.5} , \tag{164}$$

  where, from (158) and (159),

$$\begin{aligned} \tilde{T}_\alpha &\equiv \mathcal{H}\left(\left(\frac{u_{\tau_w}}{u_{\tau_c}}\right)^2 - 1\right)\left(\left(\frac{u_{\tau_w}}{u_{\tau_c}}\right)^2 - 1\right) \\ &= \mathcal{H}\left(\frac{\tau_w}{\tau_c} - 1\right)\left(\frac{\tau_w}{\tau_c} - 1\right) = \mathcal{H}\left(\frac{\tau_w}{\tau_c^* \Delta \rho g \mathfrak{d}_\alpha} - 1\right)\left(\frac{\tau_w}{\tau_c^* \Delta \rho g \mathfrak{d}_\alpha} - 1\right) ; \end{aligned} \tag{165}$$

- According to EINSTEIN [11],

$$E_\alpha = \psi_E \rho_s \left(\Delta\, g \mathfrak{d}_\alpha\right)^{0.5} P_\alpha\,, \quad P_\alpha = \text{constant}\,. \tag{166}$$

Subsequently we shall employ (162)–(165).

4.2.3 Detritus layer as a singular material surface

The basal surface, separating the particle laden fluid and the rigid bed from which sediment can be eroded and to which washload is deposited, will be conceived as a surface with its own material properties intended to model the thin detritus layer. As for the bulk material in layer I, the surface detritus will be treated as a mixture of class I. Thus, as dynamic boundary conditions in Model 2 we formulate the averaged balance laws of mass for the sediments of classes α and the detritus-mixture as a whole, as well as the momentum balance law for the mixture as a whole, the master equation being (132).

The surface is defined by

$$F \equiv -b(x,y,t) + z = 0\,, \tag{167}$$

or, parametrically with $\xi^1 \equiv x$, $\xi^2 \equiv y$,

$$\boldsymbol{x} = x\boldsymbol{e}_1 + y\boldsymbol{e}_2 + b(x,y,t)\boldsymbol{e}_3 \equiv \boldsymbol{r}(x,y,t)\,, \quad (\boldsymbol{e}_3 \equiv \boldsymbol{e}_z)\,. \tag{168}$$

With definition (167) of F, $\boldsymbol{n}_b = \operatorname{grad} F/\|\operatorname{grad} F\|$ points *into* the fluid domain and satisfies (109) with

$$\boldsymbol{\tau}_1 \equiv \frac{\partial \boldsymbol{r}}{\partial x} = \boldsymbol{e}_1 + \frac{\partial b}{\partial x}\,\boldsymbol{e}_3\,, \quad \boldsymbol{\tau}_2 \equiv \frac{\partial \boldsymbol{r}}{\partial y} = \boldsymbol{e}_2 + \frac{\partial b}{\partial y}\,\boldsymbol{e}_3\,.$$

We have

$$\boldsymbol{n}_b = c\left(-\frac{\partial b}{\partial x}\,\boldsymbol{e}_1 - \frac{\partial b}{\partial y}\,\boldsymbol{e}_2 + \boldsymbol{e}_3\right)\,, \quad c \equiv \left[1 + \left(\frac{\partial\, b}{\partial\, x}\right)^2 + \left(\frac{\partial\, b}{\partial\, y}\right)^2\right]^{-1/2}\,.$$

Corresponding to (168), the surface velocity $\boldsymbol{w}$ is given by, see (115),

$$\boldsymbol{w} = \frac{\partial b}{\partial t}\,\boldsymbol{e}_3\,,$$

so that, with respect to the basis $\{\boldsymbol{\tau}_1, \boldsymbol{\tau}_2, \boldsymbol{n}_b\}$, $\boldsymbol{w}$ has the representation[29]

$$\boldsymbol{w} = c\,\frac{\partial b}{\partial x}\,\mathcal{U}_b\,\boldsymbol{\tau}_1 + c\,\frac{\partial b}{\partial y}\,\mathcal{U}_b\,\boldsymbol{\tau}_2 + \mathcal{U}_b\,\boldsymbol{n}_b\,, \quad \mathcal{U}_b = c\,\frac{\partial\, b}{\partial\, t}\,. \tag{169}$$

[29] To prove this, we write

$$\boldsymbol{w} = \alpha\boldsymbol{\tau}_1 + \beta\boldsymbol{\tau}_2 + \mathcal{U}_b\boldsymbol{n}_b = \frac{\partial\, b}{\partial\, t}\boldsymbol{e}_3\,.$$

If the above expressions for $\boldsymbol{\tau}_1$ and $\boldsymbol{\tau}_2$ are substituted this yields

$$\boldsymbol{w} = \left(\alpha - c\mathcal{U}_b\frac{\partial\, b}{\partial\, x}\right)\boldsymbol{e}_1 + \left(\beta - c\mathcal{U}_b\frac{\partial\, b}{\partial\, y}\right)\boldsymbol{e}_2 + \left(\alpha\frac{\partial\, b}{\partial\, x} + \beta\frac{\partial\, b}{\partial\, y} + c\mathcal{U}_b\right)\boldsymbol{e}_3 = \frac{\partial\, b}{\partial\, t}\boldsymbol{e}_3\,,$$

implying

$$\alpha = c\mathcal{U}_b\frac{\partial\, b}{\partial\, x}\,, \quad \beta = c\mathcal{U}_b\frac{\partial\, b}{\partial\, y}\,.$$

Table 6: Elements for the averaged surface balance relation (132) when referring to the detritus mixture and Model 2 ($\langle\cdot\rangle$ are omitted)

$f_{\mathcal{S}}$	$\boldsymbol{\phi}^{f_{\mathcal{S}}}$	$\pi^{f_{\mathcal{S}}}$	$s^{f_{\mathcal{S}}}$	f	$\boldsymbol{\phi}^{f}$
μ_α	$\mathbf{0}$	0	0	$\rho_\alpha = \rho\, c_\alpha$	$\boldsymbol{\phi}^{\rho_\alpha} = \boldsymbol{J}_\alpha - \rho\, c_\alpha \boldsymbol{w}^s_\alpha$
$\mu \equiv \sum_\alpha \mu_\alpha + \mu_f$	$\mathbf{0}$	0	0	ρ	$\boldsymbol{\phi}^{\rho} = 0$
$\mu \boldsymbol{v}_{\mathcal{S}} \equiv \sum_\alpha \mu_\alpha \boldsymbol{v}_{\mathcal{S}\alpha} + \mu_f \boldsymbol{v}_{\mathcal{S}f}$	$-\boldsymbol{R}_{\mathcal{S}}$	0	$\mu \boldsymbol{g}$	$\rho \boldsymbol{v}$	$\boldsymbol{\phi}^{\rho \boldsymbol{v}} = p\boldsymbol{I} - \boldsymbol{R}$

The displacement speed $\mathcal{U}_b$ is interpreted as *erosion/deposition rate* or *entrainment rate* and for it we will give a law according to the discussion in Sec. 4.2.2. So, we may keep in mind that $\mathcal{U}_b$ is a known quantity. In particular, we note that $(169)_2$ stands for the determination of the basal elevation function b once $\mathcal{U}_b$ is known.

With the identification of the fields $f_{\mathcal{S}}$, $\boldsymbol{\phi}^{f_{\mathcal{S}}}$, $\pi^{f_{\mathcal{S}}}$, $s^{f_{\mathcal{S}}}$, $\boldsymbol{\phi}^{f}$ and f in equation (133) as stated in Table 6, it can be shown (see Appendix C) that the surface mass balance law takes the forms:

- For the sediment classes α, $\alpha = 1, \ldots, N$,

$$\begin{aligned} &\frac{\partial \mu_\alpha}{\partial\, t} + (\mu_\alpha \boldsymbol{v}_{\mathcal{S}\alpha})^{\mathfrak{a}}{}_{;\mathfrak{a}} - \frac{\partial \mu_\alpha}{\partial \xi^{\mathfrak{a}}}\, w^{\mathfrak{a}} - 2\mu_\alpha\, \mathcal{U}_b K = \\ &\qquad (-\boldsymbol{\phi}^{\rho_\alpha} \cdot \boldsymbol{n}_b)^+ - (\rho\, c_\alpha\, \boldsymbol{v} \cdot \boldsymbol{n}_b)^+ - \left(\rho^{\text{bed}}_\alpha - \left(\rho c_\alpha\right)^+\right) \mathcal{U}_b\,; \end{aligned} \tag{170}$$

- For the mixture

$$\frac{\partial \mu}{\partial\, t} + (\mu \boldsymbol{v}_{\mathcal{S}})^{\mathfrak{a}}{}_{;\mathfrak{a}} - \frac{\partial \mu}{\partial \xi^{\mathfrak{a}}}\, w^{\mathfrak{a}} - 2\mu\, \mathcal{U}_b K = -(\rho\, \boldsymbol{v} \cdot \boldsymbol{n}_b)^+ - (\rho^{\text{bed}} - \rho^+)\mathcal{U}_b\,. \tag{171}$$

Here the (+)-sign indicates the water side of $\mathcal{S}_b$ and μ_α, μ, as well as the other quantities in (170), (171) are functions of $(\xi^1 \equiv x, \xi^2 \equiv y, t)$. Moreover, the components w^1, w^2 of the surface velocity $\boldsymbol{w}$ are given by

$$w^1 = c\, \frac{\partial b}{\partial x}\, \mathcal{U}_b\,, \quad w^2 = c\, \frac{\partial b}{\partial y}\, \mathcal{U}_b\,,$$

see (169). In deducing (170), (171) it is assumed that the motion of the basal surface is not subject to turbulent fluctuations, implying that $\langle \boldsymbol{n}_b \rangle = \boldsymbol{n}_b$, $\langle\, K\, \rangle = K$, $\langle \boldsymbol{w} \rangle = \boldsymbol{w}$ and $\langle \mathcal{U}_b \rangle = \mathcal{U}_b$.

The balance laws of mass, (170) and (171), contain unknown velocity components tangential to the surface $\mathcal{S}$ of the constituent classes α and the mixture. These velocities need be determined and for this determination essentially two procedures are at our disposal, namely

- We complement these laws with momentum equations for the surface flows of μ_α $(\alpha = 1, ..., N)$ and μ. These laws then allow determination of the momenta $\mu_\alpha \boldsymbol{v}_{\mathcal{S}\alpha}$ and $\mu \boldsymbol{v}_{\mathcal{S}}$ (or $\mu_f \boldsymbol{v}_{\mathcal{S}f}$). This defines a surface mixture of class II.

- We are less ambitious and introduce instead diffusion mass fluxes of the α-class sediments,

$$\boldsymbol{j}_{\mathcal{S}\alpha} \equiv \mu_\alpha\, (\boldsymbol{v}_{\mathcal{S}\alpha} - \boldsymbol{v}_{\mathcal{S}})\,, \tag{172}$$

for which closure relations are postulated, while the barycentric velocity is determined from the surface momentum balance law for the mixture as a whole. This defines a mixture of class I.

As already mentioned, we follow this second route. Note that, since $\boldsymbol{v}_{\mathcal{S}\alpha} \cdot \boldsymbol{n}_b = \boldsymbol{v}_{\mathcal{S}} \cdot \boldsymbol{n}_b \ (= \mathcal{U}_b)$, the diffusive surface mass flux is parallel to $\mathcal{S}_b$:

$$\boldsymbol{j}_{\mathcal{S}\alpha} = \boldsymbol{j}_{\mathcal{S}\alpha\|} \quad \Longrightarrow \quad \mu_\alpha \boldsymbol{v}_{\mathcal{S}\alpha\|} = \boldsymbol{j}_{\mathcal{S}\alpha} + \mu_\alpha \boldsymbol{v}_{\mathcal{S}\|} \, .$$

So, with definition (172) of $\boldsymbol{j}_{\mathcal{S}\alpha}$ we rewrite equation (170) as

$$\begin{aligned} &\frac{\partial \mu_\alpha}{\partial \, t} + (\mu_\alpha \boldsymbol{v}_{\mathcal{S}})^{\mathfrak{a}}{}_{;\mathfrak{a}} - \frac{\partial \mu_\alpha}{\partial \xi^{\mathfrak{a}}} \, w^{\mathfrak{a}} - 2\mu_\alpha \, \mathcal{U}_b K = \\ &\quad - (\boldsymbol{j}_{\mathcal{S}\alpha})^{\mathfrak{a}}{}_{;\mathfrak{a}} + (-\boldsymbol{\phi}^{\rho_\alpha} \cdot \boldsymbol{n}_b)^+ - (\rho \, c_\alpha \, \boldsymbol{v} \cdot \boldsymbol{n}_b)^+ - \left(\rho_\alpha^{\text{bed}} - (\rho c_\alpha)^+\right) \mathcal{U}_b \, . \end{aligned} \tag{173}$$

Now, the (averaged) surface momentum balance equation for the detritus mixture follows from (132) with the choices stated in Table 6, where $\boldsymbol{R}_{\mathcal{S}}$ is the surface Reynolds stress tensor, see (240) in App. D, which can be represented as

$$\boldsymbol{R}_{\mathcal{S}} = \underbrace{S^{\mathfrak{a}\mathfrak{b}} \boldsymbol{\tau}_{\mathfrak{a}} \otimes \boldsymbol{\tau}_{\mathfrak{b}}}_{\text{in-plane surface stress}} + \underbrace{S^{\mathfrak{a}} (\boldsymbol{\tau}_{\mathfrak{a}} \otimes \boldsymbol{n}_b + \boldsymbol{n}_b \otimes \boldsymbol{\tau}_{\mathfrak{a}})}_{\text{surface shear } \perp \text{ to } \mathcal{S}} + \underbrace{S \boldsymbol{n}_b \otimes \boldsymbol{n}_b}_{\text{normal surface pressure}} \tag{174}$$

Splitting this surface momentum balance law into a tangential component and a normal component to $\mathcal{S}_b$, we obtain the following results (see the derivation in Appendix D):

- Tangential surface momentum balance for the detritus mixture ($\mathfrak{a}, \mathfrak{b} = 1, 2$),

$$\begin{aligned} &\frac{\partial \mu v_{\mathcal{S}}^{\mathfrak{a}}}{\partial t} + \left(\mu v_{\mathcal{S}}^{\mathfrak{a}} v_{\mathcal{S}}^{\mathfrak{b}} - S^{\mathfrak{a}\mathfrak{b}}\right)_{;\mathfrak{b}} + \mu v_{\mathcal{S}}^{\mathfrak{b}} \frac{\partial w^{\mathfrak{a}}}{\partial \xi^{\mathfrak{b}}} - \mu w^{\mathfrak{b}} \frac{\partial v_{\mathcal{S}}^{\mathfrak{a}}}{\partial \xi^{\mathfrak{b}}} - \mu \mathcal{U}_b g^{\mathfrak{a}\mathfrak{b}} \frac{\partial \mathcal{U}_b}{\partial \xi^{\mathfrak{b}}} - v_{\mathcal{S}}^{\mathfrak{a}} w^{\mathfrak{b}} \frac{\partial \mu}{\partial \xi^{\mathfrak{b}}} - \\ &\left(2\mu \mathcal{U}_b v_{\mathcal{S}}^{\mathfrak{b}} - S^{\mathfrak{b}}\right) b_{\mathfrak{b}\mathfrak{c}} g^{\mathfrak{c}\mathfrak{a}} - 2K \left(\mu \mathcal{U}_b v_{\mathcal{S}}^{\mathfrak{a}} - S^{\mathfrak{a}}\right) = \\ &-(-p\boldsymbol{I} + \boldsymbol{R})^+ \boldsymbol{n}_b \cdot \boldsymbol{\tau}^{\mathfrak{a}} + \left((\rho \boldsymbol{v})^+ \cdot \boldsymbol{\tau}^{\mathfrak{a}}\right) (\boldsymbol{v}^+ \cdot \boldsymbol{n}_b - \mathcal{U}_b) + \\ &(-p\boldsymbol{I} + \boldsymbol{R})^- \boldsymbol{n}_b \cdot \boldsymbol{\tau}^{\mathfrak{a}} + \mu \boldsymbol{g} \cdot \boldsymbol{\tau}^{\mathfrak{a}} \, ; \end{aligned} \tag{175}$$

- Normal surface momentum balance for the detritus mixture,

$$\begin{aligned} &\frac{\partial \mu \mathcal{U}_b}{\partial t} + (\mu \mathcal{U}_b v_{\mathcal{S}}^{\mathfrak{a}} - S^{\mathfrak{a}})_{;\mathfrak{a}} + \mu (v_{\mathcal{S}}^{\mathfrak{a}} - w^{\mathfrak{a}}) \frac{\partial \mathcal{U}_b}{\partial \xi^{\mathfrak{a}}} - w^{\mathfrak{a}} \mathcal{U}_b \frac{\partial \mu}{\partial \xi^{\mathfrak{a}}} - 2K \left(\mu \mathcal{U}_b^2 - S\right) = \\ &-(-p\boldsymbol{I} + \boldsymbol{R})^+ \boldsymbol{n}_b \cdot \boldsymbol{n}_b + \left((\rho \boldsymbol{v})^+ \cdot \boldsymbol{n}_b\right) (\boldsymbol{v}^+ \cdot \boldsymbol{n}_b - \mathcal{U}_b) + \\ &(-p\boldsymbol{I} + \boldsymbol{R})^- \boldsymbol{n}_b \cdot \boldsymbol{n}_b + \mu \boldsymbol{g} \cdot \boldsymbol{n}_b \, . \end{aligned} \tag{176}$$

Note that (176) describes the evolution of the speed of displacement $\mathcal{U}_b$. However, we have chosen to prescribe $\mathcal{U}_b$ by giving an erosion/deposition law, so that (176) will be next omitted.[30] Equations (171),

[30] Developing a model with the consideration of (176) requires further assumptions on S, $(-p\boldsymbol{I} + \boldsymbol{R})^+ \boldsymbol{n}_b \cdot \boldsymbol{n}_b$, $(-p\boldsymbol{I} + \boldsymbol{R})^- \boldsymbol{n}_b \cdot \boldsymbol{n}_b$. We prefer to give an erosion/deposition law and so omit (176).

(173) and (175) stand for the determination of the surface fields μ, μ_α and $\boldsymbol{v}_{\mathcal{S}\|}$. However, there are quantities therein which must be prescribed, and this is dealt with in the next subsection.

4.2.4 Boundary conditions at the bed

Equations (171), (173) and (175) must be complemented by closure relations for the diffusive fluxes $\boldsymbol{j}_{\mathcal{S}\alpha}$, the stresses $S^{\mathfrak{ab}}$, $S^{\mathfrak{a}}$, and for the bulk quantities c_α^+, ρ^+, $\boldsymbol{v}^+$, $(\boldsymbol{\phi}^{\rho_\alpha})^+ \cdot \boldsymbol{n}_b$, $(-p\boldsymbol{I} + \boldsymbol{R})^{\pm}\boldsymbol{n}_b \cdot \boldsymbol{\tau}^{\mathfrak{a}}$. Thus, we make the following assumptions:

- For $\boldsymbol{j}_{\mathcal{S}\alpha}$ we assume the FICK law

$$j_{\mathcal{S}\alpha} = -D_\alpha \nabla_{\mathcal{S}} \mu_\alpha \iff (j_{\mathcal{S}\alpha})^{\mathfrak{a}} = -D_\alpha\, g^{\mathfrak{ab}} \frac{\partial\, \mu_\alpha}{\partial \xi^{\mathfrak{b}}}\,,$$

  where D_α [$\mathrm{m}^2\,\mathrm{s}^{-1}$] are the surface mass diffusivities. This parameterization ignores cross dependencies analogous to those in $(50)_4$.

- The shear stresses $S^{\mathfrak{a}}$ are assumed to be negligibly small, because they represent physically thickness integrated shear forces perpendicular to $\mathcal{S}$ and the thickness is infinitely small. For the surface parallel stresses $S^{\mathfrak{ab}}$ we assume

$$S^{\mathfrak{ab}} = S^{\mathfrak{ab}}_{\text{elastic}} + S^{\mathfrak{ab}}_{\text{viscous}}\,, \tag{177}$$

  where

$$\begin{aligned} S^{\mathfrak{ab}}_{\text{elastic}} &= -p(\mu)\, g^{\mathfrak{ab}}\,, \\ S^{\mathfrak{ab}}_{\text{viscous}} &= \zeta_{\mathcal{S}}\, \mathrm{tr}(\boldsymbol{D}_{\mathcal{S}})\, g^{\mathfrak{ab}} + 2\nu_{\mathcal{S}} \left[D^{\mathfrak{ab}}_{\mathcal{S}} - \tfrac{1}{2}\mathrm{tr}\,(\boldsymbol{D}_{\mathcal{S}})\, g^{\mathfrak{ab}} \right]. \end{aligned} \tag{178}$$

  p is an elastic pressure depending on the surface mass density (and also on the temperature in non-isothermal processes), $\zeta_{\mathcal{S}}$ is an aerial viscosity analogous to the bulk viscosity in three dimensions, $\nu_{\mathcal{S}}$ is a surface shear viscosity which operates on the surface deviator of $\boldsymbol{D}_{\mathcal{S}}$, and $\boldsymbol{D}_{\mathcal{S}}$ is the surface rate of deformation tensor,

$$\boldsymbol{D}_{\mathcal{S}} \equiv \tfrac{1}{2} \left(\boldsymbol{P}\, (\nabla_{\mathcal{S}} \boldsymbol{v}_{\mathcal{S}}) + (\nabla_{\mathcal{S}} \boldsymbol{v}_{\mathcal{S}})^T\, \boldsymbol{P} \right) = D^{\mathfrak{ab}}_{\mathcal{S}} \boldsymbol{\tau}_{\mathfrak{a}} \otimes \boldsymbol{\tau}_{\mathfrak{b}}\,. \tag{179}$$

  In (179), $\nabla_{\mathcal{S}}$ is the surface gradient and $\boldsymbol{P}$ is the projection operator onto the tangent plane to $\mathcal{S}$:

$$\nabla_{\mathcal{S}} \boldsymbol{u} \equiv \frac{\partial \boldsymbol{u}}{\partial \xi^{\mathfrak{a}}} \otimes \boldsymbol{\tau}^{\mathfrak{a}}\,, \quad \boldsymbol{P} \equiv \boldsymbol{\tau}_{\mathfrak{a}} \otimes \boldsymbol{\tau}^{\mathfrak{a}}\,,$$

  where $\boldsymbol{u}$ is a vector field defined on $\mathcal{S}$. With $\boldsymbol{u} = u^{\mathfrak{a}} \boldsymbol{\tau}_{\mathfrak{a}} + u\boldsymbol{n}$, we deduce

$$\boldsymbol{P} \nabla_{\mathcal{S}} \boldsymbol{u} \equiv u^{\mathfrak{a}}_{;\mathfrak{b}} \boldsymbol{\tau}_{\mathfrak{a}} \otimes \boldsymbol{\tau}^{\mathfrak{b}}\,,$$

  so that definition of $\boldsymbol{D}_{\mathcal{S}}$ implies the following expression for the components $D^{\mathfrak{ab}}_{\mathcal{S}}$:

$$D^{\mathfrak{ab}}_{\mathcal{S}} = \tfrac{1}{2} \left(u^{\mathfrak{a}}_{;\mathfrak{c}}\, g^{\mathfrak{cb}} + u^{\mathfrak{b}}_{;\mathfrak{c}}\, g^{\mathfrak{ca}} \right).$$

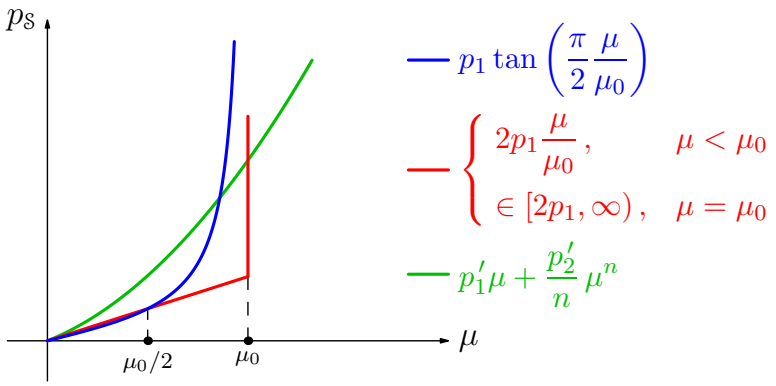

Figure 10: Pressure p as a function of μ for the 3 choices in (182)

Note that $\mathrm{tr}(\boldsymbol{D}_{\mathcal{S}}) = D_{\mathcal{S}}^{\mathfrak{a}\mathfrak{b}} g_{\mathfrak{a}\mathfrak{b}} = (\boldsymbol{D}_{\mathcal{S}})^{\mathfrak{a}}{}_{\mathfrak{a}}$. If one assumes $\zeta_{\mathcal{S}} = 0$ the correspondingly reduced equation $(178)_2$, viz.,

$$\left(S^{\mathfrak{a}\mathfrak{b}}_{\text{viscous}}\right)_{\text{Stokes}} = 2\nu_{\mathcal{S}}\left[D_{\mathcal{S}}^{\mathfrak{a}\mathfrak{b}} - \tfrac{1}{2}\,\mathrm{tr}(\boldsymbol{D}_{\mathcal{S}})\, g^{\mathfrak{a}\mathfrak{b}}\right], \tag{180}$$

corresponds to the STOKES approximation of $(178)_2$. Note, since no 'areal preserving' is implemented, the tensor on the right-hand side of $(178)_2$ is (still) the deviator of the surface stretching.

A closure relation for $p(\mu)$ is still needed. The intuitive understanding is that surface pressure can only build under areal compaction but not dilatation. Moreover, with increasing density μ, compaction will be more and more inhibited, or the corresponding pressure more and more increased. So,

$$p(\mu) = \mathcal{H}\left(-\mathrm{tr}(\boldsymbol{D}_{\mathcal{S}})\right)\mathsf{P}(\mu). \tag{181}$$

Three choices for P are

$$\mathsf{P}(\mu) = p_1 \tan\left(\frac{\pi}{2}\frac{\mu}{\mu_0}\right), \quad \mu > 0\,,$$

$$\mathsf{P}(\mu) = \begin{cases} 2p_1\dfrac{\mu}{\mu_0} & \mu<\mu_0\,, \\ \in[2p_1,\infty) & \mu=\mu_0\,, \end{cases} \tag{182}$$

$$\mathsf{P}(\mu) = p_1'\mu + \frac{p_2'}{n}\mu^n = \left(p_1' + \frac{p_2'}{n}\mu^{n-1}\right)\mu\,,$$

where $p_1,\, p_{1,2}' > 0$ and $n > 1$. For $(182)_{1,2}$, $p(\mu_0) = \infty$, so preventing μ from going beyond μ_0. Such a limit is not built into $(182)_3$, but selecting n large, produces physically effectively the same (for the graphs of $(182)_{1,2,3}$ see Fig. 10). These proposals account for the fact that with $\mu > 0$ also $p > 0$; furthermore, the larger μ is, the larger will be the pressure. Relations $(182)_{1,2}$ incorporate a densest packing condition, $(182)_3$ does not, which is more realistic since grains can escape perpendicular to $\mathcal{S}$. This completes the postulation of the stress parameterization for $S^{\mathfrak{a}\mathfrak{b}}$.

- The sliding laws

$$(-p\boldsymbol{I}+\boldsymbol{R})^{+}\boldsymbol{n}_b-\left((-p\boldsymbol{I}+\boldsymbol{R})^{+}\boldsymbol{n}_b\cdot\boldsymbol{n}_b\right)\,\boldsymbol{n}_b=\rho^{+}\mathcal{C}_1\|\boldsymbol{v}_{\parallel}^{+}-\boldsymbol{v}_{\mathbb{S}\parallel}\|\,\left(\boldsymbol{v}_{\parallel}^{+}-\boldsymbol{v}_{\mathbb{S}\parallel}\right)\,, \tag{183}$$

$$(-p\boldsymbol{I}+\boldsymbol{R})^{-}\boldsymbol{n}_b-\left((-p\boldsymbol{I}+\boldsymbol{R})^{-}\boldsymbol{n}_b\cdot\boldsymbol{n}_b\right)\,\boldsymbol{n}_b=\rho^{\mathrm{bed}}\mathcal{C}_2\|\boldsymbol{v}_{\mathbb{S}\parallel}\|\,\boldsymbol{v}_{\mathbb{S}\parallel}\,, \tag{184}$$

with the (dimensionless) drag coefficients $\mathcal{C}_1,\,\mathcal{C}_2>0$, will determine $(-p\boldsymbol{I}+\boldsymbol{R})^{\pm}\boldsymbol{n}_b\cdot\boldsymbol{\tau}^{\mathfrak{a}}$ in (175). In the BOUSSINESQ approximation ρ^{+} may be replaced by $\rho^{*}=\rho(4^{\circ}\mathrm{C})$; and in the shallow water approximation, $\boldsymbol{v}_{||}$ reduces to the horizontal component of $\boldsymbol{v}$, $\boldsymbol{v}_H$, so that (183) reads

$$(\tau_{xz},\tau_{yz})=\rho^{*}\mathcal{C}_1\sqrt{(u^{+}-u_{\mathbb{S}})^2+(v^{+}-v_{\mathbb{S}})^2}\,((u^{+}-u_{\mathbb{S}}),(v^{+}-v_{\mathbb{S}})).$$

- For $(\boldsymbol{\phi}^{\rho_\alpha})^{+}\cdot\boldsymbol{n}_b$ we simply evaluate $\boldsymbol{\phi}^{\rho_\alpha}$ on $\mathcal{S}_b$:

$$(\boldsymbol{\phi}^{\rho_\alpha})^{+}\cdot\boldsymbol{n}_b=\boldsymbol{\phi}^{\rho_\alpha}|_{z=b(x,y,t)}\cdot\boldsymbol{n}_b\,.$$

- Now we refer to $\boldsymbol{v}^{+}$, ρ^{+}, c_α^{+}.

  First, for the velocity $\boldsymbol{v}^{+}$ it is natural to request a kinematic condition of sliding or no-slip. When expressed in terms of the linear velocity profile across the thickness of the diffusive interface, see Fig. 11, this request implies

$$\boldsymbol{v}^{+}=\Xi v_s^{\mathfrak{a}}\boldsymbol{\tau}_{\mathfrak{a}}+\mathcal{U}_b\boldsymbol{n}\,,\quad \Xi\in[1,2]\,. \tag{185}$$

  Now, the velocity tangential to $\mathcal{S}_b$ at the 'upper' interface of this thin layer is twice the barycentric tangential surface velocity $\boldsymbol{v}_{\mathbb{S}\parallel}$. If a plug flow profile is assumed, then the sliding velocity is $\|\boldsymbol{v}_{\parallel}^{+}-\boldsymbol{v}_{\mathbb{S}\parallel}\|$. So, $\Xi\in[1,2]$, but $\Xi=2$ is the likelier value. These considerations lead to the above representation (185).

  Second, since

$$\rho^{+}=\textstyle\sum_\alpha\underbrace{\nu_\alpha^{+}\rho_s}_{\rho_\alpha^{+}}+\underbrace{\left(1-\sum_\alpha\nu_\alpha^{+}\right)\rho_w}_{\tilde{\rho}_f^{+}}\,,\quad \rho_\alpha^{+}=\rho^{+}c_\alpha^{+}\;\longrightarrow\;\nu_\alpha^{+}=\frac{\rho^{+}}{\rho_s}\,c_\alpha^{+}\,, \tag{186}$$

  where ν_α is the solid volume fraction of α constituent and ρ_w is the true density of the fluid, we find

$$\rho^{+}=\frac{\rho_w}{1-\sum_\alpha c_\alpha^{+}\left(1-\frac{\rho_w}{\rho_s}\right)}\,. \tag{187}$$

  So, according to (186)$_1$, (187), ρ^{+} is known, once $\sum_\alpha\nu_\alpha^{+}$ or $\sum_\alpha c_\alpha^{+}$ is known. We postulate closure conditions for c_α or ν_α ($\alpha=1,\ldots,N$).

  Third, to postulate a phenomenological relation for c_α^{+} or ν_α^{+} is the hardest, because it is physically not obvious. In such a situation it is probably easiest to formulate a surface balance law for c_α^{+} as stated in (133), viz.,

$$\frac{\partial\,c_\alpha^{+}}{\partial\,t}+\left(c_\alpha^{+}\boldsymbol{v}_{\parallel}^{+}+\boldsymbol{\phi}^{c_\alpha^{+}}\right)^{\mathfrak{a}}{}_{;\mathfrak{a}}-\frac{\partial\,c_\alpha^{+}}{\partial\,\xi^{\mathfrak{a}}}\,w^{\mathfrak{a}}-2c_\alpha^{+}\mathcal{U}_bK=\pi^{c_\alpha^{+}}\,. \tag{188}$$

In this equation the jump terms of the bulk quantities are absent as is the supply term. For none of them the introduction would be justified. Moreover, $\boldsymbol{\phi}^{c_\alpha^+}$ is the flux of c_α^+ (parallel to $\mathcal{S}_b$),

$$\left(\boldsymbol{\phi}^{c_\alpha^+}\right)^{\mathfrak{a}} = -d_{c_\alpha^+}\left(c_\alpha^+\right)_{;\,\mathfrak{b}}\, g^{\mathfrak{a}\mathfrak{b}}\,, \tag{189}$$

in which $d_{c_\alpha^+}$ are diffusivities, and cross dependences on the concentrations c_β^+ ($\beta \neq \alpha$) have been ignored. If one considers the evolution of c_α^+ to be non-diffusive, then $\boldsymbol{\phi}^{c_\alpha^+} = \boldsymbol{0}$, and (188) becomes a pure evolution equation for c_α^+. The production rate density is assumed to depend on quantities in the slurry at $\mathcal{S}_b$ and of the moving interface,

$$\pi^{c_\alpha^+} = \hat{\pi}^{c_\alpha^+}(\mathfrak{d}_\alpha, c_\alpha^+, Re_\alpha^+, \mu_\alpha, \|\boldsymbol{v}_\parallel^+ - \boldsymbol{v}_{\mathcal{S}\parallel}\|, \ldots)\,, \tag{190}$$

such that $\pi^{c_\alpha^+}|_{\text{equil}} = 0$. Equilibrium conditions are characterized by uniform and time independent c_α^+ and $\mathcal{U}_b = 0$, so that the left-hand side of (189) vanishes. It transpires that appropriate selection of $\hat{\pi}^{c_\alpha^+}$ is crucial.

We now incorporate into (171), (173) the *entrainment-erosion* and *deposition* rates for which specialists in sediment transport substitute parameterizations. The mass flow from below into the basal bed is identified as entrainment, erosion or pick-up rate, and from the moving bed to the base as deposition rate. With

$$\rho^{\text{bed}} \equiv \sum_{\alpha=1}^{N} \rho_\alpha^{\text{bed}} + \rho_f^{\text{bed}}\,,$$

they are, obviously, given by

$$\mathcal{M}_b^\alpha \equiv -\mathcal{U}_b\, \rho_\alpha^{\text{bed}}, \quad \mathcal{M}_b^f \equiv -\mathcal{U}_b\, \rho_f^{\text{bed}}, \quad \mathcal{M}_b \equiv -\mathcal{U}_b\, \rho^{\text{bed}}\,, \tag{191}$$

from which we easily deduce

$$\mathcal{M}_b^\alpha = \frac{\rho_\alpha^{\text{bed}}}{\rho^{\text{bed}}}\,\mathcal{M}_b, \quad \mathcal{M}_b^f = \frac{\rho_f^{\text{bed}}}{\rho^{\text{bed}}}\,\mathcal{M}_b\,. \tag{192}$$

Positive (negative) $\mathcal{U}_b$ [negative (positive) $\mathcal{M}_b$] corresponds to deposition (erosion). The result (192) implies that we are not free to select closure relations for $\mathcal{M}_b^{\alpha,f}$ independently and evaluate $\mathcal{M}_b$ from these via

$$\mathcal{M}_b = \sum_{\alpha=1}^{n} \mathcal{M}_b^\alpha + \mathcal{M}_b^f\,.$$

On the contrary, we must postulate a closure relation for $\mathcal{M}_b$ and evaluate $\mathcal{M}_b^{\alpha,f}$ from $(192)_{1,2}$ via the known grain size distribution and the corresponding densities $\rho_{\alpha,f}^{\text{bed}}$ just below $\mathcal{S}_b$. Erosion and deposition occur below the detritus layer. It is convenient to write

$$\mathcal{M}_b = \mathcal{M}_b^{\text{eros}} - \mathcal{M}_b^{\text{dep}}\,, \tag{193}$$

and to independently postulate representations for erosion and deposition. On the basis of the concepts of 'erosion inception' and 'erosion amount' we now postulate

$$
\begin{aligned}
\mathcal{M}_b^{\text{eros}} &= \sum_{\alpha=1}^{N^*} (c_\alpha)^{\text{bed}} (E_\alpha)^{\text{eros}} \quad \text{(erosion)}\,, \\
\mathcal{M}_b^{\text{dep}} &= -\rho^+ \sum_\alpha c_\alpha^+ \left(w_\alpha^{s+} \boldsymbol{e}_z \cdot \boldsymbol{n}_b + \mathcal{U}_b \right) \quad \text{(deposition)}\,,
\end{aligned}
\tag{194}
$$

where N^* follows from the evaluation of the critical shear stress according to formula (153):

$$
N^* = \max_{\alpha=1,\dots,N} \left\{ \alpha \;\middle|\; (\tau_c^*)_\alpha < \frac{(II_{\boldsymbol{\sigma}_E})^{1/2}}{\Delta \rho g \mathfrak{d}_\alpha} \right\}_{\mathcal{S}_b} . \tag{195}
$$

Here $II_{\boldsymbol{\sigma}_E}$ is the second stress deviator invariant in the basal material evaluated at the basal surface. The parameterization for $\mathcal{M}_b^{\text{dep}}$ makes use of the terminal velocity of a particle in an ambient fluid field, $\boldsymbol{w}_\alpha^{s+}$, see (9) and (10). For particle class α this yields the mass flow $-\rho_\alpha^+ \boldsymbol{w}_\alpha^{s+} \cdot \boldsymbol{n}_b$ towards the basal surface. However, this surface itself moves with the displacement speed $\mathcal{U}_b$ in the direction of $\boldsymbol{n}_b$. Thus, the mass flow of class-α particles is $-\rho_\alpha^+ (\boldsymbol{w}_\alpha^{s+} \cdot \boldsymbol{n}_b + \mathcal{U}_b)$. Summation over all α-classes now yields the total depositing mass flow

$$
\mathcal{M}_b^{\text{dep}} = -\sum_\alpha \rho_\alpha^+ \left(\boldsymbol{w}_\alpha^{s+} \cdot \boldsymbol{n}_b + \mathcal{U}_b \right) \overset{\boldsymbol{w}_\alpha^s = w_\alpha^s \boldsymbol{e}_z}{=} -\rho^+ \sum_\alpha c_\alpha^+ \left(w_\alpha^{s+} \boldsymbol{e}_z \cdot \boldsymbol{n}_b + \mathcal{U}_b \right) ,
$$

which is $(194)_2$, and where expression (69) is to be substituted for w_α^s. When the shallowness approximation is justified then $\boldsymbol{e}_z \cdot \boldsymbol{n}_b \approx 1$.

With (191) and (192) the mass balance relations (173) and (171) can respectively be written as

$$
\begin{aligned}
&\frac{\partial \mu_\alpha}{\partial t} + (\mu_\alpha \boldsymbol{v}_{\mathcal{S}})^{\mathfrak{a}}{}_{;\mathfrak{a}} - \frac{\partial \mu_\alpha}{\partial \xi^{\mathfrak{a}}} w^{\mathfrak{a}} - 2\mu_\alpha \mathcal{U}_b K = \\
&\qquad - (\boldsymbol{j}_{\mathcal{S}\alpha})^{\mathfrak{a}}{}_{;\mathfrak{a}} + (-\boldsymbol{\phi}^{\rho_\alpha} \cdot \boldsymbol{n}_b)^+ - \rho_\alpha^+ \left(\underbrace{\boldsymbol{v}^+ \cdot \boldsymbol{n}_b - \mathcal{U}_b}_{} \right) + \frac{\rho_\alpha^{\text{bed}}}{\rho^{\text{bed}}} \mathcal{M}_b \,,
\end{aligned}
\tag{196}
$$

$$
\frac{\partial \mu}{\partial t} + (\mu \boldsymbol{v}_{\mathcal{S}})^{\mathfrak{a}}{}_{;\mathfrak{a}} - \frac{\partial \mu}{\partial \xi^{\mathfrak{a}}} w^{\mathfrak{a}} - 2\mu \mathcal{U}_b K = -\rho^+ \left(\underbrace{\boldsymbol{v}^+ \cdot \boldsymbol{n}_b - \mathcal{U}_b}_{} \right) + \mathcal{M}_b \,, \tag{197}
$$

for $\alpha = 1, \dots, N$. In these relations the underbraced term vanishes when the normal component of the barycentric velocity follows the displacement speed $\mathcal{U}_b$ of $\mathcal{S}_b$. If $\mathcal{M}_b$ is known as a function of space and time on $\mathcal{S}_b$, (196) and (197) are field equations for μ_α and μ. Of course, also $\mathcal{U}_b$ must be known; it is determined by $(191)_3$, (193), (194).

Equation (197) states that the time rate of change of the specific surface mass μ grows by the mass flow from the slurry, $[(\boldsymbol{v}^+ \cdot \boldsymbol{n}_b - \mathcal{U}_b) < 0]$ and by the erosion rate ($\mathcal{M}_b > 0$) from below. (Note, $\mathcal{M}_b$ contains both erosion and deposition, but $\mathcal{M}_b > 0$ is a net erosion.) For $\mu \equiv 0$ the two contributions on the right-hand sides of (196), (197) must balance. Equation (196) allows an analogous inference, but for constituent α a diffusive flow normal to $\mathcal{S}_b$ is added to this balance.

For the boundary condition of heat we proceed as for the traction boundary condition. In fact, we impose either a DIRICHLET or NEUMANN condition on the slurry side of $\mathcal{S}_b$. The simplest procedure is to impose

$$
T(x, y, z, t)|_{z=b(x,y,t)} = \Theta(x, y, t) \,,
$$

where $\Theta(x, y, t)$ is the temperature profile at the deepest position of the lake domain which is subject to the study. As an alternative the NEUMANN condition

$$\kappa \frac{\partial T}{\partial \boldsymbol{n}_b} = Q_\perp(x, y, z, t)|_{z=b(x,y,t)} \ ,$$

where $Q_\perp$ is the geothermal heat, can also be used.

There remains the formulation of boundary conditions along the lake shore and at the corresponding boundary lines on the surface $\mathcal{S}$.

For the domain of the particle laden fluid It is convenient to think that the lake domain is divided into a number of layers which are bounded by fixed horizontal surfaces. Identify the layers by the subscript k and let h_k be their thicknesses. In each layer we think the corresponding portion of basal surface to be replaced by a vertical wall. For $k = 1$ this wall defines the mathematical shore line. Along the vertical walls fields of unit vectors $\boldsymbol{N}_k$ can be introduced which lie in horizontal planes parallel to the (x, y)-plane. If no detritus moves, then $\boldsymbol{v}_{\mathcal{S}}^k = 0$ and $\mu_{\mathcal{S}}^k = 0$, and boundary conditions are given by

$$(h_k \rho_k \boldsymbol{v}_k) \cdot \boldsymbol{N}_k = \begin{cases} 0 \ , & \text{for impermeable wall,} \\ \mathfrak{M}_k \ , & \text{for discharge into ground;} \end{cases}$$

$$(h_k \boldsymbol{J}_k^\alpha) \cdot \boldsymbol{N}_k = \begin{cases} 0 \ , & \text{for impermeable wall,} \\ \mathfrak{M}_k^\alpha \ , & \text{for discharge of } \alpha\text{- mass into ground;} \end{cases}$$

$$(h_k \boldsymbol{Q}_k^{\epsilon,h}) \cdot \boldsymbol{N}_k = \begin{cases} 0 \ , & \text{for no heat loss,} \\ Q_k^{\text{geoth}} \ , & \text{for prescribed heat flow,} \end{cases} \qquad \text{or} \quad T_k = T_k^{\text{geoth}}.$$

The usual boundary conditions are those describing the ground as impermeable surface; else $\mathfrak{M}_k$ and $\mathfrak{M}_k^\alpha$ must be prescribed, which requires a model for the ground.

For the boundaries of the sediment 'layer' For the detritus layer the boundary value problem is that on a curved surface, which is bounded by a closed loop, most of which can be identified with the mathematical shore line. Because of the Fick-type diffusive constitutive relations for the constituent mass fluxes $\boldsymbol{j}_{\mathcal{S}\alpha}$ and the NAVIER-STOKES-type stress parameterizations for $S^{\mathfrak{a}b}$ closure conditions are analogous to those of the three-dimensional case. However no boundary condition must be formulated for the surface heat flow in our case, because energy considerations have been left unspecified. So, let $\mathcal{C}$ be a loop along the mathematical shore line (including a segment of the river bank and across the tributary). Define by $\boldsymbol{h}$ the unit vector field along $\mathcal{C}$ which is tangent to $\mathcal{S}$ and perpendicular to $\mathcal{C}$. With $\boldsymbol{v}_{\mathcal{S}}$, the barycentric surface velocity vector, and $\boldsymbol{j}_{\mathcal{S}\alpha}$ the surface mass flux, we may now write

$$\boldsymbol{j}_{\mathcal{S}\alpha} \cdot \boldsymbol{h} = \begin{cases} 0 \ , & \text{along } \mathcal{C} \text{ where } \boldsymbol{v}_{\mathcal{S}} = \boldsymbol{0}, \\ -\mathfrak{m}_{\mathcal{S}}^\alpha \ , & \text{along } \mathcal{C}, \text{ where wash-load enters the lake from the tributary ;} \end{cases}$$

$$(\mu \boldsymbol{v}_{\mathbb{S}}) \cdot \boldsymbol{h} = \begin{cases} 0 & , \text{ at the shore segments where } \boldsymbol{v}_{\mathbb{S}} \text{ is tangential to the shore,} \\ -\left(\sum_\alpha \mathfrak{m}_{\mathbb{S}}^\alpha + \mathfrak{m}^f\right) & , \text{ at the river cross section.} \end{cases}$$

5 Transformation of the surface mass distribution into a detritus layer thickness

From a practical point of view the surface mass densities of the sediment classes μ_α ($\alpha = 1, \ldots, N$) are not very useful variables. Better is the determination of the thickness h of the detritus layer; so, let us assume

$$\mu = \rho_s \nu_{\text{mean}}\, h\,, \quad \nu_{\text{mean}} \equiv \sum_\alpha \nu_{\text{mean}}^\alpha\,,$$

where ρ_s is the true density of the sand, and ν_{mean}^α are mean values of the solid volume fractions of the sediment classes $\alpha = 1, \ldots, N$ in the detritus layer. Note that $\nu_{\text{mean}} = (1 - n)$, where n is the average porosity within the detritus layer. Subsequently, the thickness of the detritus layer follows from

$$h = \frac{\mu}{\rho_s \nu_{\text{mean}}}\,, \tag{198}$$

and our aim is to provide a model for ν_{mean}[31].

First, we consider that the detritus layer has linear volume fraction and velocity distributions across its thickness. The expectations are that the linear volume fraction through the layer has a maximum at the bottom and a minimum at the top. Similarly, the layer velocity vanishes at the bottom and reaches a maximum at the top surface, u_{max}, see Fig. 11. So, their distributions are given by

$$\nu = \frac{\nu_{\text{min}} - \nu_{\text{max}}}{h}\, z + \nu_{\text{max}}, \quad u = \frac{u_{\text{max}}}{h}\, z\,. \tag{199}$$

As the figure shows, the layer may become instable if it is sufficiently sheared from above. A RICHARDSON number dependence of the mean volume fraction in an arbitrary detritus layer (i.e., not necessarily as in Fig. 11) is then suggested.

So, still referring to Fig. 11, we define

$$Ri = \frac{-\dfrac{1}{\rho_{\text{mean}}}\dfrac{\mathrm{d}\,\rho}{\mathrm{d}z}\, g}{\left(\dfrac{\mathrm{d}u}{\mathrm{d}z}\right)^2} = \frac{-\dfrac{1}{\nu_{\text{mean}}}\dfrac{\mathrm{d}\,\nu}{\mathrm{d}z} g}{\left(\dfrac{\mathrm{d}\,u}{\mathrm{d}z}\right)^2} = \left\{\frac{2(\nu_{\text{max}} - \nu_{\text{min}})}{\nu_{\text{max}} + \nu_{\text{min}}}\right\} \frac{gh}{u_{\text{max}}^2}\,, \tag{200}$$

where $\nu_{\text{mean}} \equiv (\nu_{\text{max}} + \nu_{\text{min}})/2$ has been used. For particular values of ν_{min}, ν_{max}, u_{max}, the RICHARDSON number Ri is a function of the thickness h: $Ri = Ri(h)$. Now, our assumption for the mean volume

[31] If we assume $\mu_\alpha = \rho_s \nu_{\text{mean}}^\alpha h$, then the mean volume fractions ν_{mean}^α are known once the height h is known: $\nu_{\text{mean}}^\alpha = \mu_\alpha/(\rho_s h)$; or, equivalently, if ν_{mean} is known, see (198): $\nu_{\text{mean}}^\alpha = (\mu_\alpha/\mu)\nu_{\text{mean}}$. For the detritus layer the mean volume fractions ν_{mean}^α are practically better quantities than the surface densities μ_α.

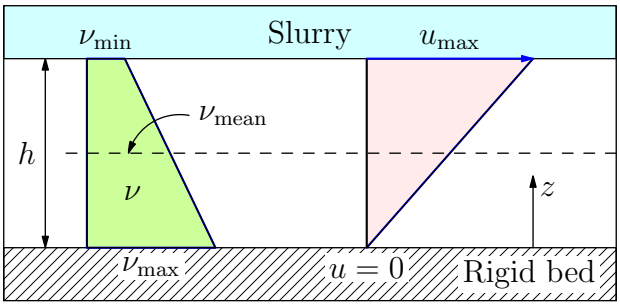

Figure 11: Detritus layer with thickness h. Distribution of the volume fraction ν and detritus velocity u as functions of z.

fraction in an arbitrary detritus layer is

$$\nu_{\text{mean}} = \nu_{\text{mean}}(Ri(h))\,.$$

When inserted into (198), this yields an equation for the determination of h:

$$\frac{\mu}{\rho_s h} = \nu_{\text{mean}}(Ri(h))\,. \tag{201}$$

Moreover, with an obvious reminiscence to the KELVIN-HELMHOLTZ instability of two stratified viscous fluids with different constant densities under simple shear, MILES [28] (1967), we suppose a Ri-dependence as shown in Fig. 12. This function can qualitatively and quantitatively be given as

$$\begin{aligned} \nu_{\text{mean}} &= \tfrac{1}{2}(\nu_{\text{top}} + \nu_{\text{bottom}}) + a\tanh\left(b(Ri - Ri^{\text{crit}})\right)\,, \\ a = \tfrac{1}{2}(\nu_{\text{top}} - \nu_{\text{bottom}})\,, &\quad b = \tfrac{1}{\varepsilon}\,\text{atanh}\left\{\frac{2s\,\nu_{\text{top}} - (\nu_{\text{top}} + \nu_{\text{bottom}})}{\nu_{\text{top}} - \nu_{\text{bottom}}}\right\}\,. \end{aligned} \tag{202}$$

Here, $0 < \varepsilon < 1$, $0 \ll s < 1$, and a, b are so adjusted that

$$\begin{aligned} Ri \to \infty \quad &\longrightarrow \quad \nu_{\text{mean}} = \nu_{\text{top}}\,, \\ Ri \to -\infty \quad &\longrightarrow \quad \nu_{\text{mean}} = \nu_{\text{bottom}}\,, \\ Ri = Ri^{\text{crit}} \quad &\longrightarrow \quad \nu_{\text{mean}} = \nu_{\text{crit}} \equiv \tfrac{1}{2}(\nu_{\text{top}} + \nu_{\text{bottom}})\,, \\ Ri = Ri^{\text{crit}} + \varepsilon \quad &\longrightarrow \quad \nu_{\text{mean}} = s\,\nu_{\text{top}}\,. \end{aligned}$$

The modeler can pick values for ν_{top}, ν_{bottom}, Ri^{crit}, ε and s. Suggestions are given in Table 7. Obviously, for a Newtonian fluid Ri^{crit} is the value of the RICHARDSON number below which instability sets in.

With the parameterization (202), relation (201) becomes a nonlinear equation for h, which is easily seen to possess a unique solution. An iterative solution h is best found as

$$h^{(m+1)} = \frac{\mu}{\rho_s \nu_{\text{mean}}(Ri(h^{(m)}))}\,, \quad h^{(0)} = \frac{2\mu}{\rho_s(\nu_{\text{top}} + \nu_{\text{bottom}})}\,,$$

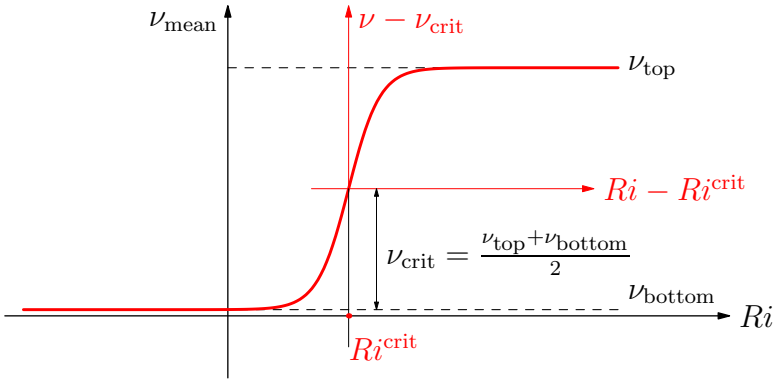

Figure 12: Qualitative behaviour of the mean volume fraction ν_{mean} of the mixture.

Table 7: Suggested values for the parameters in equation (202).

$\nu_{\text{top}} = 0.8$	$Ri^{\text{crit}} = 0.25$	$\nu_{\text{bottom}} = 0.02$	$\varepsilon = 0.02$	$s = 0.98$

and computations are interrupted when

$$\left| h^{(m+1)} - h^{(m)} \right| \ll 1 \,.$$

This computation must be performed for all x, y and each time step t.

6 Discussion and Conclusion

In this article transport of sediments in suspension and in the detritus layer of an alluvial river-lake (or ocean) system was analyzed from a perspective of global processes, taking place in the lake or ocean basin, on the one hand, and in the moving or stagnant detritus layer at the bottom of the water body, on the other hand. These two regimes interact at their common boundary via erosion of sediments from the basal surface or as deposition of wash-load to the rigid bed. The suspended sediment fractions are transported by the wind-induced barotropic or baroclinic circulation of the homogeneous or density stratified lake or ocean water. These sediment fractions are carried into the lake as wash loads from river inlets. The bed-load detritus, on the other hand, is carried into the estuarine environment of the lake and contributes thereby its deposition to deltaic formations. In the vicinity of the river mouth both sediment formations are subjected to a new flow regime, which is governed by large scale circulation dynamics, in which the current speeds are generally smaller. This leads to an enhanced sedimentation of the coarser grain fractions and associated aggradation with progressing delta formations.

Whereas on decadal time scales the important regions of such land aggradation in oceans is restricted to estuarine zones, these zones may in lakes extend over substantial portions of the basins or the entire lake. This is particularly so for artificial reservoirs and mountainous terrain. Rigorous models on this complex detritus-particle-laden fluid interaction are still missing. It was our intention to present in this memoir the foundation for a class of such models as a basis for later use in attempts of software developments for sediment transport of this sort.

To this end, the lake domain was divided into two regions, the actual water domain with suspended

(non)-buoyant particles, called also slurry, and the detritus layer with moving sediments, also a solid-fluid mixture, but very thin. Because of its thinness, this layer was collapsed into an infinitely thin moving and deforming surface, covered by a mixture of the N sediment classes α $(= 1, \ldots, N)$ and a fluid. This mixture moves along the surface, with each constituent having its own tangential velocity, and thus intermixing with the others by surface parallel diffusion. However, further mass exchanges with the slurry above and the ground below takes also place as erosion and deposition processes. The mathematical description of this local interaction problem turned out to be rather subtle, even in the simplest possible form as dealt with here.

In the slurry domain (domain I in Fig. 3), the governing field equations for the lake as a particle laden fluid are handled as a continuous mixture of class I, i.e., the balance laws of mass are formulated for the sediment classes α $(= 1, \ldots, N)$ and the mixture as a whole, but balances of linear momentum and energy are only formulated for the mixture as a whole. This is done for a nearly density preserving fluid, whose density changes due to variations of the temperature, mineralization and pressure but also the distribution of the wash-load. The formulation is also complicated by the presence of turbulence. As a consequence, a considerable number of approximate models exists, all of which are claimed to be relevant to describe the three-dimensional circulation dynamics, including dispersion of the suspended wash-load. They differ in certain terms but the differences are seldom explained in the context of their physical implications. We have tried to close this gap.

Two model families were presented. In *model family 1*, referenced as generalized BOUSSINESQ models, two subfamilies were distinguished:

- In the *classical* BOUSSINESQ *assumption* variations of the density are ignored, except in the gravity term. This implies that the velocity field is solenoidal. This property is preserved also when turbulence averaging is performed and averaged equations are looked at.

- A *generalized* BOUSSINESQ *fluid* is defined by a mixture-density composition, $\rho = \rho_0(z) + \rho_d(\boldsymbol{x}, t)$, in which $\rho_d(\boldsymbol{x}, t)$ is ignored everywhere except in the gravity term. In this case the mass flux or momentum density $\rho_0 \boldsymbol{v}(\boldsymbol{x}, t)$ is solenoidal. This property is also preserved in the turbulent-averaged equations.

Model family 2 is based on the assumption of small turbulent density variations; it was coined by us

- *Small density fluctuation assumption.* It is based on the assumption that approximations are only introduced after the turbulent averaging operations have been performed with the compressible governing equations. Then, with $\rho = \langle \rho \rangle + \rho'$, every correlation term $\langle \rho' a \rangle$ is ignored. This assumption implies that the averaged mass balance of the mixture is preserved, see (39). So, acoustic waves can be studied in a turbulent fluid as can the influence of the pressure dependence of the equation of state, both effects which may be significant in very deep lakes.

A further popular approximation is the Shallow Water Approximation (SWA), in which the ratio of typical depth to length scales is used as a perturbation parameter $\mathcal{A}$ and the lowest order approximation to the reduced equations in the limit $\mathcal{A} \to 0$ is constructed. This implies that the vertical momentum balance reduces to a force balance between the gravity force and the vertical pressure gradient. This approximation is known as the *hydrostatic pressure assumption*. Moreover, the divergence of the stress

deviator, and the divergences of the heat flux and the species mass fluxes reduce to

$$\frac{\partial\,\tau_{xz}}{\partial\,z},\quad \frac{\partial\,\tau_{yz}}{\partial\,z},\quad \frac{\partial\,Q_z^{\epsilon,h}}{\partial\,z},\quad \frac{\partial\,\mathfrak{J}_z^{\alpha}}{\partial\,z},$$

whilst all other terms drop out. Both assumptions are today regarded as critical. An in-between compromise, which is sometimes used, still employs the hydrostatic pressure assumption but accounts for the horizontal stress, heat flux and species mass flux gradients. The modern trend, however, abandons the SWA altogether. These formulations are known as *non-hydrostatic models*. They are certainly needed in the aftermaths of incessant heavy rain fall with strong detritus and wash-load discharge from a river into the river-mouth region, when strong up- and down-welling are likely to occur, see Fig. 13. In such systems it may be advantageous to employ nesting, where a simpler model is used for the circulation dynamics of the entire lake, and the river-inlet environs are analyzed with a more complex model subject to the current, pressure, temperature, etc., input along the open boundary. A word of caution or alertness

Figure 13: Sediment laden water in the forefront of the estuary mouth of the river Rhine (Alpen-Rhein) at Fussach near Bregenz, Austria. The picture demonstrates that up-welling and down-welling processes must be active, indicating that the Shallow Water Approximation in computational software should not be applied. A full non-hydrostatic three dimensional model is required. Copyright: 'Tino Dietsche - airpics4you.ch'

concerns the formulation of the heat equation (first law of thermodynamics), which has consistently been given in two different forms, one in which the caloric potential is the HELMHOLTZ free energy (and the energy equation is written in terms of this free energy), and a second one, where the potential is the free enthalpy. As explained in the appendix, if ρ and T are the independent thermodynamic variables, then the heat equation is based on the free energy formulation, and, strictly in this case, the thermal equation of state has the form $p = p(\rho, T)$. Alternatively, if p and T are the independent thermodynamic variables, then $\rho = \rho(p, T)$ is the appropriate thermal equation of state and the energy is expressed in terms of the free enthalpy. In applications confusion may arise, since for most situations the thermal equation of state is given as $\rho = \rho(T)$ without a pressure dependence. In these cases it is irrelevant which energy equation

is employed, the enthalpy formulation would be logical. Luckily it does not matter, since numerical values for the specific heats c_v and c_p are nearly the same.

Closure relations of the flux terms in the slurry have consistently been proposed as being of gradient type. A critical point in this formulation concerns only the constituent mass fluxes $\mathfrak{J}_\alpha$, defined in (8). These mass fluxes are written as compositions of two contributions, (i) a diffusive flux due to the difference of the velocity of particles of the same class relative to a representative particle velocity within this same sediment class plus a slip velocity of this representative particle of class α to the barycentric velocity of the mixture at the same position, which is fundamentally related to the free fall velocity of the representative particle in still water. Even though this latter choice is questionable in its own right,[32] this kind of parameterization tries to explicitly account for the convective motion of the non-buoyant particles and the diffusive nature of the analogous process due to particle size differences in the same sediment class.

Domain II is in reality a very thin layer of a granular fluid mixture with N sediment classes and an interstitial fluid at saturation. This system has been collapsed in our theoretical formulation into a moving singular surface with surface particles being equipped with surface masses, momenta, etc. This procedure is tantamount to replacing a mixture layer and its top and bottom boundary by a sharp interface, which is equipped with surface mass and evolves under the influence of the sedimentation and erosion processes. As a first approach, we have assumed this interface to be a material surface, being aware that in reality it is nourished from above and below by settling and eroding particles. Essential in this approach was the surface balance law (132), which is based on the transport theorem (130), valid for material surfaces.

The complications with the above described boundary conditions are connected with the fact that N surface sediment classes are introduced, which each may have its own motion tangential to the deforming surface, whose motion is defined by the kinematic equation of motion. If on either side of the deforming surface simple constituent continua are present, the possible surface material is also a simple constituent continuum. Then, the subtle issue is that the geometric motion of the surface from its reference state to its present state and given by the kinematic equation of the surface moving with the velocity $\boldsymbol{w}$, is not the same as the motion of a material body, geometrically-kinematically constrained to the surface, but free to move and deform tangentially to the surface with the material velocity $\boldsymbol{v}_{\mathcal{S}}$. The two are related by (see Fig. 10)

$$\boldsymbol{v}_{\mathcal{S}} = \dot{\xi}^{\mathfrak{a}} \boldsymbol{\tau}_{\mathfrak{a}} + \boldsymbol{w} \quad \longrightarrow \quad \boldsymbol{v}_{\mathcal{S}} \cdot \boldsymbol{n} = \boldsymbol{w} \cdot \boldsymbol{n} \,,$$

were $(\xi^1, \xi^2) \in \tilde{\Delta}$ is the coordinate cover of the moving surface $\mathcal{S}$ and $\boldsymbol{\tau}_{\mathfrak{a}}$ are the base vectors $\boldsymbol{\tau}_{\mathfrak{a}} = \partial \boldsymbol{r} / \partial \, \xi^{\mathfrak{a}}$, with $\boldsymbol{x} = \boldsymbol{r}(\xi^1, \xi^2, t)$. With these prerequisites the derivation of the local surface balance law for a physical quantity (132) from the corresponding global form (129) due to SLATTERY et al. (2007) [40] is more general than corresponding equations of earlier surface models for which $\boldsymbol{v}_{\mathcal{S}} = \boldsymbol{w}$ was assumed, see e.g. MÜLLER (1985) [30], or for which $\boldsymbol{w} = \mathcal{U}\boldsymbol{n}$ is assumed, see e.g. ALTS and HUTTER (1988) [2]–[5] and references therein. The more general equation has then served as master equation for the derivation of the physical balance laws for the surface-detritus-water mixture involving among others, the surface mass densities μ_α, μ and velocities $\boldsymbol{v}_{\mathcal{S}\alpha}$, $\boldsymbol{v}_{\mathcal{S}}$ ($\alpha = 1, \ldots, N$), such that $\boldsymbol{v}_{\mathcal{S}\alpha} \cdot \boldsymbol{n}_b = \boldsymbol{v}_{\mathcal{S}} \cdot \boldsymbol{n}_b = \mathcal{U}_b$. These equations also contain the surface jump quantities from the bulk fields which represent, for mass balance

[32] The determination of the velocity of a particle in a moving and perhaps accelerating fluid field relative to the velocity of the fluid at the same position before the latter was inserted in the fluid, is a complex topic of fluid dynamics which does not, in general, agree with the free fall velocity.

physically the deposition and erosion rates and, for momentum balance laws the traction and impulse jump quantities. Parameterization of erosion consisted of two statements, (i) a criterion defining the onset of erosion of sediments of grain class α and (ii) a statement of the amount of eroded material. Reviews for both have been provided.

A conceptually decisive decision in connection with the detritus motion is whether a surface mixture theory of class II ought to be pursued or a less complicated mixture model of class I should be employed. The latter makes only use of the balance law of momentum for the mixture as a whole, but mass balances of all constituents, and it is technically simpler. The constituent surface velocities have been eliminated by introducing the diffusive surface-mass flux

$$\boldsymbol{j}_{\mathbb{S}\alpha} \equiv \mu_\alpha(\boldsymbol{v}_{\mathbb{S}\alpha} - \boldsymbol{v}_{\mathbb{S}}) = \mu_\alpha(\boldsymbol{v}_{\mathbb{S}\alpha} - \boldsymbol{v}_{\mathbb{S}})_{\|}$$

as a new variable of the sediment class α and writing a FICK-type constitutive relation for it. If the class α-velocity needs to be computed, this can a posteriori be done by

$$\boldsymbol{v}_{\mathbb{S}\alpha\|} = \frac{1}{\mu_\alpha}\boldsymbol{j}_{\mathbb{S}\alpha} + \boldsymbol{v}_{\mathbb{S}\|}\,.$$

The surface mixture momentum balance law entailed the parameterization of the surface parallel stress components S^{ab}, which were postulated as a two-dimensional linear viscous fluid with areal compressibility (but vanishing resistance to expansion). This avoids build-up of cohesion.

Further closure relations were needed in the form of detritus interface sliding laws from above and below and values of the particle concentrations c_α^+ ($\alpha = 1, \ldots, N$) immediately above the detritus interface. These are N statements, which were postulated in terms of surface balance laws (188), each involving a FICKian gradient postulate for its flux quantity and N production terms. These balance relations for the boundary value of c_α^+ are likely the most esoteric feature of the model and call for the application and the use of the entropy principle and experiments to constraining the coefficients. A last set of relations completing the theory are explicit relations for the erosion and deposition rates, (194).

To treat the dynamics of the detritus layer by concepts of sharp interfaces is a simplification. In reality the detritus region is a thin layer of finite thickness, which is sheared by the bottom near flow of the wind induced motion of the lake water. By mimicking the thin detritus region as a sheared layer with linear volume fraction and velocity distributions across the layer and assuming the mean volume fraction in this layer to depend on the RICHARDSON number with stable and unstable regimes, the detritus layer thickness can be evaluated, see (198), and its transition from stable (and thin) to unstable (and thick) regimes be estimated.

To summarize, this theory of sediment transport in alluvial systems is fairly substantial but the modeler has some freedom to adjust its complexity somewhat by selecting the number of sediment classes when approximating the grain size distribution curve. There is also some flexibility in selecting the model equations for the lake circulation flow as a slurry and in the application of sub-structuring techniques by dividing the lake domain in subdomains with and without detritus transport. However, apart from these simplifications and some variation in the constitutive postulates the presented equations likely constitute the minimum complexity accounting for the essential physics. Further extensions are possible and have transpired in the derivation of the model. For instance, in (176) the momentum equation perpendicular to the moving detritus interface was presented, but it was ignored. Paired with additional closure state-

ments involving jumps of bulk fields across $\mathcal{S}$, this equation is interpreted as an evolution equation for the displacement speed $\mathcal{U}_b$. When used, it would make postulation of deposition and entrainment rates obsolete. This fact would give sediment transport theories a completely different structure from what it has been so far. Moreover, the entire concept could also be pursued with a mixture of class II with all of its consequences. Presently the most urgent activities would be validation of the model by parameter identification, development of software for its use and application to realistic cases, such as that shown in Figs. 1, 2, 13.

Acknowledgment The authors thank Prof. Rutschmann for publication of this work in his 'Mitteilungen' and Dr. D. Vetsch for commenting on an earlier version of this text. They also thank Dr. F. Zunic and his crew for handling all editing details. While performing this work we have been self-supporting.

Appendix

A Implications from the Second Law of Thermodynamics

This appendix gives a justification for the approximation (44). The results which are presented can be taken from any book on thermodynamics, e.g. Hutter (2003) [16]. The basis of the considerations is the so-called GIBBS relation of a heat conducting fluid,

$$\mathrm{d}\eta = \frac{1}{T}\left(\mathrm{d}\epsilon - \frac{p}{\rho^2}\,\mathrm{d}\rho\right)\,, \tag{203}$$

in which η is the entropy, T the KELVIN temperature, ϵ the internal energy, p the pressure and ρ the fluid density; (203) is a consequence of the second law of thermodynamics. Solving (203) for $\mathrm{d}\epsilon$,

$$\mathrm{d}\epsilon = T\mathrm{d}\eta + \frac{p}{\rho^2}\,\mathrm{d}\rho\,, \tag{204}$$

identifies ϵ as a function of η and ρ, so that, alternatively and with $\epsilon = \hat{\epsilon}(\eta,\rho)$,

$$\mathrm{d}\epsilon = \frac{\partial\,\hat{\epsilon}}{\partial\,\eta}\,\mathrm{d}\eta + \frac{\partial\,\hat{\epsilon}}{\partial\,\rho}\,\mathrm{d}\rho\,. \tag{205}$$

Comparison of (204) and (205) implies

$$T = \frac{\partial\,\hat{\epsilon}}{\partial\,\eta}\,,\quad p = \rho^2\,\frac{\partial\hat{\epsilon}}{\partial\,\rho}\,. \tag{206}$$

The internal energy, interpreted as a function of entropy η and density ρ, is a thermodynamic potential for the absolute temperature and the pressure.

With the functions

$$\psi = \epsilon - T\eta \quad \text{HELMHOLTZ free energy},$$

$$h = \epsilon + \frac{p}{\rho} \qquad \text{enthalpy}, \tag{207}$$

$$g = h - T\eta \quad \text{GIBBS free energy},$$

(these are LEGENDRE transformations) the GIBBS relation (204) takes the alternative forms

$$\begin{aligned} \mathrm{d}\psi &= -\eta \mathrm{d}T + \frac{p}{\rho^2}\,\mathrm{d}\rho \quad \longrightarrow \quad \psi = \hat{\psi}(T,\rho)\,, \\ \mathrm{d}h &= -T\mathrm{d}\eta + \frac{1}{\rho}\,\mathrm{d}p \quad \longrightarrow \quad h = \hat{h}(\eta,p)\,, \\ \mathrm{d}g &= -\eta \mathrm{d}T + \frac{1}{\rho}\,\mathrm{d}p \quad \longrightarrow \quad g = \hat{g}(T,p)\,. \end{aligned} \tag{208}$$

With the indicated different dependencies and the obvious potential properties, analogous to (206), we have

$$\begin{aligned} \eta &= -\frac{\partial\,\hat{\psi}}{\partial\,T}\,, \quad p = \rho^2 \frac{\partial\,\hat{\psi}}{\partial\,\rho}\,, \\ T &= -\frac{\partial\,\hat{h}}{\partial\,\eta}\,, \quad \frac{1}{\rho} = \frac{\partial\,\hat{h}}{\partial\,p}\,, \\ \eta &= -\frac{\partial\,\hat{g}}{\partial\,T}\,, \quad \frac{1}{\rho} = \frac{\partial\hat{g}}{\partial\,p}\,, \end{aligned} \tag{209}$$

and the integrability conditions

$$\begin{aligned} -\frac{\partial\,\eta}{\partial\,\rho} &\equiv \frac{\partial}{\partial\,T}\left(\frac{p}{\rho^2}\right) \quad \text{for} \quad \hat{\psi}(T,\rho)\,, \\ -\frac{\partial\,T}{\partial\,p} &\equiv \frac{\partial}{\partial\,T}\left(\frac{1}{\rho}\right) \quad \text{for} \quad \hat{h}(T,p)\,, \\ -\frac{\partial\,\eta}{\partial\,p} &\equiv \frac{\partial}{\partial\,T}\left(\frac{1}{\rho}\right) \quad \text{for} \quad \hat{g}(T,p)\,. \end{aligned} \tag{210}$$

Internal energy formulation

If we regard T and ρ as the independent thermodynamic variables, then according to $(207)_1$ we have

$$\epsilon = \psi - T\frac{\partial\,\psi}{\partial\,T} = -T^2\frac{\partial}{\partial\,T}\left(\frac{\psi}{T}\right)\,, \tag{211}$$

and therefore,

$$\rho\frac{\mathrm{d}\epsilon}{\mathrm{d}\,t} = \rho\,c_v\frac{\mathrm{d}T}{\mathrm{d}\,t} + \rho\,c_{T\rho}\frac{\mathrm{d}\rho}{\mathrm{d}\,t}\,,$$
$$c_v := -\frac{\partial}{\partial\,T}\left(T^2\frac{\partial}{\partial\,T}\left(\frac{\hat{\psi}}{T}\right)\right) = \frac{\partial\,\hat{\epsilon}}{\partial\,T}\,, \tag{212}$$
$$c_{T\rho} := -T^2\frac{\partial}{\partial\,T}\left(\frac{\partial\,\hat{\psi}/\partial\,\rho}{T}\right) = \frac{\partial\,\hat{\epsilon}}{\partial\,\rho}\,.$$

With the separation assumption

$$\psi = \hat{\psi}_T(T) + \hat{\psi}_\rho(\rho)\,, \tag{213}$$

$c_v = \hat{c}_v(T)$ and $c_{T\rho} = \hat{c}_{T\rho}(\rho) = \mathrm{d}\hat{\psi}_\rho/\mathrm{d}\,\rho$. Therefore, $(212)_1$ can be written as

$$\rho\frac{\mathrm{d}\epsilon}{\mathrm{d}\,t} = \rho\,\hat{c}_v(T)\frac{\mathrm{d}\,T}{\mathrm{d}\,t} + \underbrace{\rho\frac{\mathrm{d}\hat{\psi}_\rho}{\mathrm{d}\,\rho}\frac{\mathrm{d}\,\rho}{\mathrm{d}\,t}}_{\text{nearly }0} \approx \rho\hat{c}_v(T)\frac{\mathrm{d}\,T}{\mathrm{d}\,t}\,. \tag{214}$$

The second term on the right-hand side of (214) can be ignored since density veriations in a nearly incompressible fluid are minute.

Enthalpy formulation If we regard T and p as the independent thermodynamic variables, the GIBBS free energy is the thermodynamic potential and the enthalpy the adequate internal energy function. In view of (208) we now have

$$h = g - T\frac{\partial\,g}{\partial\,T} = -T^2\frac{\partial}{\partial\,T}\left(\frac{g}{T}\right)\,, \tag{215}$$

and therefore,

$$\rho\frac{\mathrm{d}h}{\mathrm{d}\,t} = \rho\,c_p\frac{\mathrm{d}T}{\mathrm{d}\,t} + \rho\,c_{Tp}\frac{\mathrm{d}p}{\mathrm{d}\,t}\,,$$
$$c_p := -\frac{\partial}{\partial\,T}\left(T^2\frac{\partial}{\partial\,T}\left(\frac{\hat{g}}{T}\right)\right) = \frac{\partial\,\hat{h}}{\partial\,T}\,, \tag{216}$$
$$c_{Tp} := -T^2\frac{\partial}{\partial\,T}\left(\frac{1}{T}\frac{\partial\,g}{\partial\,p}\right) = \frac{\partial\,\hat{h}}{\partial\,p}\,.$$

With the separation assumption

$$h = \hat{g}_T(T) + \hat{g}_p(p)\,, \tag{217}$$

we have $c_p = \hat{c}_p(T)$ and $c_{Tp} = \hat{c}_{Tp}(p) = \mathrm{d}\hat{g}_p/\mathrm{d}\,p$. Therefore, $(203)_1$ can be written as

$$\rho\frac{\mathrm{d}h}{\mathrm{d}\,t} = \rho\,\hat{c}_p(T)\frac{\mathrm{d}\,T}{\mathrm{d}\,t} + \underbrace{\rho\frac{\mathrm{d}\hat{g}_p}{\mathrm{d}\,p}\frac{\mathrm{d}\,p}{\mathrm{d}\,t}}_{\text{nearly }0} \approx \rho\hat{c}_p(T)\frac{\mathrm{d}T}{\mathrm{d}\,t}\,. \tag{218}$$

Here the second term on the right-hand side can be ignored, since $\mathrm{d}\hat{g}_p/\mathrm{d}p$ must be very small, the growth of the enthalpy due to a pressure rise cannot be large as its working is due to dilatational deformations, which are small.

Parameterizations Because the temperature range of lake or ocean water is small, $0°\mathrm{C} \leqslant T \leqslant 50°\mathrm{C}$, the coefficients c_v and c_p exhibit a constrained variability and may well be assumed to be constant or

linear functions of T. This then suggests to use

- for constant specific heats,

$$\epsilon = \int_{T_0}^{T} c_v(\bar{T})\,\mathrm{d}\bar{T} = c_v^0(T - T_0) + \epsilon_0\,, \quad h = \int_{T_0}^{T} c_p(\bar{T})\,\mathrm{d}\bar{T} = c_p^0(T - T_0) + h_0\,, \tag{219}$$

- for specific heats as linear functions of T:

$$\begin{aligned} \epsilon &= \int_{T_0}^{T} [c_v^0 + c_v'(\bar{T} - T_0)]\,\mathrm{d}\bar{T} = c_v^0(T - T_0) + \frac{1}{2}c_v'(T - T_0)^2 + \epsilon_0\,, \\ h &= \int_{T_0}^{T} [c_p^0 + c_p'(\bar{T} - T_0)]\,\mathrm{d}\bar{T} = c_p^0(T - T_0) + \frac{1}{2}c_p'(T - T_0)^2 + h_0\,. \end{aligned} \tag{220}$$

The expressions (214), (218) (219), (220) provide a thermodynamic justification of relations (44).

B Turbulent closure by Large Eddy Simulation

Large Eddy Simulation (LES) is another popular approach for simulating turbulent flows. In this technique the large, geometry-dependent eddies are explicitly accounted for by using a subgrid-scale (SGS) model. Equations (76)–(80) are now interpreted as resolved field equations obtained by applying a non-statistical filter to the NAVIER-STOKES equations.[33]

The effect of the small eddies on the resolved filtered field is included in the SGS-parameterization of the stress $\boldsymbol{R}$, as shown in (52) but now given by

$$\boldsymbol{R} = 2\rho\nu_{SGS}\boldsymbol{D}, \quad \operatorname{tr}\boldsymbol{D} = 0\,, \tag{221}$$

where ν_{SGS} is the SGS-turbulent viscosity,

$$\nu_{SGS} \equiv (C_s\Delta)^2 \left(\operatorname{tr}\left(2\boldsymbol{D}^2\right)\right)^{1/2}\,. \tag{222}$$

This parameterization is due to SMAGORINSKY (1963) [41]. C_s is a dimensionless coefficient, called SMAGORINSKY constant, and Δ is a length scale, equal to the local grid spacing. Thus, (221) with (222) is the classical viscous power law relating stress and stretching. According to KRAFT et al. [23], the above 'model is found to give acceptable results in LES of homogeneous and isotropic turbulence. With $C_s \approx 0.17$ according to LILLY (1967) [25], it is too dissipative [...] in the near wall region because of the excessive eddy-viscosity arising from the mean shear (MOIN & KIM (1982) [29]). The eddy viscosity predicted by SMAGORINSKY is nonzero in laminar flow regions; the model introduces spurious dissipation which damps the growth of small perturbations and thus restrains the transition to turbulence (PIOMELLI & ZANG (1991) [33]).

The limitations of the SMAGORINSKY model have led to the formulation of more general SGS models. The best known of these newer models may be the dynamic SGS (DSGS) model of GERMANO et al. (1991) [12]. In this model C_s is not a fixed constant but is calculated as a function of position and time, $C_s(\mathbf{x}, t)$, which vanishes near the boundary with the correct behaviour (PIOMELLI (1993) [32], [23]).

[33] Such a filter need not to fulfil the condition $\langle\langle\cdot\rangle\rangle = \langle\cdot\rangle$, where $\langle\cdot\rangle$ is the filter operation.

The parameterisations for the energy flux, $\boldsymbol{Q}_\epsilon$ and constituent mass fluxes, $\boldsymbol{J}_\alpha$, are the same as stated in $(52)_{2,3}$, however, with ν_{SGS} evaluated as given in (222). It is also evident from this presentation that the $(k-\varepsilon)$ - equations are not needed.

C Justification for (150)

In this appendix we provide a derivation of formula (150) for erosion inception on the basis of dimensional analysis. We consider sediment transport at a lake basal surface. It is rather intuitive that the erosion inception will likely depend on a stress (the shear stress) on the lake side of the basal surface, τ_c, the true densities, ρ_s, ρ_f, of the sediment grains and the fluid, the solid concentration, c_s, gravity acceleration, g, mixture kinematic viscosity, ν, and the nominal diameter, $\mathfrak{d}$, of the sediment corn, all evaluated at the base. So, inception of sediment transport can likely be described by an equation of the form

$$f(\tau_c, \rho_s, \rho_f, g, \mathfrak{d}, \nu, c_s) = 0\,. \tag{223}$$

The dimensional matrix of the above 7 variables has rank 3; so, there are 4 independent dimensionless π-products, which we choose as follows:

$$\pi_1 = \frac{\tau_c}{\Delta\rho\, g\, \mathfrak{d}}\,, \quad \pi_2 = \frac{\rho_s}{\rho_f}\,, \quad \pi_3 = c_s\,, \quad \pi_4 = \Big(\frac{g}{\Delta\nu^2}\Big)^{1/3}\mathfrak{d}\,, \tag{224}$$

where ρ is the mixture density and $\Delta \equiv (\rho_s/\rho - 1)$. Here, τ_c has been scaled with the 'submerged' density $(\rho_s - \rho)$. Furthermore, it is not difficult to see that for small c_s the mixture density in (224) may approximately be replaced by ρ_f. We may thus write

$$f(\pi_1, \pi_2, \pi_3, \pi_4) = 0 \quad \text{or} \quad \frac{\tau_c}{\Delta\,\rho\, g\mathfrak{d}} = \tilde{f}(\pi_2, \pi_3, \pi_4)\,. \tag{225}$$

The number of variables is now reduced from 7 to 4, a dramatic reduction! However, even further reduction is possible. For sediment transport in the geophysical environment π_2 is very nearly a constant on the entire Globe, and π_3 is very small ($\leqslant 10^{-2}$); so, the π_3-dependence may be dropped (i.e. expressed in a Taylor series expansion of π_3 and restricted to the term $\tilde{f}(\pi_2, 0, \pi_4)$). Thus, we may assume

$$\theta_c \equiv \frac{\tau_c}{\Delta\,\rho\, g\mathfrak{d}} = \tilde{f}(Re_c^*) = \tilde{f}(\mathfrak{d}^*)\,, \quad \pi_4 = Re_c^* = \mathfrak{d}^* \equiv \Big(\frac{g}{\Delta\,\nu^2}\Big)^{1/3}\mathfrak{d}\,. \tag{226}$$

This derivation assumes that only a single sediment fraction is present. It is important to note that the viscosity ν of the mixture is present in the variables describing the erosion inception. If it is dropped, then $\tilde{f}$ in (226) reduces to a constant and

$$\tau_c = \text{const.} \times \Delta\,\rho\, g\mathfrak{d}^*\,,$$

which is not supported by experiments. Omitting g as a governing parameter is disastrous, because π_1 and π_4 are then missing as π-products. In this case $\tilde{f}(\pi_2, \pi_3) = 0$ is simply meaningless.

D Justification for (170), (171) and (175), (176)

Justification for (170), (171): For the constituent masses, noting that

$$\rho_\alpha(\boldsymbol{v}_\alpha - \boldsymbol{w}) = \underbrace{\rho_\alpha(\boldsymbol{v}_\alpha - \boldsymbol{v})}_{\equiv \mathfrak{J}_\alpha,\ \text{see eq. (8)}} + \rho_\alpha(\boldsymbol{v} - \boldsymbol{w})\,,$$

the non-averaged balance (133), in which $f_{\mathbb{S}} = \mu_\alpha$, $\boldsymbol{\phi}^{f_{\mathbb{S}}} = \boldsymbol{0}$, $f = \rho_\alpha$, $\boldsymbol{v} = \boldsymbol{v}_\alpha$, $\boldsymbol{\phi}^f = \boldsymbol{0}$, can be written as

$$\frac{\partial \mu_\alpha}{\partial t} + (\mu_\alpha \boldsymbol{v}_{\mathbb{S}\alpha})^{\mathfrak{a}}{}_{;\mathfrak{a}} - \frac{\partial \mu_\alpha}{\partial \xi^{\mathfrak{a}}}\, w^{\mathfrak{a}} - 2\mu_\alpha\, \mathcal{U}_b K = -[\![\mathfrak{J}_\alpha + \rho_\alpha(\boldsymbol{v} - \boldsymbol{w})]\!] \cdot \boldsymbol{n}_b\,. \tag{227}$$

Analogously, for the fluid we deduce

$$\frac{\partial \mu_f}{\partial t} + \big(\mu_f \boldsymbol{v}_{\mathbb{S}f}\big)^{\mathfrak{a}}{}_{;\mathfrak{a}} - \frac{\partial \mu_f}{\partial \xi^{\mathfrak{a}}}\, w^{\mathfrak{a}} - 2\mu_f\, \mathcal{U}_b K = -[\![\mathfrak{J}_f + \tilde{\rho}_f(\boldsymbol{v} - \boldsymbol{w})]\!] \cdot \boldsymbol{n}_b\,, \tag{228}$$

where $\mathfrak{J}_f \equiv \tilde{\rho}_f(\boldsymbol{v}_f - \boldsymbol{v})$, with $\tilde{\rho}_f$ and $\boldsymbol{v}_f$ the mass density and velocity of the fluid ($\tilde{\rho}_f = \rho - \sum_\alpha \rho_\alpha$). Now we sum equations (227) and (228) over all constituents. Using relation

$$\sum_\alpha \mathfrak{J}_\alpha + \mathfrak{J}_f = \boldsymbol{0}\,, \tag{229}$$

and definitions

$$\mu \equiv \sum_\alpha \mu_\alpha + \mu_f\,, \quad \mu \boldsymbol{v}_{\mathbb{S}} \equiv \sum_\alpha \mu_\alpha \boldsymbol{v}_{\mathbb{S}\alpha} + \mu_f \boldsymbol{v}_{\mathbb{S}f} \tag{230}$$

for the mixture surface density μ and mixture velocity $\boldsymbol{v}_{\mathbb{S}}$, we obtain the mass balance for the mixture by summation of (227) and (228):

$$\frac{\partial \mu}{\partial t} + (\mu \boldsymbol{v}_{\mathbb{S}})^{\mathfrak{a}}{}_{;\mathfrak{a}} - \frac{\partial \mu}{\partial \xi^{\mathfrak{a}}}\, w^{\mathfrak{a}} - 2\mu\, \mathcal{U}_b K = -[\![\rho(\boldsymbol{v} - \boldsymbol{w})]\!] \cdot \boldsymbol{n}_b\,. \tag{231}$$

We now average equations (227) and (228). In so doing we assume that the interface does not perform any fluctuations, whence necessarily $\langle\, \boldsymbol{n}_b \,\rangle = \boldsymbol{n}_b$, $\langle\, K \,\rangle = K$, $\langle\, \boldsymbol{w} \,\rangle = \boldsymbol{w}$ and $\langle \mathcal{U}_b \rangle = \mathcal{U}_b$. Thus, for the averaged equations we get

$$\begin{aligned} &\frac{\partial \langle \mu_\alpha \rangle}{\partial t} + (\langle \mu_\alpha \rangle \langle\, \boldsymbol{v}_{\mathbb{S}\alpha} \,\rangle)^{\mathfrak{a}}{}_{;\mathfrak{a}} + \big(\langle\, \mu'_\alpha\, (\boldsymbol{v}_{\mathbb{S}\alpha})' \,\rangle\big)^{\mathfrak{a}}{}_{;\mathfrak{a}} - \frac{\partial \langle \mu_\alpha \rangle}{\partial \xi^{\mathfrak{a}}}\, w^{\mathfrak{a}} - 2\langle \mu_\alpha \rangle\, \mathcal{U}_b K \\ &\qquad = -[\![\langle\, \mathfrak{J}_\alpha \,\rangle + \langle\, \rho'_\alpha \boldsymbol{v}' \,\rangle + \langle\, \rho_\alpha \,\rangle(\langle\, \boldsymbol{v} \,\rangle - \boldsymbol{w})]\!] \cdot \boldsymbol{n}_b\,, \end{aligned} \tag{232}$$

$$\begin{aligned} &\frac{\partial \langle \mu_f \rangle}{\partial t} + \big(\langle \mu_f \rangle \langle\, \boldsymbol{v}_{\mathbb{S}f} \,\rangle\big)^{\mathfrak{a}}{}_{;\mathfrak{a}} + \Big(\langle\, \mu'_f\, \big(\boldsymbol{v}_{\mathbb{S}f}\big)' \,\rangle\Big)^{\mathfrak{a}}{}_{;\mathfrak{a}} - \frac{\partial \langle \mu_f \rangle}{\partial \xi^{\mathfrak{a}}}\, w^{\mathfrak{a}} - 2\langle \mu_f \rangle\, \mathcal{U}_b K \\ &\qquad = -[\![\langle\, \mathfrak{J}_f \,\rangle + \langle\, \tilde{\rho}'_f \boldsymbol{v}' \,\rangle + \langle\, \tilde{\rho}_f \,\rangle(\langle\, \boldsymbol{v} \,\rangle - \boldsymbol{w})]\!] \cdot \boldsymbol{n}_b\,. \end{aligned} \tag{233}$$

If we sum (232) and (233), because of (229), (230) we obtain

$$\begin{aligned}\frac{\partial\langle\mu\rangle}{\partial\, t} + (\langle\mu\rangle\langle\, \boldsymbol{v}_{\mathbb{S}}\,\rangle)^{\mathfrak{a}}{}_{;\mathfrak{a}} + \big(\langle\, \mu'\ (\boldsymbol{v}_{\mathbb{S}})'\,\rangle\big)^{\mathfrak{a}}{}_{;\mathfrak{a}} - \frac{\partial\,\langle\mu\rangle}{\partial\xi^{\mathfrak{a}}}\, w^{\mathfrak{a}} - 2\langle\mu\rangle\,\mathcal{U}_b K \\ = -[\![\quad \underbrace{\langle\, \rho'\boldsymbol{v}'\,\rangle}_{\equiv\, \boldsymbol{\phi}^{\rho}\text{ in Table 6}} \quad + \langle\, \rho\,\rangle(\langle\boldsymbol{v}\,\rangle - \boldsymbol{w})]\!]\cdot\boldsymbol{n}_b\,.\end{aligned} \tag{234}$$

Of course, (234) is the average of (231), and only two of (232)–(234) are independent. For computations of initial boundary value problems we recommend to use (232) and (234) and to infer $\langle\mu_f\rangle$ a posteriori from $\langle\mu_f\rangle = \langle\mu\rangle - \sum_\alpha\langle\mu_\alpha\rangle$.

It follows: with REYNOLDS averaging we have a non-vanishing mass flux in the mass balance (234). A FAVRE-type averaging would have to be performed. However, if ρ' is small on both sides of the basal surface we can drop $\langle\, \rho'\boldsymbol{v}'\,\rangle$ in (234). Moreover, with $\rho' \approx 0$, $\rho_\alpha = \rho c_\alpha$, decomposition (9) and definition of $\boldsymbol{J}_\alpha$ (see (43)), for the constituent class α the mass flux $\langle\,\mathfrak{J}_\alpha\rangle + \langle\, \rho'_\alpha\boldsymbol{v}'\,\rangle$ takes the form

$$\langle\,\mathfrak{J}_\alpha\rangle + \langle\, \rho'_\alpha\boldsymbol{v}'\,\rangle = \boldsymbol{J}_\alpha - \rho\,\langle\, c_\alpha\rangle\langle\boldsymbol{w}^s_\alpha\rangle\,,$$

which explains Table 6 for Model 2. The main text, formulae (170), (171) (as deduced from (232), (234)) and Table 6 show the averaged fields without the averaging operator $\langle\cdot\rangle$ and with negligible correlations

$$\langle\, \mu'_\alpha\ (\boldsymbol{v}_{\mathbb{S}\alpha})'\,\rangle\,, \quad \langle\, \mu'\ (\boldsymbol{v}_{\mathbb{S}})'\,\rangle\,.$$

Justification for (175) and (176): Now we consider (132), in which $f_{\mathbb{S}} = \mu_\alpha\boldsymbol{v}_{\mathbb{S}\alpha}$, $\boldsymbol{\phi}^{f_{\mathbb{S}}} = -\boldsymbol{\sigma}_{\mathbb{S}\alpha}$, $\pi^{f_{\mathbb{S}}} = 0$, $s^{f_{\mathbb{S}}} = \mu_\alpha\boldsymbol{g}$, $f = \rho_\alpha\boldsymbol{v}_\alpha$, $\boldsymbol{v} = \boldsymbol{v}_\alpha$, $\boldsymbol{\phi}^f = -\boldsymbol{\sigma}_\alpha$, for each $\alpha = 1,\dots,N$:

$$\begin{aligned}\frac{\partial}{\partial t}\,(\mu_\alpha\boldsymbol{v}_{\mathbb{S}\alpha}) + \mathrm{Div}\ (\mu_\alpha\boldsymbol{v}_{\mathbb{S}\alpha}\otimes\boldsymbol{v}_{\mathbb{S}\alpha} - \boldsymbol{\sigma}_{\mathbb{S}\alpha}) - \frac{\partial}{\partial\xi^{\mathfrak{a}}}(\mu_\alpha\boldsymbol{v}_{\mathbb{S}\alpha})\, w^{\mathfrak{a}} = \\ -[\![\rho_\alpha\boldsymbol{v}_\alpha\otimes(\boldsymbol{v}_\alpha - \boldsymbol{w}) - \boldsymbol{\sigma}_\alpha]\!]\,\boldsymbol{n}_b + \mu_\alpha\boldsymbol{g}\,.\end{aligned} \tag{235}$$

A similar equation holds for the interstitial fluid:

$$\begin{aligned}\frac{\partial}{\partial t}\,\big(\mu_f\boldsymbol{v}_{\mathbb{S}f}\big) + \mathrm{Div}\,\big(\mu_f\boldsymbol{v}_{\mathbb{S}f}\otimes\boldsymbol{v}_{\mathbb{S}f} - \boldsymbol{\sigma}_{\mathbb{S}f}\big) - \frac{\partial}{\partial\xi^{\mathfrak{a}}}(\mu_f\boldsymbol{v}_{\mathbb{S}f})\, w^{\mathfrak{a}} = \\ -[\![\tilde\rho_f\boldsymbol{v}_f\otimes(\boldsymbol{v}_f - \boldsymbol{w}) - \boldsymbol{\sigma}_f]\!]\,\boldsymbol{n}_b + \mu_f\boldsymbol{g}\,.\end{aligned} \tag{236}$$

Summing (235), (236) and using definition (230) we obtain

$$\frac{\partial}{\partial t}\,(\mu\boldsymbol{v}_{\mathbb{S}}) + \mathrm{Div}\,(\mu\boldsymbol{v}_{\mathbb{S}}\otimes\boldsymbol{v}_{\mathbb{S}} - \boldsymbol{\sigma}_{\mathbb{S}}) - \frac{\partial}{\partial\xi^{\mathfrak{a}}}(\mu\boldsymbol{v}_{\mathbb{S}})\, w^{\mathfrak{a}} = -[\![\rho\boldsymbol{v}\otimes(\boldsymbol{v} - \boldsymbol{w}) - \boldsymbol{\sigma}]\!]\,\boldsymbol{n}_b + \mu\boldsymbol{g}\,, \tag{237}$$

where the bulk, $\boldsymbol{\sigma}$, and surface, $\boldsymbol{\sigma}_{\mathbb{S}}$, mixture stress tensors are defined by

$$\rho\boldsymbol{v}\otimes\boldsymbol{v} - \boldsymbol{\sigma} \equiv \sum_\alpha(\rho_\alpha\boldsymbol{v}_\alpha\otimes\boldsymbol{v}_\alpha - \boldsymbol{\sigma}_\alpha) + \tilde\rho_f\boldsymbol{v}_f\otimes\boldsymbol{v}_{\mathbb{S}f} - \boldsymbol{\sigma}_f\,, \tag{238}$$

$$\mu \boldsymbol{v}_{\mathcal{S}} \otimes \boldsymbol{v}_{\mathcal{S}} - \boldsymbol{\sigma}_{\mathcal{S}} \equiv \sum_{\alpha} \left(\mu_{\alpha} \boldsymbol{v}_{\mathcal{S}\alpha} \otimes \boldsymbol{v}_{\mathcal{S}\alpha} - \boldsymbol{\sigma}_{\mathcal{S}\alpha} \right) + \mu_f \boldsymbol{v}_{\mathcal{S}f} \otimes \boldsymbol{v}_{\mathcal{S}f} - \boldsymbol{\sigma}_{\mathcal{S}f} \,. \tag{239}$$

Averaging (237) under the assumptions $\mu' \approx 0$, $\rho' \approx 0$, recalling definition $(43)_1$ of the Reynolds stress tensor $\boldsymbol{R}$ and introducing the laminar and turbulent surface mixture stress tensor $\boldsymbol{R}_{\mathcal{S}}$ according to

$$\boldsymbol{R}_{\mathcal{S}} \equiv \langle \boldsymbol{\sigma}_{\mathcal{S}} \rangle - \mu \langle \boldsymbol{v}'_{\mathcal{S}} \otimes \boldsymbol{v}'_{\mathcal{S}} \rangle \,, \tag{240}$$

we deduce (we omit the angular brackets)

$$\begin{aligned} \frac{\partial}{\partial t} \left(\mu \boldsymbol{v}_{\mathcal{S}} \right) + \mathrm{Div} \left(\mu \boldsymbol{v}_{\mathcal{S}} \otimes \boldsymbol{v}_{\mathcal{S}} - \boldsymbol{R}_{\mathcal{S}} \right) - \frac{\partial}{\partial \xi^{\mathfrak{a}}} \left(\mu \boldsymbol{v}_{\mathcal{S}} \right) w^{\mathfrak{a}} = \\ - [\![\rho \boldsymbol{v} \otimes (\boldsymbol{v} - \boldsymbol{w}) + p \boldsymbol{I} - \boldsymbol{R}]\!] \, \boldsymbol{n}_b + \mu \boldsymbol{g} \,, \end{aligned} \tag{241}$$

which explains the last line in Table 6.

Next we want to write (241) using the components of vectors and tensors with respect to the local basis $\{\boldsymbol{\tau}_1, \boldsymbol{\tau}_2, \boldsymbol{n}_b\}$, which will give (175) and (176). To this end we use the formulae (for simplicity in this derivation we omit the lower index b in $\mathcal{U}_b$ and $\boldsymbol{n}_b$ referring to the basal surface)

$$\begin{aligned} \frac{\partial \boldsymbol{\tau}_{\mathfrak{a}}}{\partial \xi^{\mathfrak{b}}} = \Gamma^{\mathfrak{c}}_{\mathfrak{a}\mathfrak{b}} \boldsymbol{\tau}_{\mathfrak{c}} + b_{\mathfrak{a}\mathfrak{b}} \boldsymbol{n} \,, \quad \frac{\partial \boldsymbol{n}}{\partial \xi^{\mathfrak{a}}} = -b_{\mathfrak{a}\mathfrak{b}} \boldsymbol{\tau}^{\mathfrak{b}} \,, \quad \frac{\partial \boldsymbol{n}}{\partial t} = -g^{\mathfrak{a}\mathfrak{b}} \left\{ \frac{\partial \mathcal{U}}{\partial \xi^{\mathfrak{a}}} + b_{\mathfrak{c}\mathfrak{b}} w^{\mathfrak{c}} \right\} \boldsymbol{\tau}_{\mathfrak{b}} \,, \\ \frac{\partial \boldsymbol{\tau}_{\mathfrak{a}}}{\partial t} = \frac{\partial \boldsymbol{w}}{\partial \xi^{\mathfrak{a}}} = \left\{ \frac{\partial w^{\mathfrak{b}}}{\partial \xi^{\mathfrak{a}}} + w^{\mathfrak{c}} \Gamma^{\mathfrak{b}}_{\mathfrak{c}\mathfrak{a}} - \mathcal{U} b_{\mathfrak{a}\mathfrak{c}} g^{\mathfrak{c}\mathfrak{b}} \right\} \boldsymbol{\tau}_{\mathfrak{b}} + \left\{ \frac{\partial \mathcal{U}}{\partial \xi^{\mathfrak{a}}} + w^{\mathfrak{b}} b_{\mathfrak{b}\mathfrak{a}} \right\} \boldsymbol{n} \,, \end{aligned} \tag{242}$$

and for a scalar function f, vector fields $\boldsymbol{u}$, $\boldsymbol{v}$ and a second order tensor field $\boldsymbol{T}$ defined on the surface $\mathcal{S}$, the rules of differentiation[34]

$$\begin{gathered} \mathrm{Div} \left(f \boldsymbol{v} \right) = f \mathrm{Div} \, \boldsymbol{v} + \mathrm{Grad} \, f \cdot \boldsymbol{v} \,, \quad \mathrm{Div} \left(f \boldsymbol{T} \right) = f \mathrm{Div} \, \boldsymbol{T} + \boldsymbol{T} \mathrm{Grad} \, f \,, \\ \mathrm{Div} \left(\boldsymbol{u} \otimes \boldsymbol{v} \right) = v^{\mathfrak{a}} \frac{\partial \boldsymbol{u}}{\partial \xi^{\mathfrak{a}}} + \left(\mathrm{Div} \, \boldsymbol{v} \right) \boldsymbol{u} \,, \quad \mathrm{Div} \, \boldsymbol{n} = -2K \,, \quad \mathrm{Div} \left(\boldsymbol{n} \otimes \boldsymbol{n} \right) = -2K \boldsymbol{n} \,, \\ \mathrm{Div} \left(\boldsymbol{n} \otimes \boldsymbol{\tau}_{\mathfrak{a}} \right) = -b_{\mathfrak{a}\mathfrak{b}} \boldsymbol{\tau}^{\mathfrak{b}} + \Gamma^{\mathfrak{b}}_{\mathfrak{a}\mathfrak{b}} \boldsymbol{n} \,, \quad \mathrm{Div} \left(\boldsymbol{\tau}_{\mathfrak{a}} \otimes \boldsymbol{n} \right) = -2K \boldsymbol{\tau}_{\mathfrak{a}} \,, \end{gathered} \tag{243}$$

where

$$\mathrm{Grad} \, f \equiv \frac{\partial \, f}{\partial \, \xi^{\mathfrak{a}}} \, \boldsymbol{\tau}^{\mathfrak{a}} \,, \quad \mathrm{Div} \, \boldsymbol{v} \equiv \frac{\partial \, \boldsymbol{v}}{\partial \, \xi^{\mathfrak{a}}} \cdot \boldsymbol{\tau}^{\mathfrak{a}} \,, \quad \mathrm{Div} \, \boldsymbol{T} \equiv \frac{\partial \, \boldsymbol{T}}{\partial \, \xi^{\mathfrak{a}}} \, \boldsymbol{\tau}^{\mathfrak{a}} \,.$$

Thus, using the decomposition

$$\boldsymbol{v}_{\mathcal{S}} = \boldsymbol{v}_{\mathcal{S}\|} + \mathcal{U} \boldsymbol{n} = v^{\mathfrak{a}} \boldsymbol{\tau}_{\mathfrak{a}} + \mathcal{U} \boldsymbol{n} \,,$$

we obtain

$$\begin{aligned} \frac{\partial}{\partial \, t} (\mu \boldsymbol{v}_{\mathcal{S}}) = \frac{\partial \mu v^{\mathfrak{a}}}{\partial \, t} \, \boldsymbol{\tau}_{\mathfrak{a}} + \mu v^{\mathfrak{b}} \left\{ \frac{\partial w^{\mathfrak{a}}}{\partial \xi^{\mathfrak{b}}} + w^{\mathfrak{c}} \Gamma^{\mathfrak{a}}_{\mathfrak{c}\mathfrak{b}} - \mathcal{U} b_{\mathfrak{b}\mathfrak{c}} g^{\mathfrak{c}\mathfrak{a}} \right\} \boldsymbol{\tau}_{\mathfrak{a}} - \\ \mu \mathcal{U} g^{\mathfrak{a}\mathfrak{b}} \left\{ \frac{\partial \mathcal{U}}{\partial \xi^{\mathfrak{b}}} + b_{\mathfrak{b}\mathfrak{c}} w^{\mathfrak{c}} \right\} \boldsymbol{\tau}_{\mathfrak{a}} + \left\{ \frac{\partial \mu \, \mathcal{U}}{\partial \, t} + \mu v^{\mathfrak{a}} \frac{\partial \mathcal{U}}{\partial \xi^{\mathfrak{a}}} + \mu b_{\mathfrak{b}\mathfrak{a}} v^{\mathfrak{a}} w^{\mathfrak{b}} \right\} \boldsymbol{n} \,. \end{aligned} \tag{244}$$

[34] (243) can be easily deduced with the aid of (242).

Then,

$$\mathrm{Div}\,(\mu \boldsymbol{v}_{\mathcal{S}} \otimes \boldsymbol{v}_{\mathcal{S}}) =$$

$$\mathrm{Div}\,(\mu \boldsymbol{v}_{\mathcal{S}\|} \otimes \boldsymbol{v}_{\mathcal{S}\|}) + \mathrm{Div}\,(\mu \mathcal{U} \boldsymbol{v}_{\mathcal{S}\|} \otimes \boldsymbol{n}) + \mathrm{Div}\,(\mu \mathcal{U} \boldsymbol{n} \otimes \boldsymbol{v}_{\mathcal{S}\|}) + \mathrm{Div}\,(\mu \mathcal{U}^2 \boldsymbol{n} \otimes \boldsymbol{n}) = \tag{245}$$

$$\mathrm{Div}\,(\mu \boldsymbol{v}_{\mathcal{S}\|} \otimes \boldsymbol{v}_{\mathcal{S}\|}) - \mu \mathcal{U}\, v^{\mathfrak{b}}\, b_{\mathfrak{b}\mathfrak{c}}\, g^{\mathfrak{c}\mathfrak{a}}\, \boldsymbol{\tau}_{\mathfrak{a}} + \mathrm{Div}\,(\mu \mathcal{U} \boldsymbol{v}_{\mathcal{S}\|})\, \boldsymbol{n} - 2\mu K \mathcal{U} \boldsymbol{v}_{\mathcal{S}}\,,$$

and with the notations (174) for the components of $\boldsymbol{R}_{\mathcal{S}}$,

$$\mathrm{Div} \boldsymbol{R}_{\mathcal{S}} = \mathrm{Div}\,(S^{\mathfrak{a}\mathfrak{b}} \boldsymbol{\tau}_{\mathfrak{a}} \otimes \boldsymbol{\tau}_{\mathfrak{b}}) - \left\{ S^{\mathfrak{c}} b_{\mathfrak{c}\mathfrak{b}} g^{\mathfrak{b}\mathfrak{a}} + 2K S^{\mathfrak{a}} \right\} \boldsymbol{\tau}_{\mathfrak{a}} + \{\mathrm{Div}\,(S^{\mathfrak{a}} \boldsymbol{\tau}_{\mathfrak{a}}) - 2SK\}\, \boldsymbol{n}\,. \tag{246}$$

Finally, we have

$$\frac{\partial}{\partial \xi^{\mathfrak{b}}} (\mu \boldsymbol{v}_{\mathcal{S}})\, w^{\mathfrak{b}} = w^{\mathfrak{b}} \left\{ \frac{\partial \mu v^{\mathfrak{a}}}{\partial \xi^{\mathfrak{b}}} + \mu v^{\mathfrak{c}}\, \Gamma^{\mathfrak{a}}_{\mathfrak{c}\mathfrak{b}} - \mu \mathcal{U}\, b_{\mathfrak{b}\mathfrak{c}} g^{\mathfrak{c}\mathfrak{a}} \right\} \boldsymbol{\tau}_{\mathfrak{a}} + w^{\mathfrak{b}} \left\{ \mu v^{\mathfrak{c}}\, b_{\mathfrak{c}\mathfrak{b}} + \frac{\partial \mu \mathcal{U}}{\partial \xi^{\mathfrak{b}}} \right\} \boldsymbol{n}\,. \tag{247}$$

Now, substituting (244)–(247) into (241) and separating the tangential and normal parts of the emerging relation yields (175) and (176).

E List of symbols

Roman Symbols

a	Parameter in the representation (202) of the volume fraction ν
A	Parameter arising in formula (61) for the particle drag coefficient $\mathcal{C}_{\mathfrak{d}_\alpha}$
$\boldsymbol{A}$	Unspecified symmetric second rank tensor
$\mathcal{A}_L$	$\equiv [H]/[L]$ Aspect ratio for lengths
$\mathcal{A}_V$	$\equiv [W]/[V]$ Aspect ratio for velocities
$\mathcal{A}$	$\equiv \mathcal{A}_L = \mathcal{A}_V$ Aspect ratio for lengths and velocities
b	Parameter in the representation (202) of the volume fraction ν
$b(x, y, t)$	z-coordinate of the basal surface: $z = b(x, y, t)$
$b_{\mathfrak{ab}}$	Coefficients of the second fundamental form of a surface
B	Parameter arising in formula (61) for the particle drag coefficient $\mathcal{C}_{\mathfrak{d}_\alpha}$
$\mathcal{B}^{\pm}$	Material body parts on the $\pm$ sides of a singular surface
$\mathcal{B}$	$\equiv g[\sigma][H]/[f][L][V] \approx 10^{-2} - 10^{2}$ Buoyancy parameter; material body
c	Function arising in the formula for the unit normal, $\boldsymbol{n}_b$, at the basal surface
c_α	Mass concentration (fraction) of sediment class α
$[c_\alpha]$	$\approx 10^{-3} - 10^{-1}$ Scale for mass concentration of sediment class α
c_k	Coefficient in the zeroth order parameterization of the turbulent kinetic energy k
$c_v,\ c_p$	Specific heats at constant volume and constant pressure, respectively
$c_v^0,\ c_p^0$	Constant specific heats
$c_v',\ c_p'$	Parameters in the linear representations (220) for specific heats
c_{T_ρ}	Specific heat at constant temperature in the energy formulation
c_{T_p}	Specific heat at constant temperature in the enthalpy formulation
$[c_v],\ [c_p]$	$\approx 4200\ \mathrm{m^2\ s^{-2}\ K^{-1}}$ Typical values of the specific heats c_v and c_p
c_1, c_2, c_3	'Universal' coefficients in the zeroth and first order parameterizations
$c_k, c_\mu,\ c_\varepsilon$	for $k - \varepsilon$
C_s	SMAGORINSKY coefficient

$\mathcal{C}$	Closed double point free curve bounding a surface
$\mathcal{C}_1, \mathcal{C}_2$	Drag coefficients of basal sliding laws (183), (184)
C_d^{wind}	$\approx 2 \times 10^{-3}$ Wind drag coefficient
$\mathcal{C}_{\mathfrak{d}_\alpha}$	Drag coefficient for sediment class α with the mean diameter $\mathfrak{d}_\alpha$
$[d_{\min}, d_{\max})$	Range of particle diameters of sediment classes α, $\alpha = 1, \ldots, N$
$[d_{\alpha-1}, d_\alpha)$	Range of nominal particle diameters of sediment class α
$\mathfrak{d}$, $\mathfrak{d}_\alpha$	Nominal mean diameter of sediment grains and in class α:
	$\mathfrak{d}, \mathfrak{d}_\alpha \in [d_{\alpha-1}, d_\alpha)$
$\mathfrak{d}^*$, $\mathfrak{d}_\alpha^*$	$\equiv (\Delta\, g/\nu^2)^{1/3}\, \mathfrak{d}(\mathfrak{d}_\alpha)$ Dimensionless mean particle diameter of class α
D_α	Surface mass diffusivities
$D^{(T)}$	$\equiv \chi_\ell^{(T)} + \dfrac{\nu_t}{\sigma_T}$ Laminar + turbulent thermal mass flux diffusivity
$D^{(c_\alpha)}$	$\equiv \chi_\ell^{(c_\alpha)} + \dfrac{\nu_t}{\sigma_{c_\alpha}}$ Laminar + turbulent species mass flux diffusivity
$\mathcal{D}^{(T)}$	$\equiv D^{(T)}/[f][H^2] \approx 10^{-4} - 10^0$ Dimensionless thermal diffusivity
$\mathcal{D}^{(c_\alpha)}$	$\equiv D^{(c_\alpha)}/[f][H^2] \approx 10^{-4} - 10^0$ Dimensionless species mass diffusivity
$\boldsymbol{D}$	Rate of strain-rate (strain rate, stretching) tensor of the mixture
$\boldsymbol{D}_{\mathbb{S}}$	Surface rate of strain-rate tensor of the detritus surface mixture
$\boldsymbol{e}_1, \boldsymbol{e}_2, \boldsymbol{e}_3$	Unit vectors in the x, y, z-directions
$\boldsymbol{e}_z$	$\equiv \boldsymbol{e}_3$ Unit vector in the z-direction
E	Relative error for settling velocities of different authors
E, E_α	Erosion (entrainment) rate of sediments α from the base
f	$\equiv 2\Omega \sin\varphi$ First CORIOLIS parameter;
	specific density of an unspecified physical bulk quantity
$\tilde{f}$	$\equiv 2\Omega \cos\varphi$ Second CORIOLIS parameter
$f_{\mathbb{S}}$	Specific density of an unspecified physical surface quantity
F	Function identifying a singular surface by $F(\boldsymbol{x}, t) = 0$
$\mathcal{F}$	$\equiv [V^2]/[c_v][\Delta T] \approx 10^{-7} - 10^{-1}$ Pressure work parameter
$[f]$	$\approx 10^{-4}\,\text{s}^{-1}$ CORIOLIS parameter

$1/[f]$ Time scale

g Gravity constant; GIBBS free energy ($\equiv h - T\eta$)

$\boldsymbol{g}$ Gravity vector

$g_{\mathfrak{ab}}$ Coefficients of the first fundamental form of a surface

$g^{\mathfrak{ab}}$ Components of the inverse matrix of $(g_{\mathfrak{ab}})$

$\mathcal{G}$ $\equiv g[H]/[f^2][L^2] \approx 10^0 - 10^3$ Squared velocity ratio

h Specific enthalpy ($\equiv \epsilon + p/\rho$); thickness of the detritus layer

h_0 Reference specific enthalpy

$\boldsymbol{h}$ Unit vector tangent to a surface $\mathcal{S}$ and normal to the closed curve $\mathcal{C}$ bounding $\mathcal{S}$

$\mathcal{H}$ Heaviside function

$[H]$ $\approx 10^1 - 10^3$ m Vertical length scale

$\boldsymbol{j}_\alpha$ $\equiv \rho c_\alpha(\boldsymbol{v}_\alpha - \boldsymbol{v}^s_\alpha)$

Diffusive flux of sediment class α vs. a representative particle in the class α

$\mathfrak{J}_\alpha$ $\equiv \rho c_\alpha(\boldsymbol{v}_\alpha - \boldsymbol{v})$

Diffusive flux of sediment class α with respect to the barycentric motion

$\mathfrak{J}_f$ $\equiv \tilde{\rho}_f(\boldsymbol{v}_f - \boldsymbol{v})$

Diffusive flux of the bearer fluid with respect to the barycentric motion

$\boldsymbol{J}_\alpha$ Laminar + turbulent specific species mass flux of sediment class α:

$\equiv \langle \boldsymbol{j}_\alpha \rangle + \rho_0 \langle c'_\alpha \boldsymbol{v}' \rangle - \rho_0 \langle c'_\alpha \boldsymbol{w}^{s'}_\alpha \rangle$ in BOUSSINESQ model,

$\equiv \langle \boldsymbol{j}_\alpha \rangle + \rho \langle c'_\alpha \boldsymbol{v}' \rangle - \rho \langle c'_\alpha \boldsymbol{w}^{s'}_\alpha \rangle$ in Model 2

k Specific turbulent kinetic energy

K $\equiv \frac{1}{2} g^{\mathfrak{ab}} b_{\mathfrak{ab}}$ Mean curvature of a surface

$\boldsymbol{L}$ $\equiv \operatorname{grad} \boldsymbol{v}$ Spatial velocity gradient

$\boldsymbol{L}^T$ Transpose of $\boldsymbol{L}$

$[L]$ $\approx 10^4 - 10^6$ m Horizontal length scale

$\mathcal{M}, \mathcal{M}^\pm$ Mass flow through a singular surface (in (126))

$\mathcal{M}_b^{\text{eros/dep}}$ Erosion and deposition mass flow through the basal surface

$\mathcal{M}_b, \mathcal{M}_b^{\alpha/f}$ Mass flow through the basal surface (in (191))

n	Average porosity within the detritus layer
$\boldsymbol{n}$	Unit normal vector to a surface
$\boldsymbol{n}_b$	The unit normal vector to the basal surface pointing into the flowing material
$\boldsymbol{n}_s$	The unit normal vector to the free surface pointing into atmosphere
N	Number of constituents α
N^*	Limit index for α determining $\mathfrak{d}_{N*}$ such that α classes for which $\mathfrak{d}^*_\alpha < \mathfrak{d}_{N*}$ are erosive sediment classes
$\mathcal{N}$	$\equiv \nu_t/[f][H^2] \approx 10^{-6} - 10^1$ Dimensionless kinematic turbulent viscosity
p	Mixture pressure
p^{atm}	Atmospheric pressure
p_d	Dynamic mixture pressure (see (22))
p_{st}	(Quasi)-static pressure (see (22))
P, P_α	Fraction of time during which a sediment particle is suspended by the flow; P - surface pressure function (in (181), (182))
$\mathcal{P}_x$, $\mathcal{P}_y$, $\mathcal{P}_z$	Cartesian components of the average pressure work $\boldsymbol{\mathcal{P}}$
$\mathcal{P}^{(T)}_\epsilon$	$\equiv [\phi^{(T)}]/\rho^*[f][c_v][\Delta T]$ Power working parameter
$\mathcal{P}^{(T)}_h$	$\equiv [\phi^{(T)}]/\rho^*[f][c_p][\Delta T]$ Power working parameter
$\mathcal{P}^{(c_\alpha)}$	$\equiv [\phi^{(c_\alpha)}]/\rho^*[f][c_\alpha]$ Dimensionless constituent mass production parameter
$\boldsymbol{\mathcal{P}}$	$\equiv \langle p'\boldsymbol{v}' \rangle$ Pressure velocity correlation
$\mathcal{P}_x$, $\mathcal{P}_y$, $\mathcal{P}_z$	Cartesian components of the pressure velocity correlation $\boldsymbol{\mathcal{P}}$
$\boldsymbol{q}$	Heat flux vector
$Q^{\epsilon,h}_{x,y,z}$	Cartesian components of the heat flux vectors $\boldsymbol{Q}_\epsilon$, $\boldsymbol{Q}_h$
$Q^{\text{atm}}_\perp$	$\equiv \boldsymbol{Q}^{\text{atm}}_\perp \cdot \boldsymbol{n}_s$ Atmospheric heat flux through the water surface
Q^{atm}_{ir}	Radiative atmospheric heat flow at the water surface
Q^{water}_{ir}	Radiative water heat flow at the water surface
Q_ℓ	Latent heat flow between water and air
Q_s	Sensible heat flow between water and air
$Q_\perp$	Geothermal heat from the rigid bed

$\boldsymbol{Q}_\epsilon$ Laminar +turbulent heat flux:

$\equiv \langle\, \boldsymbol{q} \,\rangle + \rho_0 \langle\, \epsilon' \boldsymbol{v}' \rangle$ in generalized BOUSSINESQ model,

$\equiv \langle\, \boldsymbol{q} \,\rangle + \rho \langle\, \epsilon' \boldsymbol{v}' \rangle$ in Model 2

$\boldsymbol{Q}_h$ Laminar +turbulent heat flux:

$\equiv \langle\, \boldsymbol{q} \,\rangle + \rho_0 \langle\, h' \boldsymbol{v}' \rangle$ in generalized BOUSSINESQ model,

$\equiv \langle\, \boldsymbol{q} \,\rangle + \rho \langle\, h' \boldsymbol{v}' \rangle$ in Model 2

$\boldsymbol{Q}_\perp^{\text{atm}}$ Atmospheric heat flux vector through the water surface

$\boldsymbol{r}$ Position vector of a point on a surface

Re $\equiv (w_\alpha^s \mathfrak{d}_\alpha)/\nu$ Particle REYNOLDS number of sediment class α

Re_c^* $\equiv (u^* \mathfrak{d})/\nu$ Critical particle REYNOLDS number

Ri RICHARDSON number

Ri^{crit} Critical RICHARDSON number

$\mathcal{R}o$ $\equiv [V]/[f][L] \approx 10^{-4} - 10^0$ ROSSBY number

$R_{xx}, \ldots$ Components of $\boldsymbol{R}$ with respect to a Cartesian coordinate system

$\boldsymbol{R}$ Laminar + turbulent mixture stress tensor:

$\equiv \langle \boldsymbol{\sigma}_E \rangle - \rho_0 \langle \boldsymbol{v}' \otimes \boldsymbol{v}' \rangle$ in generalized BOUSSINESQ model,

$\equiv \langle \boldsymbol{\sigma}_E \rangle - \rho \langle \boldsymbol{v}' \otimes \boldsymbol{v}' \rangle$ in Model 2

$\boldsymbol{R}_\mathcal{S}$ $\equiv \langle \boldsymbol{\sigma}_\mathcal{S} \rangle - \mu \langle \boldsymbol{v}'_\mathcal{S} \otimes \boldsymbol{v}'_\mathcal{S} \rangle$ Laminar + turbulent surface mixture stress tensor

s Constant salinity; parameter in the representation (202) of ν_{mean}

$s(x, y, t)$ z-coordinate of the free surface: $z = s(x, y, t)$

s^f Supply rate density of the physical bulk quantity f

$s^{f_\mathcal{S}}$ Supply rate density of the physical surface quantity $f_\mathcal{S}$

$\mathcal{S}$ Surface

$\mathcal{S}_b$ Basal surface

$\mathcal{S}_s$ Free surface

t Time

T Temperature measured in KELVIN or Celsius scales

T_0 Reference temperature in energy/enthalpy constitutive relation (44)

T^* $= 4^\circ$C Reference temperature in the law (46) of the water density ρ_w

$\tilde{T}$, $\tilde{T}_\alpha$ Function of shear velocities (in (158), (165))

u Mixture velocity component in the x-direction

u^* $\equiv (g\nu/\Delta)^{1/3}$ Critical shear velocity

$u_{\max}$ Maximum value of the velocity u within the detritus layer in the linear representation (199)

u_{τ_c} $\equiv \sqrt{\tau_c/\rho}$ Critical wall shear velocity

u_{τ_w} $\equiv \sqrt{\tau_w/\rho}$ Actual wall shear velocity

$\mathcal{U}$ $= \boldsymbol{w} \cdot \boldsymbol{n}$ Displacement speed of an unspecified singular surface

$\mathcal{U}_b$ Displacement speed of the basal surface

v Mixture velocity component in the y-direction

$\boldsymbol{v}$ Barycentric velocity vector

$\boldsymbol{v}_\alpha$ Velocity vector of sediment class α

$\boldsymbol{v}_f$ Fluid velocity

$\boldsymbol{v}_\alpha^s$ Velocity vector of a representative particle in sediment class α

$\boldsymbol{v}_H$ Horizontal component of the barycentric velocity at the basal surface $\mathcal{S}_b$

$\boldsymbol{v}^{\text{wind}}$ Wind velocity at the water surface

$\boldsymbol{v}_H^{\text{wind}}$ Horizontal component of the wind velocity at the water surface

$\boldsymbol{v}^{\mathcal{S}}$ Velocity of a material point moving on a surface

$\boldsymbol{v}_\parallel^{\mathcal{S}}$ Component of $\boldsymbol{v}^{\mathcal{S}}$ tangent to the surface

$\boldsymbol{v}_\alpha^{\mathcal{S}}$ Velocity of a sediment material point in class α which moves on the basal surface

$(\boldsymbol{v}_\alpha^{\mathcal{S}})_\parallel$ Component of $\boldsymbol{v}_\alpha^{\mathcal{S}}$ tangent to the basal surface

$[V]$ $\approx 10^{-2} - 10^{1}\ \mathrm{m\,s^{-1}}$ Horizontal velocity scale

w Mixture velocity component in the z-direction

w_α^s Terminal fall velocity of a particle of sediment class α

w^1, w^2 Components of the surface velocity $\boldsymbol{w}$ with respect to $\boldsymbol{\tau}_1$, $\boldsymbol{\tau}_2$

$\boldsymbol{w}$ Surface velocity of a moving surface

$\boldsymbol{w}_\alpha^s$ $\equiv -(\boldsymbol{v}_\alpha^s - \boldsymbol{v})$ Negative of the relative velocity of a representative particle in sediment class α vs. the barycentric motion

$[W]$	Vertical velocity scale
x	x-coordinate of a Cartesian coordinate system
$\boldsymbol{x}$	Position vector in R^3
$\boldsymbol{X}$	Position vector of a surface material point in a reference configuration
y	y-coordinate of a Cartesian coordinate system
z	z-coordinate of a Cartesian coordinate system

Greek Symbols

α	Counting index for the sediment classes
$\tilde{\alpha}$	$= 6.493 \times 10^6\,\mathrm{K}^{-2}$ Thermal expansion coefficient of water
β	Parameter arising in the formula for w_α^s in equation (70)
$\lambda(\mu, k)$	Exponent coefficient in formula for Λ
$\Gamma^{\mathfrak{c}}_{\mathfrak{ab}}$	CHRISTOFFEL symbols
Δ	Ratio of submerged sediment density to water density ($\equiv \rho_s/\rho - 1$); local grid spacing scale in SMAGORINSKI viscosity (222)
$[\Delta T]$	$\approx 10^\circ$ C Temperature scale
ϵ	Specific internal energy
ϵ_0	Reference specific internal energy
ε	Turbulent specific energy dissipation ($\equiv 4\nu_\ell \langle \mathit{\Pi}_{\boldsymbol{D}'} \rangle$); parameter in the representation (202) of the volume fraction ν
ε_0	Parameter in the boundary layer representation of ε
η	Specific entropy
θ	A tilt angle (see (11))
θ_c	Critical SHIELDS parameter (also called τ_c^*)
θ'_w	Root mean square turbulent fluctuation of wall shear stress
$\Theta(z, t)$	Temperature profile at the deepest position of the lake domain
κ	Thermal conductivity
$\lambda_{\alpha\beta}$	$(N \times N)$-matrix for species mass flux α due to sediment class β

μ	Dynamic viscosity of the bearer fluid;
	surface mass density of the mixture moving on the basal surface
μ_α	Surface mass density of sediments in class α moving on the basal surface
μ_f	Surface fluid mass density
μ_0, μ_1	Constant coefficients in (182)
ν	Kinematic viscosity of the bearer fluid $\equiv \mu/\rho$;
	volume fraction within the detritus layer
ν_{mean}	$\equiv \sum_\alpha \nu^\alpha_{\text{mean}}$ Mean averaged sediment volume fraction in the detritus layer
ν^α_{mean}	Mean averaged volume fraction of the sediments α in the detritus layer
$\nu_{\text{top/bottom}}$	Parameters in the representation (202) of the volume fraction ν
$\nu_{\text{min/max}}$	Minimum and maximum values of the volume fraction ν in the linear
	representation (199)
ν_{crit}	Critical sediments volume fraction in the detritus layer
ν_ℓ, ν_t	Laminar, turbulent kinematic viscosities of the mixture
ν_{SGS}	SMAGORINSKI turbulent viscosity
ξ^1, ξ^2	Parameters on a surface
π^f	Specific production rate density of a physical bulk quantity f
$\pi^{f_{\mathbb{S}}}$	Specific production rate density of a physical surface quantity $f_{\mathbb{S}}$
π^k	Specific production rate density of turbulent kinetic energy
π^ε	Specific production rate density of turbulent dissipation
Π	$\equiv [f][L][V]/[c_p][\Delta T] \approx 10^{-7} - 10^{-2}$ Pressure work parameter
ρ_α	Mass density of constituent α
$\tilde{\rho}_f$	$\equiv n\rho_f$ Mass density of the interstitial fluid (porosity $\times$ true density)
ρ	$\equiv \sum_\alpha \rho_\alpha + \tilde{\rho}_f$ Mixture density
ρ_s	$\approx 2100\,\text{kg}\,\text{m}^{-3}$ Buoyancy corrected density of the suspended sediment
ρ_f	True mass density of the interstitial fluid
ρ^*	= $1000\,\text{kg}\,\text{m}^{-3}$ Reference density of water at 4° C
ρ^{bed}	Mass density in the rigid bed immediately below the basal surface

ρ_α^{bed}	Mass density of particles in class α in the rigid bed immediately below the basal surface
ρ_f^{bed}	Mass density of fluid in the rigid bed immediately below the basal surface
$\rho_0(z)$	Steady density function describing vertical ground stratification
$\rho_d(\boldsymbol{x}, t)$	$\equiv \rho - \rho_0(z)$ The excess of mixture density over the steady density $\rho_0(z)$
$\rho_w(T, s)$	Natural water density as function of temperature and salinity
σ	Standard deviation; dimensionless mixture density
$[\sigma]$	$\approx 10^{-3}$ Scale for density variations of water; density anomaly
σ_T	PRANDTL number of heat
σ_{c_α}	SCHMIDT number of species α
σ_k	PRANDTL number of turbulent kinetic energy
σ_ε	PRANDTL number of turbulent dissipation rate
$\boldsymbol{\sigma}$	(CAUCHY) stress tensor
$\boldsymbol{\sigma}_E$	Extra (CAUCHY) stress tensor of the mixture ((CAUCHY) stress deviator)
$\boldsymbol{\sigma}^{\text{atm}}$	(CAUCHY) stress tensor at the water surface
$\boldsymbol{\tau}_1$, $\boldsymbol{\tau}_2$	Tangent vectors to a surface
τ_c	Critical shear traction
τ_c^*, $(\tau_c^*)_\alpha$	$\equiv \tau_c / \Delta\rho\, g\, \mathfrak{d}$ ($\mathfrak{d}_\alpha$) Critical shear traction (dimensionless)
τ_w	Shear stress on the basal surface
$\boldsymbol{\tau}^{\text{wind}}$	Wind shear traction at the water surface
$\boldsymbol{\tau}_H^{\text{wind}}$	$= (\tau_{xz}^{\text{wind}}, \tau_{yz}^{\text{wind}})$ Horizontal shear traction components
φ	Latitude angle; angle of internal friction (water submerged)
ϕ_p	VAN RIJN's erosion rate per unit mass, area and time
$\phi^{(T)}$	Laminar + turbulent internal energy/enthalpy production rate density $\equiv \operatorname{tr}\langle\boldsymbol{\sigma}_E\rangle\langle\boldsymbol{D}\rangle + \operatorname{tr}\langle\boldsymbol{\sigma}_E'\boldsymbol{D}'\rangle - \langle p' \operatorname{div}\boldsymbol{v}'\rangle$
$\phi^{(c_\alpha)}$	Production mass density of sediment class α
$[\phi^{(T)}]$	Scale for energy/enthalpy production density rate
$[\phi^{(c_\alpha)}]$	Scale for production of mass density of tracer α

$\boldsymbol{\phi}^f$	Flux density of a physical bulk quantity f
$\boldsymbol{\phi}^{f_S}$	Flux density of a physical surface quantity f_S
$\boldsymbol{\phi}^k$	Flux of turbulent specific kinetic energy k
$\boldsymbol{\phi}^\varepsilon$	Flux of turbulent specific energy dissipation ε
$\chi_\ell^{(T)}, \chi_\ell^{(c_\alpha)}$	Laminar kinematic heat/species mass diffusivities
$\boldsymbol{\chi}$	Function describing the motion of a material point on a surface
ψ	$\equiv \epsilon - T\eta$ HELMHOLTZ free energy
$\psi^{\mathfrak{a}}_{;\mathfrak{b}}$	Covariant derivative of the surface vector field $\boldsymbol{\psi}$
ψ_E	Parameter in EINSTEIN's erosion rate formula
ψ_Y	Parameter in YALIN's erosion rate formula
ψ_Z	Parameter in ZANKE's critical shear stress
$\boldsymbol{\Omega}$, Ω	Angular velocity of the Earth

Miscellaneous Symbols

$\langle\cdot\rangle$	Turbulent averaging operator
$\langle\langle\cdot\rangle\rangle = \langle\cdot\rangle$	Statistical averaging property of the REYNOLDS filter
$\{\cdot\}$	$\langle\rho(\cdot)\rangle/\langle\rho\rangle$ FAVRE filter (barycentric)
$\langle f\rangle$	Turbulent average of f
f'	Turbulent fluctuation of f
$[\![f]\!]$	$\equiv f^+ - f^-$ Jump of f across a singular surface
$I_{\boldsymbol{A}}$	$\equiv \mathrm{tr}\boldsymbol{A}$ First invariant of $\boldsymbol{A}$
$II_{\boldsymbol{A}}$	$\equiv \frac{1}{2}\left(I_{\boldsymbol{A}^2} - (I_{\boldsymbol{A}})^2\right)$ Second invariant of $\boldsymbol{A}$
$III_{\boldsymbol{A}}$	$\equiv \det\boldsymbol{A}$ Third invariant of $\boldsymbol{A}$
$II^{\varepsilon,k}_{\boldsymbol{\sigma}'}$	Parameters in the boundary layer representation of ε and k
$\nabla_S f$, $\mathrm{Grad}\, f$	$\equiv \dfrac{\partial f}{\partial \xi^{\mathfrak{a}}}\boldsymbol{\tau}^{\mathfrak{a}}$ Surface gradient
Div	Surface divergence: $\mathrm{Div}\boldsymbol{v} \equiv \dfrac{\partial \boldsymbol{v}}{\partial \xi^{\mathfrak{a}}}\cdot\boldsymbol{\tau}^{\mathfrak{a}}$, $\quad \mathrm{Div}\,\boldsymbol{T} \equiv \dfrac{\partial \boldsymbol{T}}{\partial \xi^{\mathfrak{a}}}\boldsymbol{\tau}^{\mathfrak{a}}$

References

[1] Ahrens, J.P. A fall velocity equation. *J. Waterways, Port, Coastal and Ocean Engineering* **126**(2), 99-102 (2000)

[2] Alts, T. and Hutter, K. Continuum description of the dynamics and thermodynamics of phase boundaries between ice and water. Part I: Surface balance laws and their interpretation in terms of three dimensional balance laws averaged over the phase change boundary layer. *J. Non-Equilibrium Thermodyn.* **13**, 221-257 (1988)

[3] Alts, T. and Hutter, K. Continuum description of the dynamics and thermodynamics of phase boundaries between ice and water. Part II: Thermodynamics. *J. Non-Equilibrium Thermodyn.* **13**, 259-280 (1988)

[4] Alts, T. and Hutter, K. Continuum description of the dynamics and thermodynamics of phase boundaries between ice and water. Part III: Thermostatics and its consequences. *J. Non-Equilibrium Thermodyn.* **13**, 301-329 (1988)

[5] Alts, T. and Hutter, K. Continuum description of the dynamics and thermodynamics of phase boundaries between ice and water. Part IV: On thermostatic stability and well posedness. *J. Non-Equilibrium Thermodyn.* **14**, 1-22 (1989)

[6] Brown, P.P. and Lawler, D.F. Sphere drag and settling velocity revisited. *J. Environmental Engineering*, **129**(3), 222-231 (2003)

[7] Caamenen, B. Simple and general formula for the settling velocity of particles. *J. Hydraulic Engineering*, **133**(2), 229-233 (2007)

[8] Cheng, N.S. Simplified settling velocity formula for sediment particle. *J. Hydraul. Engineering*, **123**(2), 149-152 (1997)

[9] Concha, F. and Almendra, E.R. Settling velocities of particle systems: I Settling velocities of individual spherical partiles. *Int. J. Mineral Processing.* **5**(4), 349-367 (1979)

[10] Eglund, F. and Hansen, E. *A monograph on sediment transport in alluvial streams*, third Ed. Technical Press, Copenhagen (1972)

[11] Einstein, H.A. The bedload function for sediment transportation in open channel flow. *Technical Bulletin Nr 1026* U.S. Dept. Agriculture, Washington DC. (1950)

[12] Germano, M., Piolelli, U., Moin, P. and Cabiot, W.H. A dynamic subgrid-scale eddy viscosity model. *Phys. Fluids A* **3**(7), 1760-1765 (1991)

[13] Guo, J. Logarithmic matching and its application in computational hydraulics and sediment transport. *J. Hydraul. Research*, **40**(5), 555-565 (2002)

[14] Hanjalic, K. and Launder, B.E. A Reynolds stress model of turbulence in its application to thin shear flows. *J. Fluid Mech.* **52**, 609-638 (1972)

[15] Hutter, K. The physics of ice-water phase change surfaces In: CISM Lectures: *Modelling macroscopic phenomena at liquid boundaries*, Murdoch, I. and Kosinski, W., eds., Springer Verlag New York, Vienna (1992)

[16] Hutter, K. *Fluid und Thermodynamik, eine Einführung*. Springer Verlag Berlin etc. (2003)

[17] Hutter, K. and Jöhnk, K. *Continuum Methods of Physical Modeling*. Springer, Berlin, 635p (2004)

[18] Hutter, K., Wang, Y. and Chubarenko, I. *Physics of Lakes - Foundation of the Mathematical and Physical Background* Vol. I. Springer, Berlin, 434p (2011)

[19] Hutter, K., Wang, Y. and Chubarenko, I. *Physics of Lakes - Lakes as Oscillators* Vol. II, Springer, Berlin, 646p (2011)

[20] Jimenez, J.A. and Madsen, O.S. A simple formula to estimate settling velocity of natural sediments. *J. Waterways, Port, Coastal and Ocean Engineering***129**(2), 70-78 (2003)

[21] Jones, W.P and Launder, B.E. The prediction of laminarisation with a two-equation model of turbulence. *J. Heat Mass Tranf.* **15**, 301-314 (1972)

[22] Julien, Y.P. *Erosion and Sedimentation*. Cambridge University Press, Cambridge (1995)

[23] Kraft, S. Wang, Y. and Oberlack, M. Large eddy simulation of sediment deformation in a turbulent flow by means of level set method. *J. Hydr. Eng.* ASCE, November 2011, 1-12 (2011)

[24] Launder, B.E and Spalding, D.B. The numerical computation of turbulent flow. *Comp. Meth. Appl. Mech. Eng.* **3**, 269-288 (1974)

[25] Lilly, D. K. The representation of small-scale turbulence in numerical simulation experiments. *Proc. IBM Scientific Computing Symp. Environ. Sci.*, 195-210 (1967)

[26] Luca, I., Fang, Ch. and Hutter, K. A thermodynamic model of turbulent motion in a granular material. *Continuum Mech. Thermodyn.* **16**, 363-390 (2004)

[27] McGauhay, P.H. Theory of Sedimentation. *J. of the American Water Works Assoc.* **48**, 437-448 (1956)

[28] Miles, J. W. On the stability of heterogeneous shear flows. *J. Fluid Mech.* **10**, 496-508 (1967)

[29] Moin, P. and Kim, J. Numerical investigation of turbulent channel flow. *J. Fluid Mech.*, **118**(1), 341-377 (1982)

[30] Müller, I. Thermodynamics, Pitman, London (1985)

[31] Munk, W. H. On the wind-driven ocean circulation *J. Meteorology*, **7**, 79 (1950)

[32] Piomelli, U. High Reynolds number calculations using the dynamic subgri-scale stress model. *Phys. Fluids A* **5**(6), 1484 (1993)

[33] Piomelli, U. and Zang, T. A. Large eddy simulation of transitional channel flow. *Comput. Phys. Commun.* **65**(1-3), 224-230 (1991)

[34] Prandtl, L. Neuere Ergebnisse der Turbulenzforschung. *Zeitschr. VDI* **77**, 105-113 (1933)

[35] Rodi, W. Examples of calculation methods for flow and mixing in stratified fluids. *J. Geophys. Res.* (C5), **92**, 5305-5328 (1987)

[36] Rodi, W. *Turbulence Models and Their Application in Hydraulics* IAHR Monograph Series. A.A. Balkema, Rotterdam/Brookfield (1993)

[37] Rotta, J.C. *Turbulente Strömungen, eine Einführung in die Theorie und ihre Anwendung*, Teubner, Stuttgart, 267 p (1972)

[38] She, K., Trim, L. and Pope, D. Fall velocities of natural sediment particles: A simple mathematical presentation of the fall velocity law. *J. Hydraul. Research*, **43**(2), 189-195 (2005)

[39] Shields, A. Anwendung der Ähnlichkeitsmechanik und der Turbulenzforschung. *Mitt. der Preussischen Versuchsanstalt für Wasser- und Schiffsbau*, Heft 26, Berlin (1936)

[40] Slattery, J. C., Sagis, L. and Oh, E.-S. Interfacial transport phenomena. 2^{nd} Ed., Springer (2007)

[41] Smagorinsky, J. General circulation experiments with the primitive equations I. The basic experiment. *Mon. Weather Rev.* **91**(3), 99-165 (1963)

[42] Song, Z., Wu, T., Xu, F. and Li, R. A simple formula for predicting settling velocity of sediment particles. *Water Science and Engineering*, **1**(1) 37-43 (2008) DOI:10.3882/j.issn.1674-2370.2008.01.005

[43] Soulsby, R.L. *Dynamics of Marine Sands.* Thomas Telford, London (1997)

[44] Thomas, T.Y. *Plastic Flow and Fracture in Solids.* Academic Press, New York, London (1961)

[45] Turton, R. and Clark, N.N. An explicit relationship to predict spherical particle terminal velocity. *Power Technol.* **53**(2), 1127-129 (1987)

[46] Van Rijn, L.C. Sediment pick-up functions. *J. Hydraul. Eng. ASCE* **110**(10), 1494-1502 (1984)

[47] Van Rijn, L.C. Sediment transport, Part II: Suspended load transport. *J. Hydraul. Eng. ASCE* **110**(11), 1613-1641 (1984)

[48] Van Rijn, L.C. Unified view of sediment transport by currents and waves. I: Initiation of motion, bed roughness, and bed-load transport. *J. Hydraul. Eng. ASCE* **133**(6), 649-667 (2007)

[49] Vetsch, D. *Numerical Simulation of Sediment Transport with Meshfree Methods*. Doctoral Dissertation, Laboratory of Hydraulics, Hydrology and Glaciology, Swiss Federal Institute of Technology, Zurich p. 200 (2012)

[50] Wang, Y. *Windgetriebene Strmungen in einem Rechteckbecken und im Bodensee.* PhD thesis, TH Darmstadt, Germany, Shaker Verlag, Aachen, ISBN 3-8265-1381-9. p. 432 (1996)

[51] Wilcox, D.C. Reassessment of the scale determining equation for advanced turbulence models. *AIAA J.* **26**(11), 1299-1310 (1988)

[52] Wilcox, D.C. *Turbulence modeling for CFD*. DWC Industries, Inc.,La Cañada, California, 2nd Edition (1998)

[53] Yalin, M.S. *Mechanics of sediment transport*. Second Edition Pergamon Press, Oxford, (1977)

[54] Yalin, M.S. On the determination of ripple geometry. *J. Hydraul. Eng.* **111**(8), 1148-1155 (1985)

[55] Yalin, M.S. and da Silva, A.M.F. *Fluvial processes*. IAHR International Association of Hydraulic Engineering and Research (2001)

[56] Zanke, U. Berechnung der Sinkgeschwindigkeiten von Sedimenten. *Mitt. des Franzius-Instituts für Wasserbau* **46**, 243 p (1977)

[57] Zanke, U.C.E. Zum Einfluss der Turbulenz auf den Beginn der Sedimentbewegung *Mitt. Institut für Wasserbau und Wasserwirtschaft* Techn. Hochschule Darmstadt p 120 (2001)

[58] Zhang, R.J *Sediment Dynamics in Rivers*. Water Resources Press (in Chinese) (1989)

[59] Zhu, L.J. and Cheng, N.S. *Settlement of settling particles*. River and Harbour Engineering Department, Nanjing Hydraulic Research Institute, Nanjing (in Chinese) (1993)

Manuscript received: 09. May 2012

Force-coupled Lagrangian Approach for Numerical Modelling of Bed-load Transport

David Vetsch[1]

[1]Laboratory of Hydraulics, Hydrology and Glaciology,
ETH Zürich, Switzerland, vetsch@vaw.baug.ethz.ch

Abstract

The assessment of sediment transport and involved processes is a major issue in hydraulic and river engineering. The common approaches for the determination of sediment transport rates are mostly based on empirical relations. Since these approaches are not able to describe the underlying physics in detail, they are not suitable to study the generally complex sediment transport processes. However, numerical models which are able to reproduce and to resolve the involved processes are not very common, since they would have to imply the rather complex fluid-sediment interaction. In the present work, a numerical model which is based on a Lagrangian approach with force-coupling, namely the combination of two meshfree particle methods, is presented. The fluid is modelled by a continuum approach which is discretised by the Smoothed Particle Hydrodynamics method. The sediment particles are represented by discrete elements, where the interactions between the discrete sediment grains are modelled by a force law, which is also able to account for various kinds of friction. A similar approach is applied to the interaction between the fluid and sediment particles. The definition of the interface and the exchange of forces between the fluid and sediment grains are inherent to the applied approaches. Thus, the application of special techniques to describe a movable or deformable interface as used for grid-based methods is not necessary. The satisfying simulation results demonstrate the potential of the presented model for the detailed investigation of sediment transport processes as well as for complex practical applications.

1 Introduction

Investigations of river morphology have mainly an experimental background. The processes involved in sediment transport, as the inception of motion, the transport itself and the deposition of sediment, are usually reduced to empirical relations and are combined in the form of a transport formula. Especially, the common concept of incipient motion, where the motion of sediment depends on a threshold condition, has to be questioned. Alternative approaches based on probability distributions used to describe the state of the sediment seem to be more reliable, since their concept corresponds to the natural continuous motion of sediment. Furthermore, the driving forces acting on the sediment, which actually cause the transport, are usually derived from averaged flow quantities. These approaches are useful and of great importance for engineering practice, but they only allow for the determination of a temporally and spatially averaged sediment transport. For river engineering problems, where the morphological development plays an important role, a variety of numerical tools exists. These are able to simulate

sediment transport from a local to a regional scale with satisfying accuracy as far as sufficient data for their calibration is available. By the application of modern numerical tools it is nowadays possible to resolve the flow field, i.e. the water phase, in detail. However, depending on the resolved scales, the gained advantage will be lost due to the rather approximate approach for sediment transport, i.e. the solid phase of the water-sediment mixture flow. In the last decades, many researchers tried to overcome the shortcomings of physics in the common approaches, however, with limited success. Despite investigations using state-of-the-art measuring techniques and providing an in-depth view of acting forces at the sediment bed, a reasonable approach, which does not need calibration but is still convenient for practical application, does not seem to be available in the near future. However, such kinds of investigations highlight the complexity of the involved processes and the sediment transport per se. Furthermore, the detailed experimental data may serve for the validation of advanced numerical models. Because of the availability of increasing computational resources, the application of numerical models for the investigation of the mechanics of sediment transport becomes more and more popular. Such numerical tools are rather sophisticated, since they have to be able to model the interaction between the fluid and the sediment grains as well as the interactions between the grains themselves. Such models also have to include friction to correctly reproduce the constitutional behaviour of the sediment and the different modes of bed load transport, as sliding, rolling and saltating. One of the main challenges in developing such approaches is the appropriate modelling of the movable interfaces between the fluid and the sediment grains and the exchange of forces. Although several different numerical techniques exist which are suitable for such problems, they often have deficits concerning efficiency or accuracy. Furthermore, many common numerical approaches for the simulation of fluid flow use computational grids for the spatial discretisation, which may reduce the flexibility for the modelling of arbitrary geometries and lead to quite complex schemes for movable boundaries. However, when it comes to three dimensional applications, the main handicap of these approaches is the computational expense necessary to obtain qualitatively good results, and the use of high performance computing seems to be inevitable.

In this article a novel modelling approach is presented, which is able to simulate sediment transport and reproduce the involved processes in detail. To reduce the complexity of this challenging task, the primary focus of this work is on bed load transport. Since the involved physical processes rely on fluid and rigid body dynamics, numerical discretisation techniques are applied, which account for the distinct characteristics of these disciplines and which allow for flexible modelling of fluid-structure interaction. Thus, the combination of two meshfree particle methods, namely the Smoothed Particle Hydrodynamics method and the Discrete Element Method, is considered. These are able to model the different properties of the fluid and the sediment as well as their interaction without the need for a computational grid. Furthermore, this hybrid approach allows for the description of the processes of bed load and the corresponding transport modes by discrete forces. The successful application of the model to various problems shows the potential of this approach for the numerical simulation of bed load transport. The model is a suitable numerical research tool and may serve for future investigations, especially with regard to increasing computing power.

2 Basic Considerations

2.1 Bed Load Transport

The mechanism of bed load transport is described by processes occurring in the upper-most layer of the river bed. Sediment grains are moved in different forms due to stream forces or strikes of other grains in motion (Bagnold (1941)). The transport modes are comparable with Aeolian transport which can be observed at sand dunes in deserts; grains move in flow direction by saltating, or, which is less usual, by rolling or even by sliding along the bed (Fig. 2-1). The distinction between transport in the form of saltation or in suspension is not obvious. Bagnold (1973) defines transport of a solid in suspension as a state in which the excess weight of the solid is compensated by a random succession of upward impulses due to eddy currents of fluid turbulence moving upwards relative to the bed. Therefore, the solid may remain out of contact with the bed for an indefinite period depending on the random nature of turbulence. In contrast, saltation as well as bed load transport in general may be characterised as motion with successive contacts between the grains and the bed.

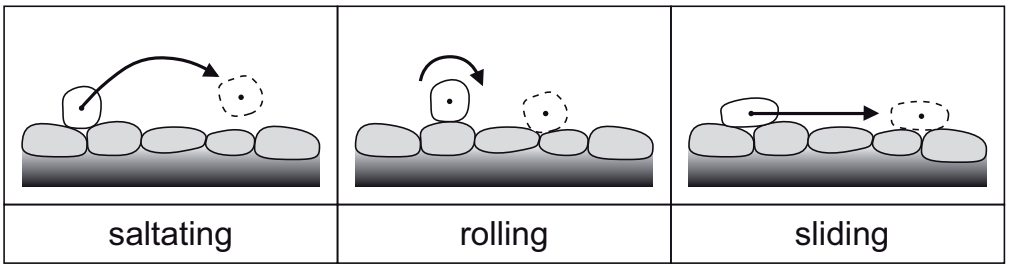

Fig. 2-1: Modes of bed load transport

Church (2006) gives an overview on the different sediment transport regimes, on the categorization of fluvial sediments as well as on the relation of bed load transport and morphology in alluvial rivers. A quantitative distinction between bed load and suspended load can be found in Murphy and Aguirre (1985).

2.2 Incipient Motion

The topic of incipient motion - the onset of transport of sediment - has been studied by many researchers in the last hundred years or so. In most cases, the goal was to define a threshold for sediment motion which is an essential premise for the estimation of sediment transport in alluvial rivers. The main motivation for the investigations was and still is the development of a transport relation to asses bed load discharge in rivers that serves as essential tool for river engineering works. The methodology to find a criterion for the threshold is usually based on theoretical investigations or visual observations as well as measured reference bed load transport rates, acquired in a laboratory flume or in a natural river. Consequently, in engineering practice the rate of sediment transport is calculated with empirically based transport equations which are usually defined as a function of a certain threshold. From a physical point of view it is obvious to express a threshold condition in terms of stream force. Thus, approaches based only on the mean flow velocity seem not to be reasonable because they do not account for flow depth and turbulence. Thus, the criterion for incipient motion is usually determined by threshold quantities

like the critical bed shear stress τ_c, the critical shear velocity u_{*c} or the amount of the critical lift force $F_{L_c} = \left|\vec{F}_{L_c}\right|$. Dey and Papanicolaou (2008) provide a review on the different concepts.

A very common approach for the definition of incipient motion was introduced by Shields (1936). Based on the consideration of equilibrium of moments and dimensional analysis, he proposed to express the dimensionless critical shear stress τ_c^* as a function of the grain or particle Reynolds number. This finding may be formulated in terms of critical values (see e.g. Yalin (1977)) for a grain of size d_s as

$$\tau_c^* = \frac{\tau_c}{\Delta\rho g d_s} = f(\mathrm{Re}_c^*)\,, \quad \mathrm{Re}_c^* = \frac{u_{*c} d_s}{\nu}\,, \tag{2.1}$$

where $\Delta\rho = (\rho_s - \rho_f)$ is the density difference between sediment (subscript s) and fluid (subscript f), g is the gravitational acceleration, Re_c^* is the critical particle Reynolds number, ν is the kinematic viscosity. The dimensionless critical shear stress τ_c^* (also denoted as the critical Shields parameter θ_c) and the critical shear velocity u_{*c} were determined by observations in a laboratory flume. However, the definition of the point of inception is not clear and varies considerably among the various studies. This means that in practical cases of turbulent flow there is no single criterion for the beginning of movement of sediment. Buffington and Montgomery (1997) give an extensive review on the issue.

Due to the ambiguity in the determination of a value for the critical shear stress and to account for the random nature of turbulence and sediment movement, some researchers developed approaches which describe and quantify an observable state of motion, rather than a hypothetical state of zero movement. These kinds of approaches are termed probabilistic or stochastic. One of the first derivations of a stochastic concept for bed load transport was presented by Einstein (1937) within his doctoral thesis. Einstein (1950) defined the pickup probability for a particle as “the probability of the dynamic lift force on the particle being larger than its weight (under water)”. For the evaluation of the pickup probability p_e, he derived theoretically the following formula:

$$p_e = 1 - \frac{1}{\sqrt{\pi}} \int_{-B_*\Psi_* - 1/\eta_0}^{+B_*\Psi_* - 1/\eta_0} e^{-t^2} dt \tag{2.2}$$

where $\Psi_* = 1/\tau_b^*$ is the flow intensity with dimensionless shear stress τ_b^*, $\eta_0 = 0.5$ is the standard deviation and t is the only variable of integration. The constant $B_* = 1/7$ was obtained for uniform sediment by using the data of Meyer-Peter *et al.* (1934) and others. The non-central probability density function (abbreviated as pdf) on the right hand side of equation (2.2), i.e. the definite integral of the Gaussian normalized by its total area $\sqrt{\pi}$, can be interpreted as the probability for a particle being stationary for a given flow intensity Ψ_*. A solution for the integral in closed form in terms of elementary functions does not exist but can be gained by approximation. Cheng and Chiew (1998) reviewed approximations of different authors and Wu and Lin (2002) provide improved approximations for the probability distribution with application of a log-normal pdf for the instantaneous velocity at the bed and appropriate values for the lift coefficient best fitting experimental data. Further enhancements for smooth turbulent flows were contributed by Wu and Chou (2003), who, apart from lifting also considered rolling probabilities and defined the mean total probability of entrainment as the sum of both. The results reveal that a distinct probability for the critical state of sediment entrainment cannot be found, i.e. a critical shear stress does not exist. This finding is also acknowledged by other researchers

(see review by McEwan and Heald (2001)). Further refinement of the approaches noted above can be found e.g. in Wu and Yang (2004) or Hofland and Battjes (2006).

The fundamental different views of the two approaches described above for incipient motion - the conventional threshold criterion according to Shields and the stochastic or probabilistic approach - are depicted in Fig. 2-2. The first is most commonly applied in river engineering due to its simple use. However its correct application requires calibration and experience, especially because of the explicit form of the motion threshold. Besides Einstein's or comparable subsequent work, the latter is still subject to current research driven by new measurement techniques allowing for a more and more detailed insight into the flow properties. For both, useful bed load transport formulas exist.

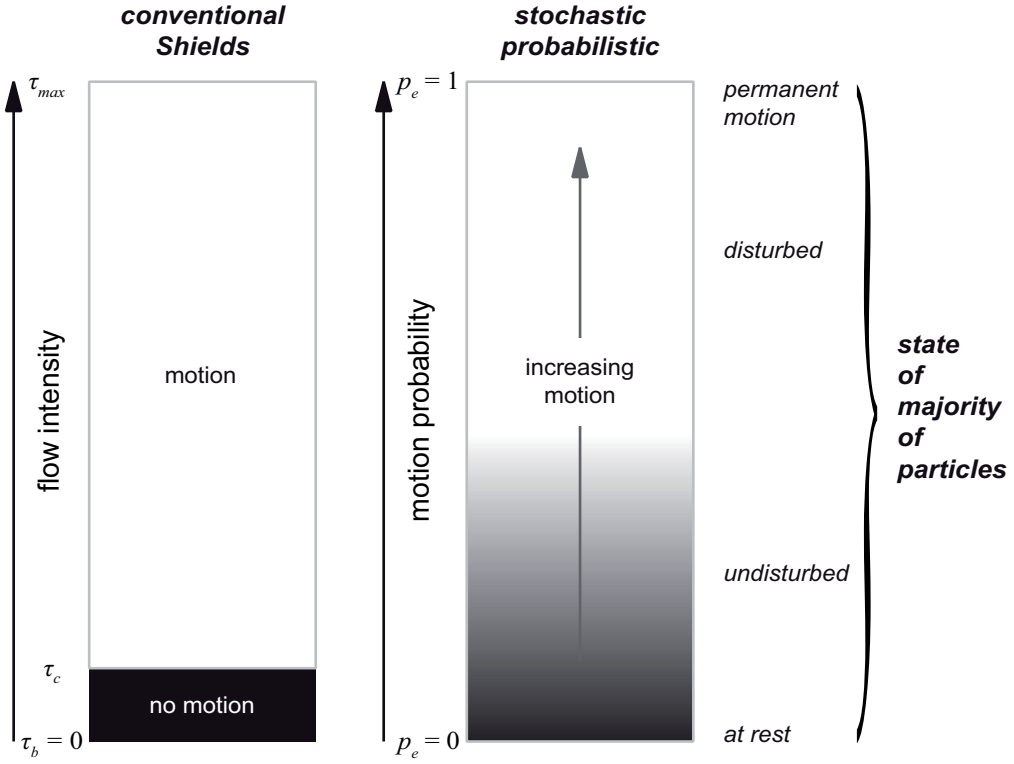

Fig. 2-2: Comparison of the two different concepts for particle motion

In addition, Fig. 2-2 shows a classification according to the state of the majority of the particles in direction of the flow intensity and the motion probability, respectively, which is valid for both models. In Bagnold's sense (Bagnold (1936)), the expression 'undisturbed' describes a particle which has not been displaced, whereas a particle that is displaced and then is resting is called 'disturbed'. Furthermore, the rather undefined state of permanent motion, where $\tau_b = \tau_{\max}$ and $p_e = 1$, can be interpreted as transition from bed load to suspended transport, ending up in hyperconcentrated or debris flow.

2.3 Fluid and Rigid Bodies

Two effects are crucial for a correct simulation of the different transport modes of rigid bodies in fluids (see Fig. 2-1). On the one hand, applied forces and torques on spheres occur due to their interaction. On the other hand, the applied forces and torques due to the presence of the fluid and its flow also play an

important role. By way of illustration, both effects are composed in Fig. 2-3. In this section the basic hydro-mechanical forces are introduced from an integral and partially empirical point of view. Notice that for the present work, rigid bodies are considered as spheres for the sake of simplification. The approaches for the modelling of the detailed particle interaction forces are introduced in section 4.2.

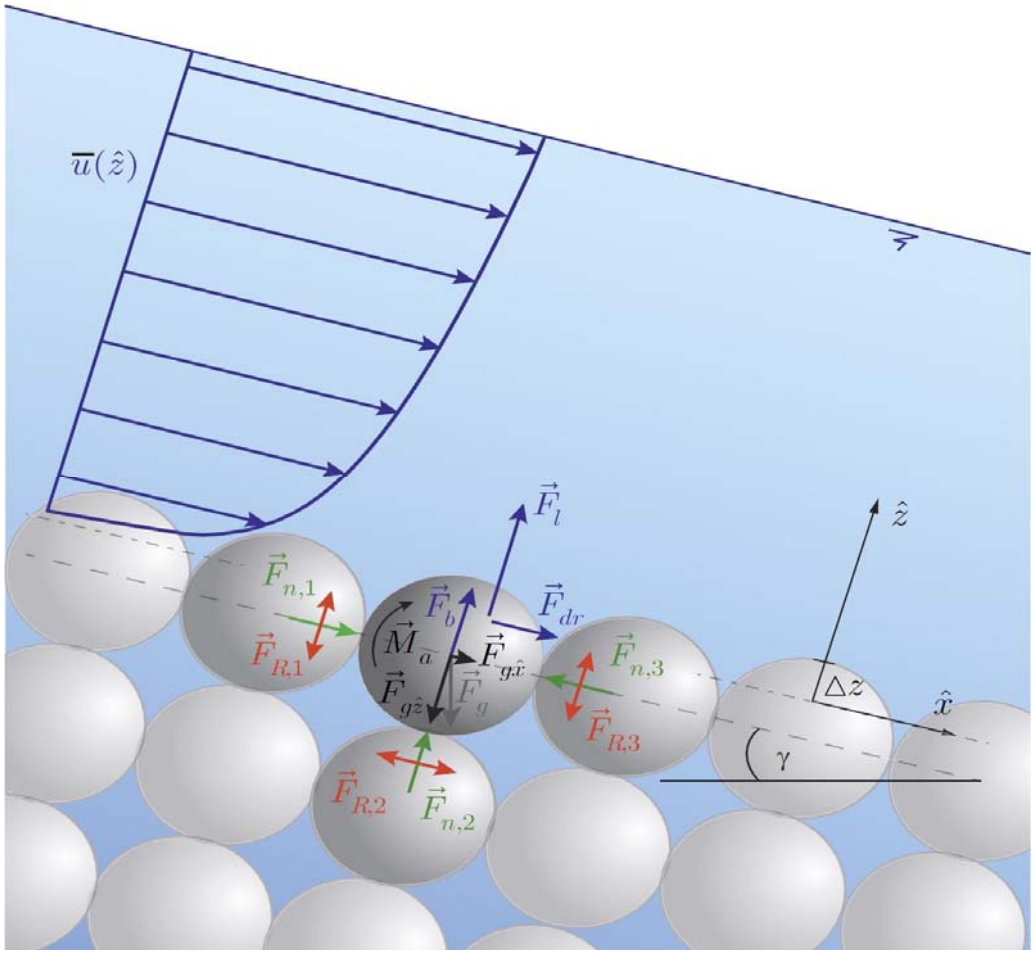

Fig. 2-3: Acting forces at a river bed consisting of spheres. The depicted velocity distribution $\overline{u}(z)$ is based on the logarithmic law for wall-bounded turbulent flow.

2.3.1 Hydrostatic Forces

The effect of buoyancy, also known as Archimedes' principle, occurs when a body has surfaces in contact with the fluid which have a normal with a non-zero component in downward direction. The buoyancy force $\vec{F}_b$ is due to the pressure difference above and below the immersed body and is equivalent to the weight of the fluid displaced by the body. The use of an appropriate model allowing for fluid between the spheres of the channel bed (as illustrated in Fig. 2-3) and including buoyancy effects correctly may be crucial in order to obtain reliable simulations of bed load transport. This is also affirmed by the fact that the hydrostatic pressure distribution is implicit in the definition of the Shields parameter (see equation (2.1)). The effect of non-hydrostatic pressure distributions on bed load transport has been pointed out e.g. by Francalanci *et al.* (2008) and is discussed in the next section.

2.3.2 Hydrodynamic Forces

The force $\vec{F}_{dr}$ acting in the direction of relative motion of a body immersed in a fluid is called drag or fluid resistance. In other words, drag is the force in the direction of relative motion that has to be applied to move a body through a stagnant fluid or to keep the same body at rest in case of fluid flow (the weight of the body is neglected). The drag is made up of two contributions, namely the pressure drag arising from the non-uniform pressure distribution on the body and the skin friction drag due to shear stresses on the body surface. Besides the drag force but with the same origin, the second component of the force exerted on an immersed body due to fluid flow is the lift force $\vec{F}_l$ acting perpendicular to the direction of relative motion.

For the flow over a channel bed made of spheres, as depicted in Fig. 2-3, the nature of the drag and lift forces is rather complex. Close to the rough boundary, the velocity is not uniform and the flow is turbulent. Since the acting pressure is a combination of hydrostatic and hydrodynamic pressure, the lift force may be reduced to a pressure difference that occurs due to the turbulent effects on the side of the sphere facing the flow; which has been measured by Einstein and Elsamni (1949) for hemispheres, by Dwivedi *et al.* (2010) for spheres, by Detert *et al.* (2010) for spherical as well as mixed sediments and by Smart and Habersack (2007) for natural gravel in a river, for example. Investigations into the drag force exerted on a sphere set on top of a bed of closely packed spheres have been carried out by Coleman (1972). He concludes that the drag coefficient function for this situation corresponds with the function for a sphere in free fall. Schmeeckle *et al.* (2007) studied the situation of a sphere surrounded by other spheres without contact and for different exposure of the sphere to the flow. For decreasing exposure the drag force also decreases due to sheltering by the other particles while the lift force increases. The residual drag which exerts forces on the sphere can cause angular momentum; this is not covered in the mentioned study, but may be of importance in the process of particle entrainment.

For open channel flow, the most common engineering approach is to express the forces close to the bed by temporally and spatially averaged quantities, i.e. the bottom shear stress τ_b or the shear velocity u_* (cp. section 2.2). However, the quantities which entrain and move sediment are neither bed shear stress nor any other average characteristic of the flow, but instead the fluctuating forces, such as lift and drag, exerted directly by the flow on the particles, as stated by Schmeeckle *et al.* (2007). Thus, a force expressed in terms of $F = \tau_b A$ is a rough simplified model of reality. The hydrodynamic forces discussed herein certainly play an important role for the incipient motion or entrainment of sediment particles, but peak values of the forces may not be sufficient. The duration of the peak values is also a significant factor as pointed out by Valyrakis *et al.* (2010). Therefore, they conjectured that impulse, rather than just the magnitude of hydrodynamic forcing, is relevant to the description of the incipient motion phenomenon.

2.4 Modelling Approach

The modelling approach applied in the present work comprises the representation of the gravel bed and the water flow by particles which interact with each other. Therefore, Lagrangian methods, also called meshfree or particle methods, are applied to both the hydrodynamics and the bed load transport, which allows for a homogeneous discretisation of the underlying equations of motion. In other words, for discretisation of the computational domain and the multi-phase system, basically the same kind of approach is used; however with respect to the distinct properties of each phase, different methods are applied. The single grains of the gravel bed are modelled by discrete elements in the form of rigid spheres and their motion and interactions are resolved by application of the Discrete Element Method (DEM). For the water flow, i.e. the hydrodynamic equations, a continuum approach, namely the Smoothed Particle Hydrodynamics (SPH) method, is applied. The modelling approach used is depicted in Fig. 2-4.

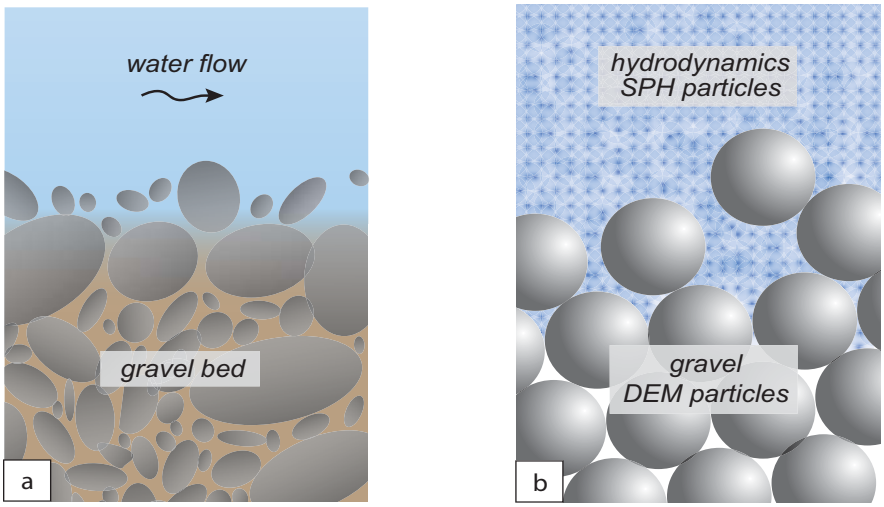

Fig. 2-4: Representation of (a) water flow and gravel bed by (b) SPH and DEM particles, respectively.

The primary advantage of this approach relies on the fact that any phase interface or fluid-structure coupling as well as interaction between solid objects is treated on a particle to particle basis. The basic difference between grid-based methods and meshfree methods is that no grid is necessary for the discretisation of the computational domain. For meshfree methods, a set of arbitrary distributed particles is used which represent the nodes required for the spatial discretisation. This permits to overcome many of the problems arising from the use of a computational mesh, especially the treatment of movable boundaries and the generation of grids. Furthermore, meshfree methods seem to be a promising approach for the simulation of fluid-structure interaction as discussed in this paper. An overview on some common meshfree methods is given by Huerta *et al.* (2004), Nguyen *et al.* (2008) and Koumoutsakos (2005) shows the potential of particle methods for multi-scale flow simulations. For the present work, the simulation software *Pasimodo*, which is a multi-purpose particle simulation tool developed by Fleissner (2010), is used (see also Lehnart (2008), Fleissner *et al.* (2010)).

3 Governing Equations

3.1 Fluid Flow

3.1.1 Euler equations

For the present work, a simplification of the Navier-Stokes equations is applied, where the fluid is considered to be inviscid. The assumption of an inviscid fluid may be appropriate for convectively dominated flows with large Reynolds number (ratio of inertial force to viscous force) where laminar boundary layer effects do not have a significant influence. The corresponding equations are called Euler equations. Note that their general formulation is for a compressible fluid. They consist of the conservation of mass and the conservation of momentum,

$$\frac{\partial \rho_f}{\partial t} + \vec{\nabla} \cdot \left(\rho_f \vec{u} \right) = 0 \ , \tag{3.1}$$

$$\frac{\partial \left(\rho_f \vec{u} \right)}{\partial t} + \vec{\nabla} \cdot \left(\rho_f \vec{u} \otimes \vec{u} \right) = -\vec{\nabla} p + \rho_f \vec{f}_e \ , \tag{3.2}$$

where ρ_f is the density of the fluid, $\vec{u}$ is the flow velocity, p is the pressure and $\vec{f}_e$ are applied external volume forces per unit mass.

3.1.2 Lagrangian Form of the Euler equations

For the derivation of the conservation laws in the previous sections the time-dependent quantities, i.e. density, velocity and total energy, were considered as infinitesimal parts of a continuum. From the Eulerian viewpoint which is well-established in computational fluid dynamics, their time rate of change has to be evaluated at fixed points, e.g. at $\left(x_i \ y_j \right)$ as depicted in Fig. 3-1. Hence, the history of a quantity is limited to these points and it is generally not possible to track the path of a fluid particle.

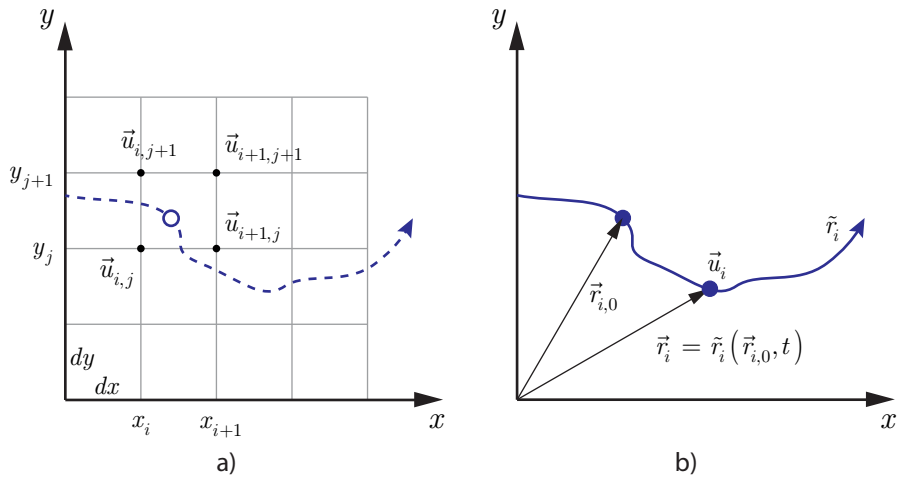

Fig. 3-1: Eulerian (a) and Lagrangian (b) viewpoint.

An alternative viewpoint is the Lagrangian description; it can be regarded as a natural extension of particle mechanics. The fluid is considered to consist of material particles that move with the flow. Each particle is identified by its initial position $\vec{r}_{i,0}$ and a quantity carried with the particle is given in Lagrangian variables by

$$\Psi = \Psi_L\left(\vec{r}_{i,0}, t\right) . \tag{3.3}$$

The position $\vec{r}_i$ of a particle can be obtained by its path function or trajectory $\tilde{r}_i$ (Fig. 3-1b),

$$\vec{r}_i = \tilde{r}_i\left(\vec{r}_{i,0}, t\right) . \tag{3.4}$$

Based on the path function, the velocity, $\vec{u}_i = \partial\tilde{r}_i \big/ \partial\, t$ and acceleration, $\vec{a}_i = \partial^2\tilde{r}_i \big/ \partial\, t^2$ of a particle can be defined. With this approach, the history of a particle can easily be tracked. However, since the Lagrangian analysis of fluid flow is usually quite difficult it is rarely applied. Nevertheless, when the fluid is discretised by particles, the use of the Lagrangian approach is reasonable. Therefore, a time derivative for Eulerian variables is introduced that can be evaluated for a moving particle, called the substantive or material derivative,

$$\frac{D(.)}{Dt} \coloneqq \frac{\partial(.)}{\partial t} + \vec{u} \cdot \vec{\nabla}(.) . \tag{3.5}$$

By application of the substantial derivative, the Euler equations can be written in Lagrangian form as

$$\frac{D\rho_f}{Dt} = -\rho_f \vec{\nabla} \cdot \vec{u} , \tag{3.6}$$

$$\frac{D\vec{u}}{Dt} = -\frac{1}{\rho_f}\vec{\nabla} p + \vec{f}_e . \tag{3.7}$$

The energy conservation equation has been omitted, since for the present work the fluid is considered to be isothermal water at 20° C. Thus, the fluid is a liquid that generally can be regarded as incompressible. Nevertheless, under specific circumstances it may be necessary to take the small variation of density with change of pressure into account. Therefore, Batchelor (2005) presented an equation of state for water. A similar relation is useful to obtain an approximate solution of the Euler equations as discussed in section 4.1.4.

3.2 Motion of Rigid Bodies

3.2.1 Equations of Motion

For moving bodies Newton's laws apply. The three laws describe the relation between the acting forces and the motion of the body. Newton's first law states that a body with mass m at rest will stay at rest or the same body with velocity $\vec{v}$ will not change its velocity, if no unbalanced force acts on the body. The state of a body in motion can be described by its linear momentum as

$$\vec{p} = m\vec{v} . \tag{3.8}$$

Accordingly, the time rate of change of linear momentum, if not zero, demands an acting, non-balanced force $\vec{F}_a$. This fact is postulated by Newton's second law which reads for constant mass

$$\frac{d\vec{p}}{dt} = m\frac{d\vec{v}}{dt} = m\vec{a} = \vec{F}_a , \tag{3.9}$$

where $\vec{a}$ is the acceleration of the body. Newton's third law describes the interaction of two bodies in contact; it is also called the law of action and reaction. Based on this third law, Newton derived the

conservation of linear momentum that is elementary for the description of colliding bodies. In the absence of dissipative forces due to deformation, it states that the sum of linear momentum of the colliding bodies before and after collision is constant, i.e. linear momentum is conserved.

Newton's laws are said to deal with point masses; they describe the translational motion of an extended body only, while its rotation is not covered. Therefore, Euler introduced equations that describe the time rate of change of angular momentum; they are called Euler's equations (not to be confused with the homonymous equations for fluid dynamics from the same author introduced in section 3.1.1). In analogy to equation (3.8) for linear momentum, angular momentum reads

$$\vec{L} = \mathbf{I}\vec{\omega} \ , \tag{3.10}$$

where $\vec{\omega}$ is the angular velocity and $\mathbf{I} = \mathbf{I}^T$ is the tensor of moment of inertia in the fixed principal frame of the body. Similar to Newton's second law, the time rate of change of angular momentum is caused by the applied torque $\vec{M}_a$. Accordingly, the dynamic Euler equations read in the general vector form

$$\mathbf{I} \cdot \frac{d\vec{\omega}}{dt} + \vec{\omega} \times \left(\mathbf{I} \cdot \vec{\omega} \right) = \vec{M}_a \tag{3.11}$$

Equations (3.9) and (3.11) are the equations of motion and actually the conservation laws for linear and angular momentum. They describe the time dependent motion of a body due to applied forces and torques and can be solved for their time dependent terms, i.e. the linear, $d\vec{v}/dt$, and angular, $d\vec{\omega}/dt$, accelerations (see e.g. Fleissner (2010)).

3.2.2 Applied Forces and Torques

For a modelling approach like the discrete element method, the forces $\vec{F}_{a,i}$ and contact torques $\vec{M}_{a,i}$ applied on a particle i are the sum of contact forces $\vec{F}_{c,ij}$ and torques $\vec{M}_{c,ij}$ due to interacting particles j plus external forces $\vec{F}_{e,i}$ or torques $\vec{M}_{e,i}$, respectively,

$$\vec{F}_{a,i} = \sum_j \vec{F}_{c,ij} + \vec{F}_{e,i} \ , \tag{3.12}$$

$$\vec{M}_{a,i} = \sum_j \vec{M}_{c,ij} + \vec{M}_{e,i} \ . \tag{3.13}$$

The forces acting on a sphere surrounded by other spheres are depicted in Fig. 2-3. The contact forces are split into components normal and tangential to the contact surface and are treated differently depending on their orientation. The primary contact or interaction forces act normally to the contact surface (normal forces). If the body is a sphere, they will only apply as a concentric force and thus not cause a torque at the centre. Force laws used to model the interaction of rigid bodies in terms of spheres are discussed in section 4.2.2. The secondary contact forces act tangentially to the contact surface and are due to friction (tangential forces). In most cases they lead to a torque. Two kinds of friction are distinguished, namely static and kinetic friction. In a static system, tangential forces due to static friction may be of importance, e.g. for a block on an inclined ramp. This effect can also be observed at sand piles. Kinetic or slip friction occurs when bodies interact with relative lateral velocities. Kinetic friction

depends on the material properties of the interacting bodies and the normal force acting between them. Friction forces as used in this work are briefly discussed in section 4.2.3.

Besides contact forces, also external forces have to be considered. The main external force is due to gravity. Assuming a constant acceleration of gravity of $\vec{g} = \left(0, 0, -g\right)$ with $g = 9.81$ [m/s^2], the weight of a rigid body is given by

$$\vec{F}_g = V\rho\vec{g} = m\vec{g} \ , \tag{3.14}$$

where m is the mass of the body, V is its volume and ρ its density.

4 Numerical Methods

4.1 Smoothed Particle Hydrodynamics

4.1.1 General

Monaghan (2005b) describes the basic idea behind SPH as replacing the fluid by a set of points that follow the motion of the fluid and carry information about the properties of the fluid. These points can be seen either as interpolation points for the discretisation of the governing equations or as real material particles. Monaghan (1994) applied the method to free surface flows and demonstrated that SPH requires no explicit treatment of the free surface. In contrast, other methods like finite difference or finite volume schemes need special approaches that would require very fine meshes or adaptive grids for the modelling of complex flow with one or several convoluted free surfaces. Furthermore, the interaction with rigid bodies or boundaries can be handled as particle to particle interaction without the need of additional tracking or capturing of the movable interface. An example which illustrates these capabilities is depicted in Fig. 4-1. Overviews about SPH can be found in Monaghan (2005a), Monaghan (1992) or Liu and Liu (2003) for example. Compared to established numerical schemes like the Finite Difference Method, the SPH method is still under development. It has been improved by contributions of many researchers during the last two decades and the number of applications increases continuously. Nevertheless, one of the main and well-recognised drawbacks is the high computational cost when it comes to 3D applications, especially when a fine special resolution is desired (Gomez-Gesteira *et al.* (2010)).

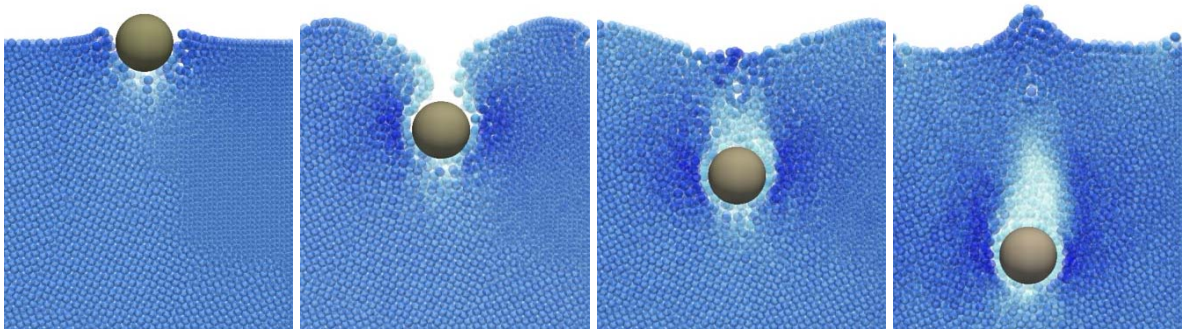

Fig. 4-1: Impacting of a sphere on a free surface simulated with the presented approach (Vetsch (2012)). Colour indicates the vertical velocity: lighter negative, darker positive with respect to the z-direction.

The standard SPH method (Monaghan (2005a)) used in this work is also termed "*weakly compressible SPH*" (WCSPH), because the computation of the pressure is based on an equation of state for water. This approach is suitable for flows where relative density variations range within 1% (see Monaghan (1992)). Some draw backs are for instance pressure fluctuations and long computation times. The latter are due to the used CFL condition that depends on the velocity of sound (or a propagation velocity specific to a problem) instead of the fluid velocity. The velocity of sound is usually many times larger than the maximum velocity of the fluid. To circumvent these problems, a different approach has been introduced by Cummins and Rudman (1999) for flows without free surfaces and has been extended by Shao and Lo (2003) to free surface flows. This alternative approach is often termed "*truly incompressible SPH*" (ISPH). Instead of an equation of state, a Poisson equation is used to predict the pressure. The approach to solve the Poisson equation is similar to grid-based Navier-Stokes solvers. The different approaches to treat the compressibility of the fluid are still an open topic in the SPH community. By comparison of the approaches, Hughes and Graham (2010) reach the conclusion that WCSPH performs as well as ISPH does and in some respects even better. Alternatively, Lee *et al.* (2010) show that ISPH is superior for some cases.

4.1.2 Particle Approximation

Since SPH is a Lagrangian method, each particle moves with the fluid flow and carries quantities such as the velocity $\vec{u}_i$, the density $\rho_{f,i}$ and its mass m_i. In other words, these quantities are only known at the location of the particle itself. For numerical discretisation, any quantity or function $A_r(\vec{r})$ at location $\vec{r}$ can be obtained by interpolation based on a kernel function $W(r_{ab},h)$, where $r_{ab} = \left|\vec{r}_a - \vec{r}_b\right|$ is the distance between two particles and h is the smoothing length. For the present work, the Gaussian kernel with a cut-off at distance of $2h$ is preferred. The Gaussian kernel has proved to be a good choice with regard to accuracy and efficiency and has been successfully applied in many simulations. Considering particles (interpolation points) with mass m, density ρ and position $\vec{r}$ identified by indices a and b, where a identifies the particle of interest and b the neighbouring particles with masses according to a volume element of the fluid $m_b = \rho_b(\vec{r}_b)d\vec{r}_b$ and $A_b = A_r(\vec{r}_b)$, the summation interpolant can be written as

$$A_a(\vec{r}_a) = \sum_b m_b \frac{A_b}{\rho_b} W(r_{ab},h) \ . \tag{4.1}$$

For example, the density can be estimated by

$$\rho_a(\vec{r}_a) = \sum_b m_b W(r_{ab},h) \ . \tag{4.2}$$

By using a kernel function that is differentiable, the derivative of A_a can be obtained by ordinary differentiation as

$$\vec{\nabla} A_a(\vec{r}_a) = \sum_b m_b \frac{A_b}{\rho_b} \vec{\nabla}_a W_{ab} \ . \tag{4.3}$$

For the sake of clarity, the notation $\vec{\nabla}_a W_{ab}$ was introduced to denote the gradient $\vec{\nabla} W(r_{ab},h)$ taken with respect to the position of particle a. Since the derivative in form of equation (4.3) is not very

accurate even for a constant function, it should not be used for practical applications. According to Lehnart (2008), other forms of the derivative are used that are more accurate; they depend on the properties of the equation to be discretised.

4.1.3 Discrete Form of Euler Equations

Due to the Lagrangian approach, the original partial differential equations reduce to a set of ordinary differential equations which can be discretised for particles according to the concept introduced in the previous section. Hence the conservation of mass reads

$$\frac{d\rho_a}{dt} = \rho_a \sum_b \frac{m_b}{\rho_b} \left(\vec{u}_a - \vec{u}_b \right) \cdot \vec{\nabla}_a W_{ab} \ , \tag{4.4}$$

and the conservation of momentum in its discretised form reads

$$\frac{d\vec{u}_a}{dt} = -\sum_b m_a \left(\frac{p_a}{\rho_a^2} + \frac{p_b}{\rho_b^2} + \Pi_{ab}\left(\alpha, \beta\right) \right) \vec{\nabla}_a W_{ab} + \vec{f}_e \ , \tag{4.5}$$

where $\Pi_{ab}\left(\alpha, \beta\right)$ is the artificial viscosity term (see section 4.1.5). The particles are moved by

$$\frac{d\vec{r}_a}{dt} = \vec{u}_a \ . \tag{4.6}$$

The index a denotes the actual particle and index b its neighbours within the cut-off distance. The properties of particle a are mass m_a, density ρ_a, velocity $\vec{u}_a$, pressure p_a and position $\vec{r}_a$ and similar for neighbouring particles with index b. Equations (4.4) and (4.5) are the Euler equations discretised by the SPH method according to Monaghan (1992). The equation system is closed by an appropriate equation of state for the pressure p.

4.1.4 Equation of State

For WCSPH, the motion of the fluid particles is simulated based on the compressible Euler equations, i.e. particles may be regarded as the molecules of a gas and their motion is driven by local density gradients. According to the laws of thermodynamics, the pressure can be related to the density by an equation of state for a compressible fluid to close the governing equations. Thus, a quasi-incompressible equation of state is used for the present approach, which reads

$$p_a = B\left(\left(\frac{\rho_a}{\rho_0} \right)^{\gamma_p} - 1 \right), \quad B = \frac{c_s^2 \rho_0}{\gamma_p} \, , \tag{4.7}$$

where ρ_0 is the reference density of the fluid, ρ_a is the particle density and usually $\gamma_p = 7$. The choice of B determines the speed of sound c_s. Since the time-step size of the simulation may depend on the speed of sound, a rather small value of c_s compared to its effective value of ~1500 m/s is preferred to gain a faster simulation progress. In order to limit density variations to a maximum of 1%, Monaghan (1994) argues that the sound velocity has been chosen so that the Mach number of the flow should be 0.1 or less; this yields

$$c_s = 10 u_{ref} \ . \tag{4.8}$$

The reference velocity u_{ref} depends on the problem, i.e. for a dam break problem with initial water depth H_0 the approximate upper bound to the velocity is $u_{ref} = \sqrt{2gH_0}$ whereas for shallow water flows, where the ratio of wavelength to water depth tends to zero, the reference velocity is equal to the wave propagation velocity $u_{ref} = \sqrt{gh_f}$. In terms of a conservative estimate, the first expression has been used for this work.

4.1.5 Enhancements

Artificial Viscosity

The introduction of some sort of damping similar to finite difference schemes may be necessary for the stability of the numerical scheme. Therefore an artificial viscosity in terms of an artificial pressure $\Pi_{ab}\left(\alpha,\beta\right)$ is introduced in the momentum equation (see e.g. Monaghan (2005a)). Even though the parameters controlling the artificial viscosity, α and β , are not critical, good results were obtained for free surface flows by a choice of $\alpha = 0.01$ and $\beta = 0$ (compare Monaghan (1994)).

Turbulence Models

The standard formalism of SPH was successfully applied to complex flow types such as wave breaking, e.g. by Landrini *et al.* (2007). It was shown that detailed properties of vortices can be recovered. According to Cottet (1996), artificial viscosity models can be seen as eddy viscosity models but parameters have no explicit reference to any regularization of motion, i.e. the parameters have to be calibrated according to the problem at hand. However, in general the approach allows for taking into account turbulent effects in a similar way as algebraic turbulence models. For the present work, only artificial viscosity was considered. An overview on SPH and advanced turbulence modelling, e.g. the k-ε model or Large Eddy Simulation, is given by Violeau and Issa (2007).

Correction for Free Surface Flows

The XSPH correction is useful to obtain better results for free surface flows (see Monaghan (1994)) or for immiscible multiphase flows. A correction for the velocity is introduced that leads to an adaptation of the particle velocity to the mean velocity of the surrounding particles, which keeps the particles to move more orderly. The correction term, added to the right-hand side of equation (4.6) is

$$\triangle\vec{u}_a = \varepsilon_X \sum_b m_b \frac{(\vec{u}_b - \vec{u}_a)}{\overline{\rho}_{ab}} W_{ab} \ , \tag{4.9}$$

where $\overline{\rho}_{ab} = \left(\rho_a + \rho_b\right)\big/2$. The parameter $0 \leq \varepsilon_X \leq 1$ was introduced by Monaghan (1992) and is usually chosen as $\varepsilon_X = 0.5$.

4.1.6 Time Integration and Time-Step Size

The fluid particles are advanced in time by solving equations (4.4) to (4.6) numerically. Since these equations are ordinary differential equations, theoretically any stable time-stepping scheme for ordinary differential equations can be used. However, for dissipative systems, Lehnart (2008) proposed a predictor-corrector method based on the leapfrog scheme (PC-leapfrog) as presented by Monaghan *et al.* (2003).

For the SPH method applied here, three characteristic time scales exist. The first corresponds to the general stability condition for numerical problems where advection is dominant, i.e. the CFL-condition.

It means that in the time step $\triangle t$ a quantity must not advance further than a given length scale. For SPH, the relevant length scale is the smoothing length h and the reference velocity u_{ref} is the higher of the maximum flow velocity or the specified sound velocity c_s, i.e. $u_{ref} = \max\left(\left|\vec{u}\right|_{\max}, c_s\right)$. The second and the third characteristic time scales restrict the time step to the maximum of acting internal and external forces, i.e. the viscous forces and the applied forces in terms of the maximum particle acceleration $a_{\max}$, whereas the former is only relevant for flows with low Reynolds numbers. According to these considerations, the size of a time step can be obtained by the assignment

$$\triangle t = \alpha_s \min\left(\frac{h}{u_{ref}},\ \frac{h^2}{\nu},\ \sqrt{\frac{h}{a_{\max}}}\right), \tag{4.10}$$

where α_s is a safety factor similar to the CFL number. According to the results reported by other researchers, α_s lies in the range of 0.125 and 0.5 (see e.g. Lee *et al.* (2008)). Values around 0.25 may be preferred for flows with strongly varying boundary forces like those in the present work.

4.2 Discrete Element Method

4.2.1 Basic Concepts

For simulations of interacting rigid bodies, the focus is on their contact and the balancing of the occurring contact forces. Cundall and Hart (1992) distinguish between hard contacts where interpenetration of the bodies is regarded as non-physical and soft contacts that allow for interpenetration (see Fig. 4-2). For solids, the first seems to be reasonable from a physical point of view since a collision results in surface deformation. However, a simulation model for hard contacts at least has to exactly track the moment of contact (the deformation of the surface would be a further task, if required). This usually requires the application of an iterative scheme. Hence, corresponding applications are commonly restricted to a rather small number of interacting bodies. If soft contacts are considered, the interpenetration is regarded to be an equivalent for the surface deformation. The contact forces are related to the displacement or the amount of interpenetration δ in general. A well-known example for that is the Hertz contact theory (see section 4.2.2) which describes the contact between two deformable spheres. Furthermore, the approach of soft contacts is the basic concept of the discrete element method, since it allows for stable and accurate interaction modelling of rigid bodies and can be applied to an almost unlimited number of particles as far as computational resources are available. An overview of applications in mechanical engineering is presented by Fleissner *et al.* (2007). Lanru and Ove (2007) present the application of DEM to rock engineering, Tavarez and Plesha (2007) demonstrate the capabilities of the method for the modelling of solid materials and Teufelsbauer *et al.* (2011) investigated the interaction between granular flow and rigid obstacles by application of DEM – to mention some recent applications of the method.

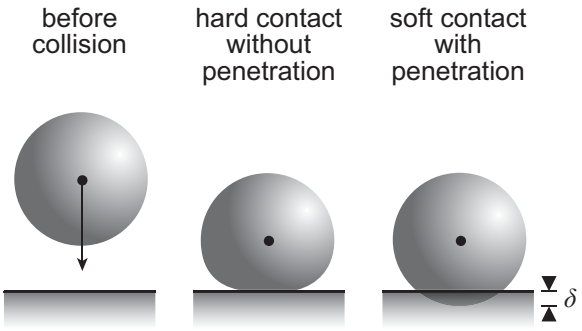

Fig. 4-2: Modelling approaches of interacting rigid bodies: collisions with and without penetration of the colliding bodies.

The procedure of a DEM simulation may be outlined as follows. In a first step it has to be detected for each particle whether collisions with neighbouring particles will take place or not, i.e. whether interpenetration occurs or not. If a collision occurs, a so-called penalty force depending on the amount of interpenetration will be applied. With regard to a pair of colliding particles, the penetration continues until the forces exerted by the particles are balanced by the penalty force, i.e. when maximum penetration is reached.

4.2.2 Penalty Force Models

A common approach to model penalty forces between two colliding rigid objects is the implementation of a spring-damper system (e.g. Cundall and Strack (1979)). Such a system of two colliding spheres P_i and P_j is depicted in Fig. 4-3. The spring is responsible for putting back the spheres to the state of contact. It exerts a penalty force $\vec{F}_n\left(k(\delta)\right)$ depending on material properties and penetration depth δ in the direction of relative motion along the spring-damper system axis $\vec{e}_{sd}$, i.e. normal to the contact surface,

$$\vec{F}_n\left(k(\delta)\right) = -k(\delta)\vec{e}_{sd} \ . \tag{4.11}$$

A simple approach for modelling dissipation is the application of a viscous damper. The exerted force of the damper depends on the collision velocity $\dot{\delta} = \left|\vec{v}_i - \vec{v}_j\right|$ in the direction of the spring-damper system axis,

$$\vec{F}_d = -d\dot{\delta}\vec{e}_{sd} \ , \tag{4.12}$$

where d is the viscous damping coefficient. By adding equations (4.11) and (4.12) the collision force $\vec{F}_c$ results as

$$\vec{F}_c = \vec{F}_n\left(k(\delta)\right) + \vec{F}_d \ . \tag{4.13}$$

The penalty force $\vec{F}_n\left(k(\delta)\right)$ can be determined using different approaches, either linear or nonlinear depending on $k(\delta)$. A common linear approach is to model the spring according to Hooke's law, where the spring is assumed to be perfectly elastic. Thus, $k(\delta) = c\delta$ for a spring with stiffness c and displacement δ. A more physically motivated approach for modelling the interaction of two perfectly elastic spheres with frictionless surfaces is based on the contact theory of Hertz (1882). For Hertzian contact $k(\delta) = K\delta^n$, where K is the generalised stiffness constant. The exponent n depends on the

distribution of the contact stresses and is set to 1.5, as in the original work by Hertz. For two colliding spheres the stiffness parameter depends on the radii and the material properties, i.e. the Poisson's ratio and the Young's modulus. An in-depth description of the Hertz contact theory is e.g. given by Popov (2010). To evaluate the fitness of the linear and the Hertz force law, test simulations have been carried out. The results show that the Hertz force law is the preferred choice with regard to accuracy and stability. Thus, the Hertz law is used to model the penalty force between rigid spheres.

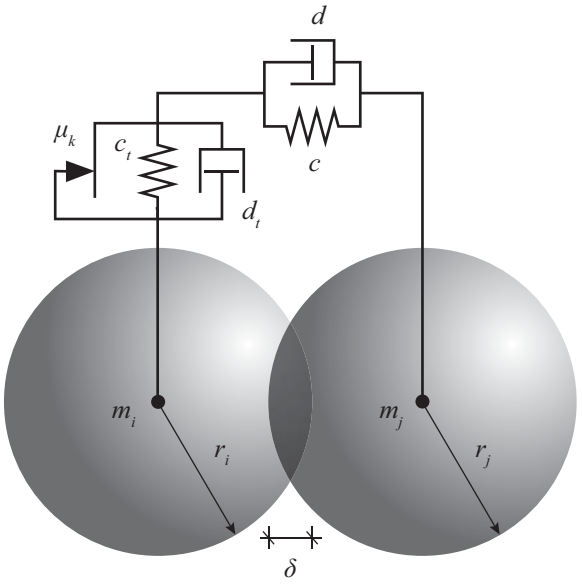

Fig. 4-3: Spring-damper system for the modelling of penalty forces due to overlapping including friction.

4.2.3 Friction

Although friction between solid bodies is a very complicated physical phenomenon, there exists a simple law for dry friction that is an appropriate approximation for engineering applications. Based on experimental investigations, Coulomb proposed the frictional force as a function of the normal force multiplied by a friction coefficient. He distinguished two kinds of friction: kinetic and static friction. One difficulty in numerical modelling of kinetic friction is the discontinuity of the friction force at zero velocity, where it changes its sign. Close to the discontinuity, in reality already for small tangential velocities v_t, relatively large forces occur. This may lead to numerical instabilities. To overcome this problem, the discontinuity is approximated by a continuous sigmoidal function, e.g. the hyperbolic tangent. Thus, the kinetic friction force reads

$$\vec{F}_{Rk} = -\mu_k \left|\vec{F}_n\right| \tanh\left(\eta\left\{v_t\right\}\right)\vec{e}_t \ , \tag{4.14}$$

where μ_k is the kinetic friction coefficient, $\vec{e}_t$ is the unit vector of the tangential component of the relative velocity perpendicular to the normal force $\vec{F}_n$ and η is the slope of the function at $v_t = 0$. Static friction is more complicated to model than kinetic friction. Cundall and Strack (1979) proposed a penalty sticking friction model that inserts a tangential spring-damper system between the bodies in contact as depicted in Fig. 4-3. Thus, the bodies will actually not statically stick at the contact point but will move constrained by the spring-damper system. The elastic force of the tangential spring-damper system is

$$\vec{F}_{s,t} = -c_t \delta_t \vec{e}_t \ , \tag{4.15}$$

where c_t is the stiffness of the tangential spring and δ_t is the tangential displacement. The maximum retaining force of the spring-damper system is given by the static friction force according to Coulomb's law

$$\vec{F}_{Rs} = -\mu_s \left| \vec{F}_n \right| \vec{e}_t \ , \tag{4.16}$$

where μ_s is the static friction coefficient. The combination of static and kinetic friction is called stick-slip friction. According to Popov (2010), this is the basic process at the contact zone when rolling occurs.

4.2.4 Time Integration and Time-Step Size

For DEM, the size of the time step actually depends on the desired accuracy, since a correct capturing of the impact process is important. This may not go hand in hand with little computational efforts and a fast simulation progress. Therefore, use of the largest possible time step that meets the accuracy requirements is desired. Fleissner (2010) presents some implicit, unconditionally stable schemes for time integration, which dynamically adjust the time step for a corresponding state of the system. However, with regard to the coupling of SPH and DEM, the same explicit PC-leapfrog scheme is used. Thus, the size of a time step can be obtained by similar conditions as for the SPH method. The relevant length scale is the radius of the smallest sphere $r_{\min}$ and the maximum occurring velocity is taken as the reference velocity, i.e. $u_{ref} = \left| \vec{u} \right|_{\max}$. Furthermore, viscous forces are not considered. Including a safety factor α_s, this leads to the following conditions for the time-step size

$$\Delta t = \alpha_s \min \left(\frac{r_{\min}}{u_{ref}}, \ \sqrt{\frac{r_{\min}}{a_{\max}}} \right) . \tag{4.17}$$

4.3 Fluid-Structure Interaction

The interaction between fluid and structures, such as spheres, can be modelled in a similar way as the interaction of two spheres. However, different laws for the interaction as well as the friction force are applied.

4.3.1 Normal Force

To model the interaction of fluid particles with a rigid body in the same manner as molecular interaction seems to be a reasonable approach. Therefore, the interaction force is obtained by a so-called Modified Lennart-Jones (MLJ) potential suggested by Muller *et al.* (2004). Other than the original Lennard-Jones potential that leads to an infinitely large force for a particle distance towards zero, they propose a force law with a finite value k of the force at the boundary. For the investigation of wall bounded flows, an approach depending on the particle distance to the boundary δ_w, i.e. the surface of the sphere, is preferable. Furthermore, only repulsive forces are considered (notice that the original form also includes attractive forces). Thus, the according interaction force reads

$$\vec{F}_n(\delta_w) = \frac{k}{(\delta_{w0} + r_s)^4} (\delta_{w0} - \delta_w)^4 \vec{e}_{ij}, \quad \delta_w \leq \delta_{w0} \ . \tag{4.18}$$

where r_s is the radius of the sphere and δ_{w0} is the maximum influence distance of the potential from the boundary. Please refer to Vetsch (2012) for a detail discussion on interaction laws and their properties.

4.3.2 Tangential Force

The friction between the fluid and the surface of a sphere or triangle can be modelled in a similar way as the friction between solid bodies as described in section 4.2.3. However, the exerted tangential force is actually a viscous shear force plus effects due to the character of the surface. Thus, the friction coefficient depends rather on the viscosity of the fluid and the surface roughness than on dry material-to-material properties.

4.3.3 Time Integration for Coupled Simulation

For the combination of DEM and SPH, the use of different time integration algorithms can lead to an asynchronism, resulting in an unstable simulation. Hence, the same integration scheme with identical parameters is preferred. Therefore, the use of the PC-leapfrog integrator for both methods is suggested. The time-step size is determined by a combination of conditions (4.10) and (4.17).

5 Model Validation

The applied models are validated by comparing the results of the test cases with reference solutions obtained by physical or empirical relations from the literature. If necessary, the relevant model parameters will be varied in terms of a model calibration until the result of the numerical experiment is in reasonable agreement with reference data. The applications comprise a hydrostatic buoyancy experiment and the settling of a rigid body in a tank filled with water. For the experiments, the size of the fluid particles in terms of their initial particle spacing $\triangle s$ is chosen several times smaller than the diameter d_s of the corresponding DEM particle. In the present work, this modelling approach where fluid particles are smaller than the rigid body, say $\triangle s \leq d_s / 3$, is termed High Resolution Force Model (HRFM). The spheres are uniform with diameter $d_s = 0.03$ m. The initial particle spacing and other parameters vary according to the configuration. The size of the smoothing length is chosen to be $h = 1.5 \triangle s$, which corresponds to 29 and 123 neighbouring particles in two and three dimensions, respectively. Since the accuracy of SPH depends on the relation between the number of neighbours and the smoothing of local quantities, this is a good choice but also has its computational cost.

5.1 Buoyancy

The numerical buoyancy experiments are carried out in a small tank filled with an initially quiescent fluid, i.e. particles are at rest. The dimensions of the water body are: length $l_f = 0.2$ m and height $h_f = 0.1$ m for the two-dimensional (2-D) discretisation and $h_f = l_f = w_f = 0.1$ m in the three dimensional (3-D) case. Three model configurations have to be distinguished: for case A the sphere is located in the middle of the tank at height $z_s = 0.5 h_f$, for cases B and C the sphere sits on top of fixed spheres arranged in a close packing. For the given cases, experiments with different resolution of fluid particles in terms of the initial particle distance $\triangle s$, hereafter referred to as particle resolution, are carried out as listed in Tab. 5-1. In addition, the ratio of the number of fluid particles per sphere diameter is given (column 2); it can be seen as an alternative indicator for the level of discretisation. Furthermore, the average size of the computational time step $\triangle t$ is listed since it depends on the smoothing length. The initial particle discretisations for the studied cases and the different configurations are illustrated in Fig. 5-1 (notice that each configuration was studied with the three different particle resolutions).

The resultant submerged weight of the sphere is measured by a kind of load cell connected to the sphere. Actually, the load cell is modelled as a fixed special particle that interacts only with the sphere and not with fluid particles. This special particle overlaps with the sphere and its initial position corresponds to a penalty force that is equal to the submerged weight. For their interaction, the linear force law is applied. The interaction of the fluid particles with the sphere is modelled by a MLJ potential. The distance to the sphere surface where the penalty force is zero is set equal to the smoothing length, i.e. $\delta_{w0} = h$, which corresponds to an active penalty force as soon as interaction takes place. The stiffness of the potential is obtained by evaluating a slightly modified form of equation (4.18), namely

$$k = F\left(\frac{h+r}{h\left(1-\psi_{eq}\right)}\right)^4, \tag{5.1}$$

where $\psi_{eq} = \delta_{weq}/h$ and the amount F of the force is equal to the median pressure acting on the sphere. Hence, the force law depends on the parameter ψ_{eq} which actually defines the equilibrium distance between the fluid particles and the sphere by $\delta_{weq} = h\psi_{eq}$. Thus, the parameter ψ_{eq} indirectly controls the amount of displaced fluid and, consequently, the buoyancy force. Furthermore, the mass of the fluid particles is set to $\rho_f\left(\triangle s\right)^\sigma$, where the term $\left(\triangle s\right)^\sigma$ with dimensionality of the problem σ corresponds to a finite area or volume of fluid.

Tab. 5-1: Initial particle spacing used for buoyancy experiments and resulting number of fluid particles including boundary particles. The second column indicates the number of fluid particles per sphere diameter.

$\triangle s$	$d_s/\triangle s + 1$	*number of particles*		*average* $\triangle t$
[m]	[-]	2-D	3-D	[s]
0.01	4	266	2456	2.10E-04
0.005	7	920	13018	1.10E-04
0.0025	13	3376	82116	5.30E-05

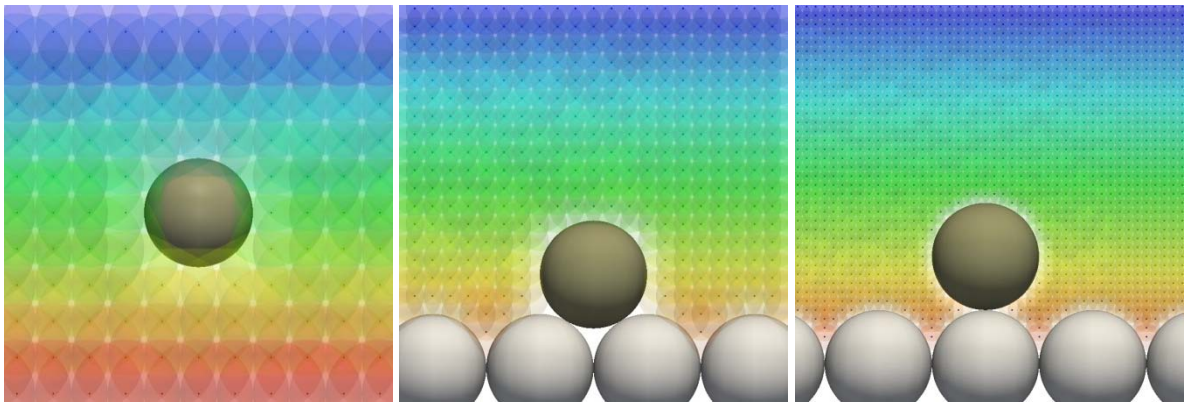

Fig. 5-1: Configurations of cases A, B and C (from left to right) with initially evenly spaced fluid particles in the vicinity of the sphere. The particle spacing is $\triangle s$ =0.01, 0.005 and 0.0025 m from left to right. The colour indicates the hydrostatic pressure, where red corresponds to larger values than blue.

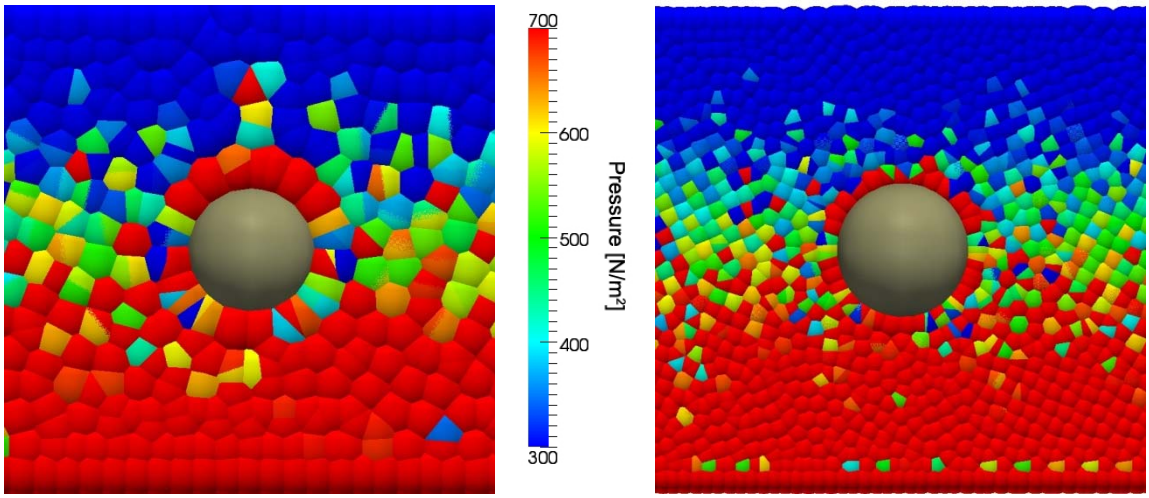

Fig. 5-2: Case A: final arrangement of the fluid particles in the vicinity of the sphere for the two dimensional experiments with $\triangle s$ =0.005 m (left) and $\triangle s$ = 0.0025 m (right).

For the numerical experiments with a configuration according to case A, the parameter ψ_{eq} was varied until the difference of the exact submerged weight and the force measured by the load cell was within a few per cent. For the present case with $h = 1.5\triangle s$, it could be expected that δ_{weq} converges to $\triangle s/2$ for decreasing values of $\triangle s$ and $\psi_{eq} \rightarrow 1/3$. This tendency was quite well reproduced by the experiments. By taking a closer look at the results, it can be seen that the fluid particles arrange in a corona like manner around the sphere as depicted in Fig. 5-2. This corresponds to the expected behaviour since the pressure acts in the normal direction of the curved surface. However, the resulting pressure distribution around the sphere, i.e. the pressure of the fluid particles in contact with the sphere, is not in agreement with the surrounding fluid particles and is incorrect. Although the final pressure distribution corresponds to an equilibrium state, there are large pressure gradients in the particle corona and fluid particles with relatively small pressure are squeezed.

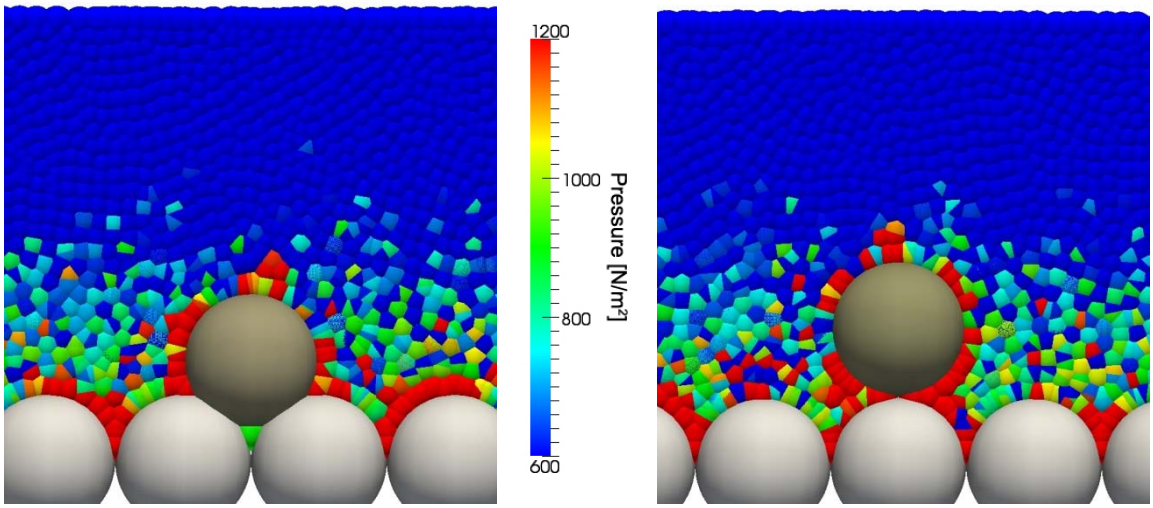

Fig. 5-3: Final arrangement of the fluid particles in the vicinity of the sphere for the two dimensional experiments of case B (left) and case C (right) with $\triangle s$ = 0.0025 m.

For the configurations B and C the force law between the fluid particles and the sphere is configured in the same way as for case A. Since the situation is similar to the experiments of case A, the above determined parameters ψ_{eq} are also used for the present cases. To allow for the measurement of the submerged weight, no interaction has been specified between the sphere and the fixed spheres at the bottom. Thus, in case B, the sphere sinks a little due to the smaller buoyancy force and the larger submerged weight, respectively. In case C, the sphere is raised a bit due to the fluid particles which squeeze into the gap between the spheres (see Fig. 5-3).

According to the results of case A, the pressure distribution around the sphere is incorrect for the cases B and C; this also holds true for the pressure around the fixed boundary spheres. Furthermore, the sphere is initially not completely surrounded by fluid particles as depicted in Fig. 5-1. However, in reality the sphere would be covered by fluid except for the small areas at the contact points. Thus, it could be expected that the exact submerged weight of the sphere is the same as in case A. The simulation results show that for decreasing values of $\triangle s$ the measured submerged weight converges to the exact value. However, that rate of convergence strongly depends on the particle resolution, i.e. the number of fluid particles located in the spacing between the spheres. This fact confirms the importance of a correct simulation of the buoyancy force.

5.2 Settling Velocity

For the settling velocity experiments, a tank filled with initially quiescent water is considered. The dimensions of the water body are length $l_f = 0.15$ m and height $h_f = 0.3$ m in the case of 2-D discretisation and in addition width $w_f = 0.15$ m for 3-D. To study the influence of the spatial discretisation on the settling velocity, two and three dimensional experiments with different particle resolution are carried out as listed in Tab. 5-2.

Tab. 5-2: Initial particle spacing used for settling velocity experiments and resulting number of fluid particles including boundary particles.

case	*dim*	$\triangle s$ [m]	*number of particles*	*average* $\triangle t$ [s]
A	2	0.01	620	1.20E-04
AA	2	0.005	2135	6.20E-05
AAA	2	0.0025	7865	3.10E-05
AAAA	2	0.00125	45125	1.50E-05
A3D	3	0.01	12400	1.20E-04
AA3D	3	0.005	74725	6.20E-05

Similar to the buoyancy experiments, the interaction of the fluid particles with the sphere is modelled by a MLJ potential. Thus, the stiffness of the potential is obtained by equation (5.1), where ψ_{eq} is chosen corresponding to the initial particle distance and the dimensionality according to the parameters obtained by the calibration of the buoyancy experiments. Since there will be no hydrostatic pressure distribution around the settling body, the reference pressure is not known a priori. Hence, the dynamic pressure is taken as reference and the amount of the reference force is obtained by $F = 0.5\rho_f w_s^2 \triangle s^{\sigma-1}$.
The terminal settling velocity w_s of a rigid body in a fluid is reached when the drag force acting on the sphere is balanced by its submerged weight. Considering Newtonian flow, the terminal settling velocity of a sphere with the given properties is $w_{s,sphere} \approx 1.27$ m/s. This corresponds to the three dimensional case. If the situation is reduced to a two dimensional problem, the sphere is replaced by a cylinder with distinct properties. Hence, for a cylinder the terminal settling velocity is $w_{s,cyl} \approx 0.83$ m/s. To account for the effect of wall interference on the settling velocity of the body (see e.g. DiFelice (1996)), the unaffected terminal velocity w_s is reduced to $\hat{w}_s$, i.e. $\hat{w}_{s,sphere} = 1.16$ m/s and $\hat{w}_{s,cyl} = 0.76$ m/s. For both cases, the cylinder and the sphere, the boundary layer around the body is mainly laminar and the dominant contribution to the drag force is the pressure drag (compare e.g. Douglas *et al.* (2001)). Thus, for the current experiments the influence of the friction drag is not considered.

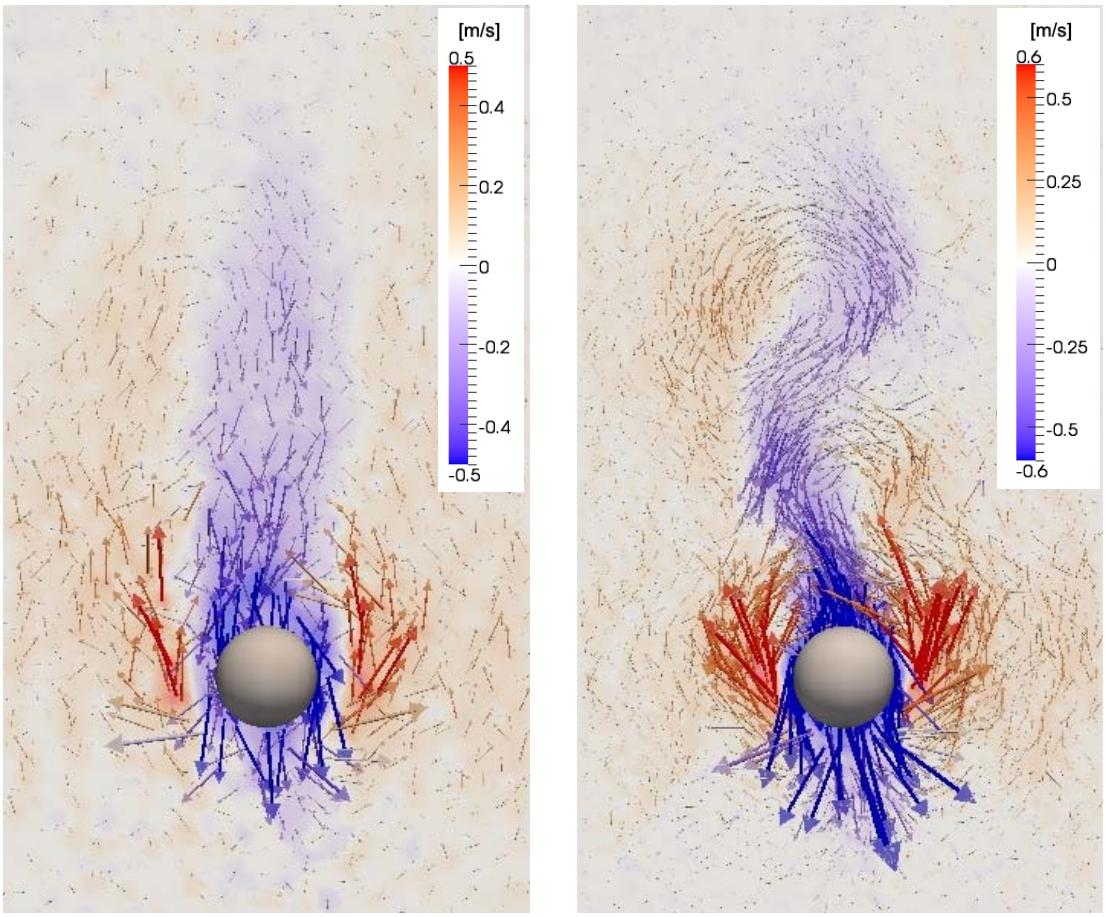

Fig. 5-4: Case AA (left) and case AAA (right): contour plot of vertical velocity and velocity vectors, where the colour indicates magnitude.

With increasing number of particles, i.e. smaller initial particle spacing, larger terminal settling velocities $\overline{w}_s$ are observed. The measured settling velocity for the coarsest two dimensional particle resolution (case A) is $\overline{w}_s = 0.262$ m/s which increases up to $\overline{w}_s = 0.733$ m/s for the finest resolution (case AAAA) studied in this work. Thus, the measured terminal velocity approaches the intended value of $\hat{w}_{s,cyl} = 0.76$ m/s, which indicates convergence of the applied methods. The finest particle resolution for the three dimensional case was limited to $\triangle s = 0.005$ m (case AA3D) due to the required computing time (19 days for this case). However, similar behaviour as for the 2-D case is rudimentary observed. Furthermore, the flow around the sphere can be reasonably reproduced already for the coarser resolutions; moreover, with smaller initial particle spacing the features of the flow become more detailed, as expected. This is shown by Fig. 5-4 for selected cases AA and AAA. Despite the reliable results of the flow field, spurious numerical oscillations in the pressure field are observed. This corresponds to results obtained by other researchers (e.g. Colagrossi *et al.* (2010)), since WCSPH is known to be noisy.

For the sake of completeness it has to be mentioned that besides the particle resolution also the role of the artificial viscosity and influence of the force law has been investigated. However, for physically correct configurations, i.e. where the fluid particles and the rigid sphere cannot interpenetrate, no reasonable improvement is observed.

5.3 Discussion

The chosen experiments have proven to be a reliable concept to evaluate the numerical methods which are used to model the fluid-structure interaction. Besides the parameters defining the interaction between SPH and DEM particles, the particle resolution plays a major role, especially when it comes to dynamic problems. The expected convergence of the SPH method is demonstrated and approved by the results of the experiments. Nevertheless, some drawbacks of the applied methods have to be pointed out. The computational cost is already quite high for two-dimensional simulations with a moderate number of particles. This limits the scope of parameter studies, and three-dimensional investigations become very time-consuming. To overcome these limitations, parallelisation of the software is necessary to allow for the use of high performance computing infrastructure. Furthermore, the significance of the pressure increase at the boundaries between fluid particles and rigid walls (fixed and movable) is not clear. For the present work, this particularly applies to the settling velocity experiments where the pressure drag results from the pressure distribution around the sinking body. The problem may have two contributions, namely the spurious numerical oscillations in the pressure field and the fluid-structure boundary condition itself. Some recent contributions by other researchers provide approaches which may be useful to overcome this shortcoming. On the one hand, to smooth out or eliminate pressure oscillations, filtering of the density (see e.g. Molteni and Colagrossi (2009)) or the application of truly incompressible SPH is suggested. On the other hand, boundary conditions for fluid-structure interaction are still an open and challenging task. A promising approach, suitable for the recent applications, is presented e.g. by Monaghan and Kajtar (2009).

It seems to be obvious that as long as the shortcomings of the current modelling approach are not adequately solved, numerical experiments with focus on detailed local forces are not reasonable. However, these kinds of experiments are necessary to investigate the fundamental physical processes occurring during incipient motion and sediment transport. Possible experiments to validate an improved version of the model would be e.g. the determination of the drag coefficient of a sphere sitting on a boundary of similar spheres as investigated by Coleman (1972) or the incipient motion experiments carried out by Fenton and Abbott (1977).

6 Applications

To demonstrate the capabilities of the present model for the simulation of bed-load transport, a slightly different modelling approach as used in the previous chapter is applied in the following. The applications to bed-load transport comprise a two-dimensional simulation of the development of a scour caused by a freefalling water jet and a three-dimensional pier scour experiment. For the present experiments, the size of the fluid particles in terms of their initial particle spacing $\triangle s$ is intentionally chosen larger than for the model-verification experiments, i.e. $\triangle s = d_s/2$. This modelling approach where fluid particles are larger than the rigid body, say $\triangle s > d_s/3$, is termed Low Resolution Force Model (LRFM). With the LRFM, simulations on a larger scale than with the HRFM are made possible. However, due to the usually larger computational domain and because the sediment layer also consists of particles, no "miracles" concerning the computational costs have to be expected.

Due to the less detailed resolution of the fluid forces acting on a solid particle, the model parameters have to be calibrated to match the desired sediment transport processes; this relates to the spatial as well as the temporal scale. Depending on the complexity of the experiment, the calibration can be quite extensive. For the present experiments only marginal calibration of the model parameters was carried out. Thus, the presented simulation results are rather of qualitative nature and primarily serve for illustration purposes.

6.1 Scour Caused by a Freefalling Water Jet

In the present experiment, the development of a scour due to a freefalling water jet is studied. This kind of scour is typical for a natural waterfall, where at the bottom of the subsequent plunge pool a scour hole develops caused by the impact of the freefalling water. For the experiment, the specific discharge is 0.04 m^2/s and the head drop is 0.16 m. Since the experiment is carried out as a two-dimensional simulation, the sediment consists of circular particles with diameter $d_s = 2r_s = 0.01$ m and density ρ_s = 2800 kg/m^3. The sediment particles are considered to consist of granite. For the interaction between the sediment particles, Hertz's law is applied and for the internal friction of the sediment layer, equal coefficients for sticking and slipping friction are considered. The interaction between the fluid and sediment particles is modelled by an MLJ potential. Due to the applied LRFM approach also the concept for the parameters of the force law is different to that used for the model verification. For the present experiments, the distance from the sediment-particle surface where the repulsive force is zero is $d_{w0} = h - r_s$ and the equilibrium distance is chosen as $d_{weq} = 0.5 d_{w0}$. The stiffness of the potential is 600 N. With this configuration, the sediment particle may behave like a heavy fluid particle when it encounters true fluid particles (notice that this only concerns the fluid-sediment interaction). Friction between the fluid and sediment particles is also considered.

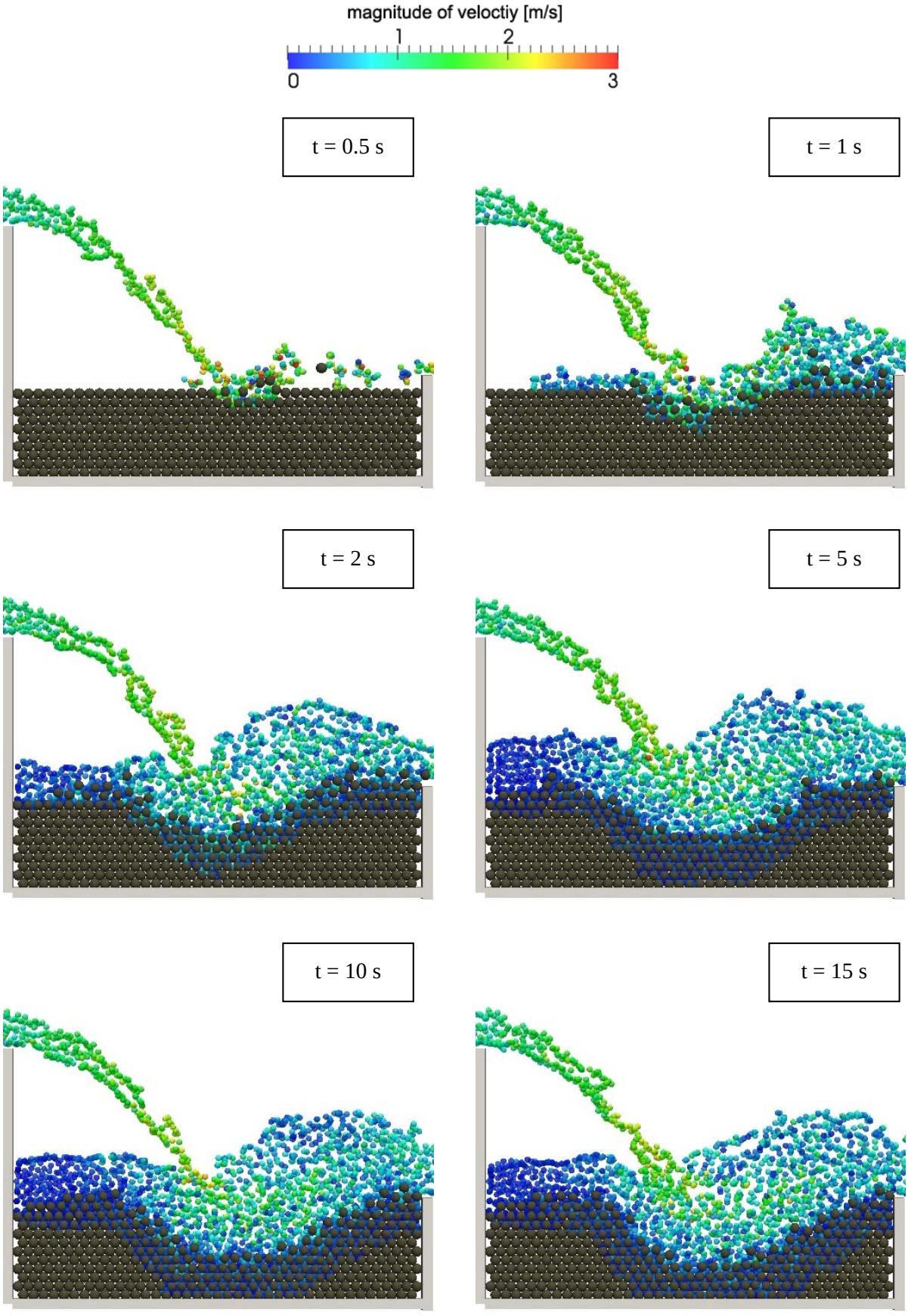

Fig. 6-1: Numerical simulation of a scour caused by a freefalling water jet.

For the present configuration, the estimated hydrodynamic time-step size is $\triangle t = \alpha_s h_f / c_s \approx 2 \cdot 10^{-3}$ s and the estimated sediment time-step is $\triangle t = \alpha_s r_s / c_s \approx 1 \cdot 10^{-4}$ s; thus the latter is relevant. The total simulation time is 15 s and the corresponding computing time for the experiment was approximately 1060 min on a modern computer using one core.

The results of the simulation at selected times are shown in Fig. 6-1. At the beginning of the simulation, the sediment erosion advances quickly due to the unimpeded impact of the water jet on the sediment surface. Already after some seconds a scour hole develops and the water depth at the impact location increases. The resulting plunge pool now alleviates the momentum of the water jet and sediment erosion diminishes. After a simulation time of about 10 s, the extent of the scour hole will barely change. The development of the scour, i.e. the profile of the bed level, is reproduced in a characteristic manner by the numerical model.

As can be seen from Fig. 6-1, the fluid particles are able to enter the sediment layer up to a certain depth, which is similar to seepage. This behaviour is depicted on the left in Fig. 6-2 in detail where the black dots indicate the locations of fluid particles. The fluid particles fill up the voids between the sediment particles. The exerted forces by the fluid particles in the pores may be interpreted as a mix of buoyancy and lift forces.

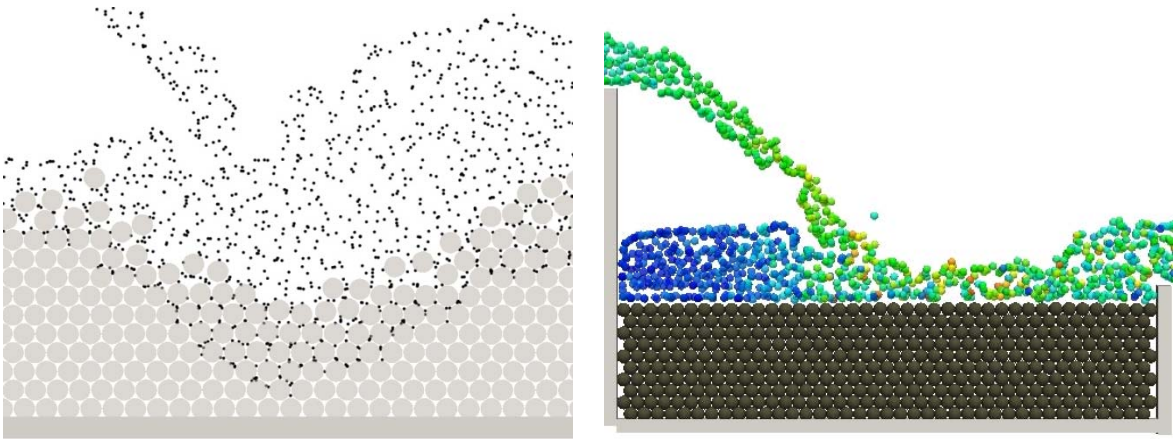

Fig. 6-2: Influence of interaction law on the erosion process. In the left picture, the result of a simulation with an interaction law based on $d_{w0} = h - r_s$ is depicted (compare Fig. 6-1), where the black dots indicate the locations of the fluid particles. On the right, the simulation result for a different configuration with $d_{w0} = h + r_s$ is shown.

The major importance of the possibility for fluid particles to enter the sediment layer for the present experiments can be illustrated by varying the parameters of the force law for the fluid-sediment interaction. For this purpose, consider a different configuration: the distance from the sediment-particle surface where the repulsive force is zero is increased to $d_{w0} = h + r_s$ while the stiffness, i.e. the size of the maximum repulsive force, is kept constant. This leads to a repulsive force which already acts at a distance between a fluid particle and the sediment-particle surface which is larger than for the previous configuration with $d_{w0} = h - r_s$. Furthermore, a reduced sediment density of ρ_s = 1800 kg/m^3 is considered to emphasize the distinct behaviour. The simulations show that the fluid particles are no

longer able to move between the sediment particles (compare Fig. 6-2, on the right), which is due to the scaling of the force law. Despite the reduced mass of the sediment, no scour is observed at all.

6.2 Clear-Water Scour at Bridge Pier

Another well-known kind of scour is the erosion of sediment observed at bridge piers. The deflection of the water at the pier and the resulting vortices lead to an erosion of sediment and the development of a characteristic scour hole around the pier (see e.g. Unger and Hager (2007)). The channel used for the three-dimensional pier-scour experiment is 0.7 m long and 0.15 m wide. The slope of the channel is 3.5 ‰. The quadratic pier with a side length of 0.05 m is placed adjacent to the left wall. The sediment consists of five layers of particles which results in a total of 2484 sediment particles. For the three-dimensional simulation, the sediment consists of spheres with diameter d_s = 0.01 m and density ρ_s = 2500 kg/m^3. The ratio of the sediment diameter to the initial fluid particle spacing is two. Similar to the jet scour experiment, Hertz's law is used to model the interaction between the sediment particles. Since the energy of the flow is distinctly smaller than in the previous experiment, the friction between the sediment particles is reduced to trigger a faster erosion process. For the interaction between the fluid and sediment particles a MLJ potential is applied. The parameters of the force law are $d_{w0} = h - r_s$ and $d_{weq} = 0.5 d_{w0}$. For the three-dimensional case the stiffness of the potential has to be strongly reduced compared to the previous 2D experiment and is 3 N. Based on the chosen particle resolution the total number of fluid particles during the simulation is approximately 70'000. The size of the time step is similar to that of the jet scour experiments. Furthermore, the simulation starts from an initially dry channel bed.

The results of the experiment at different times of the simulation are depicted in Fig. 6-3. At the beginning of the simulation, the waterfront moves across the domain and the weight of the water causes a small depression of the sediment-bed surface. However, no significant transport of sediment particles takes place at this point. At the pier, some part of the water which impinges the pier is vertically deflected in the downward direction. With increasing flow depth also this effect amplifies. The downward flow exerts larger contact forces on the sediment particles than on those exposed mainly to tangential flow. At the first, this leads to initial transport of some sediment particles and to local erosion in front of the pier. Subsequently, due to the initial erosion the transport of sediment particles is amplified and the erosion extends around the pier and along the channel with time. Due to numerical instabilities the computation was aborted after a simulation time of 1.6 s, which corresponds to a computing time of 17 days. Nevertheless, the simulation results show the initial phase of the erosion process, which is reproduced in a reliable manner and which is comparable to experimental observations (see e.g. Radice *et al.* (2008)).

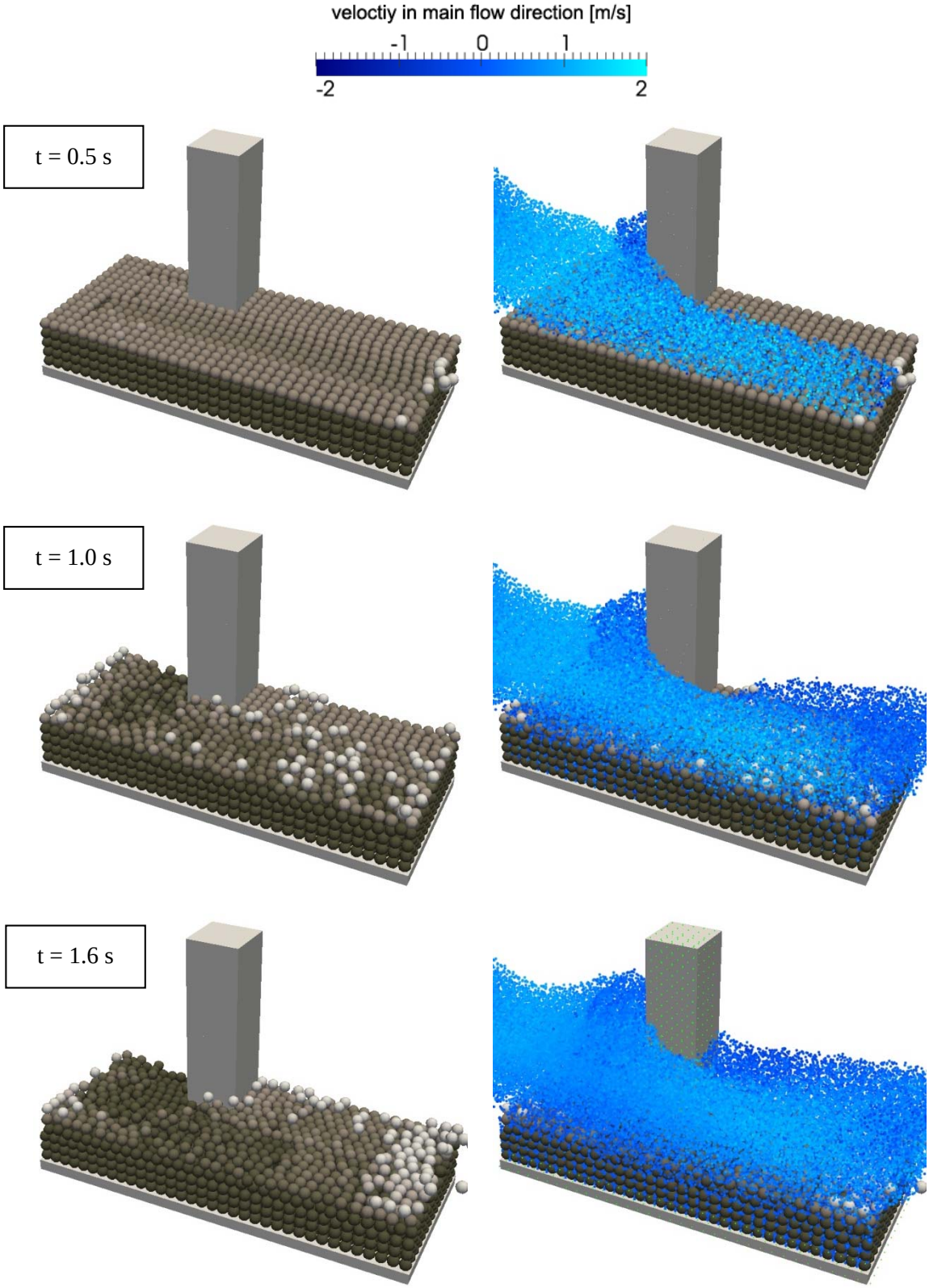

Fig. 6-3: Numerical simulation of clear-water scour at bridge pier. A lighter colour of the sediment particles indicates "higher above datum". The sidewalls, the inflow section and the outflow weir are omitted to improve visibility.

7 Conclusions

In the present work, a novel numerical modelling approach for the simulation of bed-load transport is presented. The model consists of the combination of two strictly Lagrangian methods which allow for the simulation of fluid-structure interaction problems. The interaction between the fluid and the sediment particles and between the sediment particles themselves is modelled by a well-defined force law also accounting for various kinds of friction between the grains. For the present work, the sediment grains are modelled as spherical particles. The applied model is able to reproduce the constitutive behaviour of sediment mixtures and the different transport modes of bed load, such as sliding, rolling and saltating.

The modelling of the fluid is based on a continuum approach which is discretised by the Smoothed Particle Hydrodynamics (SPH) method. The sediment particles are represented by the Discrete Element Method (DEM), where the interactions between the discrete sediment grains are modelled by a force law, which is also able to account for various kinds of friction. A similar approach is applied to the interaction between the fluid and sediment particles. The definition of the interface and the exchange of forces between the fluid and sediment grains are inherent to the applied approach. Thus, the use of a computational grid or of techniques for the tracking or capturing of the interface is not necessary.

Two basically different approaches to model bed-load transport with the proposed method are presented. On the one hand, the application of the combined methods as a High Resolution Force Model (HRFM) is investigated. For the HRFM, the fluid particles are chosen distinctly smaller than the sediment particles to simulate detailed interaction forces. To study the interaction forces on a spherical particle depending on the resolution of the fluid particles a hydrostatic and a dynamic experiment, namely the simulation of buoyancy effects and the determination of the settling velocity, are carried out. The results of the simulations show convergence of the applied methods for increasing particle resolution; they turned out to be a reliable concept to validate the chosen numerical approaches. Furthermore, the importance of the possibility to account for the effect of buoyancy is pointed out. The simulation results show the potential of the HRFM to be used for detailed investigations of bed load processes. On the other hand, the use of the model in terms of a Low Resolution Force Model (LRFM) is studied. For the LRFM, the fluid particles are chosen of similar size or larger than the sediment particles. This requires a basically different approach for the determination of the interaction-force law parameters. Due to the less detailed resolution of the fluid forces acting on a solid particle, the model parameters have to be calibrated to match the desired sediment transport processes; this concerns the spatial as well as the temporal scale. The LRFM was applied to scour caused by a freefalling water jet and to clear-water scour at a bridge pier. The qualitative simulation results are in satisfying agreement with experimental observations and illustrate the use of the applied methods for practical applications.

The methods also have some shortcomings. The force law used for the interaction of the fluid and the sediment grains depend on a reference force, which may not correspond to the actual and local fluid forces in a dynamical simulation. This may affect the accuracy of the results. However, this effect mainly applies to the HRFM, and its influence is expected to diminish for increasing particle resolution. Its role with regard to the forces on a sediment particle embedded or close to the sediment bed has to be investigated in subsequent research. Moreover, boundary conditions between the fluid and solids for SPH are still an open topic. Another problem arises due to the pressure field, which shows spurious

oscillations inherent to the weakly compressible SPH method - several approaches to overcome this issue are mentioned. As also pointed out by other researchers, the main drawback of the presented model is due to its extensive computational cost for detailed and three dimensional simulations. The common way to overcome this restriction is to implement parallelisation techniques to be able to use high performance computing infrastructure. However, as far as engineering practice is concerned, the use of the present model in the near future is not realistic, since the appropriate application is still a challenging task and the corresponding computation time requirement may not be affordable.

Acknowledgements

The present work has been carried out in the scope of the doctoral thesis of Dr. D. Vetsch. Therefore the author likes to thank his supervisor Prof. Dr. R. Boes (ETH Zurich) and the co-examiners Prof. Dr. P. Rutschmann (TU Munich) and Dr. R. Fäh (ETH Zurich). Furthermore, the author is very grateful to the co-examiner Dr. F. Fleissner (TU Stuttgart), who provided his software package *Pasimodo* for academic use and to Mrs. A. Lehnart for her substantial contributions to the software. In addition, the author would like to express his gratitude to Prof. Dr. K. Hutter for the critical review and his valuable suggestions. The present research work was financially supported by the Swiss Federal Office for the Environment and its support has been much appreciated.

Bibliography

Bagnold, R. A. (1936) 'The movement of desert sand', *Proceedings of the Royal Society of London Series a-Mathematical and Physical Sciences*, 157 (A892), pp.594-620.

Bagnold, R. A. (1941) *The Physics of Blown Sand and Desert Dunes.* London: Methuen.

Bagnold, R. A. (1973) 'Nature of saltation and of bed-load transport in water', *Proceedings of the Royal Society of London Series a-Mathematical Physical and Engineering Sciences*, 332 (1591), pp.473-504.

Batchelor, G. K. (2005) *An introduction to fluid dynamics.* Cambridge University Press, Cambridge.

Buffington, J. M. and Montgomery, D. R. (1997) 'A systematic analysis of eight decades of incipient motion studies, with special reference to gravel-bedded rivers', *Water Resources Research*, 33 (8), pp.1993-2029.

Cheng, N. S. and Chiew, Y. M. (1998) 'Pickup probability for sediment entrainment', *Journal of Hydraulic Engineering-Asce*, 124 (2), pp.232-235.

Church, M. (2006) 'Bed material transport and the morphology of alluvial river channels', *Annual Review of Earth and Planetary Sciences*, 34, pp.325-354.

Colagrossi, A., Colicchio, G., Lugni, C. and Brocchini, M. (2010) 'A study of violent sloshing wave impacts using an improved SPH method', *Journal of Hydraulic Research*, 48, pp.94-104.

Coleman, N. L. (1972) 'The drag coefficient of a stationary sphere on boundary of similar spheres', *La Houille Blanche*, (1), pp.17-22.

Cottet, G. H. (1996) 'Artificial viscosity models for vortex and particle methods', *Journal of Computational Physics*, 127 (2), pp.299-308.

Cummins, S. J. and Rudman, M. (1999) 'An SPH Projection Method', *Journal of Computational Physics*, 152 (2), pp.584-607.

Cundall, P. A. and Hart, R. D. (1992) 'Numerical Modelling of Discontinua', *Engineering Computations*, 9 (2), pp.101 - 113.

Cundall, P. A. and Strack, O. D. L. (1979) 'Discrete numerical-model for granular assemblies', *Geotechnique*, 29 (1), pp.47-65.

Detert, M., Weitbrecht, V. and Jirka, G. H. (2010) 'Laboratory Measurements on Turbulent Pressure Fluctuations in and above Gravel Beds', *Journal of Hydraulic Engineering-Asce*, 136 (10), pp.779-789.

Dey, S. and Papanicolaou, A. (2008) 'Sediment Threshold under Stream Flow: A State-of-the-Art Review', *Ksce Journal of Civil Engineering*, 12 (1), pp.45-60.

DiFelice, R. (1996) 'A relationship for the wall effect on the settling velocity of a sphere at any flow regime', *Int. J. Multiph. Flow*, 22 (3), pp.527-533.

Douglas, J. F., Gasiorek, J. M. and Swaffield, J. (2001) *Fluid mechanics.* 4th edn. Longmann, Harlow.

Dwivedi, A., Melville, B. and Shamseldin, A. Y. (2010) 'Hydrodynamic Forces Generated on a Spherical Sediment Particle during Entrainment', *Journal of Hydraulic Engineering-Asce*, 136 (10), pp.756-769.

Einstein, H. A. (1937) 'Der Geschiebetrieb als Wahrscheinlichkeitsproblem', in Meyer-Peter, E. (ed.) *Mitteilung der Versuchsanstalt für Wasserbau an der Eidg. Techn. Hochschule in Zürich.* Rascher, Zürich, pp.3-112.

Einstein, H. A. (1950) 'The bed-load function for sediment transportation in open channel flow', *U S Dept Agric Tech Bull*, 1026, pp.1-71.

Einstein, H. A. and Elsamni, E. A. (1949) 'Hydrodynamic forces on a rough wall', *Reviews of Modern Physics*, 21 (3), pp.520-524.

Fenton, J. D. and Abbott, J. E. (1977) 'Initial movement of grains on a stream bed - effect of relative protrution', *Proceedings of the Royal Society of London Series a-Mathematical Physical and Engineering Sciences*, 352 (1671), pp.523-537.

Fleissner, F. (2010) *Parallel Object Oriented Simulation with Lagrangian Particle Methods.* Shaker, Aachen.

Fleissner, F., Gaugele, T. and Eberhard, P. (2007) 'Applications of the discrete element method in mechanical engineering', *Multibody System Dynamics*, 18 (1), pp.81-94.

Fleissner, F., Lehnart, A. and Eberhard, P. (2010) 'Dynamic simulation of sloshing fluid and granular cargo in transport vehicles', *Vehicle System Dynamics*, 48 (1), pp.3-15.

Francalanci, S., Parker, G. and Solari, L. (2008) 'Effect of seepage-induced nonhydrostatic pressure distribution on bed-load transport and bed morphodynamics', *Journal of Hydraulic Engineering-Asce*, 134 (4), pp.378-389.

Gomez-Gesteira, M., Rogers, B. D., Violeau, D., Grassa, J. M. and Crespo, A. J. C. (2010) 'Foreword: SPH for free-surface flows', *Journal of Hydraulic Research*, 48, pp.3-5.

Hertz, H. (1882) 'Ueber die Berührung fester elastischer Körper', *Journal für die reine und angewandte Mathematik (Crelles Journal)*, 1882 (92), pp.156-171.

Hofland, B. and Battjes, J. A. (2006) 'Probability density function of instantaneous drag forces and shear stresses on a bed', *Journal of Hydraulic Engineering-Asce*, 132 (11), pp.1169-1175.

Huerta, A., Belytschko, T., Fernández-Méndez, S. and Rabczuk, T. (2004) 'Meshfree Methods', in *Encyclopedia of Computational Mechanics*. John Wiley & Sons, New York.

Hughes, J. P. and Graham, D. I. (2010) 'Comparison of incompressible and weakly-compressible SPH models for free-surface water flows', *Journal of Hydraulic Research*, 48, pp.105-117.

Koumoutsakos, P. (2005) 'Multiscale flow simulations using particles', *Annual Review of Fluid Mechanics*, 37, pp.457-487.

Landrini, M., Colagrossi, A., Greco, M. and Tulin, M. P. (2007) 'Gridless simulations of splashing processes and near-shore bore propagation', *Journal of Fluid Mechanics*, 591, pp.183-213.

Lanru, J. and Ove, S. (2007) *Fundamentals of discrete element methods for rock engineering : theory and applications.* Elsevier, Amsterdam

Lee, E.-S., Violeau, D., Issa, R. and Ploix, S. (2010) 'Application of weakly compressible and truly incompressible SPH to 3-D water collapse in waterworks', *Journal of Hydraulic Research*, 48 (1 supp 1), pp.50 - 60.

Lee, E. S., Moulinec, C., Xu, R., Violeau, D., Laurence, D. and Stansby, P. (2008) 'Comparisons of weakly compressible and truly incompressible algorithms for the SPH mesh free particle method', *Journal of Computational Physics*, 227 (18), pp.8417-8436.

Lehnart, A. (2008) Ein Smoothed Particle Hydrodynamics-Verfahren zur Behandlung der Eulergleichungen. *MSc Thesis*. Institut für Technische und Numerische Mechanik, Universität Stuttgart, Stuttgart.

Liu, G. R. and Liu, M. B. (2003) *Smoothed particle hydrodynamics: a meshfree particle method.* World Scientific, New Jersey.

McEwan, I. and Heald, J. (2001) 'Discrete particle modeling of entrainment from flat uniformly sized sediment beds', *Journal of Hydraulic Engineering-Asce*, 127 (7), pp.588-597.

Meyer-Peter, E., Favre, H. and Einstein, H. A. (1934) 'Neuere Versuchsresultate über den Geschiebetrieb', *Schweizer Bauzeitung*, 103 (13).

Molteni, D. and Colagrossi, A. (2009) 'A simple procedure to improve the pressure evaluation in hydrodynamic context using the SPH', *Computer Physics Communications*, 180 (6), pp.861-872.

Monaghan, J. J. (1992) 'Smoothed Particle Hydrodynamics', *Annu. Rev. Astron. Astrophys.*, 30, pp.543-574.

Monaghan, J. J. (1994) 'Simulating free-surface flows with SPH', *Journal of Computational Physics*, 110 (2), pp.399-406.

Monaghan, J. J. (2005a) 'Smoothed particle hydrodynamics', *Reports on Progress in Physics*, 68 (8), pp.1703-1759.

Monaghan, J. J. (2005b) 'Theory and Applications of Smoothed Particle Hydrodynamics', in Blowey, J. F. and Craig, A. W. (eds.) *Frontiers of Numerical Analysis.* Springer Berlin Heidelberg, pp.143-194.

Monaghan, J. J. and Kajtar, J. B. (2009) 'SPH particle boundary forces for arbitrary boundaries', *Computer Physics Communications*, 180 (10), pp.1811-1820.

Monaghan, J. J., Kos, A. and Issa, N. (2003) 'Fluid motion generated by impact', *Journal of Waterway Port Coastal and Ocean Engineering-Asce*, 129 (6), pp.250-259.

Muller, M., Schirm, S., Teschner, M., Heidelberger, B. and Gross, M. (2004) 'Interaction of fluids with deformable solids', *Computer Animation and Virtual Worlds*, 15 (3-4), pp.159-171.

Murphy, P. J. and Aguirre, E. J. (1985) 'Bed-load or suspended-load', *Journal of Hydraulic Engineering-Asce*, 111 (1), pp.93-107.

Nguyen, V. P., Rabczuk, T., Bordas, S. and Duflot, M. (2008) 'Meshless methods: A review and computer implementation aspects', *Math. Comput. Simul.*, 79 (3), pp.763-813.

Popov, V. L. (2010) *Contact Mechanics and Friction : Physical Principles and Applications.* Berlin : Springer.

Radice, A., Malavasi, S. and Ballio, F. (2008) 'Sediment kinematics in abutment scour', *Journal of Hydraulic Engineering-Asce*, 134 (2), pp.146-156.

Schmeeckle, M. W., Nelson, J. M. and Shreve, R. L. (2007) 'Forces on stationary particles in near-bed turbulent flows', *Journal of Geophysical Research-Earth Surface*, 112 (F2).

Shao, S. D. and Lo, E. Y. M. (2003) 'Incompressible SPH method for simulating Newtonian and non-Newtonian flows with a free surface', *Advances in Water Resources*, 26 (7), pp.787-800.

Shields, A. (1936) Anwendungen der Ähnlichkeitsmechanik und der Turbulenzforschung auf die Geschiebebewegungen. *Mitteilungen der Preussische Versuchsanstalt für Wasserbau und Schiffbau* Heft 26, Preussische Versuchsanstalt für Wasserbau und Schiffbau, Berlin (in German).

Smart, G. M. and Habersack, H. M. (2007) 'Pressure fluctuations and gravel entrainment in rivers', *Journal of Hydraulic Research*, 45 (5), pp.661-673.

Tavarez, F. A. and Plesha, M. E. (2007) 'Discrete element method for modelling solid and particulate materials', *International Journal for Numerical Methods in Engineering*, 70 (4), pp.379-404.

Teufelsbauer, H., Wang, Y., Pudasaini, S. P., Borja, R. I. and Wu, W. (2011) 'DEM simulation of impact force exerted by granular flow on rigid structures', *Acta Geotechnica*, 6 (3), pp.119-133.

Unger, J. and Hager, W. (2007) 'Down-flow and horseshoe vortex characteristics of sediment embedded bridge piers', *Experiments in Fluids*, 42 (1), pp.1-19.

Valyrakis, M., Diplas, P., Dancey, C. L., Greer, K. and Celik, A. O. (2010) 'Role of instantaneous force magnitude and duration on particle entrainment', *Journal of Geophysical Research-Earth Surface*, 115.

Vetsch, D. (2012) Numerical Simulation of Sediment Transport with Meshfree Methods. *VAW Mitteilung* 219, Boes, R. (ed.), VAW ETH Zurich, Zürich.

Violeau, D. and Issa, R. (2007) 'Numerical modelling of complex turbulent free-surface flows with the SPH method: an overview', *International Journal for Numerical Methods in Fluids*, 53 (2), pp.277-304.

Wu, F. C. and Chou, Y. J. (2003) 'Rolling and lifting probabilities for sediment entrainment', *Journal of Hydraulic Engineering-Asce*, 129 (2), pp.110-119.

Wu, F. C. and Lin, Y. C. (2002) 'Pickup probability of sediment under log-normal velocity distribution', *Journal of Hydraulic Engineering-Asce*, 128 (4), pp.438-442.

Wu, F. C. and Yang, K. H. (2004) 'Entrainment probabilities of mixed-size sediment incorporating near-bed coherent flow structures', *Journal of Hydraulic Engineering-Asce*, 130 (12), pp.1187-1197.

Yalin, M. S. (1977) *Mechanics of sediment transport.* 2nd edn. Pergamon Press, Toronto.

Bisher erschienene Berichte des Lehrstuhls und der Versuchsanstalt für Wasserbau und Wasserwirtschaft, Technische Universität München

Nr. 1 **Häusler Erich:** Energieumwandlung bei einem frei fallenden, kreisrunden Strahl in einem Wasserpolster, 1962, *vergriffen*

Nr. 2 **Spiekermann, Günter:** Instabile Formen des Schußstrahles beim Abfluß unter Schützen und seine Kraftwirkungen auf die Schützenkonstruktion, 1962, *vergriffen*

Nr. 3 **Linder Gaspar:** Über die Gestaltung von Durchlaßausläufen, 1963, *vergriffen*

Nr. 4 **Knauss Jost:** Modellversuche über die Hochwasserentlastungsanlagen an kleinen Rückhaltespeichern in Südbayern, 1963, *vergriffen*

Nr. 5 **Mahida Vijaysinh:** Mechanismus der Schnellsandfiltration, 1964, *vergriffen*

Nr. 6 **Rothmund, Hermann:** Energieumwandlung durch Strahlumlenkung in einer Toskammer, 1966, *vergriffen*

Nr. 7 **Häusler Erich:** Luftsiphons für den pneumatischen Verschluß von Wassereinlauföffnungen, 1966, *vergriffen*

Nr. 8 **Seus Günther J.:** Die Anfangskavitation, 1966, *vergriffen*

Nr. 9 **Knauss Jost:** Schießender Abfluß in offenen Gerinnen mit fächerförmiger Verengung, 1967, *vergriffen*

Nr. 10 **Häusler Erich; Bormann Klaus:** Schießender bzw.strömender Abfluß in Bächen
Schultz Gert A.: Die Anwendung von Computer-Programmen für das Unit-Hydrograph-Verfahren am Beispiel der Iller
Bauch Wolfram: Untersuchungen über Wasserstandsvorhersagen an einem 600 m langen Modell der Donaustrecke Regensburg-Straubing, 1967, *vergriffen*

Nr. 11 **Schultz Gert A.:** Bestimmung theoretischer Abflußganglinien durch elektronische Berechnung von Niederschlagskonzentration und Retention (Hyreun-Verfahren), 1968, *vergriffen*

Nr. 12 **Raumer Friedrich von:** Verteilung von Bewässerungswasser in Kanälen - Eine Systematik großer Kanalsysteme zur Verteilung von Bewässerungswasser unter besonderer Berücksichtigung von Regulier- und Meßvorgängen, 1968, *vergriffen*

Nr. 13 **Bormann Klaus:** Der Abfluß in Schußrinnen unter Berücksichtigung der Luftaufnahme, 1968

Nr. 14 **Scheuerlein Helmut:** Der Rauhgerinneabfluß, 1968, *vergriffen*

Nr. 15 **Koch Kurt:** Die gegenseitige Strahlablenkung auf horizontaler Sohle, 1968

Nr. 16 **Bauch Wolfram:** Die Hochwasserwelle im ungestauten und gestauten Fluß, 1968

Nr. 17 **Marr Gerhard:** Vergleich zweier Differenzenverfahren in einem mathematischen Modell zur Berechung von instationären Abflußvorgängen in Flüssen, 1970, *vergriffen*

Nr. 18 **Herbrand Karl:** Der räumliche Wechselsprung, 1970, *vergriffen*

Nr. 19 **Seus Günther J.:** Betrachtungen zur Kontinuitätsbedingung der Hydromechanik;
Zielke Werner: Zur linearen Theorie langer Wellen in Freispiegelgerinnen, 1971

Nr. 20 **Häusler Erich:** Entnahmetürme mit Luftsiphons, 1971, *vergriffen*

Nr. 21 **Herbrand Karl:** Das Tosbecken mit seitlicher Aufweitung, 1971

Nr. 22 **Knauss Jost:** Hydraulische Probleme beim Entwurf von Hochwasserentlastungsanlagen an großen und kleinen Staudämmen, 1971, *vergriffen*

Nr. 23 **Zielke Werner:** Brechnung der Frequenzganglinien und Eigenschwingungen von Rohrleitungssystemen
Zielke Werner; Wylie E. Benjamin: Zwei Verfahren zur Berechnung instationärer Strömungen in Gasfernleitungen und Gasrohrnetzen, 1971

Nr. 24 **Knauss Jost:** Wirbel an Einläufen zu Wasserkraftanlagen, 1972, *vergriffen*

Nr. 25 **Kotoulas Dimitrios:** Die Wildbäche Süddeutschlands und Griechenlands, Teil 1, 1972, *vergriffen*

Nr. 26 **Keller Andreas:** Experimentelle und theoretische Untersuchungen zum Problem der modellmäßigen Behandlung von Strömungskavitation, 1973, *vergriffen*

Nr. 27 **Horn Heinrich:** Hochwasserabfluß in automatisch geregelten Staustufen, 1973

Nr. 28 **Bonasoundas Markos:** Strömungsvorgang und Kolkproblem am runden Brückenpfeiler, 1973

Nr. 29 **Horn Heinrich; Zielke Werner:** Das dynamische Verhalten von Flußstauhaltungen, 1973

Nr. 30 **Uslu Orhan:** Dynamische Optimierung der Fließbeiwerte in mathematischen Flußmodellen und Berücksichtigung der Vorlandüberströmung - Eine Anwendung des Operations Research im theoretischen Flußbau, 1974

Nr. 31 **Kotoulas Dimitrios:** Die Wildbäche Süddeutschlands und Griechenlands, Teil 2, 1975, *vergriffen*

Nr. 32 **50 Jahre Versuchsanstalt Obernach**
Hartung Fritz: Einführung: Was treiben eigentlich die Obernacher?
Knauss Jost: Strategien und Entscheidungshilfen beim Hochwasserschutz in Städten, dargestellt am Beispiel der Hochwasserfreilegung der Stadt Harburg an der Wörnitz
Häusler Erich: Abstürze und Stützschwellen in hydraulischer und konstruktiver Betrachtung (Mindestfallhöhen zur Erzielung einer genügenden hydraulischen Wirksamkeit)
Seus Günther J.; Hack Hans-Peter: Erster Vergleich der Ergebnisse des physikalischen Modells in Obernach mit denen des neuen mathematischen Modells
Uslu Orhan; Schmitz Gerd: Parameteridentifikation und Sensitivitätsanalyse bei mathematischen Modellen in der Hydrologie
Keller Andreas; Zielke Werner: Veränderung des freien Gasgehaltes in turbulenten Rohrströmungen bei plötzlichen Druckabsenkungen
Herbrand Karl: Zusammenführung von Schußstrahlen. Zwei praktische Beispiele konstruktiver Lösungen aus Modellversuchen
Zielke Werner: Grenzen der deterministischen Betrachtungsweise in der Strömungsmechanik, 1976

Nr. 33 **Probleme der Arbeit des beratenden Ingenieurs in der Wasserwirtschaft der Entwicklungsländer.** Symposium am 13.10.1976 in Wallgau
Bauch Wolfram: Besondere Probleme bei der Planung und Ausführung der Gesamtentwässerung Busan/Korea
Bormann Klaus: Wasserkraftstudie West Kamerun und Bau der Wasserkraftanlage Batang Agam, Indonesien, zwei Entwicklungshilfe-Projekte unter extremen Bedingungen
Raumer Friedrich von: Zielvorstellungen und Verwirklichung eines wasserwirtschaftlichen Mehrzweckprojektes in Ecuador
Krombach Jürgen: Der beratende Ingenieur in Entwicklungsländern gestern und heute: Berater, Kontrolleur, Entwicklungshelfer oder Geschäftsmann? (am Beispiel wasserwirtschaftlicher Projekte), 1977

Nr. 34 **50 Jahre Versuchsanstalt Obernach,** Feierstunde am 14.10.1976 in Wallgau
Hartung Fritz: Die Wasserbauversuchsanstalt Obernach im Strom der Zeit
Bischofsberger Wolfgang: Laudatio für Professor Dr.-Ing. E. Mosonyi
Mosonyi Emil: Wasserbau, Technik oder Kunst? 1977

Nr. 35 **50 Jahre Versuchsanstalt Obernach,**
Ausleitungen aus geschiebeführenden Flüssen, Seminar am 15.10.1976 in Obernach
Cecen Kazim: Die Verhinderung des Geschiebeeinlaufes zu Wasserfassungsanlagen
Midgley D.C.: Abstraction of water from sediment-laden rivers in Southern Africa
Jacobsen J.C.: Geschiebefreie Triebwasserfassungen - Modellversuche am Beispiel des sogenannten Geschiebeabzuges
Scheuerlein Helmut: Die Bedeutung des wasserbaulichen Modellversuchs für die Gestaltung von Ausleitungen aus geschiebeführenden Flüssen, 1977

Nr. 36 **Hack Hans-Peter:** Lufteinzug in Fallschächten mit ringförmiger Strömung durch turbulente Diffusion, 1977

Nr. 37 **Csallner Klausotto:** Strömungstechnische und konstruktive Kriterien für die Wahl zwischen Druck- und Zugsegment als Wehrverschluß, 1978

Nr. 38 **Kanzow Dietz:** Ein Finites Element Modell zur Berechnung instationärer Abflüsse in Gerinnen und seine numerischen Eigenschaften, 1978

Nr. 39 **Keller Andreas; Prasad Rama:** Der Einfluß der Vorgeschichte des Testwassers auf den Kavitationsbeginn an umströmten Körpern - Ein Beitrag zur Frage der Rolle der Kavitationskeime bei Strömungskavitation, 1978

Nr. 40 **Hartung Fritz:** 75 Jahre Nilstau bei Assuan - Entwicklung und Fehlentwicklung, 1979, *vergriffen*

Nr. 41 **Knauss Jost:** Flachgeneigte Abstürze, glatte und rauhe Sohlrampen
Scheuerlein Helmut: Wasserentnahme aus geschiebeführenden Flüssen
Häusler Erich: Unkonventionelle neuere Stauhaltungswehre an bayerischen Flüssen als gleichzeitige Sohlsicherungsbauwerke, 1979, *vergriffen*

Nr. 42 **Seus Günther J.; Joeres Erhard P.; Engelmann Herbert M.:** Lineare Entscheidungsregeln und stochastische Restriktionen bei Bemessung und Betrieb von Speichern, 1979, *vergriffen*

Nr. 43 **Meier Rupert C.:** Analyse und Vorhersage von Trockenwetterabflüssen - Eine Anwendung der Systemhydrologie, 1980, *vergriffen*

Nr. 44 **Treske Arnold:** Experimentelle Überprüfung numerischer Berechnungsverfahren von Hochwasserwellen, 1980, *vergriffen*

Nr. 45 **Csallner Klausotto; Häusler Erich**: Abflußinduzierte Schwingungen an Zugsegmenten - Ursachen, Sanierung und allgemeine Folgerungen
Herbrand Karl; Renner Dietrich: Aufnahme und Wiedergabe der Bewegung von Schwimmkörpern mit einem Video-Meßsystem
Keller Andreas: Messungen des Kavitationskeimspektrums im Nachstrom eines Schiffes - die ersten Großausführungsmessungen mit der Laser-Streulichtmethode
Knauss Jost: Neuere Beispiele für Blocksteinrampen an Flachlandflüssen
Scheuerlein Helmut: Der gelbe Fluß - nach wie vor Chinas Sorge oder die Unerbittlichkeit der Natur gegenüber 4000 Jahren menschlicher Bemühungen
Seus Günther J.: Nochmals: Das Muskingum-Verfahren. Fingerübungen zu einem bekannten Thema als "gradus ad parnassum" sowie neue Gedanken zur Interpretation des Anwendungsbereiches und eine Lösung des Problems der Nebenflüsse
Treske Arnold: Hochwasserentlastung an Dämmen. Zwei konstruktiv ähnliche Lösungen im Modellversuch, 1981, *vergriffen*

Nr. 46 **Schmitz Gerd:** Instationäre Eichung mathematischer Hochwasserablauf-Modelle auf der Grundlage eines neuen Lösungsprinzips für hyperbolische Differentialgleichungs-Systeme, 1981, *vergriffen*

Nr. 47 **Scheuerlein Helmut:** Der wasserbauliche Modellversuch als Hilfsmittel bei der Bewältigung von Verlandungsproblemen in Flüssen
Knauss Jost: Rundkronige und breitkronige Wehre, hydraulischer Entwurf und bauliche Gestaltung
Keller Andreas: Maßstabseffekte bei der Anfangskavitation, 1983, *vergriffen*

Nr. 48 **Renner Dietrich:** Schiffahrtstechnische Modellversuche für Binnenwasserstraßen - Ein neues System und neue Auswertungsmöglichkeiten, 1984, *vergriffen*

Nr. 49 **Sonderheft: Erhaltung und Umbau alter Wehre** (Wasserbau im historischen Ensemble, drei Beispiele aus dem Hochwasserschutz bayerischer Städte), 1984, *vergriffen*

Nr. 50 **Knauss Jost; Heinrich B.; Kalcyk H.:** Die Wasserbauten der Minyer in der Kopais - die älteste Flußregulierung Europas, 1984, *vergriffen*

Nr. 51 **Hartung Fritz; Ertl Walter; Herbrand Karl:** Das Donaumodell Straubing als Hilfe für die Planung und Bauausführung der Staustufe Straubing, 1984

Nr. 52 **Hahn Ulrich:** Lufteintrag, Lufttransport und Entmischungsvorgang nach einem Wechselsprung in flachgeneigten, geschlossenen Rechteckgerinnen, 1985

Nr. 53 **Bergmann Norbert:** Entwicklung eines Verfahrens zur Messung und Auswertung von Strömungsfeldern am wasserbaulichen Modell, 1985

Nr. 54 **Schwarz Jürgen:** Druckstollen und Druckschächte - Bemessung und Konstruktion, 1985, *vergriffen*

Nr. 55 **Schwarz Jürgen:** Berechnung von Druckstollen - Entwicklung und Anwendung eines mathematischen Modells und Ermittlung der felsmechanischen Parameter, 1987

Nr. 56 **Seus Günther J.; Edenhofer Johann; Czirwitzky Hans-Joachim; Kiefer Ernst-Martin; Schmitz Gerd; Zunic Franz:** Ein HN-Modellsystem für zweidimensionale, stationäre und instationäre Strömungen beim Hochwasserschutz von Städten und Siedlungen, 1987

Nr. 57 **Knauss Jost:** Die Melioration des Kopaisbeckens durch die Minyer im 2. Jt.v.Chr.; Kopais 2 - Wasserbau und Siedlungsbedingungen im Altertum, 1987

Nr. 58 **Mtalo Felix:** Geschiebeabzug aus Kanälen mit Hilfe von Wirbelröhren, 1988

Nr. 59 **Yalin M. Selim; Scheuerlein Helmut**: Friction factors in alluvial rivers
Yalin M. Selim: On the formation mechanism of dunes and ripples
Keller Andreas: Cavitation investigations at one family of NACA-hydrofoils at different angles of attack, as a contribution to the clarification of scale effects at cavitation inception, 1988

Nr. 60 **Schmitz Gerd H.:** Strömungsvorgänge auf der Oberfläche und im Bodeninneren beim Bewässerungslandbau. Grundlagen, Kritik der herkömmlichen Praxis und neue hydrodynamisch-analytische Modelle zur Oberflächenbewässerung, 1989

Nr. 61 **Muckenthaler Peter:** Hydraulische Sicherheit von Staudämmen, 1989, *vergriffen*

Nr. 62 **Kalenda Reinhard:** Zur Quantifizierung der hydraulischen Versagenswahrscheinlichkeit beweglicher Wehre, 1990

Nr. 63 **Knauss Jost:** Kopais 3, Wasserbau und Geschichte, Minysche Epoche - Bayerische Zeit (vier Jahrhunderte - ein Jahrzehnt), 1990

Nr. 64 **Kiefer Ernst-Martin, Liedl Rudolf, Schmitz Gerd H. und Seus Günther J.:** Konservative Strömungsmodelle auf der Basis krummliniger Koordinaten unter besonderer Berücksichtigung von Wasserbewegungen im ungesättigt-gesättigten Boden, 1990

Nr. 65 **Hartung Fritz:** Der ägyptische Nil 190 Jahre im Spiel der Politik (1798-1988)
Hartung Fritz: Gedanken zur Problematik der Nilwehre
Döscher Hans-Dieter und Hartung Fritz: Kritische Betrachtungen zum Stützwehr im Toschka-Entlastungsgerinne des Assuan-Hochdammes, 1991

Nr. 66 **Schmitz Gerd H., Seus Günther J. und Liedl Rudolf:** Ein semi-analytisches Infiltrationsmodell für Füllung und Entleerung von Erdkanälen
Keller Andreas P.: Chinese-German comparative cavitation tests in different test facilities on models of interest for hydraulic civil engineering, 1991

Nr. 67 **Liedl Rudolf:** Funktionaldifferentialgleichungen zur Beschreibung von Wasserbewegungen in Böden natürlicher Variabilität - Beiträge zur Theorie und Entwicklung eines numerischen Lösungsverfahrens, 1991

Nr. 68 **Zunic Franz:** Gezielte Vermaschung bestehender Kanalisationssysteme - Methodische Studien zur Aktivierung freier Rückhalteräume unter besonderer Berücksichtigung der Abflusssteuerung, 1991

Nr. 69 **Eickmann Gerhard:** Maßstabseffekte bei der beginnenden Kavitation - Ihre gesetzmäßige Erfassung unter Berücksichtigung der wesentlichen Einflußgrößen, 1991

Nr. 70 **Schmid Reinhard:** Das Tragverhalten von Erd- und Steinschüttdämmen mit Asphaltbeton-Kerndichtungen, 1991

Nr. 71 **Kiefer Ernst-Martin:** Hydrodynamisch-numerische Simulation der Wasserbewegung im ungesättigten und gesättigten Boden unter besonderer Berücksichtigung seiner natürlichen Variabilität, 1991

Nr. 72 **Strobl Th., Steffen H., Haug W. und Geiseler W.-D.:** Kerndichtungen aus Asphaltbeton für Erd- und Steinschüttdämme, 1992

Nr. 73 **Symposium: Betrieb, Unterhalt und Modernisierung von Wasserbauten**
Garmisch-Partenkirchen, 29. - 31. Oktober 1992

Nr. 74 **Heilmair Thomas und Strobl Theodor:** Erfassung der sohlnahen Strömungen in Ausleitungsstrecken mit FST-Halbkugeln und Mikro-Flowmeter - ein Vergleich der Methoden, 1994

Nr. 75 **Godde Dominik:** Experimentelle Untersuchungen zur Anströmung von Rohrturbinen.
Ein Beitrag zur Optimierung des Turbineneinlaufs, 1994

Nr. 76 **Knauss Jost:** Von der Oberen zur Unteren Isar
Alte und neue Wasserbauten rund um die Benediktenwand. Bachumleitungen, Treibholzfänge, durchschwallte Rohre, eine besondere Entlastungsanlage
Sohlensicherung an der Unteren Isar. Sohlstufenkonzept - Belegung der Sohle mit größeren Steinen in offener Anordnung, 1995

Nr. 77 **Knauss Jost:** Argolische Studien: Alte Straßen - alte Wasserbauten. Talsperre von Mykene; Flußumleitung von Tiryns; Hydra von Lerna; Küstenpass Anigraia, 1996

Nr. 78 **Aufleger Markus:** Ein Beitrag zur Auswertung von Erddruckmessungen in Staudämmen, 1996

Nr. 79 **Heilmair Thomas:** Hydraulische und morphologische Kriterien bei der Beurteilung von Mindestabflüssen unter besonderer Berücksichtigung der sohlnahen Strömungsverhältnisse, 1997

Nr. 80 **Maile Willibald:** Bewertung von Fließgewässer-Biozönosen im Bereich von Ausleitungskraftwerken (Schwerpunkt Makrozoobenthos), 1997

Nr. 81 **Knauss Jost:** Olympische Studien: Herakles und der Stall des Augias. Kladeosmauer und Alpheiosdamm, die Hochwasserfreilegung von Alt-Olympia, 1998

Nr. 82 **Symposium: Planung und Realisierung im Wasserbau - Vergleich von Zielvorstellungen mit den Ergebnissen,** Garmisch-Partenkirchen 15. – 17. Oktober 1998

Nr. 83 **Hauger Stefan:** Verkehrssteuerung auf Binnenwasserstraßen – Ein Beitrag zur Optimierung der Schleusungsreihenfolge in Stillwasserkanälen und staugeregelten Flüssen, 1998

Nr. 84 **Herbrand Karl:** Schiffahrtstechnische Untersuchungen der Versuchsanstalt Obernach; Ein Rückblick auf ein traditionelles Untersuchungsgebiet der VAO, 1998

Nr. 85 **Hartlieb Arnd:** Offene Deckwerke – Eine naturnahe Methode zur Sohlstabilisierung eintiefungsgefährdeter Flußabschnitte, 1999

Nr. 86 **Spannring Michael:** Die Wirkung von Buhnen auf Strömung und Sohle eines Fließgewässers: Parameterstudie an einem numerischen Modell, 1999

Nr. 87 **Kleist Frank:** Die Systemdurchlässigkeit von Schmalwänden. Ein Beitrag zur Herstellung von Schmalwänden und zur Prognose der Systemdurchlässigkeit, 1999

Nr. 88 **Lang Tobias:** Geometrische Kriterien zur Gestaltung von Kraftwerkseinläufen. Experimentelle Untersuchungen an Rohr-S-Turbine und Durchströmturbine, 1999

Nr. 89 **Aufleger Markus:** Verteilte faseroptische Temperaturmessungen im Wasserbau, 2000

Nr. 90 **Knauss Jost:** Späthelladische Wasserbauten. Erkundungen zu wasserwirtschaftlichen Infrastrukturen der mykenischen Welt, 2001

Nr. 91 **Festschrift** aus Anlass des 75-jährigen Bestehens der Versuchsanstalt für Wasserbau und Wasserwirtschaft der Technischen Universität München in Obernach; Oskar v. Miller-Institut, 2001

Nr. 92 **Wildner Harald:** Injektion von porösem Massenbeton mit hydraulischen Bindemitteln, 2002

Nr. 93 **Wildbach Naturversuche**
Loipersberger Anton und Sadgorski Constantin: Schwemmholz in Wildbächen: Problematik und Abhilfemaßnahmen; Geschiebeuntersuchungen; 1D und 2D Abflussmodelle in einem Wildbach
Rimböck Andreas: Naturversuch Seilnetzsperren zum Schwemmholzrückhalt in Wildbächen: Planung, Aufbau, Versuchsdurchführung und Ergebnisse
Hübl Johannes und Pichler Andreas: Zur berührungslosen Erfassung der Fließtiefe und Fließgeschwindigkeit in einem Wildbachgerinne zum Zeitpunkt des Durchganges der Hochwasserwelle, 2002

Nr. 94 **Rimböck Andreas:** Schwemmholzrückhalt in Wildbächen – Grundlagen zu Planung und Berechnung von Seilnetzsperren, 2003

Nr. 95 **Nothhaft Sabine:** Die hydrodynamische Belastung von Störkörpern, 2003

Nr. 96 **Schmautz Markus:** Eigendynamische Aufweitung in einer geraden Gewässerstrecke: Entwicklung und Untersuchungen an einem numerischen Modell, 2003

Nr. 97 **Neuner Johann:** Ein Beitrag zur Bestimmung der horizontalen Sicherheitsabstände und Fahrrinnenbreiten für Wasserstraßen, 2004

Nr. 98 **Göhl Christian:** Bypasseinrichtungen zum Abstieg von Aalen an Wasserkraftanlagen, 2004

Nr. 99 **Haimerl Gerhard:** Groundwater Recharge in Wadi Channels Downstream of Dams: Efficiency and Management Strategies, 2004

Nr. 100 **Symposium: Lebensraum Fluss – Hochwasserschutz, Wasserkraft, Ökologie. Band 1;** Wallgau, Oberbayern, 16. bis 19. Juni 2004

Nr. 101 **Symposium: Lebensraum Fluss – Hochwasserschutz, Wasserkraft, Ökologie. Band 2;** Wallgau, Oberbayern, 16. bis 19. Juni 2004

Nr. 102 **Huber Richard:** Geschwindigkeitsmaßstabseffekte bei der Kavitationserosion in der Scherschicht nach prismatischen Kavitatoren, 2004

Nr. 103 **Exposed Thermoplastic Geomembranes for Sealing of Water Conveyance Canals**, Guidelines for Design, Supply, Installation, 2005

Nr. 104 **Workshop „Anwendung und Grenzen physikalischer und numerischer Modelle im Wasserbau".** Wallgau, Oberbayern, 29. und 30. September 2005

Nr. 105 **Conrad Marco:** A contribution to the thermal stress behaviour of Roller-Compacted-Concrete (RCC) gravity dams – Field and numerical investigations, 2006

Nr. 106 **Schäfer Patrick:** Basic Research on Rehabilitation of Aged Free Flow Canals with Geomembranes, 2006

Nr. 107 **Deichertüchtigung und Deichverteidigung in Bayern.** Beiträge zur Fachtagung am 13. und 14. Juli 2006 in Wallgau, Oberbayern, 2006

Nr. 108 **Porras Pablo:** Fiber optic temperature measurements – Further Development of the Gradient Method for Leakage Detection and Localization in Earthen Structures, 2007

Nr. 109 **Perzlmaier Sebastian:** Verteilte Filtergeschwindigkeitsmessung in Staudämmen, 2007

Nr. 110 **Wasserbau an der TU München** – Symposium zu Ehren von Prof. Theodor Strobl am 16. März 2007 in Wallgau, Oberbayern, 2007

Nr. 111 **Haselsteiner Ronald:** Hochwasserschutzdeiche an Fließgewässern und ihre Durchsickerung, 2007

Nr. 112 **Schwarz Peter und Strobl Theodor:** Wasserbaukunst - Oskar von Miller und die bewegte Geschichte des Forschungsinstituts für Wasserbau und Wasserwirtschaft in Obernach am Walchensee (1926-1951). 120 Seiten, Preis: 9,80 €, 2007

Nr. 113 **Flutpolder: Hochwasserrückhaltebecken im Nebenschluss**. Beiträge zur Fachtagung am 19. und 20. Juli 2007 in Wallgau, Oberbayern. ISBN 978-3-940476-03-6, 240 Seiten, durchgehend farbige Abbildungen, Preis: 34,80 €, 2007

Nr. 114 **Assessment of the Risk of Internal Erosion of Water Retaining Structures: Dams, Dykes and Levees.** Intermediate Report of the European Working Group of ICOLD. ISBN 978-3-940476-04-3, 220 Seiten, Preis: 29,80 €, 2007

Nr. 115 **14. Deutsches Talsperrensymposium** (14th German Dam Symposium) and **7th ICOLD European Club Dam Symposium**. Beiträge zur Tagung am 17. bis 19. September 2007 in Freising (Contributions to the Symposium on 17 - 19 September 2007 in Freising, Germany). ISBN 978-3-940476-05-0, 570 Seiten, Preis: 49,80 €, 2007

Nr. 116 **Niedermayr Andreas:** V-Rampen – Ökologisch weitgehend durchgängige Querbauwerke. ISBN 978-3-940476-06-7, 240 Seiten, Preis: 29,80 €, 2008

Nr. 117 **Hafner Tobias:** Uferrückbau und eigendynamische Gewässerentwicklung – Aspekte der Modellierung und Abschätzungsmöglichkeiten in der Praxis. ISBN 978-3-940476-07-4, 206 Seiten, Preis: 29,80 €, 2008

Nr. 118 **Wang Ruey-wen:** Aspects of Design and Monitoring of Nature-Like Fish Passes and Bottom Ramps. ISBN 978-3-940476-10-4, 280 Seiten, Preis: 29,80 €, 2008

Nr. 119 **Fischer Markus:** Ungesteuerte und gesteuerte Retention entlang von Fließgewässern: Beurteilung der Wirksamkeit möglicher Maßnahmen unter Verwendung hydrodynamisch-numerischer Modellierung. ISBN 978-3-940476-11-1, 220 Seiten, Preis: 29,80 €, 2008

Nr. 120 **Fiedler Katharina:** Erfassung hydromorphologischer Vorgänge in Fließgewässern mit Hilfe von ADCP-Messungen. ISBN 978-3-940476-12-8, Preis: 29,80 €, 2008

Nr. 121 **Hoepffner Roland:** Distributed Fiber Optic Strain Sensing in Hydraulic Engineering. ISBN 978-3-940476-13-5, Preis: 29,80 €, 2008

Nr. 122 **Gewässermorphologie und EU-WRRL:** Beiträge zur Fachtagung am 24. und 25. Juli 2008 in Wallgau, Oberbayern. ISBN 978-3-940476-15-9, 230 Seiten, durchgehend farbige Abbildungen, Preis: 34,80 €, 2008

Nr. 123 **Zukunftsfähiger(s) Wasserbau und Flussgebietsmanagement – Wasser- und Feststoff-transport in Fläche und Fluss**. Beiträge zur Fachtagung am 30. und 31. Juli 2009 in Wallgau, Oberbayern. ISBN 978-3-940476-19-7, 104 Seiten, durchgehend farbige Abbildungen, Preis: 9,80 €, 2009

Nr. 124 **Peter Rutschmann (Hrsg.): Wasserbau in Bewegung ... von der Statik zur Dynamik.** Beiträge zum 15. Gemeinschafts-Symposium der Wasserbau-Institute TU München, TU Graz und ETH Zürich vom 1. bis 3. Juli 2010 in Wallgau, Oberbayern. ISBN 978-3-940476-22-7, 624 Seiten, teils farbige Abbildungen, Preis: 59,00 €, 2010

Nr. 125 **14. Treffen junger WissenschaftlerInnen an Wasserbauinstituten**. Beiträge zum JuWi-Treffen am 25. und 26. Juni 2012 an der Technischen Universität München. ISBN 978-3-940476-23-4, ca. 220 Seiten, Preis: 14,80 €, 2012

Nr. 126 **Efthymiou Nikolaos:** Transient Bedload Transport of Sediment Mixtures under Disequilibrium Conditions - An Experimental Study and the Development of a New Dynamic Hiding Function. ISBN 978-3-940476-24-1, ca. 300 Seiten, Preis: 29,80 €, 2012:.

Die Berichtsbände können beim Lehrstuhl für Wasserbau und Wasserwirtschaft bestellt werden:

E-Mail: s.machauer@bv.tum.de

Telefon: +49.89.289.23174